

LIGAND BACKBONE EFFECTS IN IRIDIUM Pincer COMPLEXES
An Experimental and Theoretical Approach

EFFEKTE DES LIGANDENRÜCKGRATS AUF IRIDIUM-PINCER-
KOMPLEXE

Ein experimenteller und theoretischer Zugang

DISSERTATION

der Fakultät für Chemie und Pharmazie
der Eberhard Karls Universität Tübingen

zur Erlangung des Grades eines Doktors
der Naturwissenschaften

2010

vorgelegt von

Wolfgang Leis

Tag der mündlichen Prüfung: 15. März 2010

Dekan: Prof. Dr. Lars Wesemann

1. Berichterstatter: Prof. Dr. Hermann A. Mayer
2. Berichterstatter: Priv. Doz. Dr. Hans-Georg Mack

Die vorliegende Arbeit wurde am
Institut für Anorganische Chemie der
Eberhard Karls Universität Tübingen
unter Anleitung von
Herrn Prof. Dr. Hermann A. Mayer
durchgeführt.

Mein herzlichster Dank richtet sich zunächst an meinen Doktorvater Prof. Dr. Hermann A. Mayer, für seine Begeisterung an dieser Arbeit, seine anhaltende Unterstützung bei experimentellen und / oder theoretischen Fragestellungen und die sehr guten Arbeitsbedingungen. Zudem möchte ich mich für das anhaltend gute und freundschaftliche Arbeitsklima sowie für zahllose anregende Diskussionen über die noch immer spannende Chemie von Pincer-Komplexen bedanken.

Weiterhin danke ich den chemischen Instituten der Fakultät, im speziellen dem Institut für Anorganische Chemie und der Universität Tübingen für die Möglichkeit vielfältige, moderne analytische Techniken nutzen zu können.

Der Deutschen Forschungsgemeinschaft danke ich für die Finanzierung dieser Arbeit im Rahmen des Graduiertenkolleg „Chemie in Interphasen - Synthese, Dynamik und Anwendung polymerfixierter aktiver Zentren“.

Zudem gilt mein Dank:

Herrn Priv. Doz. Dr. Hans-Georg Mack für seine freundliche und anhaltende Unterstützung bei allen Fragestellungen die quantenchemischen Rechnungen betreffend.

Herrn Dr. Johannes W. Wielandt und seinen Mitarbeitern (D. Ruckerbauer und S. Kupsa) für das zur Verfügung stellen der ersten Proben des neuartigen PCP-Pincer Liganden, für seine synthetischen Hinweise sowie für die zahlreichen fruchtbaren Diskussionen, Ratschläge und Tipps.

Herrn Prof. Dr. William C. Kaska (University of California, Santa Barbara) für seine ansteckende Begeisterung und für zahlreiche Diskussionen und Anregungen zu experimentellen und analytischen Problemen und Vorhaben.

Herrn Dr. Klaus Eichele für seine Geduld bei den zahlreichen Erläuterungen und Diskursen über theoretische und praktische Grundlagen der NMR-Spektroskopie sowie für seine freundschaftliche Unterstützung bei allerlei Computer-technischen Schwierigkeiten.

Frau Angelika Ehmann für die Einführung in die praktische Bedienung der verschiedenen NMR-Spektrometer, für die Vorbereitung der Tieftemperatur-Messungen sowie für ihre allgemeine Unterstützung.

Frau Dr. Cäcilia Maichle-Mössmer und Frau Elke Niquet für das Aufnehmen und Auswerten der Einkristallstrukturdaten.

Herrn Dr. Graeme Nicholson, Frau Dr. Dorothee Wistuba für die Messung der ESI-FTICR Massenspektren sowie für deren Unterstützung bei der Bedienung des ESI-Iontrap-Spektrometers.

Den Mitarbeitern (Dr. Roland Müller, Frau Claudia Krause und Herrn Hans Bartholomä) der Massenspektrometrie für die Messung der Routine EI-, FAB- und FD-Spektren.

Herrn Dr. Wolfgang Bock für die Durchführung aller Elementar-Analysen.

Den Mitarbeitern (Dipl.-Phys. Walter Schaal, Robert Baart, Eberhard Braun, Gerd Vollmer) der technischen Werkstätten des chemischen Zentralinstituts für die Unterstützung bei jeglichen praktischen und technischen Schwierigkeiten und anfallenden Reparaturen.

Den Mitarbeitern der Glasbläserei (Thomas Nieß, Karin Rein, Isolde Laus) für den jederzeit

gut gelaunten Empfang, die vielfältig angefallenen Reparaturen sowie für die Spezial-Anfertigungen.

Den Mitarbeitern des Glasladens (im speziellen Cornelia Halder) für das immer wieder angenehme und unnachahmliche Einkaufserlebnis sowie für die Unterstützung bei allerlei Bestellungen.

Herrn Dr. Klaus Möschel für die freundliche Aufnahme ins IFIB und seine anhaltenden Bemühungen um unser dortiges Wohlergehen.

Meinen Vorgänger(innen) Frau Dr. Michaela Vatter (geb. Reginek), Frau Dr. Angelika Steinbrecher (geb. Winter) und Herrn Dr. Michael Marzini für die freundschaftliche Aufnahme in die Arbeitsgruppe sowie für Ihre ansteckende Begeisterung für die verschiedenen Arbeitsgebiete.

Allen Praktikanten und wissenschaftlichen Hilfskräften, die mit Ihren jeweiligen Beiträgen zum Gelingen dieser Arbeit beitragen.

Dr. Torben Gädt, Dr. Dominik Joosten, Dr. Claus Diez, Dr. Nicolas Plumere, Dr. Bernd Görlach und Adrian Ruff für zahlreiche produktive Diskussionen und gute Anregungen zu dieser Arbeit sowie für die angenehme und freundschaftliche Zusammenarbeit.

Meinen vormaligen Kolleginnen und Kollegen Dr. Flor Toledo Rodríguez, Inga Olliges-Stadler, Corinna Wetzels und Dr. David Ruiz Abad für das freundschaftliche und produktive Arbeitsklima sowie für ihre Unterstützung bei allerlei Arbeitskreis internen Aufgaben.

Meinen aktuellen Kolleginnen und Kollegen Cornelia Futter, Sophie Wernitz, Verena Feldmann und Jörg Henig für das jederzeit freundschaftliche, amüsante und anregende Arbeitsklima und für ihre Unterstützung in jeglicher Art und Weise.

Meiner Familie für ihre Unterstützung und Liebe.

Meiner Familie

Table of Contents

1	INTRODUCTION	1
2	GENERAL CONSIDERATIONS	4
2.1	<i>The different backbones in comparison</i>	4
2.2	<i>Aryl as the ligand backbone</i>	5
2.3	<i>Alkyl as the ligand backbone</i>	7
2.4	<i>Cycloheptatrienyl as the ligand backbone</i>	14
3	RESULTS AND DISCUSSION	21
3.1	<i>Functionalised phenyl PCP pincer complexes</i>	21
3.1.1	Established synthesis for functionalised phenyl PCP pincer ligands	21
3.1.2	Variations for amino functionalised phenyl PCP pincer ligands	22
3.1.3	Coordination chemistry of phenyl PCP pincer ligands	25
3.1.3.1	<i>Unmodified methoxy and nitro functionalised pincers</i>	25
3.1.3.2	<i>Coordination chemistry of protected amino functionalised pincers</i>	26
3.1.3.2.1	<i>Acetamide functionalised ligands</i>	26
3.1.3.2.2	<i>Trifluoroacetamido pincer ligand</i>	31
3.2	<i>Backbone effects in PCP pincer ligands - a theoretical approach</i>	33
3.2.1	General remarks	33
3.2.2	Functionalised phenyl backbones	35
3.2.2.1	<i>Ir(III)HCl, Ir(III)H₂ and Ir(I) complexes</i>	35
3.2.2.2	<i>Doubly-cyclometallated and metallaquinone complexes</i>	39
3.2.2.3	<i>Resume</i>	41
3.2.3	Pentane and cycloheptatriene-based backbones	42
3.2.3.1	<i>Uncharged Ir(III)HCl, Ir(III)H₂ and Ir(I) complexes</i>	43
3.2.3.2	<i>Positively charged Ir(III)HCl, Ir(III)H₂ and Ir(I) complexes</i>	47
3.2.3.3	<i>Negatively charged Ir(III)HCl, Ir(III)H₂ and Ir(I) complexes</i>	50
3.2.3.4	<i>Charged and uncharged carbonyl Ir(III)HCl, Ir(III)H₂ and Ir(I) derivatives</i>	55
3.3	<i>Calculations of the square scheme of $1b \Rightarrow 2b^+ + H_2 + e^-$</i>	61

3.4	<i>Mechanistic considerations on cycloheptatrienyl complexes</i>	65
3.4.1	General deprotonation reactions	65
3.4.2	Formation of cycloheptatriene-oxo complex	77
3.5	<i>Novel benzo-cycloheptatriene PCP pincer ligand</i>	81
3.5.1	Synthesis of the benzo-cycloheptatriene PCP Ligand	81
3.5.2	Coordination chemistry with iridium	82
3.5.3	Mass spectrometry of benzo-cycloheptatriene complexes	93
3.5.3.1	<i>Ionisation techniques and ionisation processes</i>	93
3.5.3.1.1	<i>Electro-spray ionisation</i>	93
3.5.3.1.2	<i>Fast atom bombardment ionisation</i>	93
3.5.3.1.3	<i>Ionisation process of 59</i>	94
3.5.3.2	<i>Fast atom bombardment mass spectrometry of 59</i>	97
3.5.3.3	<i>Electro-spray ionisation mass spectrometry of 59</i>	100
3.5.3.4	<i>MSⁿ experiments and FAB fragmentation</i>	105
4	COMPUTATIONAL DETAILS	111
4.1	<i>General remarks on density functional theory</i>	111
4.2	<i>Geometry optimisations</i>	112
4.3	<i>Transition state optimisations</i>	112
5	EXPERIMENTAL SECTION	114
5.1	<i>Synthetic methods</i>	114
5.1.1	Solvents and gases	114
5.1.2	Precursors and reagents	114
5.2	<i>Analytical methods and techniques</i>	115
5.2.1	Nuclear magnetic resonances spectroscopy	115
5.2.2	Infrared spectroscopy	116
5.2.3	Mass spectrometry	117
5.2.4	Elemental analysis (CHNS)	118
5.2.5	Single crystal X-ray diffraction	118
5.3	<i>Syntheses</i>	119
5.3.1	Ligand syntheses	119

5.3.1.1	<i>3,5-Di-(hydroxymethylene)aniline (51h)</i>	119
5.3.1.2	<i>N-3,5-di-(hydroxymethylene)phenyl tert-butoxycarbamate (51g)</i>	119
5.3.1.3	<i>N-3,5-di-(hydroxymethylene)phenyl acetamide (51e)</i>	119
5.3.1.4	<i>N-3,5-di-(hydroxymethylene)phenyl trifluoroacetamide (51f)</i>	119
5.3.1.5	<i>N-3,5-di-(bromomethylene)phenyl acetamide (52e)</i>	120
5.3.1.6	<i>N-3,5-di-(bromomethylene)phenyl trifluoroacetamide (52f)</i>	120
5.3.1.7	<i>N-3,5-bis-(di-tert-butyl-phosphanomethylene)phenyl acetamide (54e)</i> ...	120
5.3.1.8	<i>N-3,5-bis-(di-tert-butyl-phosphanomethylene)phenyl trifluoroacetamide (54f)</i>	121
5.3.1.9	<i>5-Nitro-iso-phthalic acid dimethyl ester (50d)</i>	122
5.3.1.10	<i>5-Nitro-iso-phthalic acid di-chloride (55d)</i>	122
5.3.1.11	<i>3,5-Di-(hydroxymethylen)nitrobenzene (51d)</i>	123
5.3.1.12	<i>3,5-Di-(bromomethylen)nitrobenzene (52d)</i>	123
5.3.1.13	<i>3,5-Bis-(di-tert-butyl-phosphanomethylen)nitrobenzene (54d)</i>	124
5.3.1.14	<i>2,7-Bis-(di-tert-butyl-phosphanomethylen)benzo[1,2-d]-1H-[7]annulene (82)</i>	125
5.3.2	Phenyl PCP complex syntheses	125
5.3.2.1	<i>Reaction of AcNHPCP with IrCl₃·H₂O</i>	125
5.3.2.2	<i>Reaction of AcNHPCP with [Ir(COD)Cl]₂</i>	125
5.3.2.3	<i>Reaction of AcNHPCP with [Ir(COE)₂Cl]₂</i>	126
5.3.2.4	<i>Reaction of FAcNHPCP with [Ir(COD)Cl]₂</i>	126
5.3.3	Benzo-cycloheptatriene PCP complex syntheses	126
5.3.3.1	<i>BCHTPCPHrHCICO (59, 83, 84)</i>	126
5.3.3.2	<i>BCHTPCPIrHCICO BF₄ (95')</i>	128
5.3.3.3	<i>Reaction of BCHTPCPHrHCICO with Me₃SiTf/HTf</i>	129
5.3.3.4	<i>Reaction of BCHTPCPIrHCICO BF₄ (95') with O₂</i>	129
6	SUMMARY	131
7	REFERENCES	135

Publikationen

- Wolfgang Leis; Hermann A. Mayer and William C. Kaska: **“Cycloheptatrienyl, alkyl and aryl PCP-pincer complexes: Ligand backbone effects and metal reactivity”** Coordination Chemistry Reviews **252** (2008) 1787-1797.
- Hermann A. Mayer, William C. Kaska, Flor Toledo Rodríguez and Wolfgang Leis: A contribution in **“Pincer ligand complexes with unusual atoms and backbones“** as chapter co-author in **“The Chemistry of Pincer Compounds”**, Eds. David Morales-Morales and Craig M. Jensen, Elsevier 2007.
- W. Leis, D. Ruckerbauer, S. Kupsa, J. W. Wielandt, W. C. Kaska, H. A. Mayer: **“Ligand Backbone Effects in Iridium-PCP-pincer complexes”** 38th International Conference on Coordination Chemistry; July 20-25, 2008; Jerusalem, Israel.
- Wolfgang Leis, Jost C. Grimm, Venkata Krishnan, Sankaran Anantharaman, Helmut Bertagnolli and Hermann A. Mayer: **“Determination of oxidation states in Ir-PCP-pincer complexes with X-ray absorption near edge spectroscopy”** 22nd International Conference on Organometallic Chemistry; July 25-29, 2006; Zaragoza, Spain.

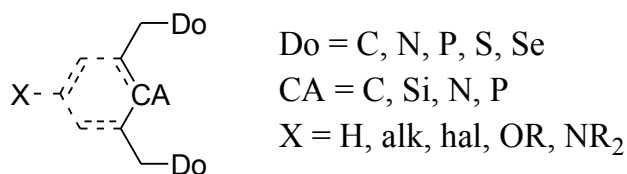
Abbreviations

APCI	atmospheric pressure chemical ionisation
accel.	accelerated
br	broad
calcd.	calculated
COD	1,5-cyclooctadiene
COE	cyclooctene
COSY	correlated spectroscopy
Cp	cyclopentadiene
DBU	1,8-diazabicyclo[5,4,0]undec-7-ene
DCM	dichloromethane
d	doublet
DFT	density functional theory
EI	electron ionisation
ESI	electro spray ionisation
Et	ethyl
FAB	fast atom bombardment
FD	field desorption
FT-ICR	Fourier transform ion cyclotron resonance
FT-IR	Fourier transform infrared spectroscopy
GGA	generalised gradient approximation
HMBC	heteronuclear multiple bond coherence (¹ H detected C,H-correlated experiment <i>via</i> two and three bonds)
HOESY	heteronuclear Overhauser enhancement spectroscopy
HOTf	trifluoromethanesulfonic acid (triflic acid)
HR	high resolution
HOMO	highest occupied molecular orbital
HSQC	heteronuclear single quantum coherence (¹ H detected X,H-correlated experiment <i>via</i> one bond)
IR	infrared
LGO	ligand group orbital
LiTMP	lithium 2,2,6,6-tetramethylpiperidide
LSDA	local spin density approximation
LUMO	lowest unoccupied molecular orbital
m	multiplet
Me	methyl
MO	molecular orbital
MS	mass spectrometry
NHC	N-heterocyclic carbene
NMR	nuclear magnetic resonance
NOESY	nuclear Overhauser enhancement spectroscopy
OTf	trifluoromethanesulfonate (triflate)

PE	polyethylene
PEEK	polyetheretherketone
Ph	phenyl
PTFE	polytetrafluoroethylene (Teflon)
q	quartet
r.t.	room temperature
RMS	root mean square
s	singlet
SCF	self consistent field
SOMO	singly occupied molecular orbital
t	triplet
^t Bu	<i>tertiary</i> -Butyl
<i>tert</i>	<i>tertiary</i>
Temp.	temperature
THF	tetrahydrofurane
TMS	tetramethylsilane
triflate	trifluoromethanesulfonate
vd	virtual doublet (higher order multiplet)
vdd	virtual doublet of doublet (higher order multiplet)
vt	virtual triplet (higher order multiplet)
XRD	X-ray diffraction
d	bond length in pm
δ	chemical shift in ppm
$\Delta\delta$	chemical shift difference in ppm
η^n	hapticity
${}^nJ_{AX}$	spin-spin coupling constant in Hz between nuclei A and X via n bonds
ν	frequency in Hz
$\tilde{\nu}$	wavenumber in cm^{-1}
m/z	mass/charge ratio
E_{ox}	oxidation potential in eV
ΔE	energies of formation for a given reaction in kJ/mol
$\Delta(\Delta E)$	difference in energies of formation in kJ/mol
$\Delta^i(\Delta E)$	difference in energies of formation for an isodesmic reaction in kJ/mol
ΔG	free enthalpies of formation for a given reaction in kJ/mol
$\Delta(\Delta G)$	difference in free enthalpies of formation in kJ/mol
\sphericalangle	bond angle in

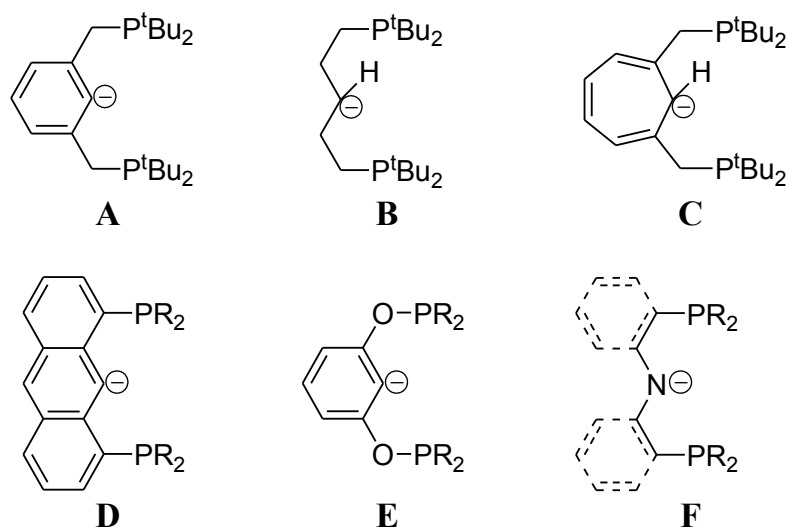
1 Introduction

The presentation in Scheme 1 offers a selection of the various pincer type ligands which were developed during the last three decades. As donor atoms (**Do**) different main group elements were applied as well as N-heterocyclic carbenes. Frequently the coordinating atoms (**CA**) are C or N while also other main group elements were used. The backbones were functionalised with different substituents (**X**) and asymmetric ligands were designed for enantioselective induction.



Scheme 1

PCAP-pincer ligands (**Do** = P and **CA** = C, N) are terdentate ligands which among others coordinate $\kappa^2P, \kappa C\text{-mer}$ for **A-E** and $\kappa^2P, \kappa N\text{-mer}$ in **F** to a metal centre (Scheme 2). These symmetric anionic bis-chelating ligands bind strongly to a wide variety of transition and non-transition metals. This bonding is achieved by the presence of at least two donor atoms (**Do**) and an *ipso*-C (**A-E**) or an *ipso*-N (**F**) metal bond, which reinforce the structure and prevent the dissociation of the metal from the ligand as well as ligand exchange processes. Early investigations have especially pointed out that the generation of two thermodynamically stable internal five-membered rings is very important.^{1,2}

**Scheme 2**

The ligand backbone and the coordinating atoms can be tailored to control the bite angle, steric environment and frontier orbitals.^{3,4} Furthermore, the meridional arrangement of the pincer ligands force all participating ligands into *cis*-positions. Taken together these factors translate into materials with exceptional thermal stability and still high reactivity.⁵⁻⁷ Since their first inceptions^{2,5,8-10} the diversity of pincer ligand systems has increased dramatically which widened the application in many areas like organometallic chemistry, reaction mechanisms, catalysis and design of new materials. Thus pincer ligand systems have left the state of curiosity and are nowadays integral parts of many concepts in chemistry.^{2,3,5,11-15}

Late transition metal complexes of the diversity of these ligands were tested in catalytic transformations. The catalytic applications of pincer complexes⁵ ranges from coupling reactions like Heck,^{6,16} Suzuki¹⁷ and Stille¹⁸ to hetero Diels-Alder,¹⁹ Michael^{20,21} and Aldol²² reactions. Especially PCP pincer complexes of iridium have been applied for the dehydrogenation of alkanes^{11,23} and the oxidative addition of ammonia.²⁴

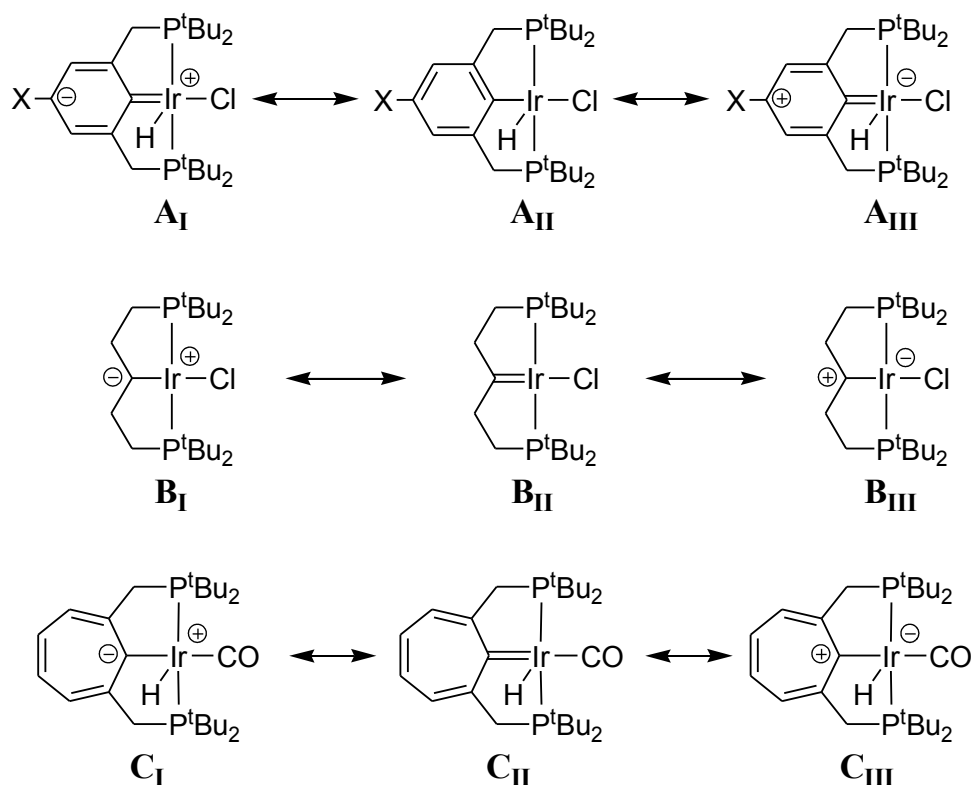
The most popular and most often used pincer ligands remain those with aryl backbones **A**, **D** and **E** (Scheme 2). The rigid phenyl or anthracene system and the strong sp^2 -carbon metal bond makes them ideal candidates for catalytic applications in synthesis. Mechanistic details were also elucidated for the complexes with phenyl backbones (**A** and **E**).^{3,11} Pincer complexes with an alkane backbone **B** have been less attractive. The high flexibility of the alkane rings as well as the higher electron-donating ability of the *ipso*- sp^3 -carbon atom in the corresponding metal complexes increase their reactivity which makes them more difficult to manip-

ulate. In comparison, recently the amine based backbone **F** became popular^{4,5,14,25-27} because of the more rigid structure and the absence of β and γ -hydrogen atoms. A novel way to expand the pincer ligand backbone is to incorporate the cycloheptatriene moiety into the ligand backbone (**C**) (Scheme 2). Previous work has demonstrated that this moiety can be an interesting and basic integral part of a pincer ligand system.²⁸⁻³⁰ The particular feature of the cycloheptatrienyl pincer complexes is their unsaturated but non-aromatic ligand backbone. This makes the cycloheptatriene moiety an intermediate between the phenyl and alkane based pincer ligands.

2 General considerations

2.1 The different backbones in comparison

The differences in chemical behaviour of the aryl, alkyl and cycloheptatriene pincer complexes can be rationalised by comparing the resonance structures given in Scheme 3. The selected examples possess metal-carbon bond polarities which are favoured by the respective ligand backbone.

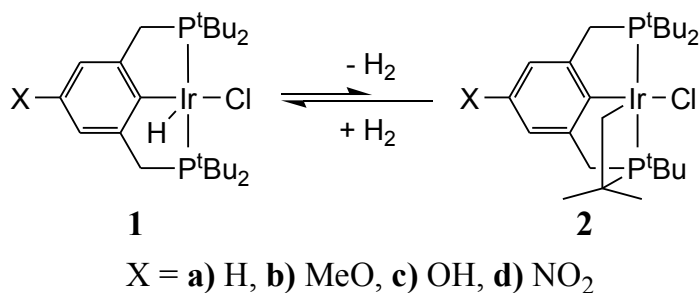


Scheme 3

For instance, if $X = \text{H}$ the resonance structures **A_I** and **A_{III}** contribute modestly to the overall bonding situation in the aryl system. Modification of the backbone with electron withdrawing or donating substituents X can influence the contribution of **A_I** and **A_{III}**. For example the metallaquinone $[\text{O}=\text{C}_6\text{H}_2-(\text{CH}_2\text{P}^t\text{Bu}_2)_2]\text{Ru}(\text{CO})_2$ ^{25,31} can be derived from **A_{III}** with $X = \text{OH}$ and formal 1,6-elimination of H_2 . Spectroscopic evidence supports the alkylidene structure **B_{II}** in the case of the alkyl complex. Furthermore it is expected that the positive charge of the aromatic 6π -electron system of the cycloheptatrienyl ring will impose a reversed polarity. Thus resonance structure **C_{III}** will gain importance.

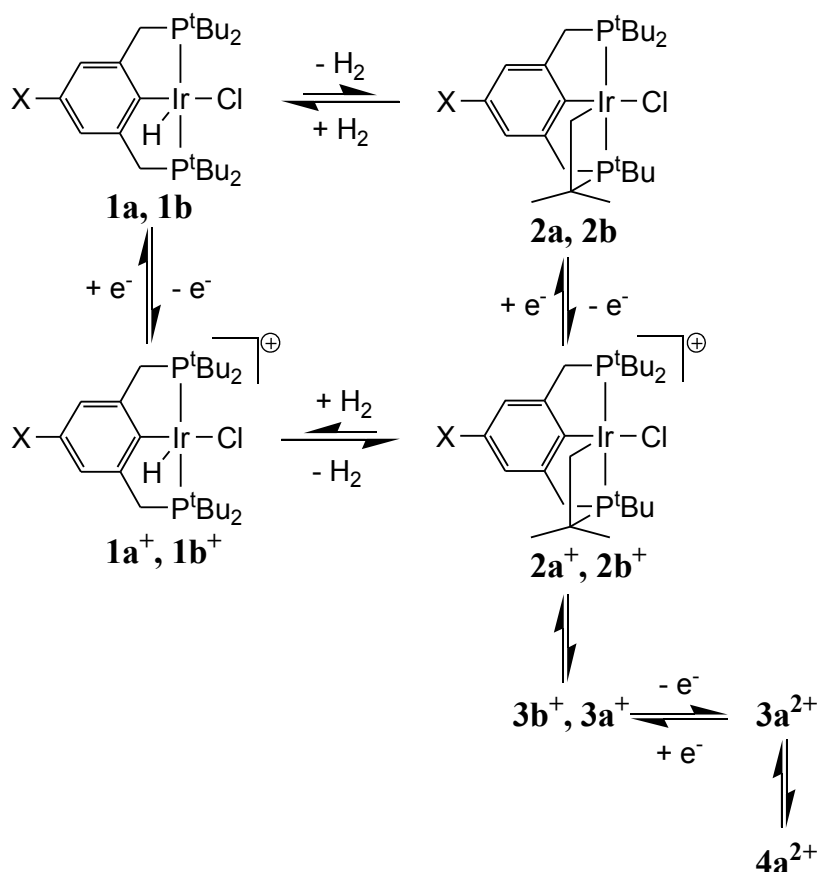
2.2 Aryl as the ligand backbone

The sensitivity of the reactivity towards substituents in the *para* position was demonstrated by the dehydrogenation/hydrogenation equilibrium displayed in Scheme 4. The substituent X is able to shift the equilibrium towards **2** or **1**.



Scheme 4

The electron donating methoxy group in compound **1b** leads to a stabilisation of the resonance structure **A_{III}** which increases the electron density at the metal and facilitates the intra-molecular oxidative addition of a *tert*-butyl C-H bond. This allows the isolation and full characterisation of **2b**.³² In the case of the unsubstituted complex **1a** (X = H) the dehydrogenation to **2a** has never been observed. On the other hand storage of the nitro compound **1d** for a few months leads to a complete conversion to **2d**, while **2c** is quantitatively formed from **1c** in solution within five days.³³ These observations agree with conclusions drawn from theoretical investigations: the π -donating/withdrawing abilities of the substituents in the *para* position influence the reactivity.^{34,35} The substituents MeO, OH, and NO₂ in the complexes **1b-d** possess these characteristics and therefore the resonance structures **A_I** and **A_{III}** contribute to the overall stability. The π -donating capability of the MeO group in **1b** is then responsible for the importance of **A_{III}** by increasing the electron density at the metal for the second C-H activation process. Thus **2b** is obtained by two consecutive intra-molecular C-H bond activations. Details about the sp³ C-H bond activation which is accompanied by a dehydrogenation are still unclear. Quantum chemical calculations show that **2a,b** are thermodynamically less stable than **1a,b**. Furthermore, electrochemical studies established an equilibrium between **1a,b** and **2a,b** + H₂. The isolation of **2b** is only realised if H₂ is released from the reaction mixture.



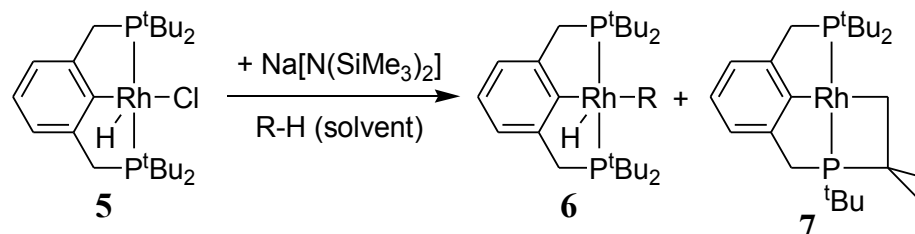
Scheme 5

A more detailed electrochemical investigation revealed that the electrode reaction mechanisms for both **1a,b** involve a joint feature called a “square scheme” with a coupled ECE reaction sequence (follow-up reactions, Scheme 5).³⁶ The electron transfer reactions are linked by two chemical equilibria which have been shown to be homogeneous hydrogenation/dehydrogenation steps. Interestingly, the one-electron transfer oxidation of both **1a,b** reverses the stability of the two pincer complexes related to C-H activation. While the hydrochloride form is favoured in the Ir(III) oxidation state, after oxidation the doubly cyclometalated species prevailed. It is important to note that for both compounds the intra-molecular C-H activation step is promoted by a one-electron oxidation. The same effect was reported previously for $\text{IrMe}_2(\eta^5\text{-C}_5\text{Me}_5)\text{PR}_3$ ($\text{R} = \text{Me, Ph}$). Here upon oxidation of the iridium(III) complex to the Ir(IV) cation $[\text{IrMe}_2(\eta^5\text{-C}_5\text{Me}_5)\text{PR}_3]^+$ the rate of the C-H activation dramatically increased.³⁷⁻³⁹ Significant differences between the electrochemical behaviour of **1a** and **1b** involve a shift of the peak potentials to more positive values in **1a** as compared to **1b**. This has been explained as a result of decreasing electron density at the iridium centre in the unsubstituted complex **1a**

as compared to the methoxy compound **1b**. Therefore the release of an electron in the oxidation process becomes more difficult. Interestingly, the chemical equilibrium in the oxidised part of the square scheme is more facile for **1a** than for **1b**.

In the case of **1b**, the one-electron oxidation product of the square scheme forms only slowly the electrochemically inactive species **3b⁺**. This is in contrast to **1a** where the product **2a⁺** quickly undergoes further transformations (Scheme 5). The follow-up products **3b⁺**, **3a⁺**, **3a²⁺** and **4a²⁺** have not been characterised in detail, however, their mechanistic importance is strongly indicated by experimental and simulated data.³⁶ From the shape and the high intensity oxidation peak of **1a** it was suggested that a further electron transfer process contributes to the initial one-electron oxidation with possible formation of an Ir(V) species. Overall, the kinetic and thermodynamic parameters derived from a comparison of cyclic voltammetric experiments and computer simulations confirm the assumption that the intra-molecular C-H activation is promoted by one-electron oxidation of **1a** or **1b**. Up to now only **2b** could be isolated and characterised possibly due to its more facile oxidation.

Thus in contrast to **1b** the hydrido chloro rhodium complex **5** has to be reduced to a highly reactive 14e⁻ species in order to oxidatively add C-H bonds (Scheme 6).⁴⁰



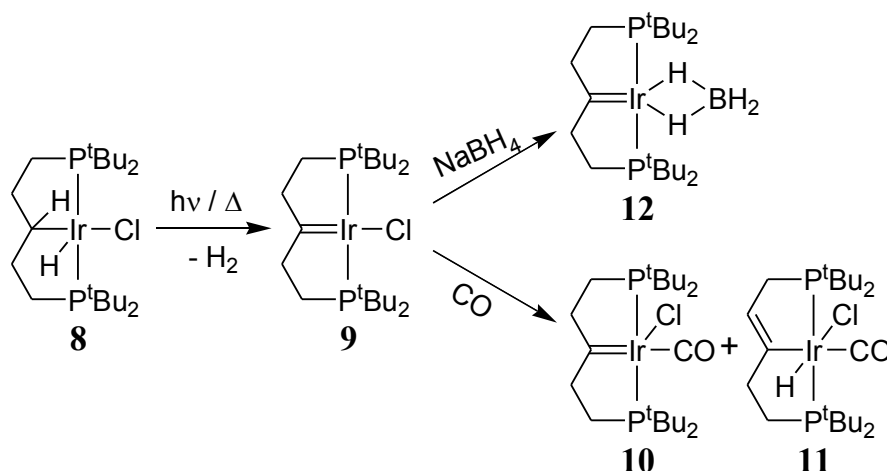
Scheme 6

As deduced from spectroscopic and experimental data intermolecular oxidative addition of solvent molecules as well as the intra-molecular addition of a *tert*-butyl C-H bond takes place. This was the first time that the *tert*-butyl groups of pincer complexes were found to be able to compete with intermolecular C-H activation. Further *tert*-butyl groups activation in iridium and ruthenium pincer complexes were reported recently.^{27,41,42}

2.3 Alkyl as the ligand backbone

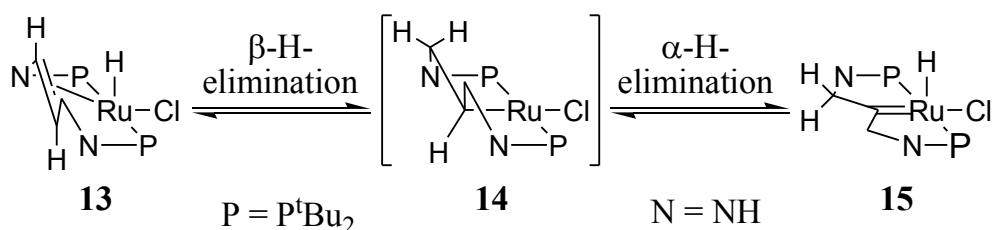
The more σ -electron donating character of sp^3 -carbon atoms as compared to sp^2 -carbons increases the electron density at the metal centre significantly. This might be one reason for the

stability of the carbene complex **9**, which was first prepared by thermal decomposition of **8** with about 5% yield⁴³ or later in yields around 60% by continuous photolysis and removal of H₂ (Scheme 7).⁴⁴ The hydride-borane complex **12** is the product of the substitution of the chloride by a hydride ligand followed by the coordination of the leaving BH₃ molecule when **9** is treated with NaBH₄. This behaviour of **9** in presence of the nucleophilic boron-hydride anion supports the importance of the alkylidene resonance structure **B_I** (Scheme 3). In **12** the *trans* orientation of the strong field carbene ligand is evaded and the μ²-bridging hydride ligands strongly reduce the donated electron density at the iridium centre.



Scheme 7

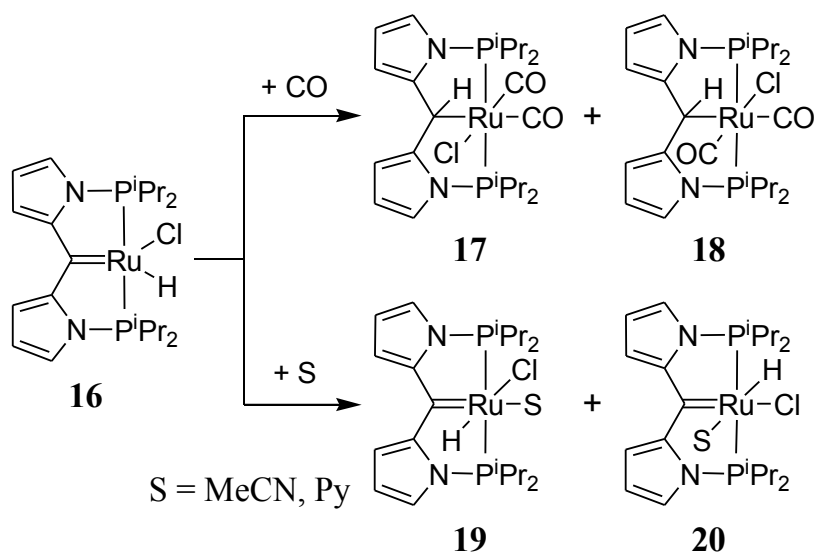
Treatment of **9** with carbon monoxide leads to the formation of the expected adduct compound **10**, accompanied by complex **11** which is the product of a β-hydride shift. Carbon monoxide as a strong σ-donor as well as an efficient π-acceptor ligand seems to destabilise the carbene metal bond and therefore induces β-H-elimination. Similar rearrangements were described for rhodium,^{45,46} ruthenium and osmium^{47,48} complexes with alkyl-based pincer ligands.



Scheme 8

The Ru(II) carbene complex **15** for example coexists in equilibrium with the olefin complex **13** (Scheme 8). According to DFT calculations⁴⁹ these 1,3-bisaminopropane-based pincer complexes show a distinct competition between α -H- and β -H-elimination. For this reason all accessible isomers are observed in the equilibrium. Thermodynamically, the Ru(II) olefin complex **13** represents the most stable form, although the carbene compound **15** is only 12.1 kJ/mol higher in energy. It should be emphasised that mechanistically a spin change from a singlet ground state in **13** or **15** to a triplet ground state for the $14e^-$ alkyl intermediate **14** seems to be involved.

In order to determine the π -acceptor properties of the carbene atom, a PCP pincer backbone without β -H-atoms was developed that is not able to undergo carbene-olefin isomerisation (Scheme 9).⁵⁰

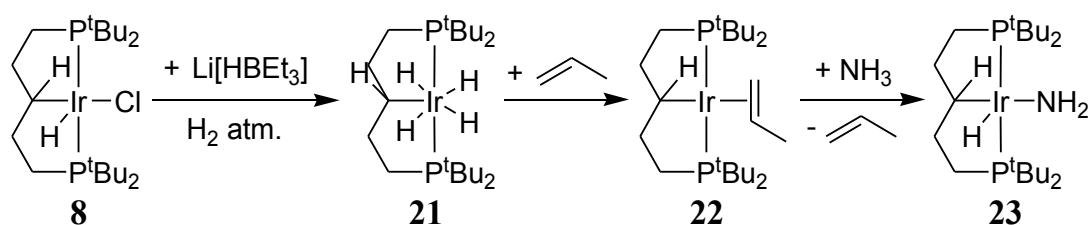


Scheme 9

The Ru(II) complex **16** (Scheme 9) is obtained in very good yield by treatment of the dipyrromethane PCP ligand with $[(p\text{-cymene})\text{RuCl}_2]_2$ and triethylamine at 100°C in toluene. The products of the reaction of **16** with pyridine or acetonitrile are proposed to be the adduct compounds **19** and **20** which are detected at low temperatures. At room temperature just an overlaid structure is observed. Again the *trans*-orientation of hydride and carbene ligands is avoided, because both are strong field ligands. Treatment of **16** with CO leads to a mixture of the two isomers **17** and **18** where two CO molecules are coordinated to the ruthenium centre. The disappearance of the hydride signal in the ¹H NMR spectrum is explained by a 1,2-hydride shift to the carbene atom. Compounds **17** and **18** are designated as the *syn*- and the

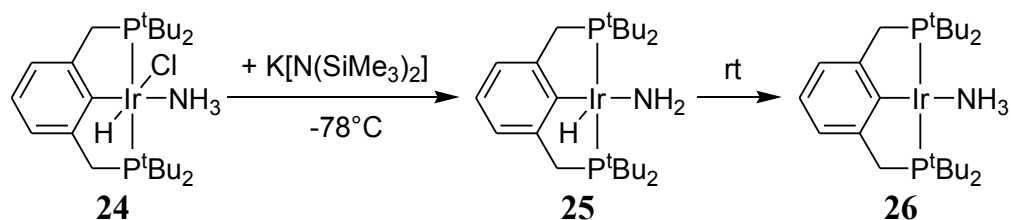
anti-isomer with respect to the H-C-Ru-Cl unit. Similar to the reaction displayed in Scheme 7 the coordination of CO *trans* to the carbene carbon atom is avoided by a 1,2-hydride shift (α -elimination) to the carbene atom (analogue Scheme 8) and the formation of a carbon metal σ -bond *trans* to CO.

Recently, the alkyl pincer complex **22** has been shown to oxidatively add ammonia leading to the hydrido amide complex **23** (Scheme 10).^{24,51} This is insofar remarkable as ammonia prefers to coordinate *via* the lone pair. To obtain an efficient precursor for the assumed highly reactive 14e⁻ Ir(I) intermediate, the hydrido chloro complex **8** is treated with super-hydride (Li[HBET₃]) in a hydrogen atmosphere. The resulting the tetra-hydrido compound **21** can be transformed subsequently to the propene complex **22**.



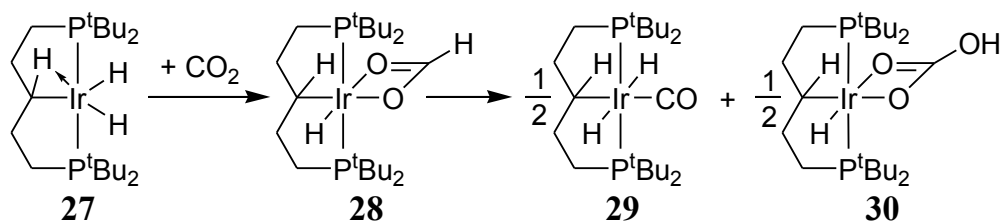
Scheme 10

Treatment of **22** with ammonia at room temperature within 5 min results in 90% yield in the hydrido amide **23**. Independently, **23** was isolated by treatment of **8** with ammonia in the presence of the strong base K[N(SiMe₃)₂]. Mechanistic considerations of the N-H activation based on thermodynamic and kinetic studies as well as labelling experiments ruled out pathways *via* hydrido carbene or double cyclometalated intermediates. An associative pathway can also be excluded. Most likely the reaction proceeds *via* the dissociation of propene followed by the N-H oxidative addition of ammonia.²⁴ In the case of the aryl based pincer complexes the analogous hydrido amide **25** is accessible *via* a two step synthesis (Scheme 11). Treatment of the hydrido chloro complex (**A_{II}** with X = H) with ammonia leads to the classical Ir(III) ammonia complex **24** which could also be converted to **25** by addition of K[N(SiMe₃)₂] to the reaction mixture at -78°C.



Scheme 11

Interestingly, the aryl pincer amide **25** is more labile than the alkyl pincer complex **23** and reductively eliminates ammonia at temperatures above -10°C rapidly to form the Ir(I) ammonia complex **26**. The aliphatic backbone induces a higher electron density on the metal centre than the aromatic backbone which enforces the oxidative addition of ammonia in the case of **23**. This is plausible because the process of oxidative addition is associated with electron donation from the metal to the substrate and hence reduces the electron density at the metal. *Vice versa* the reductive elimination increases the electron density at the metal and is therefore preferred in the aryl pincer complex.^{24,51} Further examples for small molecule activation with PCP pincer complexes are the formations of formate complexes with CO_2 (Scheme 12). The alkyl iridium di-hydride pincer complex **27** rapidly generates the formate complex **28** in the presence of carbon dioxide.⁵² Over a period of some weeks **28** undergoes a disproportionation to the *trans*-di-hydride species **29** accompanied by the crystallisation of the bicarbonate complex **30** from the reaction mixture.

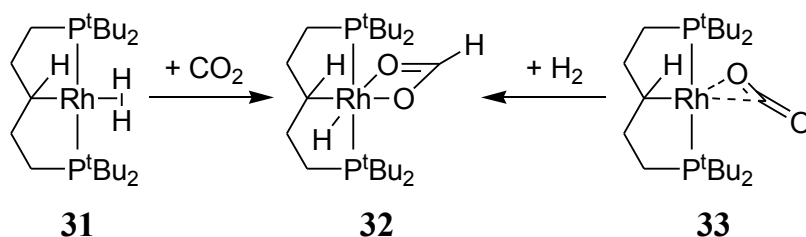


Scheme 12

Complex **27** is accessible from the tetra-hydride **21** by careful sublimation. The penta-coordinated Ir(III) di-hydride **27** is described with an agostic interaction from the methyne C-H bond.⁵³ This could be explained through donation of electron density from the electron rich metal into the σ^* -orbital of the C-H bond.

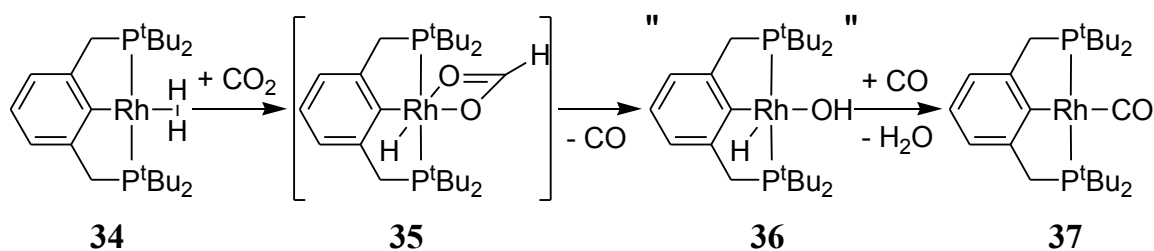
The very similar reaction of the rhodium analogue η^2 -dihydrogen complex **31** with carbon dioxide forms the rhodium formate compound **32** (Scheme 13).⁴⁵ The same product is obtained

by treating the CO₂ adduct **33** with hydrogen. It is assumed that the latter reaction proceeds *via* the dihydrogen complex **31** as intermediate.



Scheme 13

In case of the aryl based rhodium PCP pincer complex the formate **35** was characterised in the reaction mixture by ¹³C NMR and IR spectroscopy.⁵⁴ It is also available from the dihydrogen complex **34** by treatment with carbon dioxide. After some hours **35** loses CO. If the reaction is allowed to continue for one week or more, the Rh(I) carbonyl complex **37** is obtained. Independently, **37** can be prepared by treating the isolated and redissolved compound **36** with CO.



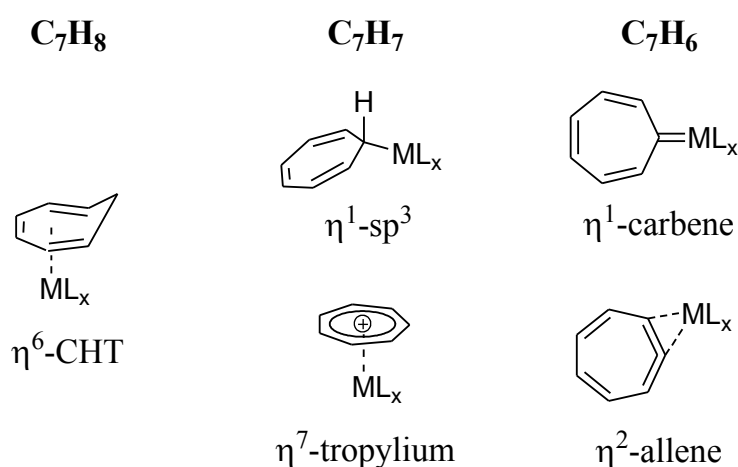
Scheme 14

In order to get a deeper understanding of the different behaviour of the rhodium PCP pincer complexes depicted in Scheme 13 and 14 a combined experimental and DFT investigation was performed recently.⁵⁵ To examine the possible reaction pathways the calculations were carried out for PCP complexes which possess hydrogen atoms instead of *tert*-butyl groups at the phosphorus atoms. The first reaction step is supposed to be the formation of the exergonic dihydrogen coordinated rhodium centre which weakly binds to form $\kappa\text{C-CO}_2$. Subsequently, the CO₂ moves to the $\kappa\text{O-CO}_2$ coordination being an endergonic process. The four-membered transition state of the hydride shift to the CO₂ carbon atom forms the $\kappa\text{O-HCO}_2$ complex which rearranges fast to the strongly exergonic hydridoformate complex **32** or **35** with the $\kappa^2\text{O-HCO}_2$ unit. It should be pointed out that the alkane based formate complex **32** is thermodynamically more stable than the phenyl based **35**. In case of reductive elimination of formic

acid the five-membered transition state is thermodynamically and kinetically favoured over the aryl based rhodium pincer complex **35**, while the alkane based pincer complex **32** requires a higher activation barrier and leads to less stable products. The observation of **36** and **37** might be realised through the ease of formic acid elimination from complex **35**.

2.4 Cycloheptatrienyl as the ligand backbone

Cycloheptatriene (CHT) and cycloheptatrienyl organometallic compounds with their various modes of bonding are depicted in Scheme 15. The η^6 -CHT as well as η^7 -tropylium complexes were studied many years ago.⁵⁶ The C_7H_6 energy surface of the seven membered mono cyclic C_7H_6 ring shows two isomers, the cycloheptatrienyliene (carbene) and the cyclohepta-1,2,4,6-tetraene (allene). Although the allene is the most stable species, the carbene presumably is the lowest energy transition state on the isomerisation pathway between enantiomeric allenes.^{57,58}



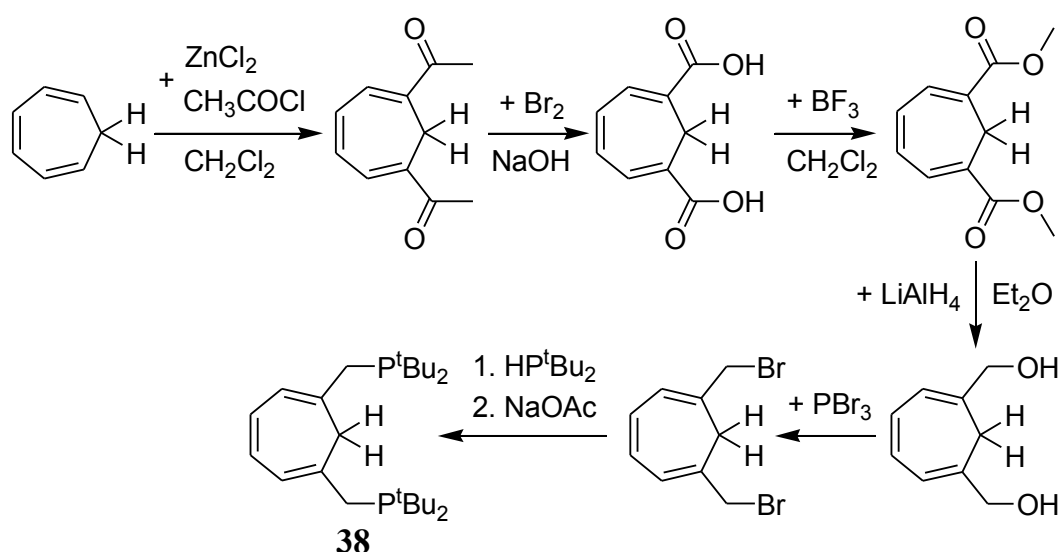
Scheme 15

Various transition metal complexes with C_7H_7 and C_7H_6 ligands have been described in the literature.^{28,59-61} The diverse characteristic structural features of the C_7H_6 isomers are stabilised *via* different bonding modes to the metal in these complexes. Thus early transition metals favour the η^1 -carbene structure (Scheme 15).⁶² This was explained by the aromaticity of the tropylium resonance form and the low-lying vacant orbitals on the metal which are important for σ -bond formation.⁶³ Late transition metals exhibit a more differentiated behaviour. While platinum(0) favours the η^2 -allene structure a η^1 -carbene could be established for a d^8 Pt(II) complex (Scheme 15) due to strong interactions between the cycloheptatrienyliene HOMO and the metal LUMO.^{56,63}

The introduction of di-*tert*-butylmethylphosphane moieties in 1,6 position of 1,3,5-cycloheptatriene generates a PCP pincer ligand which locates the metal next to the CH_2 -group of the cycloheptatriene ring. The oxidative addition of one C-H bond forms a cycloheptatrienyl

PCP pincer complex with a sp^3 carbon metal bond (η^1-sp^3 in Scheme 15) which is similar to the alkyl PCP complex **8** in Scheme 7.

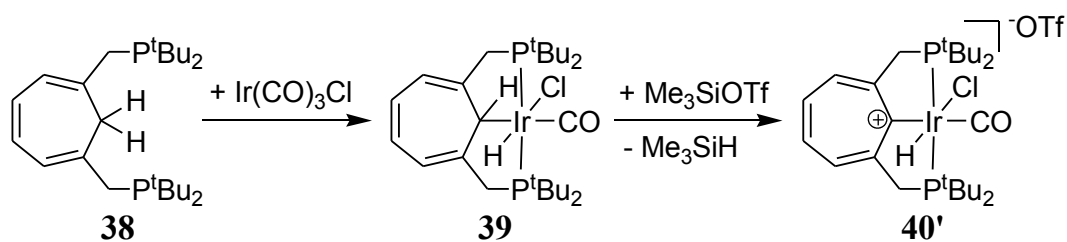
In Scheme 16 the synthetic pathway to the CHT PCP-pincer ligand **38** is depicted.²⁸ A zinc dichloride assisted acylation of cycloheptatriene is followed by oxidation with bromine and esterification to obtain the di-methyl ester. Reduction to the diol, bromination and finally introduction of the phosphine completes the ligand synthesis. The methylene protons of both phosphine arms in **38** are selectively replaced by deuterium if $LiAlD_4$ is employed for the reduction of the di-ester.⁶⁴



Scheme 16

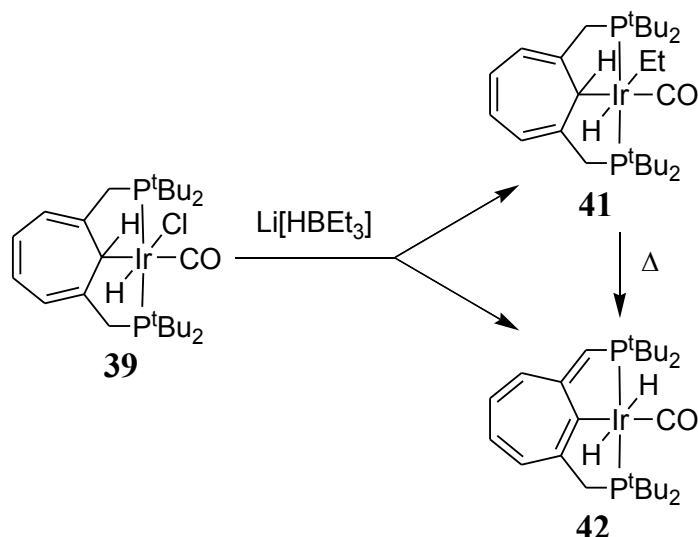
Preparation of pincer metal complexes from **38** with different metal precursors turned out to be more difficult than in the case of the analogous phenyl or alkyl pincer ligands. Indeed, **39** is generated from **38** with tri-carbonyl iridium chloride in a clean reaction (Scheme 17), whereas the procedures with iridium tri-chloride hydrate or with the cyclooctene or cyclooctadiene complexes of iridium led to complicated reaction mixtures in which no CH_2 carbon metallation could be observed. The main difference at the metal site between the alkyl pincer complex **8** and the cycloheptatrienyl pincer complex **39** is the carbonyl ligand which gives rise to the coordinatively as well as electronically saturated compound **39** in contrast to the five coordinated $16e^-$ complex **8**. This provides the carbonyl complex **39** with a higher stability. When the carbonyl in **39** is located *trans* to the metal carbon atom the hydride and the chloride ligands are forced into a mutual *trans* orientation. The C-H group in the CHT backbone in **39** is strongly bent out of the plane which encompasses the three double bonds. Con-

sequently the residual hydrogen atom at the metal bound sp^3 -carbon and the chloride ligand are *syn*-periplanar at the iridium centre. In order to transform **39** into a more reactive species several approaches to remove the CO were attempted, however, without success.²⁸ Therefore the cycloheptatrienyl PCP complex **39** has been treated with different electrophiles as well as nucleophiles displaying rather unusual reactivities.²⁸⁻³⁰ Surprisingly, when trimethylsilyltriflate was applied to displace the chlorine atom from the metal in **39** complex **40'** (with triflate as counter-ion) is formed (Scheme 17).



Scheme 17

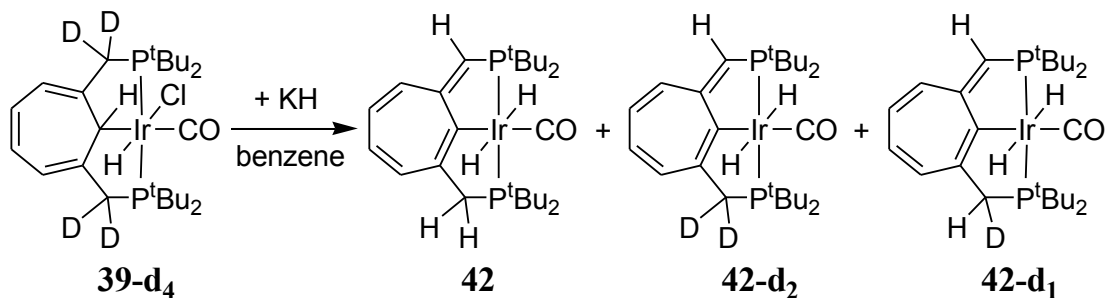
This can be explained by the abstraction of a hydride from the *ipso*-carbon atom. This generates an aromatic tropylium-cation in the ligand backbone while the chlorine at the metal remains untouched. The crystal structure analysis by XRD reveals a planar CHT backbone which is twisted by about 10 - 20° from the equatorial plane containing the two phosphorus, the *ipso*-carbon and the carbonyl.²⁹



Scheme 18

Interestingly, treatment of **39** with $\text{Li}[\text{HBET}_3]$ leads to the alkylated compound **41** and to a *trans* di-hydrido complex **42** (Scheme 18).²⁸ The unexpected ethyl complex **41** is the major product. Obviously, in this reaction $\text{Li}[\text{HBET}_3]$ is transferring an ethyl group which contrasts the general use of boron-hydrides as hydride transfer agents.⁶⁵ The isolation of **42** is also unexpected because *trans* di-hydrido complexes are rare due to the strong *trans*-effect of the hydride ligand. The formation of **42** is initiated by $\text{Li}[\text{HBET}_3]$ which is acting as a strong base. Thermal decomposition of independently synthesised **41** leads also to the di-hydride **42**. A β -elimination of ethene is unlikely because of the absence of a vacant coordination site at the metal. But the calculated ball stick structure of **41** reveals an auspicious situation for a *syn*-periplanar β -elimination of ethane forming a carbene intermediate which then rearranges to the di-hydride **42**.⁶⁶ Energetically the formal loss of HCl from **39** to **42** represents an endergonic process with $\Delta E = 119.7$ kJ/mol. Compound **41** is 70.3 kJ/mol and 115.1 kJ/mol higher in energy than the anticipated carbene and the di-hydride **42**, respectively. This renders the transformation from **41** to **42** a thermodynamically favoured process, while the elevated temperatures indicate a high activation barrier for the reaction.

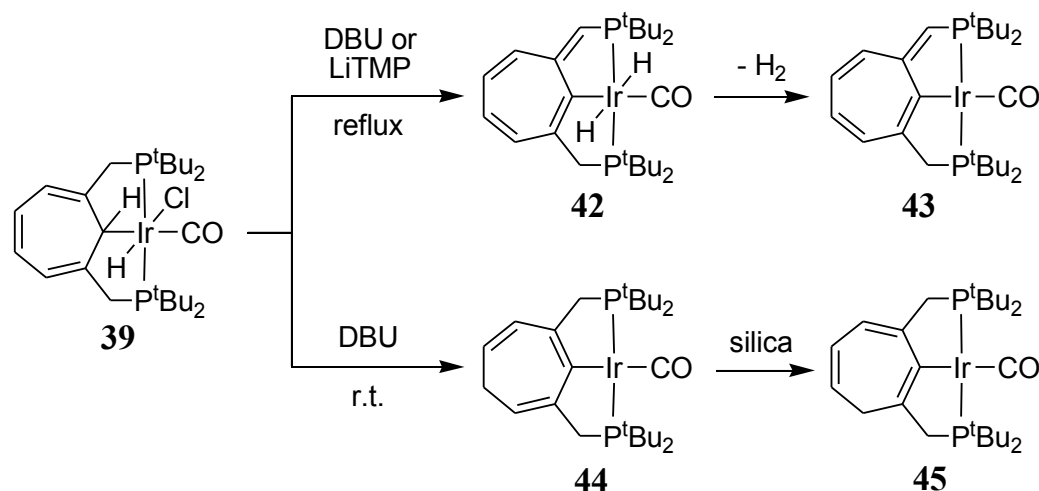
The treatment of the deuterated pincer complex **39-d₄** with potassium hydride in benzene leads to a mixture of the different *trans* di-hydride isotopomers **42**, **42-d₂** and **42-d₁** (Scheme 19).



Scheme 19

This observation suggests an initial deprotonation of the deuterated methylene bridges with subsequent proton shifts, chloride elimination and redistribution of the π -system in the backbone.

In Scheme 20 the reactions of the CHT PCP pincer complex **39** with the bases 1,8-diazabicyclo[5,4,0]undec-7-ene (DBU) and lithium 2,2,6,6-tetramethylpiperidide (LiTMP) under different conditions are illustrated.³⁰



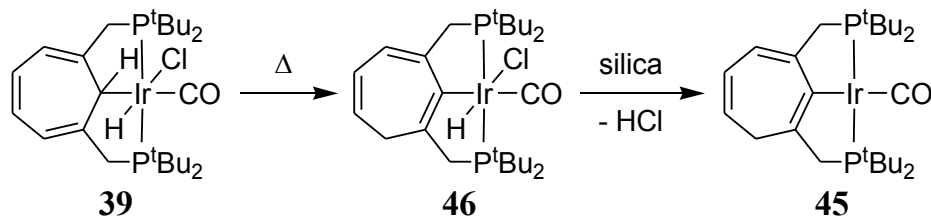
Scheme 20

Over a reaction period of 4 - 5 days in refluxing THF the non-coordinating relatively weak base DBU produces as the major product the di-hydrido Ir(III) complex **42** and, induced by column chromatography, the Ir(I) complex **43** which lost one equivalent of H_2 . The reaction of the more basic and bulkier base LiTMP under comparable conditions has been monitored by ^{31}P NMR spectroscopy. Within the first 5 days an increase of the concentration of **42** up to 70% was detected. The following decrease in concentration of the di-hydride **42** is accompanied by rising amounts of **43**.⁶⁶ Therefore, it is concluded that **42** and **43** do not form simultaneously, but the initial formation of complex **42** is followed by the loss of dihydrogen to generate **43**. If the reaction with DBU is performed at room temperature and monitored over a period of 40 days, a rearrangement to the Ir(I) complex **44** is observed (Scheme 20). Consecutive chromatographic separations of the crude reaction mixture lead to increasing concentrations of **45**.

According to DFT calculations⁶⁶ the dehydrogenation which leads to complex **43** is an endergonic reaction step with $\Delta E = 38.1$ kJ/mol. Compound **44** is 43.9 kJ/mol more stable than the di-hydride **42** and therefore destabilised by 75.7 kJ/mol relative to **39**. The formation of **42** is more endergonic than the alternative creation of **44**. Complex **45** is stabilised by 66.5 kJ/mol and 22.6 kJ/mol as compared to **42** and **44**, respectively.

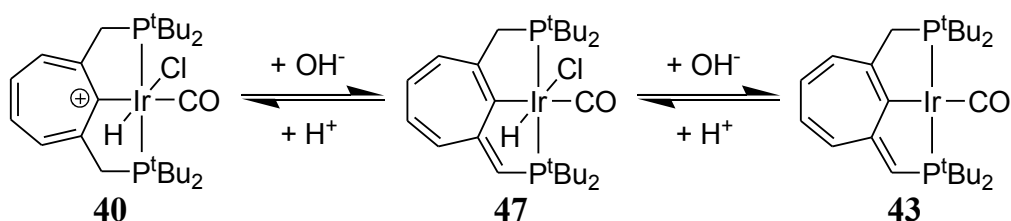
The isomeric complex **46** is accessible by heating the neutral hydrido chloro complex **39** without a base in THF and subsequent column chromatography (Scheme 21). The structure of intermediate **46** was established by NMR spectroscopy from the reaction mixture and confirmed by the observation of **45**. Calculations predict an exergonic reaction pathway from **39**

to **46** ($\Delta E = -31.8$ kJ/mol). The following silica assisted reductive elimination of HCl from the Ir(III) complex **46** forms the product **45** which is destabilised by 84.9 kJ/mol as compared to **46**.



Scheme 21

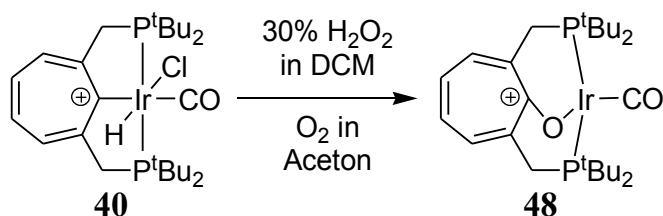
Complex **43** can also be synthesised *via* an alternative route. Treatment of the cationic complex **40** with one equivalent of aqueous sodium hydroxide deprotonates one of the methylene bridges. This is accompanied by the redistribution of the π -system generating the Ir(III) complex **47** (Scheme 22).



Scheme 22

A further equivalent of sodium hydroxide induces the reductive elimination of HCl from the iridium atom to form **43**. The reverse reaction from **43** is achieved by application of stoichiometric amounts of aqueous hydrochloric acid.

Surprisingly, the formation of the cationic oxo complex **48** (Scheme 23) is obtained with a large excess of 30% aqueous H_2O_2 in dichloromethane over a reaction period of seven days.⁶⁶



Scheme 23

The storage of an acetone solution of the cationic complex **40** in air yields, after five months, an equilibrium mixture containing nearly 60% of **48**.

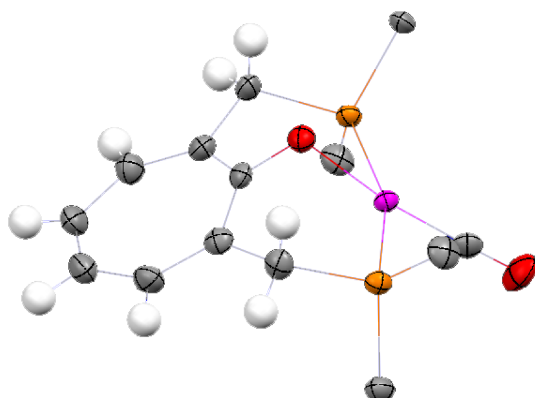


Figure 1: Crystal structure of **48**. The methyl groups and the counter ion are omitted for clarity.

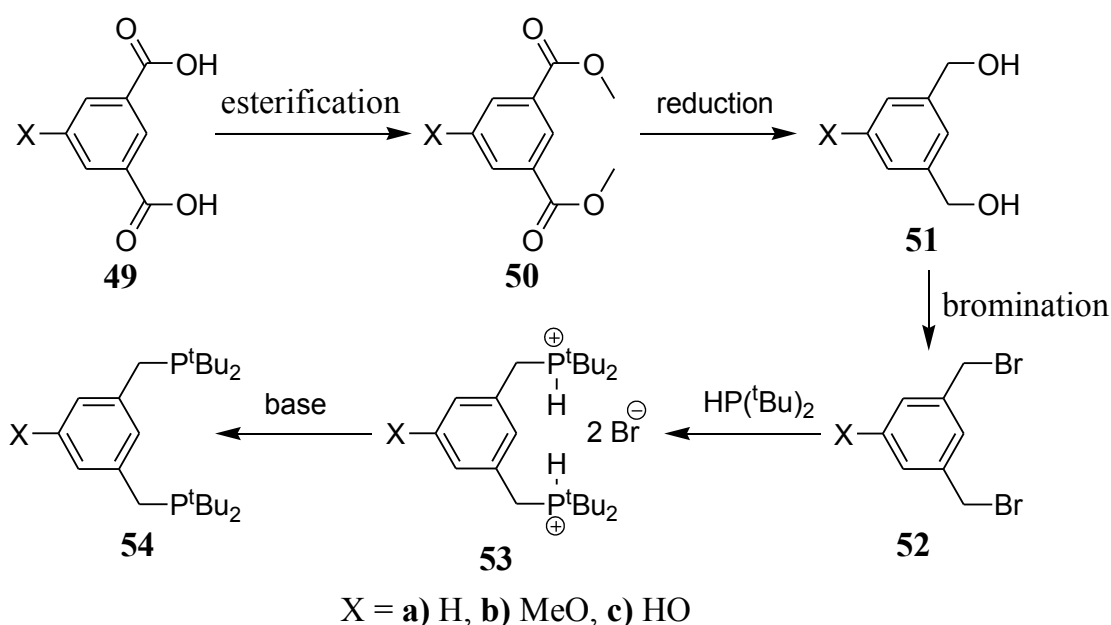
Formally, the insertion of an oxygen atom, from an oxidising agent, in the carbon metal bond of complex **40** is accompanied by the reductive elimination of HCl from the iridium centre generating the oxo species **48**. The structural characterisation of the triflate complex **48** is based on single crystal XRD (Figure 1), ^1H , $^{31}\text{P}\{^1\text{H}\}$ and $^{13}\text{C}\{^1\text{H}\}$ NMR spectroscopy and mass spectrometry.⁶⁶ Also the performed DFT calculations (B3LYP/LACVP*) are in good agreement with the XRD structure and display a planar cycloheptatriene backbone with a carbon oxygen single bond and only weak interactions between the iridium centre and the aromatic π -system. Energetically, the cationic oxo complex **48** is 164.1 kJ/mol higher in energy than the neutral complex **39**, but 686.6 kJ/mol more stable than the cationic hydrido chloro complex **40**.

3 Results and discussion

3.1 Functionalised phenyl PCP pincer complexes

3.1.1 Established synthesis for functionalised phenyl PCP pincer ligands

Scheme 24 shows a general sequence for the synthesis of phenyl PCP ligands as developed and performed in the research-group. The esterification reaction of methoxy *iso*-phthalic acid is achieved by adding gaseous hydrochloric acid to a solution of **49b** in dry methanol. The pure di-ester **50b** is obtained as a white precipitate in nearly quantitative yields.



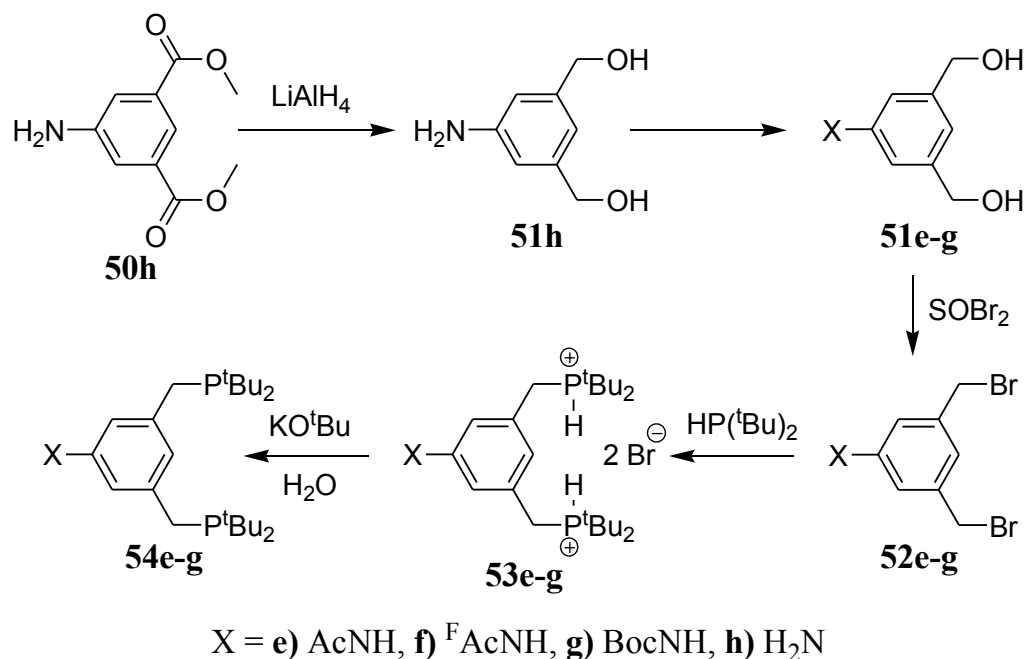
Scheme 24

As reducing agent for the di-ester reduction to the diol **51b** lithium aluminium hydride in THF was used. Thionyl bromide being a strong bromination reagent allowed the transformation of the hydroxyl groups into bromides in dichloromethane at 0°C. When di-*tert*-butylphosphane is added to a solution of the di-bromide **52b** in acetone and the mixture is refluxed for a few hours, the bis-phosphonium salt precipitates as white solid. The bis-phosphane **54b** is obtained by consecutive addition of base to the bis-phosphonium di-bromide **53b** in a bi-phasic system of diethyl ether and water. After each addition of base the ether phase containing **54b** is exchanged and the separated organic layer is evaporated yielding clean **54b** as viscous oil

or white solid. The hydroxy diol **51c** is accessible, if the methoxy diol **51b** is treated with boron-tri-bromide.⁶⁷

3.1.2 Variations for amino functionalised phenyl PCP pincer ligands

The adaptation of the general synthetic scheme for phenyl PCP pincer ligands (Scheme 24) to amino functionalised phenyl PCP ligands was one intention of this work. Starting from 5-amino *iso*-phthalic acid dimethyl ester **50h** (Scheme 25) the reduction is successful with LiAlH₄ in THF, whereas the yield for the resulting amino diol **51h** is poor compared to the yield of the methoxy compound **51b**. This is due to the difficulties in quantitative separation of the product compound containing a basic amino group from the resulting aluminium hydroxide residue.



Scheme 25

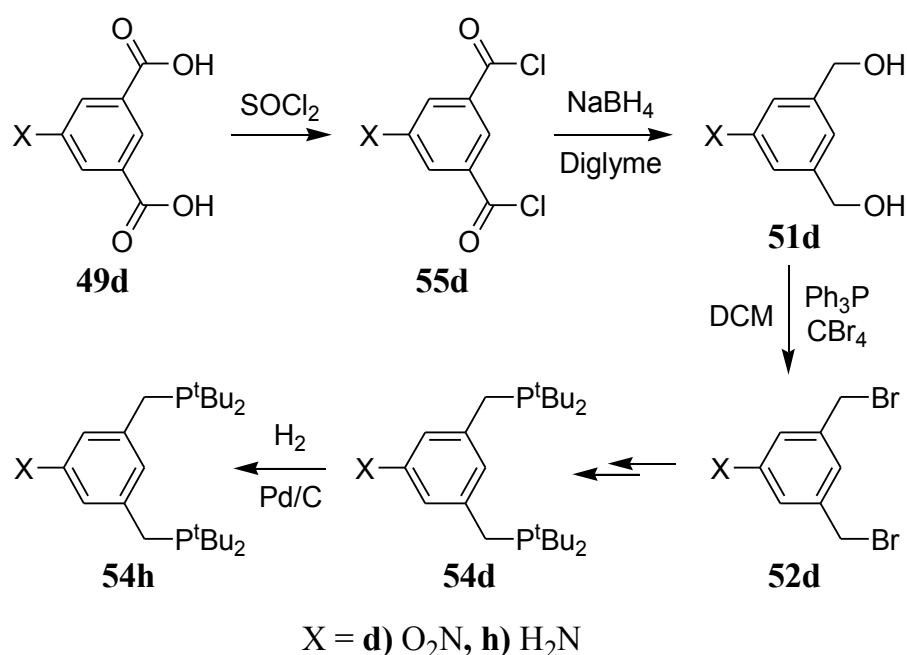
The introduction of different protecting groups (acetyl: Ac, trifluoroacetyl: ^FAc and *tert*-butoxycarbonyl: Boc) is achieved by treating the amino diol **51h** with the corresponding acid anhydride. Acetic acid anhydride is added to a suspension of **51h** in dry THF to form the acetamide diol **51e** as a white precipitating solid. After filtration and washing the precipitate the product is isolated in very good yields and could be used without further purification. The synthesis of the trifluoroacetamide diol **51f** requires longer reaction times and the product yield diminishes compared to that of **51e**. The *tert*-butyl carbamate diol **51g** was synthesised

with *tert*-butyl di-carbonate. Unfortunately, the product could not be isolated as a pure compound because of remaining *tert*-butyl di-carbonate. Interestingly, the bromination with SOBr_2 of **51g** displays no *tert*-butyl carbamate di-bromide (**52g**) formation. In contrast, the treatment of the acetamide diol **51e** or the trifluoroacetamide diol **51f** with thionyl bromide results in a clean reaction forming the corresponding di-bromides **52e** or **52f**, which could be isolated after column chromatography in good yields. The subsequent conversions to the bis-phosphonium salts **53e** and **53f** are comparable to the synthesis of the methoxy bis-phosphonium salt **53b**. A great advantage is the insolubility of the bis-phosphonium salts **53e** and **53f** in organic solvents, which allows the purification by extensive washing of the precipitate with dry acetone. The protected PCP ligands **54e** and **54f** are obtained by deprotonation of **53e** and **53f** using one or a little less than one equivalent of potassium *tert*-butanolate in water per phosphonium group. The stepwise addition of this basic aqueous solution to a bi-phasic system of diethyl ether/water containing the respective phosphonium salt, conserves a slightly acidic pH of the aqueous phase during the deprotonation. If the water phase becomes too basic during the reaction, the content of the respective phosphane oxide impurity increases according to the $^{31}\text{P}\{^1\text{H}\}$ NMR spectra. Attempts to separate the phosphane oxide impurities from the product by column chromatography or by reprotonating the phosphane groups (using hydrochloric acid in diethyl ether) and repeated deprotonation failed.

In prospective, this instability of phosphanes towards decomposition in basic media results in the inaccessibility of the amino functionalised PCP ligand **54h**, if the cleavage of the protecting group has to be accomplished in basic media. The cleavage of a protecting group is also difficult in an earlier step of the reaction scheme, because the di-bromides **52e-g** are sensitive towards nucleophilic attack and therefore the amino di-bromide **52h** is able to poly-condensate. Especially, the acetamide group is difficult to cleave due to the application of strong acidic or strong basic media. However, trifluoroacetamides are cleaved under weakly basic conditions, on the contrary the *tert*-butyl carbamate group is effectively cleaved in acidic media. Therefore the latter one is expected to be promising in terms of cleaving the protecting group without decomposition of the phosphane moieties. This could not be proven until now, as the synthesis of the *tert*-butyl carbamate protected PCP ligand **54g** failed.

An alternative synthetic pathway to prepare the amino functionalised PCP ligand **54h** without further steps of protecting group chemistry, is the reduction of the nitro functionalised PCP ligand **54d**. The preparation of the nitro di-bromide **52d**³³ was improved according to Scheme

26. Starting from 5-nitro *iso*-phthalic acid formation of the di-acid chloride **55d** is achieved by chlorination in refluxing thionyl chloride. After evaporation of the remaining SOCl_2 , the pure product is obtained in nearly quantitative yield. The subsequent reduction to the nitro diol **51d** is realised in high yields using sodium boron-hydride in diglyme. After work-up the product is obtained as white solid and could be used without further purification. An Appel reaction was performed to replace the hydroxy groups for bromides. The yields were comparable to the bromination with thionyl bromide but the work-up is more convenient and the column chromatographic purification is replaced by a filtration of Ph_3PO and vacuum filtration *via* 5 cm silica to remove the remaining tri-phenylphosphane oxide.



Scheme 26

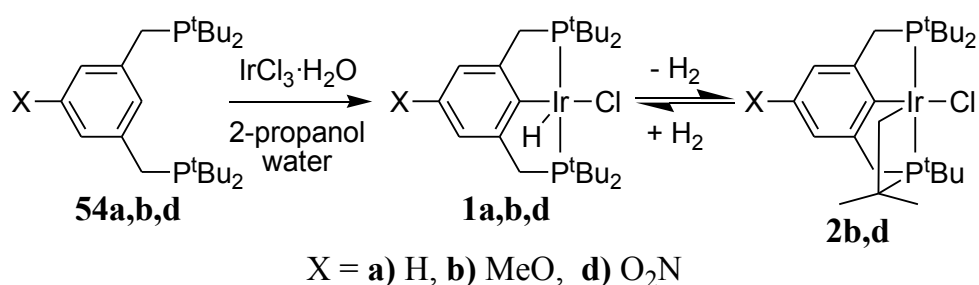
In analogy to Schemes 24 and 25, the nitro functionalised PCP ligand **54d** is synthesised from **52d** by addition of HP^tBu_2 , isolation and purification of the bis-phosphonium di-bromide **53d** and finally by deprotonation of the latter with KO^tBu in water. Different attempts to catalytically reduce, the nitro group in the di-bromide **52d** failed, because of the concurrent reduction of the benzylic bromides to methyl groups. Therefore, the catalytic reduction was tried with the nitro PCP ligand **54d**, unfortunately without observable formation of **54h**. Hitherto, the synthesis of the amino functionalised PCP ligand **54h** was not achieved, neither the synthetic route *via* protecting groups nor the route *via* nitro group reduction was successful.

Presumably, both approaches seem to be promising candidates to obtain the amino functionalised ligand, if the introduction and the cleavage of the protecting groups or the nitro group reduction are further investigated. For example, an alternative reducing agent to perform the transformation of the nitro into an amino group might be hydrazine.

3.1.3 Coordination chemistry of phenyl PCP pincer ligands

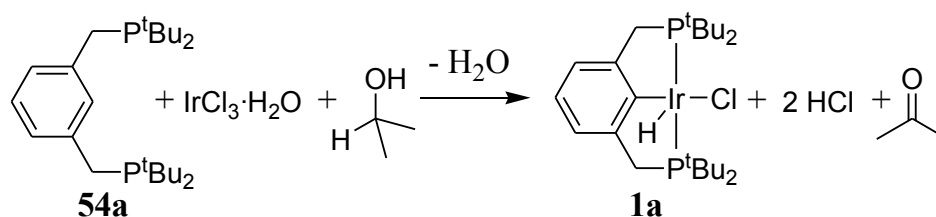
3.1.3.1 Unmodified methoxy and nitro functionalised pincers

Scheme 27 shows the coordination reactions with iridium chloride hydrate of different PCP pincer ligands. The formation of **2b,d** is only observed for the methoxy and nitro functionalised PCP ligands (compare chapter 2.2 on the pages 5 and 6).



Scheme 27

In the original synthetic procedure the respective PCP ligand and the iridium chloride hydrate were suspended in a mixture of 2-propanol water (7:1) and heated to reflux for 20 hours. A modified procedure was published with a stirring period at room temperature of 12 hours prior to refluxing the mixture.^{32,67}



Scheme 28

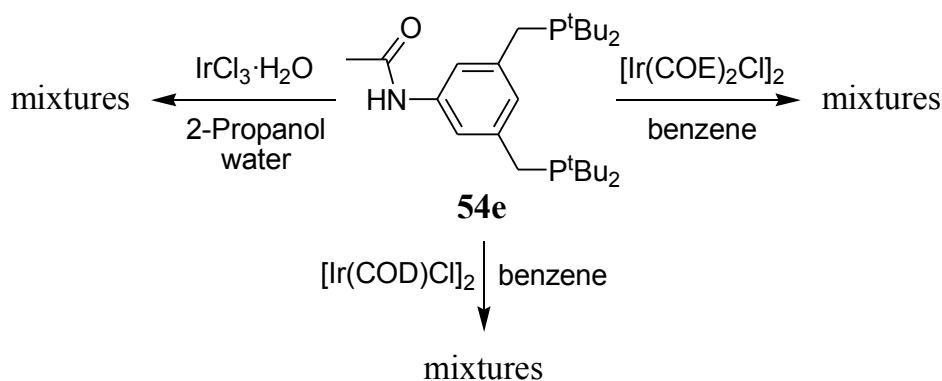
The precise mechanism is still unknown, but it is assumed that ligands from the metal centre are replaced by the phosphane arms and the reduction of the metal centre from +III to +I by 2-propanol releasing acetone and hydrochloric acid are fundamental steps prior to the oxidative addition of the C(sp²)-H bond of the phenyl ring (Scheme 28). The formation of the

double cyclometallated species **2b,d** is also unclear. Attempts to influence the chemical equilibrium $\mathbf{1b,d} \rightleftharpoons \mathbf{2b,d} + \text{H}_2$ (Scheme 27) by removal of dihydrogen at elevated temperature in solution or solid state failed. In contrast, the reverse hydrogenation of **2b,d** is achieved within 4 days in a benzene solution under an atmosphere of dihydrogen at room temperature. These results and the knowledge of the thermodynamic situation of this reaction (chapter 2.2 on the pages 5 and 6) suggest that the formation of **1b,d** from **2b,d** is thermodynamically and kinetically favoured and consequently **2b,d** is formed from **1b,d** in a kinetically hindered endergonic process. The observed mixtures of **1b,d** and **2b,d** from the coordination reaction (Scheme 27) are, therefore, most probably either built from **1b,d** in mechanistic pathways different from that mentioned before or **2b,d** is formed in competition to **1b,d** from another precursor complex.

3.1.3.2 Coordination chemistry of protected amino functionalised pincers

3.1.3.2.1 Acetamide functionalised ligands

In analogy to the coordination reaction of the methoxy and nitro functionalised ligands **54b** and **54d** as described in Scheme 27, one equivalent of iridium tri-chloride hydrate in a solvent mixture of 2-propanol and water was used to obtain the acetamide functionalised complex **1e**. Additionally, the usual Ir(I) precursor complexes with cyclooctene and cyclooctadiene were applied to realise a clean transformation of the ligand to an iridium complex (Scheme 29).



Scheme 29

Due to the unexpected observations of product mixtures in the $^{31}\text{P}\{^1\text{H}\}$ NMR spectra for the three different synthetic approaches, the reactions were monitored by $^{31}\text{P}\{^1\text{H}\}$ NMR spectroscopy. To allow stirring of the mixtures (suspension) the reaction was performed in a small

Schlenk tube, while 0.5 mL of the reaction mixture were withdrawn to measure the NMR spectra. Subsequently, the NMR sample was poured back into the reaction mixture and the reaction continued. Figure 2 shows the $^{31}\text{P}\{^1\text{H}\}$ NMR spectra (measured without deuterium-lock) after different periods of time and reaction conditions of the coordination reaction of **54e** with $\text{IrCl}_3\cdot\text{H}_2\text{O}$ in a mixture of not deuterated 2-propanol and water (7:1). The $^{31}\text{P}\{^1\text{H}\}$ NMR spectrum obtained after a stirring period of 24 hours at room temperature displays a broad resonance at approximately 35 ppm corresponding to weakly and therefore, dynamically interacting phosphanes with the iridium metal. One of the less intensive signals at 65 or 70 ppm might be attributed to the expected hydrido chloro complex **1e** considering the chemical shifts of the methoxy functionalised complex **1a** and the nitro functionalised complex **1d** at 69.1 and 67.5 ppm, respectively.

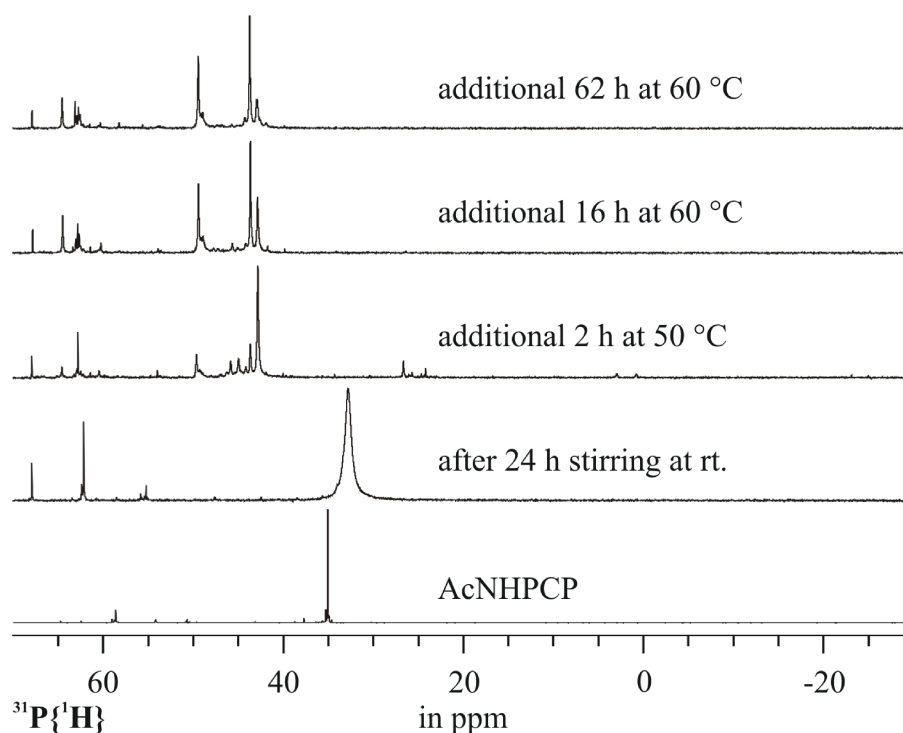


Figure 2: Reaction of AcNHPCP **54e** with $\text{IrCl}_3\cdot\text{H}_2\text{O}$ in 2-propanol, water

In the high-field region of the ^1H NMR spectrum (up to -50 ppm) no hydride signals are observed (compare **1a**: -43.2 and **1d**: -41.9 ppm). If the mixture is stirred at elevated temperatures, the broad $^{31}\text{P}\{^1\text{H}\}$ NMR resonance at 35 ppm disappears and a few signals between 45 and 52 ppm are observed. The ^1H NMR spectra display some unresolved hydride signals between -30 and -34 ppm, while after 78 hours stirring at 60°C only the hydride resonance at

-30 ppm remains with decreased intensity. The impact of the different elevated temperatures and reaction times on the $^{31}\text{P}\{^1\text{H}\}$ NMR spectra of the reaction mixture are comparatively small. An additional signal at about 66 ppm appears and increases in intensity as well as the resonance at 52 ppm.

According to Scheme 28 two equivalents of hydrochloric acid are formed beside the coordination compound. This hydrochloric acid formation and hence the low pH value might induce the cleavage of the protecting group in case of the acetamide functionalised ligand **54e**. Consequently, the resulting amino group in the ligand backbone might be responsible for the unusual coordination or the redox chemistry of **54e**.

The application of an Ir(I) precursors like $[\text{Ir}(\text{COD})\text{Cl}]_2$ or $[\text{Ir}(\text{COE})_2\text{Cl}]_2$ should avoid the redox reactions required using an Ir(III) precursor. Furthermore, instead of the formation of hydrochloric acid, cycloolefines are liberated and both reactants are soluble in solvents like benzene or toluene and, therefore, the reactions proceed in one solvent. In total, the reaction mechanism is expected to be more straight forward and the variables in the reaction conditions are decreased.

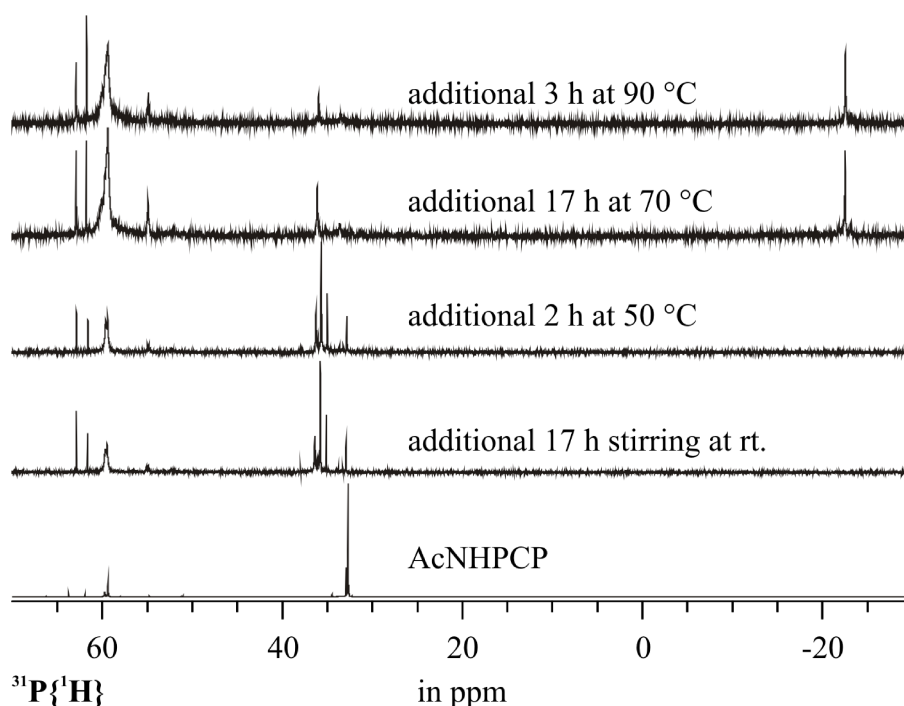


Figure 3: Reaction of AcNHPCP **54e** with $[\text{Ir}(\text{COD})\text{Cl}]_2$ in benzene

Figure 3 shows the progress of the coordination reaction of the acetamide protected ligand **54e** with the 0.5eq. of the iridium cyclooctadiene dimer precursor in benzene as solvent. After

the initial stirring period of the suspension at room temperature, the content of the pincer ligand is significantly decreased and a few low field shifted sharp signals (around 36 ppm) appear. The resonances at 60 ppm after the stirring period increase slowly over the following heating times, but they remain unchanged after the final heating to 90°C. The $^{31}\text{P}\{^1\text{H}\}$ NMR signal pattern at slightly elevated temperature of 50°C does not change, but after raising the temperature up to 70°C and 90°C the resonances around 36 ppm diminish and a new signal at approximately -22 ppm arises. Additionally, the increasing noise in the $^{31}\text{P}\{^1\text{H}\}$ NMR spectra after the heating periods indicates lower concentrations of phosphorus in the sample. This might be explained by the formation of insoluble compounds or components out of the observed phosphorus chemical shift range (200 up to -100 ppm). All corresponding proton spectra do not display any signals in the high field region down to -60 ppm.

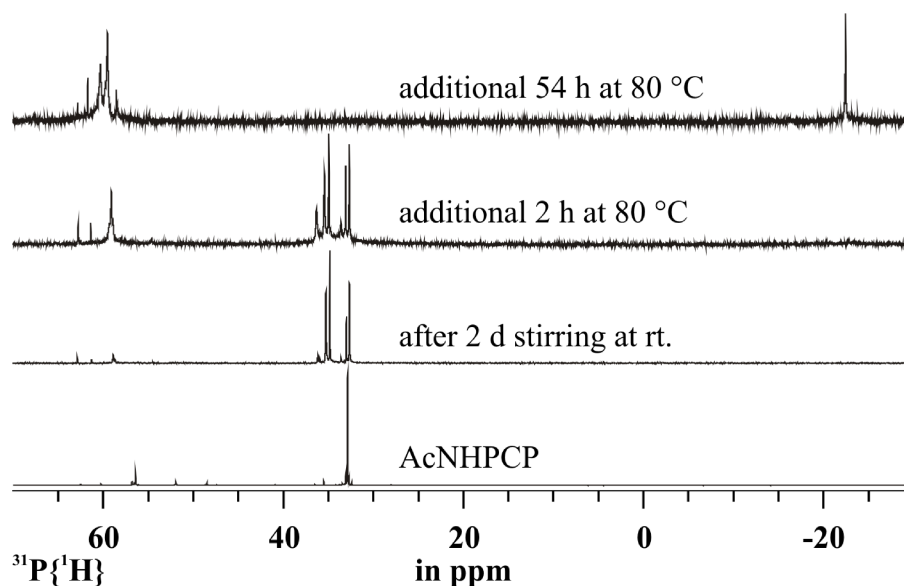


Figure 4: Reaction of AcNHPCP **54e** with $[\text{Ir}(\text{COD})\text{Cl}]_2$ in toluene

The $^{31}\text{P}\{^1\text{H}\}$ NMR spectra of a second approach of **54e** with 1eq. of iridium cyclooctadiene chloride dimer in toluene are shown in Figure 4. While the final spectra are quite comparable, the spectra after the stirring periods are different from those obtained from the former attempts (Figure 3). They display four sharp singlets slightly shifted to lower fields (35 ppm) and only negligible amounts of resonances around -60 ppm. Heating up the suspension to 80°C the intensities of the signals at 35 ppm decrease in favour of the resonances at -60 ppm. Finally, the sharp singlets (35 ppm) disappear, the signal pattern at 60 ppm slightly changes and a sharp singlet at approximately -22 ppm appears. As in the first attempt the overall intensities in the spectra decrease with increasing reaction times, maybe due to precipitation of

phosphorus containing compounds. Therefore, the solid components of the suspension were separated and tried to dissolve in DMSO. The resulting $^{31}\text{P}\{^1\text{H}\}$ NMR spectrum shows broad signals with weak intensities at around 60 ppm and the ^1H NMR spectrum mainly contains very broad signals between 0 and 8 ppm.

The reaction of **54e** with the dimer of the iridium bis-cyclooctene chloride $[\text{Ir}(\text{COE})_2\text{Cl}]_2$ in toluene, also gives no clean pincer complex formation. In Figure 5 the NMR monitoring of this coordination reaction is depicted. The $^{31}\text{P}\{^1\text{H}\}$ NMR spectra contain the singlet of remaining acetamide ligand **54e** over the entire reaction time. After the stirring period and a refluxing time of 24 hours signals between 50 and 60 ppm and a resonance at about 68 ppm appears. Further refluxing the mixture results in an increase of the intensity of the low field signal at 68 ppm, but no significant other changes in the $^{31}\text{P}\{^1\text{H}\}$ NMR spectrum.

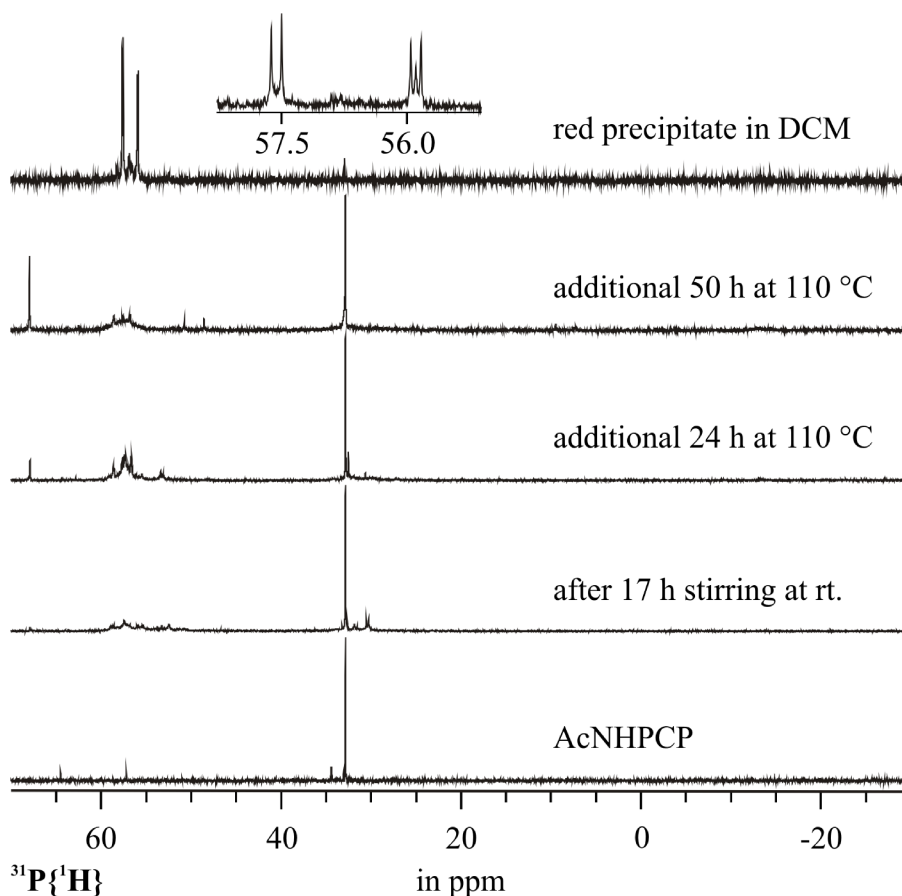


Figure 5: Reaction of AcNHPCP **54e** with $[\text{Ir}(\text{COE})_2\text{Cl}]_2$ in toluene

Furthermore the formation of a reddish precipitate is observed which is reflected in the $^{31}\text{P}\{^1\text{H}\}$ NMR spectra by an increasing noise and therefore decreasing phosphorus concentrations. The spectrum in the topmost row of Figure 5 is obtained from the precipitate dissolved

in DCM-d₂ and shows two doublets at 55.9 and 57.6 ppm with a $^2J_{PP}$ coupling constant of 20.00 Hz which is in accordance with a *cis* arrangement of the phosphorus atoms at the metal centre. The corresponding 1H NMR spectrum (Figure 6) possesses two doublets at -25.72 Hz and -27.04 ppm with $^2J_{PH}$ coupling constants of 22.05 Hz and 23.65 Hz, respectively. From the NMR spectroscopic data it is concluded that the coordination of the metal does not form the C_{2v} symmetric pincer complex with two chemically equivalent *trans* phosphorus atoms. In fact, the NMR spectra are in better agreement with an asymmetric structure containing two iridium centres per ligand or with a coordination polymer *via* the bis-phosphane moiety.

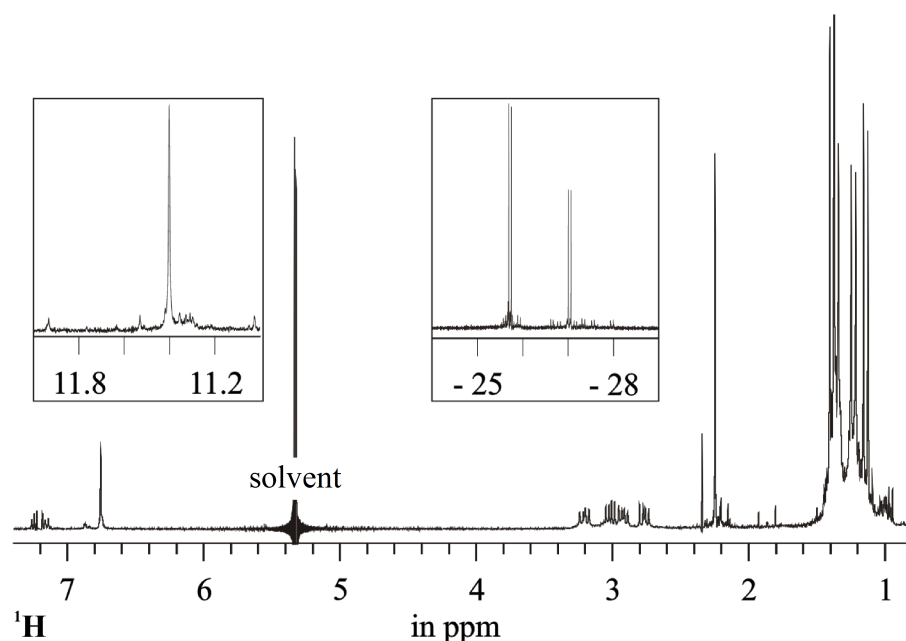


Figure 6: 1H NMR spectrum of the red precipitate (Figure 5) in DCM-d₂

3.1.3.2.2 Trifluoroacetamido pincer ligand

When the trifluoroacetamido protected amino PCP pincer ligand **54f** was stirred vigorously with the iridium cyclooctadiene chloride dimer in benzene-d₆ at room temperature the mixture contains two different phosphorus species within the first 2 h. The high field species (35 ppm) is not significantly shifted compared to the ligand, while the signal at 91 ppm is shifted by more than 55 ppm to lower field. In the 1H NMR spectrum the signals of bound COD, of two different methylene bridges and of two different *tert*-butyl groups are observed. Furthermore, there are two singlets between 7.5 and 9 ppm and a singlet at 10 ppm with an intensity ratio of 1:1:1. After stirring the reaction mixture at elevated temperatures (60 °C and 80 °C) the low

field resonance in the $^{31}\text{P}\{^1\text{H}\}$ NMR spectrum disappears very fast in favour of an accumulation of signals between 50 and 70 ppm. But independent of the reaction time or temperature there remain resonances in the chemical shift region of the uncoordinated ligand. In summary the trifluoroacetamide protected ligand **54f** undergoes a different coordination chemistry with typical iridium precursors than the well investigated methoxy functionalised ligand **54b**.⁶⁷ It is furthermore surprising that the metal coordination reaction of the varying protected ligands **54b** and **54e** proceeds in a different manner. In no attempt it was possible to identify or isolate a coordination compound which is in accordance with a hydrido chloro PCP pincer complex **1e** or **1f**.

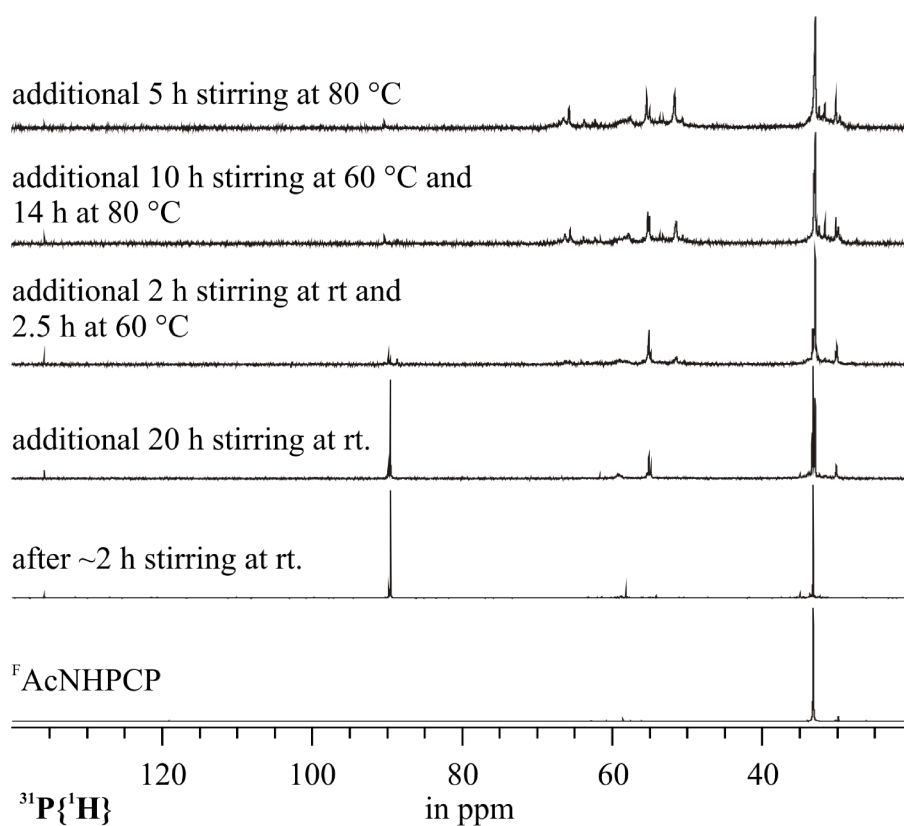
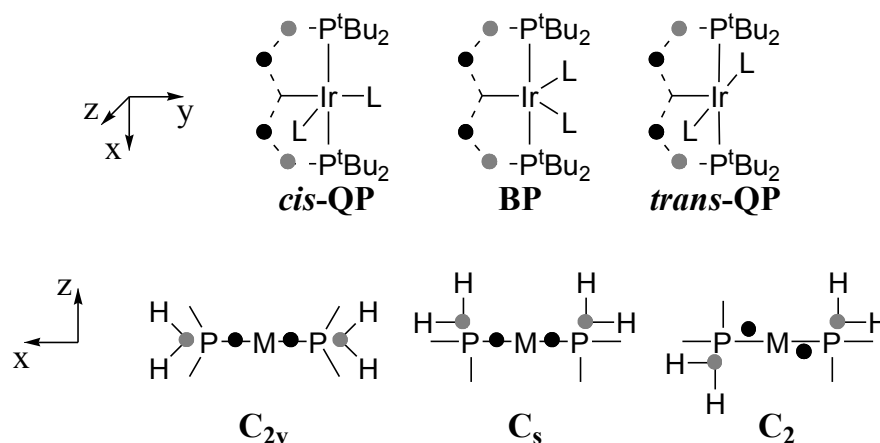


Figure 7: Reaction of $^{\text{F}}\text{AcNHPCP}$ **54f** with $[\text{Ir}(\text{COD})\text{Cl}]_2$ in benzene

3.2 Backbone effects in PCP pincer ligands - a theoretical approach

3.2.1 General remarks

The unusual behaviour in the coordination reactions of the various protected amino functionalised pincer ligands let to a comprehensive quantum chemical investigation, in order to elucidate the influence of different substituents X in basic reactions of pincer complexes. Previous studies about linear free-energy relationships on iridium PCP pincer complexes,³⁵ or thermodynamics of C-H⁸ and N-H⁵¹ activation were verified and extended by the ligands synthesised in this work.



Scheme 30

Scheme 30 illustrates different structural features which have to be considered and differentiated in the calculated structures of pincer complexes. In the upper row the varying coordination geometries of the meridional attached pincer ligand with two additional ligands (L) at the metal are depicted. Both ligands L are contiguous in the first (*cis*-QP) and in the second (BP) structure while the metal is surrounded quadratic pyramidal and trigonal bipyramidal, respectively. In the third structure a *trans* complex with respect to L (*trans*-QP) is shown with quadratic pyramidal coordination geometry. The filled circles in Scheme 30 highlight the carbon atoms (black) next to the metal bound (*ipso*) carbon and the methylene carbon atoms (grey) next to the phosphorus. The results of the DFT geometry optimisations support the C₂ symmetric geometry as the minimum energy structure with the higher energy isomer possessing C_s symmetry for pincer complexes with planar backbones. Because of the strained five-membered rings in the C_{2v} symmetric structure, this seems to be the highest energy structure or a transition state structure for pincer complexes. If not stated otherwise in the following

Schemes, the DFT energy differences are given for the complexes with *cis-QP* structure and in approximate C_2 symmetry, while the calculations are performed without any symmetry constraints.

In general the energies of formation (ΔE) in the following schemes are calculated according to equation 1.

$$\Delta E = E_{\text{products}} - E_{\text{reactands}} \quad (1)$$

Additionally, in the Schemes the energies of formation for a respective isodesmic reaction ($\Delta^i(\Delta E)$) with the unmodified PCP ligated pincer fragments are given, which were obtained from equation 2.

$$\Delta^i(\Delta E)_{\text{XPCPIr(I)}} = \Delta E_{\text{XPCPIr(I)}} + \Delta E_{\text{HPCPIr(III)HCl (1a)}} - (\Delta E_{\text{XPCPIr(III)HCl}} + \Delta E_{\text{HPCPIr(I) (56a)}}) \quad (2)$$

In an isodesmic reaction, the number and types of the broken bonds are equal to the number and types of the generated bonds. This is the case for the HCl exchange reaction which is the base for equation 2. Herein the unmodified Ir(I) fragment (**56a**) serves as the hydrochloric acid acceptor forming the corresponding hydrido chloro complex (**1a**). In case of the isodesmic formation of the different di-hydrido complexes from their Ir(I) precursors, the unmodified Ir(III) di-hydride (**57a**) complex is used as dihydrogen donor.

In order to understand the influence of the backbone on the electronic properties of the ligand, the energy and the orientation of the ligand group orbitals (LGOs) were analysed. The ligand group orbitals were obtained from a single point calculation of all ligands (PCP⁻, Cl⁻, H⁺) in the same arrangement as in the respective complex but without the iridium atom. The valence orbitals of the uncoordinated iridium atom were calculated separately to be -4.2 eV (5d), -3.8 eV (6s) and 0.0 eV (6p) with the singly occupied 5dz² orbital.

Generally the three d_π-orbitals (xy, xz, yz; coordinate system in Scheme 30) of the metal are filled in the d⁶ configuration of an Ir(III) centre in *cis-QP* and *trans-QP* structures while in a T-type d⁸ Ir(I) species one d_σ-orbital (z²) is occupied additionally. In the **BP** structure of d⁶ Ir(III) complexes with singlet ground state the d_π-orbital (yz) appropriate for π-interactions with the *ipso*-carbon atom is higher in energy and therefore unoccupied while instead a d_σ-orbital (z²) is occupied. The second metal d_σ-orbital (x²-y²) remains in all these structures unoccupied. Consequently due to increasing π-donation or diminishing σ-donation from the *ipso*-carbon or the chlorine the **BP** geometry is reinforced while rising π-acceptance or

stronger σ -donation of these ligands may stabilise the **QP** structure.^{34,68,69} For pure σ -donating ligands, the *cis*-**QP** structure is only slightly preferred over the **BP**.³⁴ In the sixfold coordinated d⁶ Ir(III) complexes the d π -orbitals (xy, xz, yz) are occupied, while d σ -orbitals (z², x²-y²) are at higher energies and remain unoccupied. A similar pattern is well known from ligand field theory of homoleptic octahedral complexes.⁶⁹

The LGOs of the different backbones show σ -donating orbitals located at the two phosphorus atoms, the chlorine atom and the *ipso*-carbon atom, at energies concisely below their highest occupied molecular orbitals (HOMOs). Furthermore, the π -donor orbitals of the chlorine and the π_z -donor orbital of the *ipso*-carbon atom (perpendicular to the plane containing both phosphorus and the *ipso*-carbon atom) are located in the same energy range. The respective π_x -donor orbital at the *ipso*-carbon (in the plane containing both phosphorus and the *ipso*-carbon atom) is located around 6 eV below the HOMOs. The HOMOs of the different hydrido chloro pincer LGOs are singly occupied molecular orbitals (SOMOs) mostly located at all ligands and adapted for σ -bonding to a metal. The lowest unoccupied molecular orbitals (LUMO) in all calculated LGOs are also capable for σ -interactions. Commonly, the energetically following orbitals are π -acceptor orbitals located at the *ipso*-carbon atom and, at increased energies, there are orbitals which might be able to realise π -acceptor interactions with the phosphorus atoms.

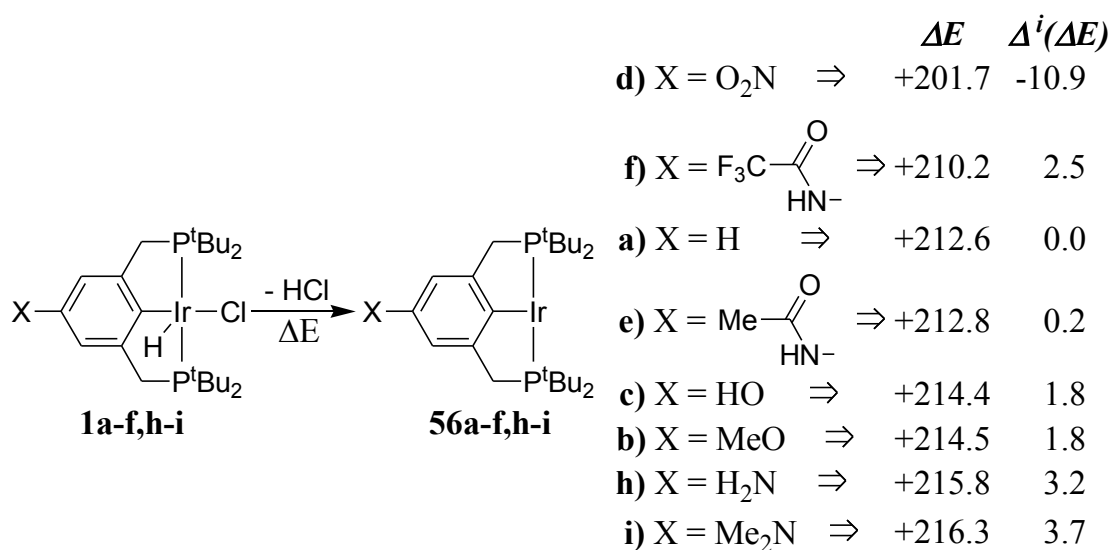
3.2.2 Functionalised phenyl backbones

3.2.2.1 *Ir(III)HCl, Ir(III)H₂ and Ir(I) complexes*

From the nitro pincer ligand to the dimethyl amino functionalised pincer ligand the energy of the HOMO rises from -4.8 to -3.7 eV. The same trend is observed for the energy of occupied molecular orbitals located at the *ipso*-carbon atom adequate for ligand to metal π -donation (from -7.5 eV for X = NO₂ to -5.6 eV for X = Me₂N). For the energy of the metal ligand σ -bonding LUMOs only a slight increase from -3 to -2.3 eV with rising +M character of the substituent X is realised. Especially the -M substituted ligands display low lying molecular orbitals located at the *ipso*-carbon atom with π -acceptor capability towards the metal. These orbitals are also shifted to higher energies (from -2.1 eV for X = NO₂ to +0.6 eV for X = Me₂N) with rising +M character of the backbone substituent. In conclusion, the -M substituted backbones possess π -acceptor orbitals which become less lewis acidic and π -donor orbitals which become more lewis basic with increasing +M character of the backbone substituent X. In the

same order the lewis basicity of the σ -donating HOMOs rises but to a smaller extent as compared to the π -orbitals.

The formation of the threefold coordinated $14e^-$ complexes **56** obtained by reductive elimination of hydrochloric acid is presumably a key intermediate in reaction mechanisms of pincer complexes.^{8,70} In Scheme 31 the energies of formation (ΔE) and the isodesmic energies of formation ($\Delta^i(\Delta E)$) of **56** from **1** are given in kJ/mol and are correlated with the donating capability of the substituent X.

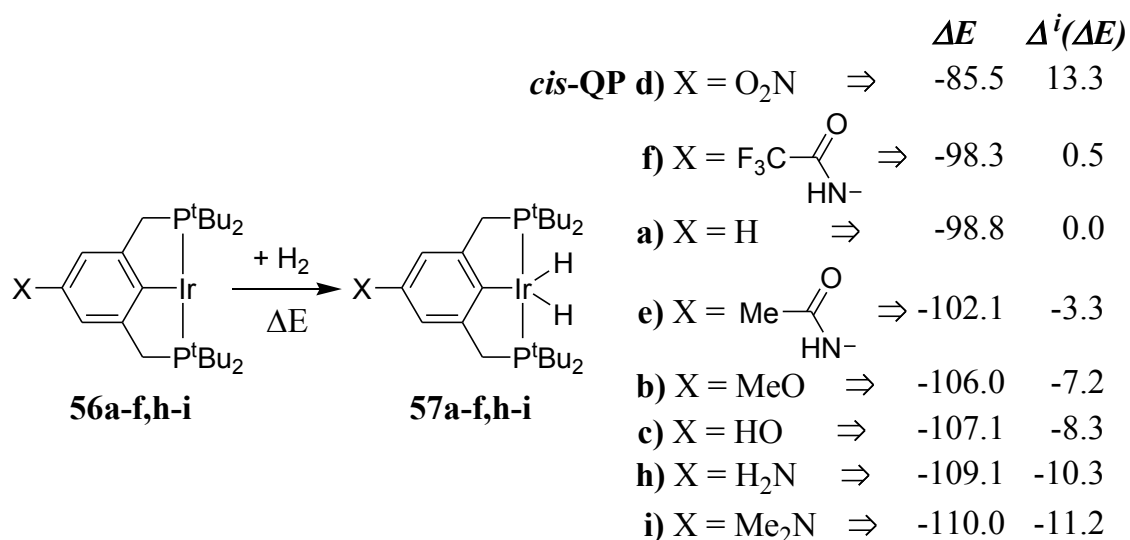


Scheme 31

The strongest -M substituted complex in the collection shows the least endergonic reductive elimination of HCl (Scheme 31), because the -M substituent amplifies the π -accepting interaction of the *ipso*-carbon atom and therefore contributes to the stabilisation of the adequate d_{π} -orbitals of the Ir(I) centre in complex **56d**. In the -M functionalised hydrido chloro complex **1d** the adapted occupied d_{π} -orbitals of the Ir(III) centre are also stabilised by the π -accepting interaction of the functionalised pincer ligand but the same d_{π} -orbitals are additionally involved in the destabilising π -donor interaction with the chlorine ligand. This competitively bonding situation allows to balance the stabilising and destabilising π -interactions by adjusting the Ir-Cl bond length and hence the overlap between the relevant π -orbitals of the metal and the chlorine atom which is one explanation for a structural *trans*-effect⁷¹ or a *trans*-influence⁷². In the case of +M functionalised complexes, the reverse arguments are applicable. Energetically, the overall influence of the different functionalised backbones on the energies of

formation (ΔE) of **56** is with about 15 kJ/mol comparatively small. The isodesmic formation of the trifluoroacetamide functionalised complex **56f** is endergonic and deviates from the trend given by the energy of formation. The negative isodesmic energy of formation ($\Delta^i(\Delta E)$) of the nitro functionalised Ir(I) species **56d** reflects its stability as compared to the unmodified complex fragment **56a**.

The dihydrogen complexes **57** are formed by oxidative addition of H_2 to the respective $14e^-$ Ir(I) fragments **56** in an exergonic process. The more efficient stabilisation of the Ir(I) fragments **56** via π -acceptance, compared to the hydrido chloro Ir(III) complexes **1**, induced by the -M functionalised backbones is reflected in the decreasing energies of formation with increasing +M capability (Scheme 32).



Scheme 32

The same trend is displayed by the formation energies of the respective isodesmic reaction with the unmodified di-hydrido complex **57a** serving as dihydrogen donor. Considering the reductive elimination of HCl and subsequently the oxidative addition of dihydrogen the formation of the di-hydrido complexes **57** remains endergonic with around 110 kJ/mol. Table 1 presents a selection of structural parameters of the different modified phenyl PCP pincer complexes in the Schemes 31 and 32. In case of the nitro functionalised hydrido chloro complex **1d** the structural parameters from the single crystal XRD structure analysis are in good agreement with those obtained from DFT geometry optimisation. The elongation of the Ir-Cl bond in the hydrido chloro complexes **1** with increasing +M-character of the backbone substituent

is rationalised as described above by the diminishing π -acceptor properties of the *ipso*-carbon atom towards an appropriate d_{π} -orbital of the metal, resulting in an increased repulsive interaction between the π -donor orbitals of the chlorine atom with the same iridium centred d_{π} -orbital.

Table 1: Structural properties of the optimised geometries (including solvating effects) and of the experimental³² structures in Schemes 31 and 32. Bond lengths d are given in pm and bond angles \sphericalangle are given in $^{\circ}$.

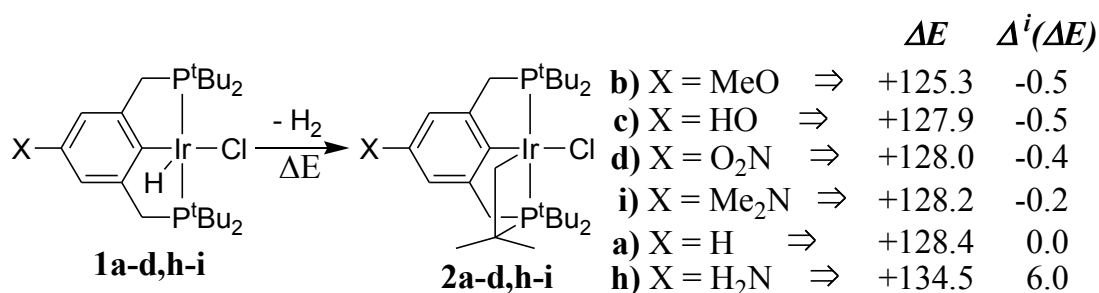
	1a calcd.	56a calcd.	57a calcd.	1d		56d calcd.	57d calcd.	1i calcd.	56i calcd.	57i calcd.
				calcd.	exp.					
$d(\text{Ir-H/Cl})$	248.9	-	161.1	245.9	244.0	-	167.7	249.3	-	161.2
$d(\text{Ir-H})$	154.6	-	161.1	154.8	-	-	154.5	154.6	-	161.4
$d(\text{Ir-C})$	205.2	198.5	211.6	204.0	201.5	196.5	210.2	205.1	199.1	210.4
$\sphericalangle(\text{C-Ir-H/Cl})$	171.6	-	149.1	171.6	179.3	-	181.2	171.5	-	148.8
$\sphericalangle(\text{H/Cl-Ir-H})$	106.2	-	61.8	106.9	-	-	83.5	105.7	-	62.9
$\sphericalangle(\text{C-Ir-H})$	82.0	-	149.1	81.4	-	-	95.5	82.8	-	148.3

Especially, the shortening of the iridium carbon bond lengths by 6 up to 7.5 pm in the $14e^{-}$ Ir(I) species **56** compared to the Ir(III) complex **1** displays the impact of the *trans* ligand. The slight shortening of the Ir-C bond by 2.6 pm in the Ir(I) fragments (**56**) when increasing the -M-character of the backbone substituent is in accordance with π -backbonding between the filled d_{π} -orbitals at the metal and π -acceptor orbital at the *ipso*-carbon atom. Interestingly, the geometry optimisations of the di-hydrido complexes yield a structural change for the nitro functionalised complex **57d** as compared to the other di-hydrido complexes. Excluding the nitro compound, the di-hydrido complexes display a trigonal bipyramidal surrounded metal centre (**BP**) with two equidistant Ir-H bonds, speaking for less efficient π -accepting ligands *trans* to the cleaved H-H bond. The occurrence of *cis*-**QP** coordination geometry with one short (~ 155 pm) Ir-H bond in *trans*-position to the vacant coordination side and one elongated (~ 163 pm) Ir-H bond *trans* to the *ipso*-carbon atom in the case of the nitro functionalised di-hydrido complex **57d** is in good agreement with a more effective π -accepting ligand *trans* to the cleaved H-H bond.^{34,68,69} Both observations, the less voluntary addition of dihydrogen with increasing -M character of the *trans*-substituent and the change of the coordination geometry from **BP** to *cis*-**QP**, are arguments for an efficient transmission of the electronic properties of

the substituent X to the metal bound *ipso*-carbon atom and further to the metal. Additionally the consideration of the LGOs support the influence of the backbone substituent.

3.2.2.2 Doubly-cyclometallated and metallaquinone complexes

The characterisation of the unexpected iridium PCP pincer complexes with an activated *tert*-butyl group in the case of the methoxy and nitro functionalised backbones **2b** and **2d** suggests an electronic influence of the backbone substituent on their formation. Especially in the light of only a few contributions in the literature about pincer complexes dealing with the activation of residual aliphatic groups at the donor atoms.^{42,73-76}

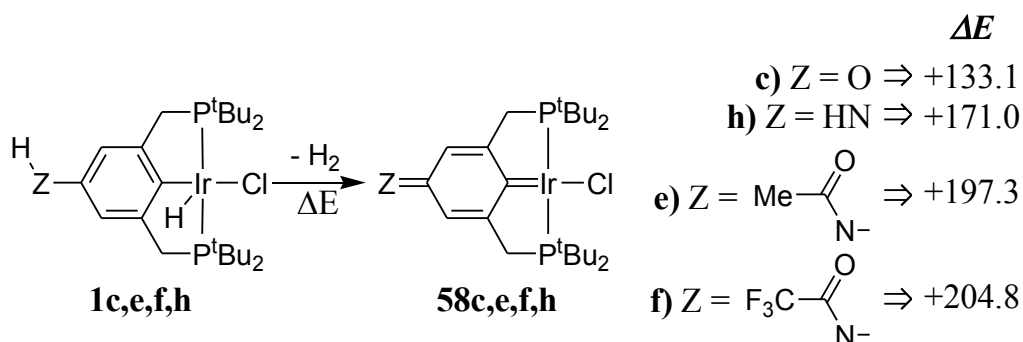


Scheme 33

Neither the energies of formation (ΔE) nor the isodesmic enthalpies of formation ($\Delta^i(\Delta E)$) for the doubly cyclometallated complexes **2** in Scheme 33 display an obvious and significant correlation with respect to the electronic properties of the substituent *para* to the metal. Furthermore, the differences between the energies of formation (ΔE) of the various functionalised complexes remain very small except for those of the amino functionalised complex **2h**. This is explained by the structural change of the pyramidal NH₂ group in **1h** or **57h** to a planar amino group in **2h**. Overall one can conclude an endergonic formation ($\Delta E \approx 130$ kJ/mol) of the doubly cyclometallated complex **2** from the hydrido chloro complex **1** which is under a thermodynamic point of view not significantly influenced by the backbone modification. This implies that either the transition state energies are significantly affected by the different substituents assuming for example a metathesis pathway or that an intermediate in a more complex multistep mechanism is the reason for the *tert*-butyl group activation. Structurally, the introduction of the four-membered ring in complexes **2** leads to a slight increase of the Ir-Cl bond length while the *ipso*-C-Ir bond length remains nearly un-

changed (Table 2). The distance between the sp^3 -carbon atom of the four-membered ring and the iridium atom is about 3 pm to 4 pm longer than the sp^2 -*ipso*-carbon metal bond.

The introduction of a ruthenium metallaquinone^{25,31} with the hydroxy functionalised PCP pincer ligand **54c** is a further example for the versatility of pincer chemistry. The availability of an acidic proton at the directly to the phenyl ring attached atom of the *para* substituent (as in the previously mentioned ligands **54c,e,f,h**) allows the formal elimination of dihydrogen and hence the formation of an iridium metallaquinone **58c** (Scheme 34).



Scheme 34

These intermediates might be one explanation for the different coordination chemistry of the protected amino functionalised ligands **54e** and **54f** (chapter 3.1.3.2 on page 26) compared to the methoxy or the nitro functionalised ligands **54a**, **54b** and **54d**. The formation of the oxo metallaquinone species **58c** from the hydroxy functionalised hydrido chloro complex **1c** with a coplanar O-H bond is the least endergonic process. Starting from the hydrido chloro compound **1h** (with a pyramidal amino group) forming the metallaquinone **58h** (with a coplanar imino group) the energy of formation (ΔE) increases by 37.9 kJ/mol compared to **58c**. If the protected complexes **1e,f** are geometry optimised, a significant structural and energetic change is observed. Structurally the complexes move from a coplanar amide group to an out of plane rotated amide and also the planarity of the benzene ring is slightly distorted. The length of the *ipso*-carbon iridium bond is reduced from approximately 205 pm in the respective hydrido chloro complexes **1c,e,f,h** (compare **1a,d,i** in Table 1) to around 192 pm in the Ir(I) carbene complexes **58c,e,f,h** (Table 2). Furthermore, the metal chlorine bond length is also slightly shortened by about 5 pm as compared to the respective hydrido chloro complexes **1c,h,f**. This inverse structural *trans*-effect is associated with the increased π -acceptor character of the *ipso*-carbon atom in the quinoide ligand. Due to the more efficient π -backdonation

from the d_{π} -orbitals of the metal the repulsive interaction from the chlorine atom diminishes and the metal chlorine bond shortens. In comparison, the pentane-based Ir(I) PCP pincer complex **9** (Scheme 7) with a carbon metal double-bond shows a longer Ir-C bond and a shorter metal chlorine bond length than the metallaquinone complexes **58c,h,f** (Table 2). Energetically, the out of plane rotation of the protecting group as compared to the imino metallaquinone **58h** is responsible for rising the energies of formation (ΔE) of the protected complexes **58e,f** to around 200 kJ/mol.

Table 2: Structural properties of single crystal XRD structure⁴³ and the calculated structure of the carbene complex **9** (Scheme 7) and the geometry optimised structures in Schemes 33 and 34. Bond lengths d are given in pm and bond angles \sphericalangle are given in $^{\circ}$.

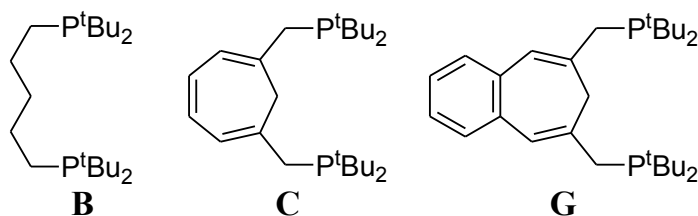
	2a calcd.	2d calcd.	2i calcd.	58c calcd.	58h calcd.	58f calcd.	9	
							calcd.	exp.
$d(\text{Ir-Cl})$	250.2	249.3	250.5	244.2	244.8	243.3	247.5	241.3
$d(\text{Ir-sp}^3\text{-C})$	209.0	209.3	208.9	-	-	-	-	-
$d(\text{Ir-}i\text{pso-C})$	205.4	204.1	205.4	192.4	192.6	192.8	188.4	199.8
$\sphericalangle(i\text{pso-C-Ir-Cl})$	170.1	170.6	171.5	179.3	179.8	178.8	178.5	166.7
$\sphericalangle(\text{Cl-Ir-sp}^3\text{-C})$	101.7	100.1	99.7	-	-	-	-	-
$\sphericalangle(i\text{pso-C-Ir-sp}^3\text{-C})$	88.0	88.3	88.6	-	-	-	-	-

3.2.2.3 Resume

In conclusion, the energies of metallaquinone formation are in-between the energies of *tert*-butyl group activation and those of hydrochloric acid reductive elimination. Therefore, it is expected that the metallaquinone complexes are possible intermediates in the coordination chemistry of **54e** and **54f** at elevated temperatures. The different coordination chemistry of these ligands at room temperature (chapter 3.1.3.2, on page 26) is presumably a result of the formation of hardly soluble coordination polymers. Moreover the coordination of the carbonyl oxygen atom of the amide group and only one of the phosphane arms to the metal might hinder the formation of the pincer complexes.

3.2.3 Pentane and cycloheptatriene-based backbones

In chapter 3.2.2.1 the influence of the modification of the phenyl backbone to some basic transformations of the respective phenyl PCP pincer complexes were investigated by quantum chemical methods. This chapter turns from the modified phenyl based pincer complexes to PCP pincer complexes with saturated and unsaturated aliphatic backbones (Schemes 2 and 3 on the pages 2 and 4). The general considerations and nomenclature about the coordination geometries of the metal centres and the conformational situation of the planar backbones for the phenyl pincer complexes (Scheme 30 on page 33) are identical to the following alkyl, cycloheptatrienyl and benzo-cycloheptatrienyl based pincer complexes (Scheme 35).



Scheme 35

The experimentally accessible cycloheptatriene based pincer complexes derived from the ligands **C** and **G** contain an octahedral-coordinated iridium atom with the meridional attached pincer ligand. The two *cis*-positions to the *ipso*-carbon atom are covered by the hydride and the chloride ligand while a carbonyl group coordinates *trans* to the *ipso*-carbon atom (Scheme 39, compound **59**). In order to be able to compare the different complexes derived from **B**, **C** and **G** and their basic reactions, with those of phenyl based complexes, the hypothetical complexes of **B**, **C** and **G** do not contain the experimentally mandatory carbonyl ligand. In the final part of this chapter the influence of the carbonyl ligand to the complexes of **B**, **C** and **G** and to their energies of formation are discussed. Besides the uncharged backbones **B**, **C** and **G** the respective positively and negatively charged backbones were calculated. For selected examples the ligand group orbitals were analysed to achieve a more quantitative description of their bonding abilities. The elementary reactions which were investigated are the reductive elimination of hydrochloric acid from the hypothetical hydrido chloro complexes and the subsequent oxidative addition of dihydrogen to the 14e⁻ Ir(I) complex fragment. Both reactions were also discussed for the different modified phenyl pincer complexes (Schemes 31 and 32 on the pages 36 and 37, respectively). As for the phenyl pincer complexes the ener-

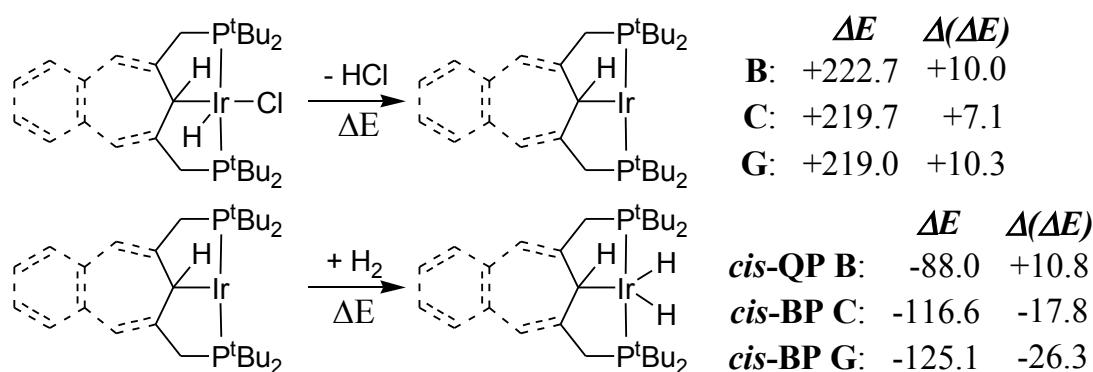
gies of formation (ΔE) and the relative energies of formation of the reaction with the adapted unmodified phenyl PCP pincer complex ($\Delta(\Delta E)$) are given in the following schemes.

$$\Delta(\Delta E_{\text{B Ir(I)}}) = \Delta E_{\text{B Ir(I)}} + \Delta E_{\text{HPCPIr(III)HCl (1a)}} - (\Delta E_{\text{B Ir(III)HCl}} + \Delta E_{\text{HPCPIr(I) (56a)}}) \quad (3)$$

Equation 3 exemplifies the calculation of the relative energy of formation using the example of the neutral Ir(I) species with the alkyl backbone. These relative energies of formation are noisodesmic formation energies because the respective complexes contain different pincer backbones (compare equation 2 on page 34).

3.2.3.1 Uncharged Ir(III)HCl, Ir(III)H₂ and Ir(I) complexes

Scheme 36 contrasts the hypothetical hydrido chloro complexes of the different aliphatic backbones **B**, **C** and **G** in a distorted *cis*-QP arrangement with a sp³-hybridised *ipso*-carbon atom of the coordinating methyne group (Figure 8). The transfer of one molecule hydrochloric acid from the hydrido chloro complexes (**B**, **C** and **G**) to the unmodified phenyl pincer Ir(I) fragment **56a** is an endergonic process, regardless of whether backbone **B**, **C** or **G** is considered. This agrees well with the assumption of better electron donating abilities of the aliphatic backbones **B**, **C** and **G** as compared to the phenyl backbones. In the neutral iridium complexes with aliphatic backbones the sp³-hybridised *ipso*-carbon atom hinders the efficient conjugation of the π -system of the ligand with the d $_{\pi}$ -orbitals of the metal centre. Therefore these neutral ligands are expected to be inefficient π -donors or π -acceptors.



Scheme 36

The analysis of the LGOs of the alkyl hydrido chloro complex **B**-HCl verifies this assumption because adequate π -donor orbitals are located at the chlorine while π -acceptor orbitals at the *ipso*-carbon atom are missing. Excluding the π -donor capabilities of the chlorine also the LGOs of the complexes **C**-HCl and **G**-HCl do not display appropriate π -donor orbitals at the

coordinating carbon. Besides the LUMO adapted for σ -interactions with the metal there are no orbitals with π -acceptor capabilities in **B**-HCl. The π -acceptor orbitals available in **C**-HCl and **G**-HCl at +0.9 and +1.3 eV, respectively are shifted to higher energies as compared to those of the NO₂ phenyl hydrido chloro complex **1d** (-2.1 eV, page 35). Exclusively the benzo-cycloheptatriene backbone **G** possesses between the LUMO and the π -acceptor orbital a further acceptor orbital at -0.3 eV which is available for σ -bonding to the metal. The energies of the ligand to metal σ -interacting HOMOs are nearly constant at -4.1 eV for the three different backbones and remains about 0.2 eV lower in energy than the corresponding SOMO of the unmodified phenyl hydrido chloro LGOs.

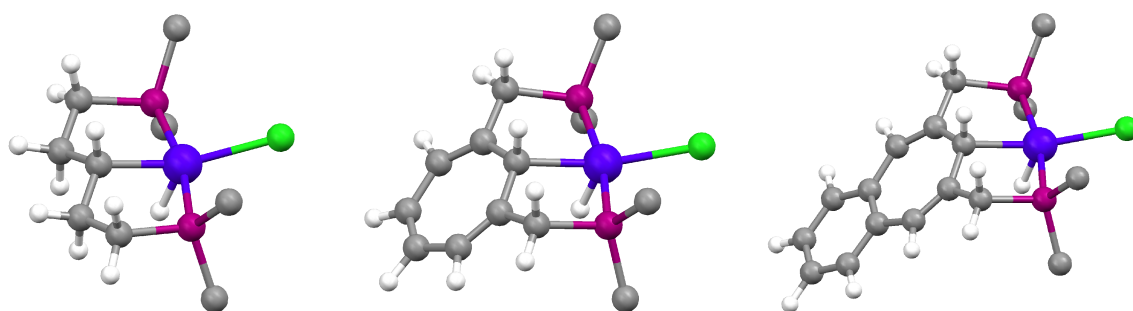


Figure 8: Geometry optimised structures of the hydrido chloro complexes of the ligands **B** (left), **C** (middle) and **G** (right), (methyl groups are omitted for clarity).

Hence the neutral aliphatic backbones (**B**, **C** and **G**) are less efficient σ -donors than the phenyl pincer ligands with strong +M substituents, but quite comparable σ -acceptors. There are orbitals appropriate for π -acceptance but their ability to effectively overlap with the d_{π} -orbitals of the metal is unclear. Therefore, the π -acceptor capability of these ligand backbones is lacking or expected to be very weak. The change of the coordination geometry from *cis*-**QP** in the alkyl based (**B**) di-hydrido complex to **BP** for the **C** and **G** based di-hydrido complexes (Figure 9) seems to reflect the absence of the low lying π -acceptor orbital in the pentane-based backbone as compared to the cycloheptatriene-based ligands. Especially this correlation between the coordination geometry and the electronic properties of the ligand is in contradiction to the observations made for the phenyl di-hydrido complexes. A quantitative analysis with pure σ -bonding ligands³⁴ reveals a *cis*-**QP** structure as minimum but with only small energy differences to the **BP** coordination geometry which might explain the facility of the structural change in the di-hydrido complexes with aliphatic pincer backbone.

The formation of the di-hydrido complex from the threefold coordinated Ir(I) fragment is an exergonic process. If the backbone is varied from **B** over **C** to **G**, their respective di-hydrido complexes are formed more voluntarily. **B-H₂** is calculated to be 10.8 kJ/mol less stable than the nitro functionalised phenyl di-hydrido complex **1d** (Scheme 32), which exhibits the same coordination geometry. While dihydrogen transfer from the unmodified phenyl Ir(I) fragment **56a** (**BP**) to the Ir(I) species with alkyl backbone **B** (*cis-QP*) is an endergonic reaction ($\Delta(\Delta E)$), the cycloheptatriene-based di-hydrido complexes **C** and **G** (**BP**) are formed exergonically. Concerning the small differences in the energies of formation of the 14e⁻ Ir(I) complexes, the discrepancies of the energies of formation of the di-hydrido complexes is attributed to the different stabilisation of the Ir(III) centre in the di-hydride and in the hydrido chloro complexes, respectively. It has to be noted that the di-hydrido complexes are 134.7 kJ/mol in **B-H₂**, 103.1 kJ/mol in **C-H₂** and 93.9 kJ/mol in **G-H₂** less stable than their hydrido chloro counterparts. In contrast to this, the energy difference between di-hydrido and hydrido chloro complexes in case of the functionalised phenyl compounds ranges from 116.2 kJ/mol for X = NO₂ to 106.3 for X = Me₂N. The endergonic formation of **B-H₂** is ascribed to the structural changes in the five-membered rings and the coordination geometry as well as the absence of π -acceptor capabilities.

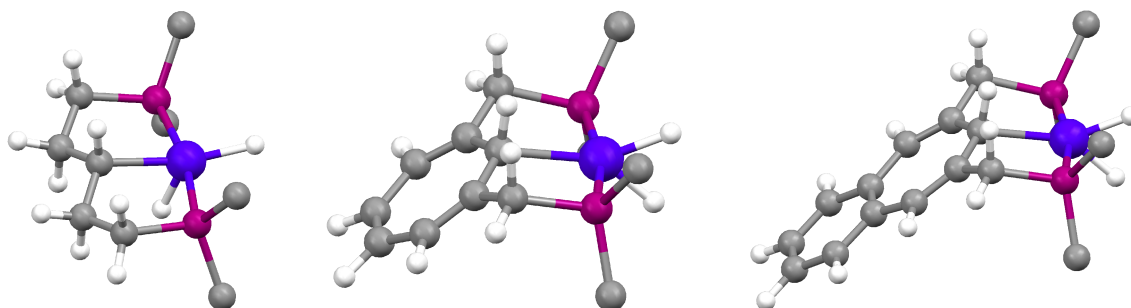


Figure 9: Geometry optimised structures of the di-hydrido complexes of the ligands **B** (left), **C** (middle) and **G** (right), (methyl groups are omitted for clarity).

The stability difference between the di-hydrido complexes **C-H₂** and **G-H₂** seems to correlate with the additional availability of low lying π -acceptor and / or σ -acceptor orbitals located at the *ipso*-carbon atom. Furthermore in the **BP** coordination geometry of the di-hydrido complexes the unoccupied orbital combination of the hydrogen atoms (π -accepting with respect to the metal) and the π -acceptor orbital at the *ipso*-carbon stabilise the same 5d orbital of the iridium. In case of the respective hydrido chloro complexes (*cis-QP*) the σ and π -donating chlorine ligand is located *trans* to the *ipso*-carbon in order to archive an efficient overlap with

d_{σ} -orbitals of the metal. The structure of the benzo-cycloheptatriene hydrido chloro complex (Figure 8) displays remarkable distortions of the square pyramidal coordination geometry. The angles between the *ipso*-C-Ir and the Ir-H bond (79°) and the *ipso*-C-Ir and Ir-Cl bond (165°) differ from the expected values of 90° and 180° , respectively (Table 3) which is ascribed to the reduced π -acceptor properties as compared to the phenyl pincer complexes. The angle between the planar backbone and the plane spanned by the *ipso*-carbon atom and the two phosphorus atoms is 132° . It is noteworthy that the cycloheptatriene-based **C** and **G** complexes, show very similar structures without any significant differences (Table 3).

Table 3: Structural properties from single crystal XRD⁴³ and the calculated complexes in Figures 8 and 9. Bond lengths d are given in pm and bond angles \sphericalangle are given $^{\circ}$.

	B-HCl		B	B-H₂	C-HCl	C	C-H₂	G-HCl	G	G-H₂
	calcd.	exp.								
$d(\text{Ir-Cl/H})$	249.4	241.8	-	171.2	248.9	-	161.9	248.6	-	161.6
$d(\text{Ir-H})$	155.3	-	-	155.7	155.1	-	158.1	155.0	-	158.0
$d(\text{Ir-}i\text{ps}o\text{-C})$	212.5	210.7	207.2	217.2	218.5	211.2	221.5	218.2	211.2	221.3
$\sphericalangle(\text{C-Ir-Cl/H})$	160.2	162.4	-	164.2	164.9	-	151.7	165.3	-	151.3
$\sphericalangle(\text{Cl/H-Ir-H})$	121.9	-	-	119.4	116.7	-	64.9	115.6	-	65.1
$\sphericalangle(\text{C-Ir-H})$	78.0	-	-	76.4	78.4	-	143.4	79.1	-	143.6

The calculated structures of the different cycloheptatriene-based complexes **C** and **G** present a significantly longer sp^3 -*ipso*-carbon iridium bond length than their counterparts with the alkyl backbone **B**. This elongation of the Ir-C bond is mainly ascribed to the change from sp^3 -hybridised β -carbon (adjacent to the *ipso*-carbon atom) in **B** to a sp^2 -hybridised β -carbon atom in **C** and **G**. One further aspect regarding the Ir-C bond length is the π -backbonding ability of the carbon atom. As mentioned above, only the cycloheptatriene-based complexes possess π -acceptor orbitals with quite similar energies. Therefore, there is a shortening of the Ir-C bond in the olefinic backbone with respect to the alkyl backbone expected due to π -backbonding, which in fact seems to be overcompensated by the ring strain effects caused by the β -carbon atom. However, it should be mentioned that the experimentally available structure⁴³ of **B-HCl** and is in good accordance with the calculated structure; excluding the Ir-Cl bond length which is 7.6 pm longer in the calculated than in the experimental structure. Table 3 shows that the metal carbon bond length decreases when HCl is reductively eliminated from the metal. This is explained by absence of the structural *trans*-effect ligand. The shortening

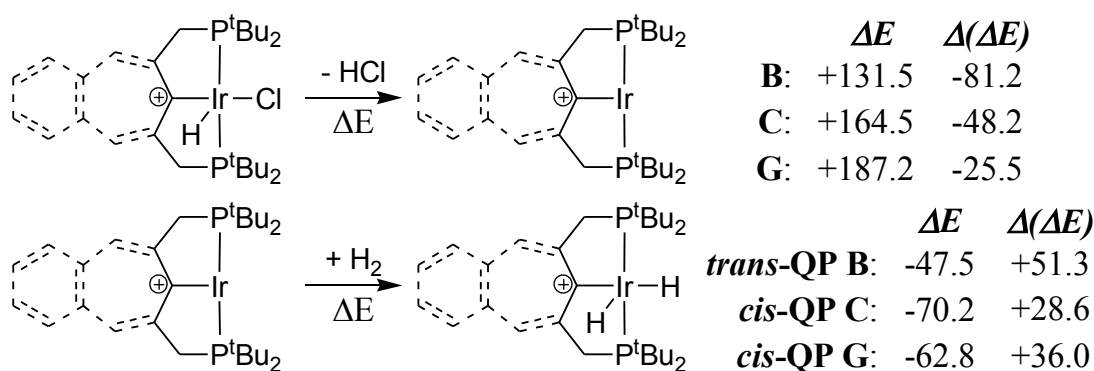
of the Ir-C bond is 5.3 pm for the alkyl backbone **B** while in case of the cycloheptatriene-based complexes the bond is shortened by 7.3 pm for the **C** and 7.0 pm for the **G** backbone. This observation is in good agreement with an additional π -acceptor interaction for the olefinic backbones **C** and **G**. In comparison the reductive elimination of HCl forming the nitro functionalised phenyl Ir(I) complex **56d** is associated with the decrease of the iridium carbon bond length by 7.5 pm. Again the alkyl Ir(I) fragment displays a shorter Ir-C bond than the respective cycloheptatriene-based Ir(I) complexes which is attributed to ring strain effects. Contrariwise in the di-hydrido complexes the Ir-C bond is lengthened by the oxidative addition of H₂. Due to the stronger structural *trans*-effect of the hydride in comparison to the chlorine ligand,^{71,72} the iridium carbon bond lengths in the di-hydrido complexes are longer than the Ir-C bonds in the corresponding hydrido chloro compounds. For the three different di-hydrido complexes (**B-H₂**, **C-H₂** and **G-H₂**), this Ir-C bond elongation is nearly independent of the backbone with about 10 pm, while the trend of the absolute carbon iridium bond lengths remains.

3.2.3.2 Positively charged Ir(III)HCl, Ir(III)H₂ and Ir(I) complexes

Especially the cycloheptatriene-based backbones allow the abstraction of a hydride ion from the sp³-*ipso*-methyne group as an aromatic tropylium analogue cation in the pincer backbone is the result (Scheme 37). All structures are derivatives of a C₂ symmetric arrangement (Scheme 30) of the planar backbone and the plane spanned by the two phosphorus, the chloride and the metal atom. The electron deficiency of the resulting backbones increases their π -acceptor character by lowering the energy of their orbitals. This is in good agreement with the results of their hydrido chloro LGO analysis. The energy of the σ -bonding HOMO is significantly lowered as compared to the neutral complexes but rises from -8.0 eV in **B⁺-HCl** to -7.4 eV in **C⁺-HCl** and remains nearly constant at -7.5 eV in **G⁺-HCl**. The LUMO (σ -bonding) energies follow the similar trend from -6.9 eV in **B⁺-HCl** and -6.5 eV in **C⁺-HCl** to -6.4 eV in **G⁺-HCl**. Energetically, the next orbitals above the LUMO at -5.8 eV (**B⁺-HCl**), -6.0 eV (**C⁺-HCl**) and -6.0 eV (**G⁺-HCl**) are π -acceptor orbitals at the *ipso*-carbon atom. The energy of these acceptor orbitals remains lower than the 5d orbitals of the iridium centre. Therefore, the interaction of these orbitals with the d _{π} -orbitals of the iridium is accompanied by a significant metal to ligand charge transfer while the previously and later on discussed interactions with π -acceptor orbitals are not accompanied by an effective charge transfer. In conclusion the

cationic alkyl backbone (\mathbf{B}^+) is less σ -basic than the respective aromatic backbones (\mathbf{C}^+ and \mathbf{G}^+) while all the cationic backbones (\mathbf{B}^+ , \mathbf{C}^+ and \mathbf{G}^+) possess orbitals with comparable π -acidity. In comparison, the LGOs of all phenyl backbones are more σ -donating as well as less π -accepting than the cationic aliphatic backbones.

The threefold coordinated d^8 -Ir(I) complex gains more stabilisation by the interaction with the π -acceptor orbitals of the ligand than the respective fivefold coordinated d^6 -Ir(III) complex. This might be rationalised by the more efficient orbital interactions between ligand backbone and metal due to the absence of ligand competition for the same orbitals at the Ir(I) centre.



Scheme 37

Consequently, the energies of formation of the cationic Ir(I) complexes (Scheme 37) are drastically reduced as compared to their uncharged counterparts (Scheme 36). Thereby, it is remarkable that the HCl transfer to the unmodified phenyl Ir(I) fragment **56a** proceeds in an exergonic reaction. The strongest exergonic transfer reaction of HCl ($\Delta(\Delta E)$) is observed for the pentane-based complex (\mathbf{B}^+). This is explained by the localised positive charge at the *ipso*-carbon atom, which is associated with the strongest weakening of the σ -donor ability in this collection and consequently a weakening of the iridium carbon σ -bond. The increased and further rising σ -donation of the aromatic backbones due to delocalisation of the positive charge is one reason for the destabilisation of the respective Ir(I) fragments and the less spontaneous formation as compared to the cationic alkyl backbone. Each of the aromatic backbones (\mathbf{C}^+ or \mathbf{G}^+) displays nearly the same but higher π -acidity than the pentane-based backbone (\mathbf{B}^+). Furthermore, there is a second π -acceptor orbital available for each of the cycloheptatriene-based backbones at -5.2 eV in \mathbf{C}^+ -HCl and at -2.6 eV in \mathbf{G}^+ -HCl. In the cycloheptatriene backbone (\mathbf{C}^+), both π -acceptor orbitals are able to contribute to a metal to ligand charge transfer, while in the benzo-cycloheptatriene backbone (\mathbf{G}^+) the higher lying π -accept-

or orbital is not associated with significant charge transfer. The variation of the energies of formation of the cycloheptatriene-based complexes is plausible due to the better stabilisation of a filled Ir(I) d_{π} -orbitals. The feasibility of the formation of the Ir(I) complex with the cationic alkyl backbone is in contradiction to these electronic arguments and has to be ascribed to the differences in their structure and the ring strain of fused five-membered rings. Quite similar arguments were previously used to explain structural differences between the uncharged alkylic and olefinic backbones (see page 44).

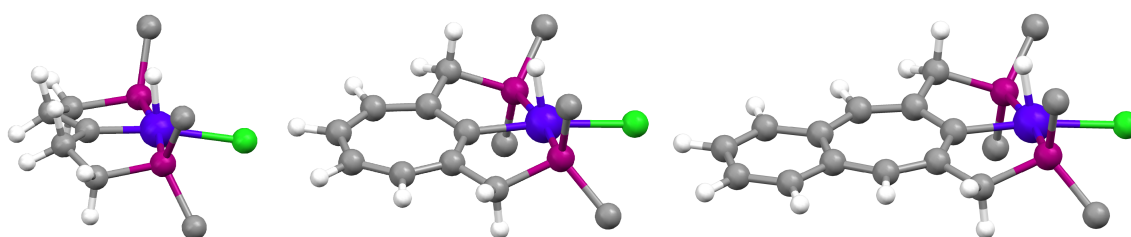


Figure 10: Geometry optimised structures of the cationic hydrido chloro complexes of the ligands **B** (left), **C** (middle) and **G** (right), (methyl groups are omitted for clarity).

The most stable cationic di-hydrido complex turns out to be the one with the cycloheptatriene backbone $\mathbf{C}^+-\text{H}_2$ followed by the benzo-cycloheptatriene backbone $\mathbf{G}^+-\text{H}_2$ and the pentane-based backbone $\mathbf{B}^+-\text{H}_2$. This can be attributed to the lower lying second π -acceptor orbital in $\mathbf{C}^+-\text{H}_2$ and therefore the more efficient stabilisation of the adequate Ir(III) d_{π} -orbital as compared to $\mathbf{G}^+-\text{H}_2$. Due to the overall weaker π -acceptance in $\mathbf{B}^+-\text{H}_2$ the Ir(III) d_{π} -orbital is least efficiently stabilised and the di-hydrido complex formation is less exergonic.

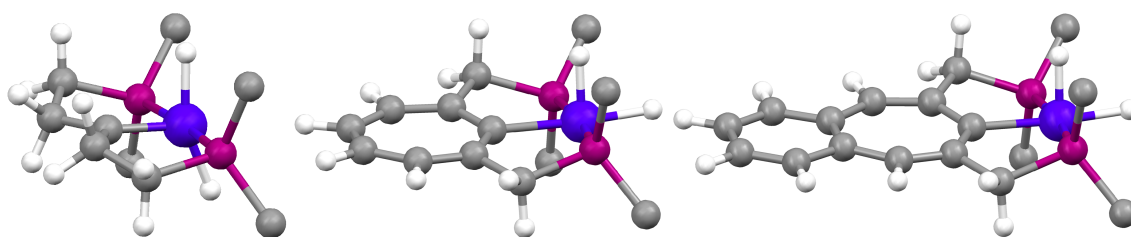


Figure 11: Geometry optimised structures of the cationic di-hydrido complexes of the ligands **B** (left), **C** (middle) and **G** (right), (methyl groups are omitted for clarity).

Remarkably, the di-hydrido complex with the pentane-based backbone $\mathbf{B}^+-\text{H}_2$ displays again a structural variation with mutual *trans* oriented hydride ligands (*trans*-QP) as compared to the cycloheptatriene-based complexes $\mathbf{C}^+-\text{H}_2$ and $\mathbf{G}^+-\text{H}_2$ with *cis*-QP structures (Figure 11). The QP structure is the predicted⁶⁸ geometry for a ligand with σ -donating and strong π -accepting

capabilities (chapter 3.2.1 on page 33). Unfortunately, there is no further discussion or differentiation between the mutual *cis* or the *trans*-orientation of the hydride ligands in this literature. Since the π -acceptor properties of the three backbones are quite comparable, this structural difference is attributed to the stronger σ -donation of the cycloheptatriene-based backbones \mathbf{C}^+ and \mathbf{G}^+ as compared to the pentane-based backbone \mathbf{B}^+ .

Table 4: Structural properties of the calculated cationic complexes in Figures 10 and 11. Bond lengths d are given in pm and bond angles \sphericalangle are given in $^\circ$.

	\mathbf{B}^+ -HCl	\mathbf{B}^+	\mathbf{B}^+ -H ₂	\mathbf{C}^+ -HCl	\mathbf{C}^+	\mathbf{C}^+ -H ₂	\mathbf{G}^+ -HCl	\mathbf{G}^+	\mathbf{G}^+ -H ₂
$d(\text{Ir-Cl/H})$	239.3	-	166.4	242.0	-	166.3	242.1	-	166.6
$d(\text{Ir-H})$	156.2	-	164.8	155.0	-	154.7	155.1	-	154.7
$d(\text{Ir-}i\text{pso-C})$	191.2	184.6	185.7	202.6	192.7	210.4	201.6	192.1	209.1
$\sphericalangle(\text{C-Ir-Cl/H})$	163.6	-	114.2	172.6	-	184.2	171.9	-	184.7
$\sphericalangle(\text{Cl/H-Ir-H})$	113.6	-	157.3	104.1	-	85.3	105.0	-	84.9
$\sphericalangle(\text{C-Ir-H})$	82.8	-	88.5	83.2	-	90.5	83.0	-	90.5

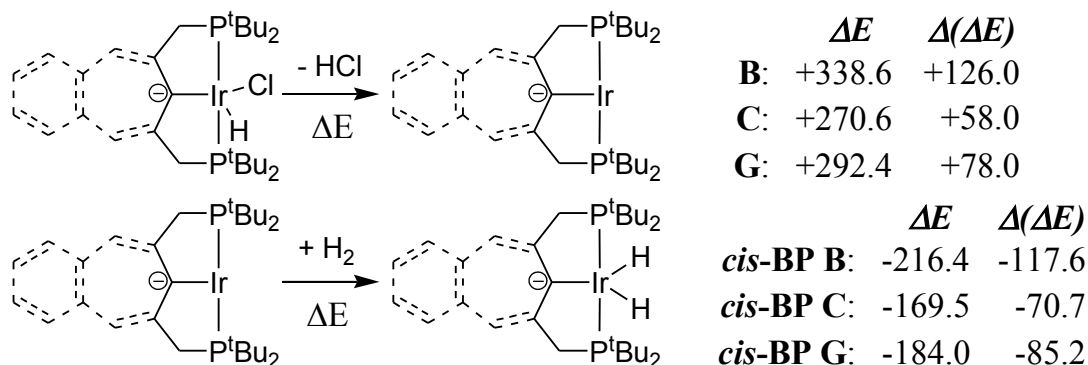
A more detailed analysis of the structural parameters of the cationic complexes given in Table 4 supports the previously mentioned increased π -acceptor character of the cationic backbones as compared to the respective neutral aliphatic or the phenyl backbones. The Ir-C bond as well as the Ir-Cl bond are drastically shorter in the positively charged hydrido chloro complexes, which reflects the structural *trans*-effect induced by the strong π -acceptance of the *ipso*-carbon atom. Analogously, the Ir-C bond is shortened in the Ir(I) fragments and the dihydrido Ir(III) complexes. Furthermore, the stronger π -acceptance of the aromatic backbones is correctly represented by the shorter iridium carbon bonds in these complexes. Especially the complexes of the pentane-based backbone \mathbf{B}^+ present very short *ipso*-carbon iridium bonds which is explained by ring strain effects in the five-membered rings due to the sp^3 -hybridised carbon atom adjacent to the *ipso*-carbon.

3.2.3.3 Negatively charged Ir(III)HCl, Ir(III)H₂ and Ir(I) complexes

Formally, the hydrogen atom from the coordinated methyne group in the neutral hydrido chloro complexes can also be removed as proton generating the respective anionic complexes (Scheme 38). In contrast to the positive charge, which is stabilised by the formation of a planar 6π -electron containing aromatic tropylium analogue cation, the negative charge cannot

be stabilised in these backbones. This is ascribed to the *anti*-aromatic character of a conjugated (planar) cycloheptatriene ring containing 8π -electrons. In order to avoid these *anti*-aromatic destabilisation, the planarity and, hence, the efficient conjugation of the π -system should be evaded. Consequently, the increased electron density of the negatively charged backbone is expected to become delocalised to a higher extent to the metal moiety.

Analysing the hydrido chloro LGOs of the different anionic backbones reveals the strong shift of all MOs towards higher energies which is in good agreement with the qualitative assumption of overall more lewis basic ligands. The pentane-based backbone **B**⁻ displays no π -acceptor orbitals while the energies of the π -acceptor orbitals of the cycloheptatriene-based backbones are +1.0 eV, +5.2 eV in **C**⁻ and +2.5 eV in **G**⁻. Excluding **C**⁻ which posses the π -accepting LUMO at +1.0 eV, the LUMOs and the HOMOs are appropriate orbitals for σ -interactions with the metal. Their energy is calculated to +2.2 eV in **B**⁻, +0.8 eV in **G**⁻ for the LUMOs and +0.3 eV in **B**⁻ and 0.0 eV in **C**⁻ and -0.3 eV in **G**⁻ for the HOMOs. Additionally, all π -donating orbitals raised to energies a few electron volts higher or a few electron volts lower than the energies of the d_{π} -orbitals of the iridium atom. These energy changes of the ligand MOs should dramatically increase the σ -donor and π -donor interactions, where the latter are associated with the destabilisation of the filled d_{π} -orbitals and the respective *trans*-ligand. Furthermore the stabilising π -acceptor interactions should be weakened due to the high energy of the appropriate acceptor orbitals.



Scheme 38

Obviously, there is a strong impact of the negatively charged backbone to the energies of formation of the reductive elimination of HCl and the oxidative addition of H₂ (Scheme 38). The energies of formation of the Ir(I) fragment display the strongest endergonic reductive elimination for the pentane-based backbone **B**⁻, which can be rationalised by the lack of π -ac-

ceptor orbitals and therefore the stronger destabilisation of the Ir(I) fragment. The stabilisation of the metal d_{π} -orbitals by π -acceptor orbitals at the ligand might be the reason for the less endergonic formation of the cycloheptatriene-based Ir(I) fragments \mathbf{C}^- and \mathbf{G}^- . Furthermore, the more facile formation of the cycloheptatriene \mathbf{C}^- Ir(I) fragment as compared to the benzo-cycloheptatriene \mathbf{G}^- Ir(I) complex is attributed to the higher lying π -acceptor orbital in \mathbf{G}^- and, therefore, the weaker stabilisation of the metal d_{π} -orbitals. Altogether, the most unstable Ir(I) fragment is obtained with the negatively charged backbones. Consequently, the most exergonic energies of formation are observed for the oxidative addition of dihydrogen to these species. If the dihydrogen molecule is transferred from the unmodified phenyl di-hydrido complex **57a**, the reaction energies ($\Delta(\Delta E)$) remain negative and their values reflect the stabilities of the corresponding Ir(I) fragments. However, the di-hydrido complexes are less stable than the respective hydrido chloro complexes (122.2 kJ/mol for \mathbf{B}^- , 101.1 kJ/mol for \mathbf{C}^- and 108.4 kJ/mol for \mathbf{G}^-).

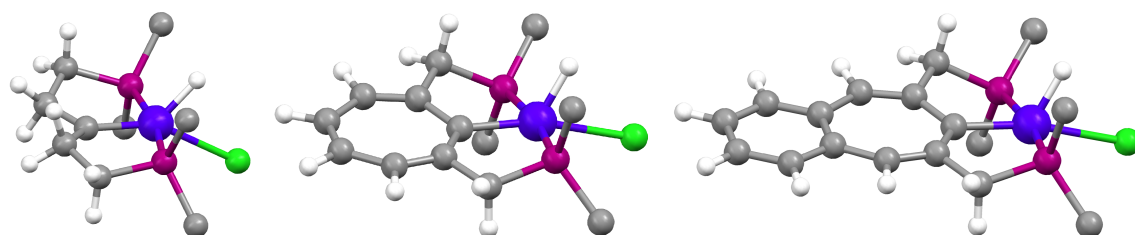


Figure 12: Geometry optimised structures of the anionic hydrido chloro complexes of the ligands \mathbf{B}^- (left), \mathbf{C}^- (middle) and \mathbf{G}^- (right), (methyl groups are omitted for clarity).

Structurally the hydrido chloro complexes of the negatively charged backbones display a coordination geometry which might be described as an intermediate between *cis*-QP structure and the BP geometry (Figure 12). The planarity of the cycloheptatriene-based backbones is slightly distorted for \mathbf{C}^- -HCl, while in \mathbf{G}^- -HCl there are no distortions obvious. Considering the *anti*-aromatic character of the planar cycloheptatrienide anion, the structures of the hydrido chloro complexes are best described by an iridium carbene complex with a negative charge delocalised over the IrHCl moiety. This description is also supported by the structural details (Table 5). The iridium carbon bonds in the hydrido chloro complexes are strongly shortened. In case of the cycloheptatriene-based compounds (\mathbf{C}^- -HCl and \mathbf{G}^- -HCl) the Ir-C bonds are a little shorter than in the respective cationic complexes (\mathbf{C}^+ -HCl and \mathbf{G}^+ -HCl, Table 4), while the Ir-C bond in \mathbf{B}^- -HCl remains a bit longer than the Ir-C bond in its cationic coun-

terpart $\mathbf{B}^+\text{-HCl}$. On the contrary, the Ir-Cl and the Ir-H bonds in the anionic complexes are drastically elongated up to 21.7 pm for the Ir-Cl bond in $\mathbf{B}^-\text{-HCl}$ as compared to their uncharged counterparts.

Table 5: Structural properties of the calculated anionic complexes in Figures 12, 13 and 14. Bond lengths d are given in pm and bond angles \sphericalangle are given in $^\circ$.

	$\mathbf{B}^-\text{-HCl}$	\mathbf{B}^-	$\mathbf{B}^-\text{-H}_2$	$\mathbf{C}^-\text{-HCl}$	\mathbf{C}^-	$\mathbf{C}^-\text{-H}_2$	$\mathbf{G}^-\text{-HCl}$	\mathbf{G}^-	$\mathbf{G}^-\text{-H}_2$
$d(\text{Ir-Cl/H})$	271.4	-	167.3	266.2	-	164.5	262.6	-	164.1
$d(\text{Ir-H})$	165.6	-	167.1	161.3	-	165.9	159.5	-	164.1
$d(\text{Ir-}i\text{ps}o\text{-C})$	193.1	192.8	197.7	200.5	203.8	205.0	201.5	202.5	207.7
$\sphericalangle(\text{C-Ir-Cl/H})$	149.7	-	141.6	164.0	-	139.5	166.7	-	145.1
$\sphericalangle(\text{Cl/H-Ir-H})$	77.8	-	75.6	76.9	-	72.0	115.6	-	145.1
$\sphericalangle(\text{C-Ir-H})$	132.5	-	142.8	119.0	-	148.5	77.7	-	69.8

In the light of these observations the alteration of the coordination geometry towards \mathbf{BP} is in very good agreement with a strongly σ -donating and a strongly π -donating ligand *trans* to the chlorine atom. Furthermore in chapter 3.2.1 on page 34 the difference in the orbital occupation of a d^6 Ir(III) centre in a *cis*- \mathbf{QP} and a \mathbf{BP} arrangement is described. Thus the distortion of the \mathbf{QP} towards the \mathbf{BP} structure destabilises the initially doubly occupied $5d_{yz}$ orbital, while concomitantly stabilising the empty $5d_{z^2}$ orbital. At a distinct distortion the $5d_{yz}$ becomes less stable with respect to $5d_{z^2}$ orbital and the orbital occupation exchanges. Since the π -interaction perpendicular to the plane of the sp^2 -*ipso*-carbon atom is realised with this $5d_{yz}$ orbital at the iridium centre the structural distortion is an imperative condition, if the ligand presents π -donor orbitals. The hydrido chloro complex with the pentane-based backbone ($\mathbf{B}^-\text{-HCl}$) displays the shortest iridium carbon bond which is ascribed to the sp^3 -methylene group in β -position to the *ipso*-carbon atom and, therefore, to the higher flexibility of the five-membered rings. Interestingly the basic structures of the anionic Ir(I) fragments are not easily derived from the respective hydrido chloro Ir(III) structure as it is possible for the previously mentioned complexes. Indeed the Ir(I) complex with pentane-based backbone (\mathbf{B}^-) shows a pyramidal structure of the *ipso*-carbon atom (Figure 13) implying for an at least incomplete sp^3 -hybridisation while the *ipso*-carbon atom in the hydrido chloro complex is planar. Consequently in this complex the negative charge is at least partially localised at the *ipso*-carbon atom. Due to the orbital occupation at the T-shaped d^8 Ir(I) centre (page 34) with an occupied d_{σ} -orbital

($5d_z^2$) and completely filled d_{π} -orbitals ($5d_{xy}$, $5d_{yz}$, $5d_{xz}$) the efficient stabilisation of the electron density in the π -orbital at the *ipso*-carbon is impossible. In all anionic complexes there is no significant change in the Ir-C bond length observed, when hydrochloric acid is reductively eliminated. The elongation of the Ir-C bond due to the repulsive π -interaction is compensated by the expected shortening of the same bond caused by the loss of the structural *trans*-effect ligand.

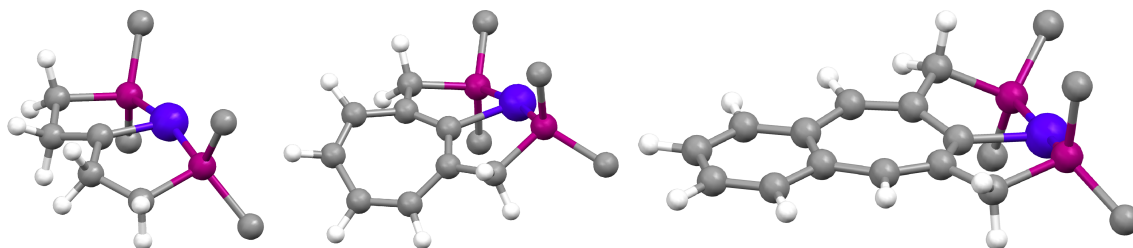


Figure 13: Geometry optimised structures of the anionic Ir(I) fragments of the ligands **B⁻** (left), **C⁻** (middle) and **G⁻** (right), (methyl groups are omitted for clarity).

In the anionic cycloheptatriene backbone **C⁻** the negative charge is at least partially localised in the organic ring-system, which becomes twisted in order to avoid the anti-aromatic character of the planar backbone. The planarity of the benzene ring in **G⁻** prohibits a pronounced twisting of the cycloheptatriene ring. From the obtained structure (Figure 13) only a slightly bending at the methyne groups of the seven-membered ring is apparent. Consequently, the charge has to be localised to a higher extend on the metal than in the anionic cycloheptatriene system **C⁻**. This is reflected by the 2.5 pm shortening of the Ir-C bond in the benzo-cycloheptatriene Ir(I) fragment.

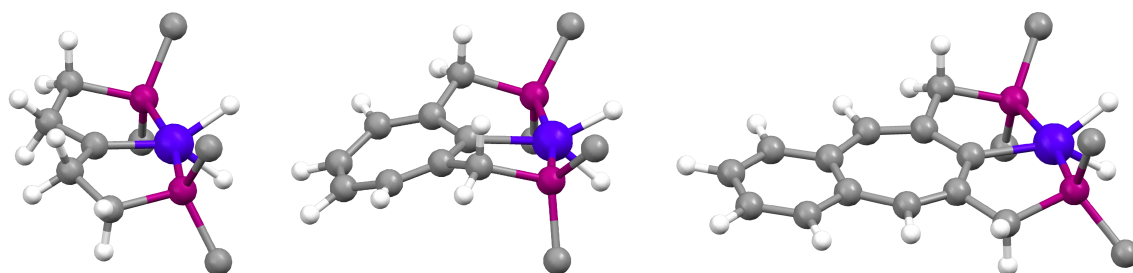


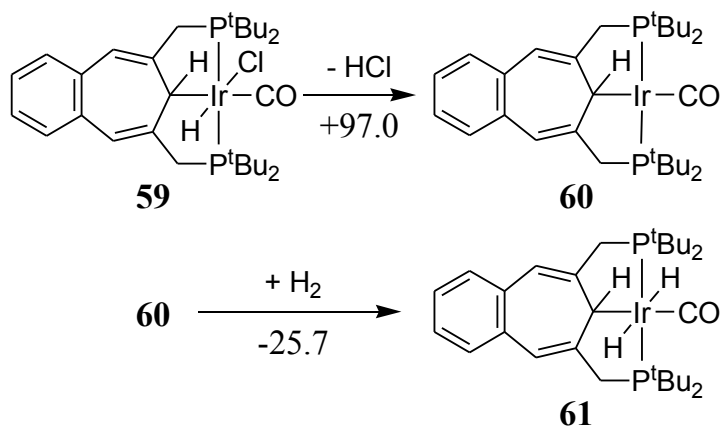
Figure 14: Geometry optimised structures of the anionic di-hydrido complexes of the ligands **B⁻** (left), **C⁻** (middle) and **G⁻** (right), (methyl groups are omitted for clarity).

All di-hydrido Ir(III) complexes **B⁻**-H₂, **C⁻**-H₂ and **G⁻**-H₂ show the **BP** coordination geometry (Figure 14) which is expected for π -donating ligands. The LGO analysis reveals the highest

π -basicity in the **B**⁻ ligand followed by the **C**⁻ and finally the **G**⁻ backbone. In fact, the structural parameters in Table 5 display slightly longer iridium carbon bonds than in the respective hydrido chloro Ir(III) complexes. This is attributed to the stronger structural *trans*-effect of the hydride ligands, especially in the **BP** structure, as compared to the hydride and the chloride ligands in the distorted *cis*-**QP** structure. The different coordination geometries of the neutral, cationic and anionic di-hydride complexes containing backbone **B** prohibits the discussion of their iridium hydrogen bond lengths. Although the Ir-H bond in **B**⁻-H₂ is slightly longer than the comparable bonds in the complexes **C**⁻-H₂ and **G**⁻-H₂, which reflects the stronger π -donation induced by **B**⁻. The Ir-H bonds of the uncharged cycloheptatriene-based di-hydrido complexes (**C**-H₂ and **G**-H₂) in the **BP** structure are shorter than the Ir-H bonds in their anionic complexes. This verifies the assumption of the overall stronger π -donating and weaker π -accepting properties of the anionic backbones as compared to their neutral counterparts.

3.2.3.4 Charged and uncharged carbonyl Ir(III)HCl, Ir(III)H₂ and Ir(I) derivatives

Finally, the experimentally accessible hexa-coordinated benzo-cycloheptatriene complexes should be compared to their theoretically predicted penta-coordinated analogues. Until now the carbon monoxide ligand is a synthetic necessity, because the parent complex **59** is obtained only with tricarbonyl iridium chloride as metal precursor.



Scheme 39

The structure of the hydrido chloro carbonyl complex **59** (Figure 15) with the chlorine adjacent to the hydrogen of the *ipso*-carbon atom turned out to be the lowest energy isomer. This structural proposal from theory is verified by experimental structure elucidation.²⁸ Calculating and analysing the LGOs of this structure by removing the iridium centre reveals as the main

difference between the penta and the hexa-coordinated Ir(III) complex the presence of the π^* -orbitals of carbon monoxide. The energy and the appearance of the former LGOs remains nearly unchanged. For the neutral ligand derived from **59** the π -acceptor orbitals located at the carbon atom of the CO are calculated to +1.3 eV and +1.5 eV. The former orbital is aligned parallel to the Ir-P bonds (*xy*-plane) while the latter is parallel to the *ipso*-carbon hydrogen bond (*yz*-plane). Energetically the π -acceptor orbital at the *ipso*-carbon atom is at +1.8 eV. Hence, the similarity of penta and hexa-coordinated LGOs is exemplified comparing this orbital energy with the previously mentioned energy of the competing CO orbital at +1.5 eV.

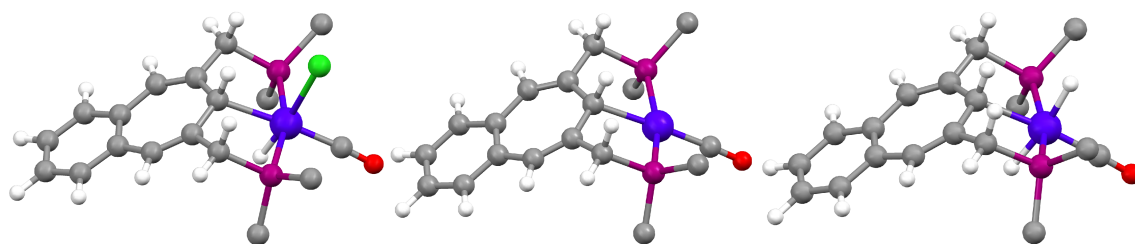
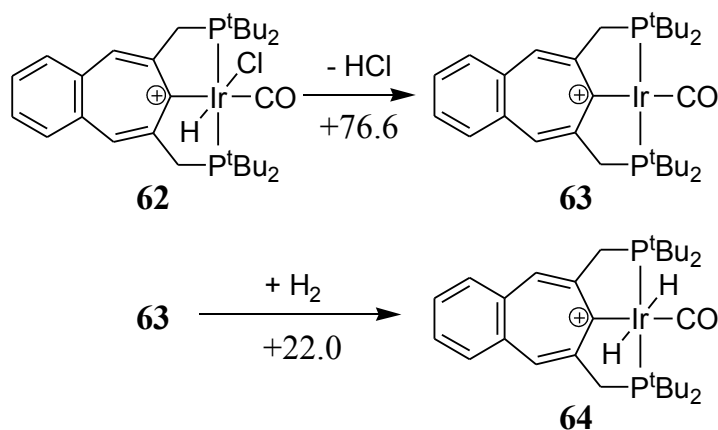


Figure 15: Geometry optimised structures of the neutral carbonyl complexes **59** (left), **60** (middle) and **61** (right) in Scheme 39, (methyl groups are omitted for clarity).

The energies of formation for the reductive elimination of hydrochloric acid and for the oxidative addition of dihydrogen reflect the increased stability of the fourfold coordinated d^8 Ir(I) centre as compared to the respective threefold coordinated metal (Scheme 39). The reductive elimination of HCl is the lowest endergonic process while the formation of the di-hydride **61** is the weakest exergonic reaction hitherto. In chapter 3.5.2 and 3.5.3 the reductive elimination of HCl is also discussed in an experimental context. Besides the stabilisation by the additional σ -bond both π -acceptor orbitals of the carbon monoxide might be adequate to interact with different d_{π} -orbitals (dyz , d_{xy}) of the iridium centre. On the contrary there is just one energetically low-lying π -acceptor orbital at the *ipso*-carbon atom, aligned alongside the *ipso*-carbon hydrogen bond. Furthermore, no strong difference is expected between the stabilisation of the occupied d_{π} -orbitals of the d^6 Ir(III) and the d^8 Ir(I) centre due to the fixed assembly of the *ipso*-carbon *trans* to the carbon monoxide ligand. The same arguments should be valid for the differences between the hexa-coordinated hydrido chloro and the di-hydrido complexes. The mutual *trans*-orientation of the hydrogen atoms in **61** is predetermined by the square planar ligand assembly in the Ir(I) precursor **60**. Structurally the Ir-C bonds in the Ir(III) complexes are about 5 pm longer than in the respective penta-coordinated Ir(III) complexes (Table 6 and

Table 3) which can be ascribed to the stronger structural *trans*-effect of the carbon monoxide as compared to the chlorine ligand. The similarity of the π -acceptor orbital energies of the *ipso*-carbon atom and the carbonyl ligand speaks for quite comparable structural *trans*-effects for both ligands which however depends on the respective bond lengths. The hydrido chloro complex **59** displays the longest Ir-CO bond while the Ir(I) fragment **60** shows the shortest Ir-CO bond. This is explained by the stronger π -backdonation from the d_{π} -orbitals of the d^8 Ir(I) into the π^* -orbitals of the carbonyl as compared to the d_{π} -orbitals of the d^6 Ir(III). The concomitant elongation of the respective C-O bond lengths are smaller but as well in accordance with the π -backdonation into the CO π^* -orbitals.

If a hydride ion is abstracted from the backbone, the resulting cationic hydrido chloro complex **62** is formed (Figure 16). The less endergonic energy of formation of the Ir(I) complex **63** (Scheme 40) is attributed to the increased acceptor properties of the ligands as previously described for cationic backbones (chapter 3.2.3.2 on page 47).



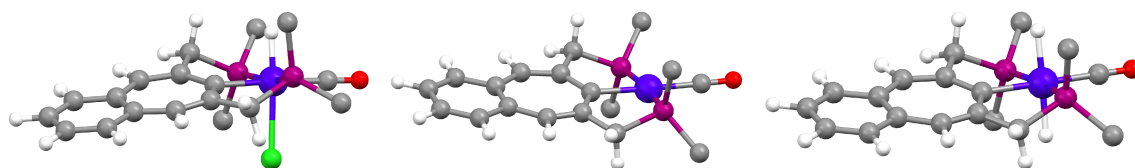
Scheme 40

From the LGO analysis the *ipso*-carbon localised π -acceptor orbital at -5.7 eV is lower in energy than the occupied d_{π} -orbitals of the iridium, which is associated with a metal to ligand charge transfer interaction. On the contrary the π^* -orbitals of the carbon monoxide ligand (-3.4 eV and -2.8 eV) remains energetically above the iridium d_{π} -orbitals. While the orbitals with π -donor capabilities at the chlorine (around -8 eV) and at the *ipso*-carbon (about -10 eV) are significantly lower in energy than the d_{π} -orbitals of the iridium centre. Due to the lower-lying π -acceptor orbital at the *ipso*-carbon atom as compared to the π^* -orbitals of the carbon monoxide the Ir-*ipso*-C is expected to be the stronger structural *trans*-effect ligand in this assembly. These predictions are well reflected by the structural parameters in Table 6.

Table 6: Structural properties of the experimental (Figure 27) and the calculated complexes in Schemes 38, 39 and 40. Bond lengths d are given in pm and bond angles \sphericalangle are given $^\circ$.

	59 calcd.	60 calcd.	61 calcd.	62		63 calcd.	64 calcd.	65 calcd.	66 calcd.	67 calcd.
				calcd.	exp.					
$d(\text{Ir-Cl/H})$	256.3	-	168.0	253.8	250.8	-	167.1	275.5	-	167.7
$d(\text{Ir-H})$	157.1	-	164.9	159.1	-	-	167.1	157.8	-	167.7
$d(\text{Ir-}i\text{psso-C})$	224.8	223.2	225.8	208.8	208.2	208.9	207.9	212.5	210.9	219.7
$d(\text{Ir-CO})$	189.9	186.0	188.5	192.7	192.9	190.3	191.8	191.0	187.3	189.0
$d(\text{C-O})$	115.9	117.1	116.3	115.0	111.5	115.8	115.3	116.8	118.5	117.1
$\sphericalangle(\text{C-Ir-Cl/H})$	90.5	-	88.9	84.4	85.2	-	88.8	89.5	-	85.9
$\sphericalangle(\text{C-Ir-H})$	82.9	-	81.7	91.1	-	-	88.9	88.4	-	85.8
$\sphericalangle(\text{C-Ir-CO})$	174.8	177.1	174.8	177.4	178.2	178.0	179.9	176.8	179.9	179.7

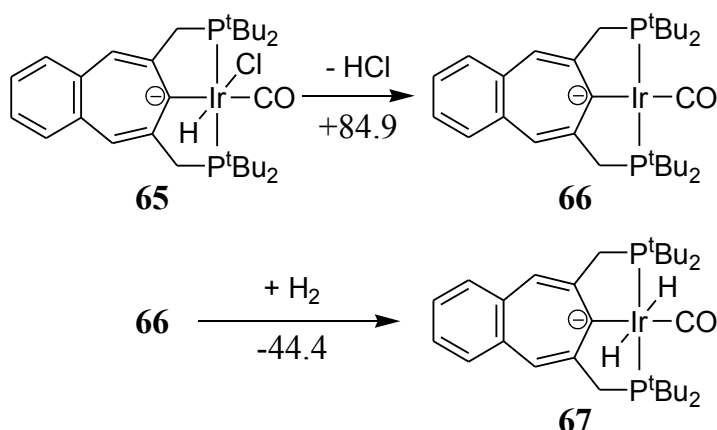
Comparing the neutral hydrido chloro complex **59** with its cationic counterpart **62** the shortening of the Ir-C bond by 16.0 pm accompanied by the lengthening of the Ir-CO bond by 2.8 pm becomes obvious. Meanwhile the changes in the Ir-H and the Ir-Cl bond lengths remain small. This is explained by the generally weaker competition between mutual *cis* ligands towards the same d_{π} -orbital at the metal centre as compared to the mutual *trans* ligands. Moreover, the efficiency of the stabilisation *via* π -acceptance is demonstrated by the endergonic and, for this reason, not spontaneous formation of the di-hydride **64**. This is hitherto the first example in the ligand collection of an Ir(I) complex **63** that is thermodynamically more stable than its Ir(III) di-hydrido complex **64**.

**Figure 16:** Geometry optimised structures of the cation carbonyl complexes **62** (left), **63** (middle) and **64** (right) in Scheme 40, (methyl groups are omitted for clarity).

The structures of the cationic hydrido chloro complex **62**, the Ir(I) compound **63** and di-hydride **64** in Figure 16 are approximately C_2 symmetric (Scheme 30 on page 33), with a planar benzo-cycloheptatriene backbone. In the hexa-coordinated hydrido chloro Ir(III) complex **62** the Ir-H bond is longer than the comparable bond in the penta-coordinated complex $B^+ \cdot HCl$.

This is ascribed to the *cis*-QP structure in $\mathbf{B}^+\text{-HCl}$ and, therefore, the absence of a ligand *trans* to the hydride ligand. The Ir-Cl bond in $\mathbf{B}^+\text{-HCl}$ is 14.5 pm shorter than the respective bond in **62** which reflects the different electronic properties of the ligand *trans* to the chlorine. In the penta-coordinated complex the σ and π -donating chlorine is *trans* to the π -accepting *ipso*-carbon atom while in the octahedral complex **62** the chlorine is located *trans* to the strongly σ -donating hydride ligand.

If a proton is removed from the *ipso*-carbon atom in **59**, the negatively charged complex **65** (Scheme 41) is created. Hydrochloric acid is easier reductively eliminated from the metal than in the neutral complex **59** but the energy of formation remains higher as compared to the cationic complex **62**. In contrast to the cationic Ir(I) complex **63** the oxidative addition of H_2 is a spontaneous reaction and the formation of the di-hydride **67** is more exergonic than for the neutral analogue **59**.



Scheme 41

As described for the anion backbone in chapter 3.2.3.3, an increased σ and π -donation besides reduced π -acceptance are the results of the overall higher orbital energies in negatively charged systems. The energies of the frontier orbitals (HOMO and LUMO) derived from **65** are not significantly different from those obtained for the penta-coordination. However, the LGO analysis of **65** yields an *ipso*-carbon localised LUMO at +1.1 eV which is available for π -acceptor interactions as well as the orbital at +2.6 eV. Furthermore the π -acceptor orbitals located at the carbon atom of the carbonyl ligand are calculated to +3.2 eV for the orbital coplanar with the backbone (*xy*-plane) and +4.1 eV for the orbital perpendicular to the backbone (*yz*-plane). The π -donor orbitals located at the *ipso*-carbon are of comparable energy or about

2 eV lower in energy than the 5d orbitals of the iridium. Orbitals capable for π -donation at the chlorine atom are energetically around 2 eV higher in energy than the iridium 5d orbitals.

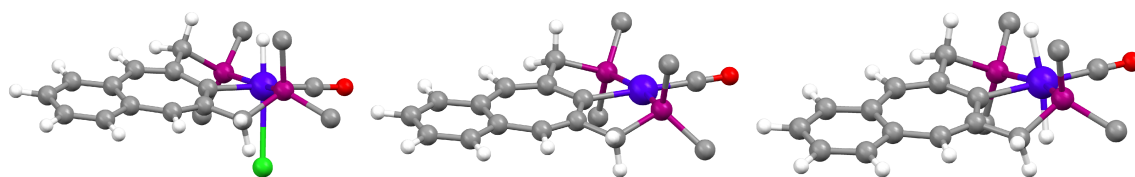
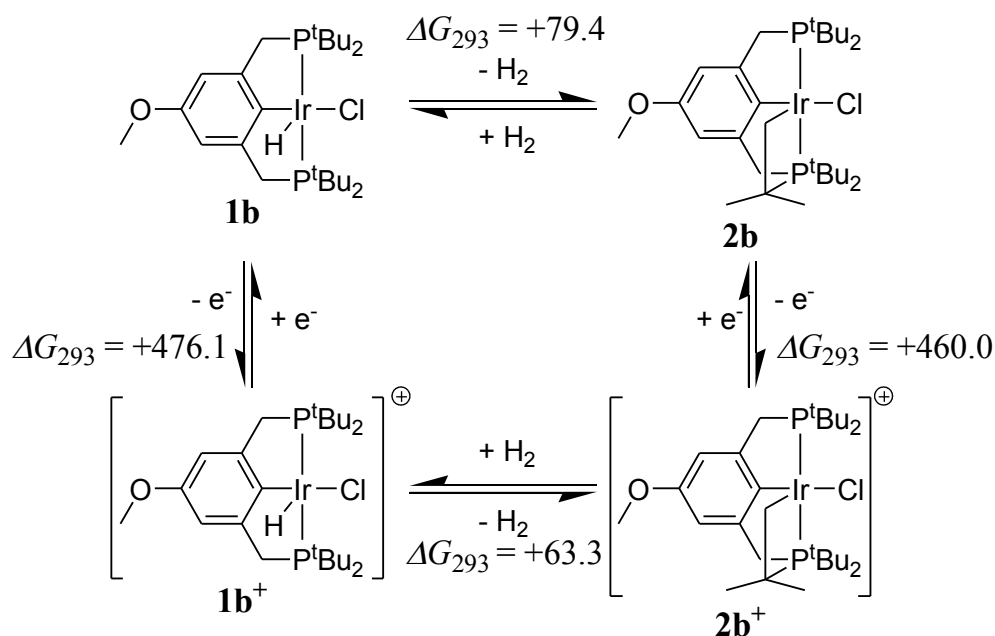


Figure 17: Geometry optimised structures of the anionic carbonyl complexes **65** (left), **66** (middle) and **67** (right) in Scheme 41, (methyl groups are omitted for clarity).

The optimised structures of the anionic complexes in Figure 17 are quite similar to their corresponding cationic compounds in Figure 16. Again the complexes display an approximate C_2 symmetry (Scheme 30 on page 33) with a planar benzo-cycloheptatriene backbone. A more detailed analysis of the structural parameters (Table 6) reveals an elongation of the C-O bond by 1.8 pm in the Ir(III) complexes and by 2.7 pm in the Ir(I) fragment as compared to the corresponding cationic compounds. This is an expected observation, if the negative charge is at least partially stabilised by the π -acceptor capabilities of the carbon monoxide ligand. However, the expected shortening of the Ir-CO bonds in the anionic complexes as compared to their cationic counterparts is less distinctive, but they show the correct trend. The Ir-C bonds in the anionic hydrido chloro Ir(III) and the Ir(I) complexes are elongated by 3.7 pm and 2.0 pm, respectively in comparison to the corresponding cationic complexes. While in the anionic di-hydrido complex **67** the bond is 11.8 pm longer than in its cationic counterpart **64**. A remarkable difference between the uncharged and the negatively charged backbones is the Ir-Cl bond elongation of 19.2 pm in **65** which is indicative for the increasing localisation of the negative charge on the chlorine atom. In comparison the Ir-Cl bond in the anionic penta-coordinated complex **G**-HCl (chapter 3.2.3.3 on page 50) is 14.0 pm longer than in the uncharged complex **G**-HCl. On the assumption that finally the chlorine is eliminated from the metal as chloride the remaining uncharged species is an Ir(I) carbene complex. In conclusion, the additional carbon monoxide ligand is able to balance the electron density in at least one of the filled d_{π} -orbitals of the metal and, thereby, contributes to the overall stabilisation of the complexes discussed in this chapter as compared to the previous chapters.

3.3 Calculations of the square scheme of $1b \rightleftharpoons 2b^+ + H_2 + e^-$

In chapter 2.2 the results of the electrochemical investigations of the methoxy functionalised pincer complexes **1b** and **2b** are summarised. As a surprising feature it turned out that the experimental thermodynamic minimum of the *tert*-butyl group activation reaction is the hydrido chloro complex **1b**, while after oxidation of **1b** the minimum is the doubly cyclometallated cationic complex **2b⁺**. The free enthalpies of all participating species previously presented in Scheme 5 are obtained from DFT calculations considering a dichloromethane solvent surrounding. Thereby, yielding the following square scheme (Scheme 42) with the respective free enthalpies of formation for the different reactions.



Scheme 42

The structures of the complex **1b** and **2b** undergo only slight changes upon oxidation. The most significant variance is observed for the metal chlorine bond length and for the *ipso*-C-Ir-Cl angle (Table 7).

Table 7: Structural differences of the geometry optimised and the experimental structures in Scheme 42. Bond lengths d are given in pm and bond angles \sphericalangle are given in $^{\circ}$.

	1b calcd.	1b⁺ calcd.	2b		2b⁺ calcd.
			calcd.	exp.	
$d(\text{Ir-Cl})$	252.2	245.0	251.6	246.4	245.0
$d(\text{Ir-H})$	154.6	155.2	-	-	-
$d(\text{Ir-}i\text{ps}o\text{-C})$	204.5	198.3	204.2	204.2	198.8
$d(\text{Ir-C})$	-	-	209.0	206.5	210.2
$\sphericalangle(\text{C-Ir-Cl})$	174.8	171.2	173.4	177.4	161.6

The shortening of the iridium chlorine and the iridium *ipso*-carbon bond length is understood, when considering the *anti*-bonding character of the highest occupied molecular orbitals (HOMOs) of the neutral complexes **1b** and **2b** and of the singly occupied molecular orbitals (SOMOs) of the cationic complexes **1b⁺** and **2b⁺** (Figure 18) with respect to the Ir-Cl and the Ir-*ipso*-C connection. For this reason, the decreased electron density in the SOMOs reduces the anti-bonding interaction and stabilises the Ir-Cl or the Ir-*ipso*-C bond. This explanation of the observed structural *trans*-effect in the molecular orbital picture of the complexes is analogous to the previous description of the competing interaction of the *trans*-ligands with the same d_{π} -orbital at the metal centre. Furthermore the SOMOs display a strong delocalisation of the unpaired electron into the phenyl ring and onto the oxygen atom of the methoxy group. This is inconsistent with an easy oxidation of an Ir(III) to an Ir(IV) centre. In fact the oxidation product is better described as a resonance stabilised organometallic radical.

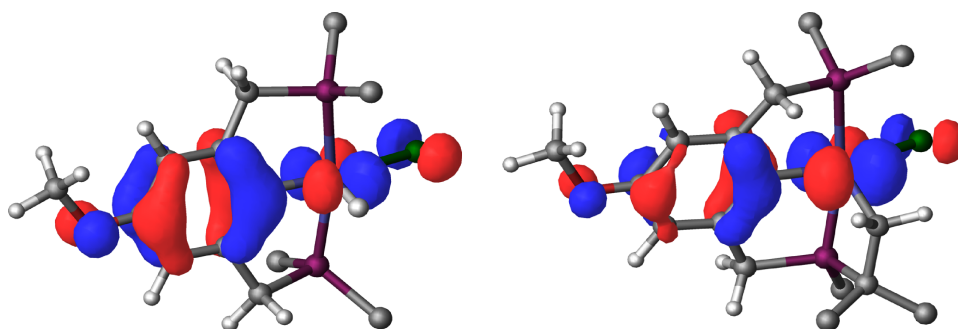
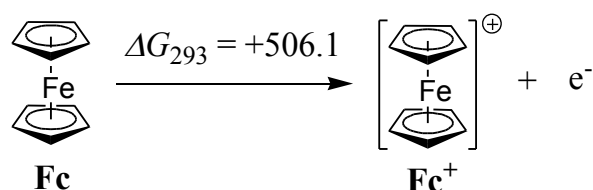


Figure 18: Left: SOMO of **1b⁺**, right: SOMO of **2b⁺** (methyl groups and protons are omitted for clarity).

A detailed cyclic voltammetric investigation of the pure complexes of **1b** and **2b** as well as the analysis of mixtures of **1b** and **2b** and the simulations of the resulting voltammograms yielded thermodynamic and kinetic parameters for the neutral and the cationic pincer complexes.³⁶ In Table 8 a selection of the experimental thermodynamic parameters is contrasted by the theoretically obtained free enthalpies. In order to compare the experimental oxidation potentials (*versus* ferrocene/ferrocenium) for the hydrido chloro complexes **1b** and the doubly cyclometallated complex **2b** with the theoretical values, the differences in the free enthalpies of formation of the redox couple **Fc**/**Fc**⁺ were calculated (Scheme 43).



Scheme 43

The geometry optimisation of the ferrocene isomers demonstrate that the ferrocene molecule in D_{5h} symmetry, which corresponds to the eclipsed orientation of the Cp-rings, is thermodynamically stabilised by 1.6 kJ/mol as compared to the D_{5d} (symmetric) isomer. Hence, the free enthalpy of formation at 293 K of the ferrocenium ion was also obtained from the D_{5h} symmetric structure (Scheme 43). As compared to the free enthalpies of formation of the oxidised complexes **1b**⁺ and **2b**⁺, the ferrocenium ion **Fc**⁺ is formed more endergonically. The experimental values for ΔG_{293} in Table 8 were obtained from the equilibriums constants (K) using:

$$\Delta G_{293} = -RT \ln(K) \quad (4)$$

Herein R denotes the gas constant while T is the absolute temperature. The oxidation potentials are obtained from the following equations:

$$E_{\text{ox}}(\mathbf{1b} \rightarrow \mathbf{1b}^+ + e^-) = -zF \Delta(\Delta G_{293}(\mathbf{1b} + \mathbf{Fc}^+ \rightarrow \mathbf{1b}^+ + \mathbf{Fc})) \quad (5)$$

With E_{ox} as the oxidation potential, z is the number of transferred electrons (in our cases $z = 1$), F the Faraday constant and $\Delta(\Delta G_{293})$ is the difference of the individual free enthalpies of formation (ΔG_{293}) of the participating species.

$$\Delta(\Delta G_{293}(\mathbf{1b} + \mathbf{Fc}^+ \rightarrow \mathbf{1b}^+ + \mathbf{Fc})) = \Delta G_{293}(\mathbf{1b} \rightarrow \mathbf{1b}^+) - \Delta G_{293}(\mathbf{Fc} \rightarrow \mathbf{Fc}^+) \quad (6)$$

The corresponding equations are valid for the oxidation of complex **2b**.

Focussing on the free enthalpies of formation in Table 8, the agreement between experimental and theoretical data is comparatively poor, while the general trend the of easier formation of $\mathbf{2b}^+$ as compared to $\mathbf{1b}$ is reproduced correctly.

Table 8: Comparison of experimental³⁶ and theoretical data. Free enthalpies of formation ΔG_{293} are given in kJ/mol and the oxidation potentials E_{ox} are given in V.

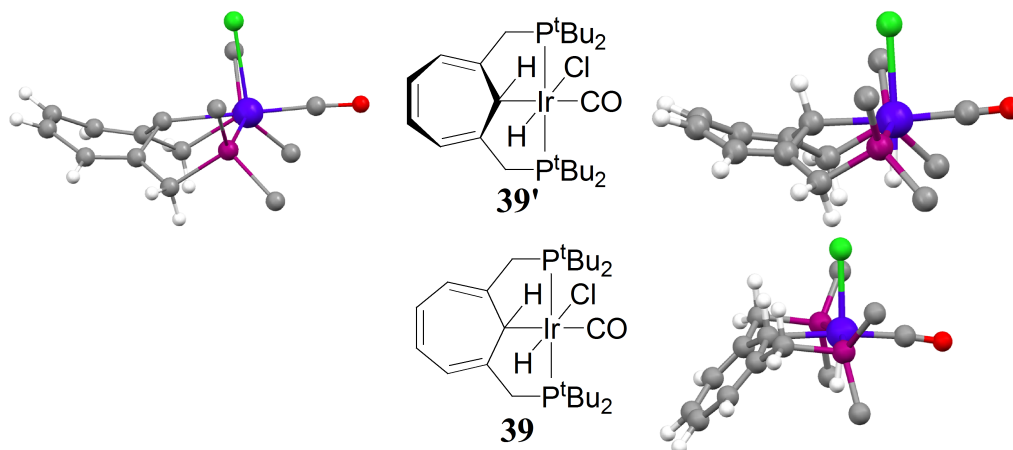
	experimental	theoretical
$\Delta G_{293}(\mathbf{1b} \rightarrow \mathbf{2b} + \text{H}_2)$	+4.3	+79.4
$\Delta G_{293}(\mathbf{1b}^+ \rightarrow \mathbf{2b}^+ + \text{H}_2)$	-5.5	+63.3
$E_{\text{ox}}(\mathbf{1b} \rightarrow \mathbf{1b}^+ + \text{e}^+)$	+0.285	+0.311
$E_{\text{ox}}(\mathbf{2b} \rightarrow \mathbf{2b}^+ + \text{e}^-)$	+0.187	+0.478

Also the experimental and theoretical results of the oxidation potentials of the complexes $\mathbf{1b}$ and $\mathbf{2b}$ are incompatible. Especially the experimentally determined oxidation potentials show an easier formation of $\mathbf{1b}$ as compared to $\mathbf{2b}$ (rows 3 and 4 in Table 8) which is not represented by the theoretical values. At least the positive sign and the order of magnitude of the oxidation potentials is correctly reproduced by the theory. Overall the free enthalpies of formation for the respective oxidation reaction are predicted too low by the calculations with respect to the ferrocenium \mathbf{Fc}^+ formation.

The discrepancies between the experimental and the theoretical data might be attributed to the deficient description of solvating effects in the quantum chemical calculations. Furthermore, the assumption of the structure of the cationic complex $\mathbf{2b}^+$ is not valid. Because of the vacant coordination site at the iridium atom also dimeric species or complexes with coordinating solvent molecules are possible structures for the cationic species. This is supported by the un-systematic deviation of the oxidation potential between $\mathbf{1b}$ and $\mathbf{2b}$.

3.4 Mechanistic considerations on cycloheptatrienyl complexes

The single crystal XRD²⁸ revealed the hydrido chloro complex **39'** with a structure containing a non-planar cycloheptatriene ring (Scheme 44) while the previous DFT calculations used the conformeric structure **39** with a planar backbone as described in chapter 3.2.3.



Scheme 44: left: the crystal structure of **39'**, right: the ball-stick structure from the geometry optimisation of **39** and **39'** (methyl groups are omitted for clarity).

Thermodynamically the planar isomer **39** is by 10.5 kJ/mol higher in energy than the experimentally obtained non-planar structure **39'** (Figure 19). Therefore consecutively the lowest energy structure for the neutral hydrido chloro complex **39'** is used.

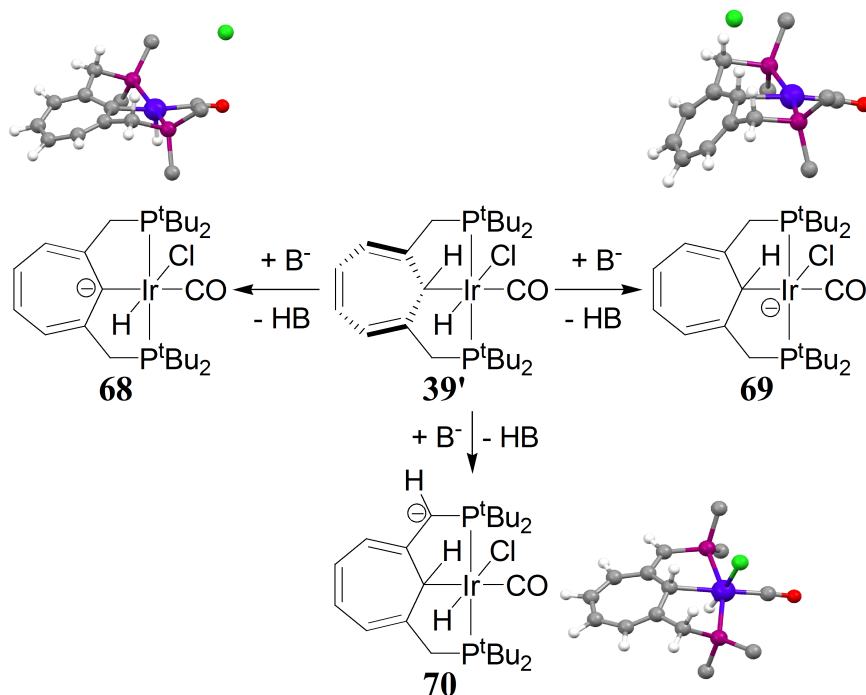
It is assumed that the broad variety of compounds (chapter 2.4 on page 14) obtained from the neutral cycloheptatriene-based hydrido chloro complex **39** are realised by its initial deprotonation.^{30,66} The in this process most probably formed anionic complexes were investigated by quantum chemical calculations to elucidate the lowest energy routes and the structures of the presumably formed intermediates. In this chapter the results of these calculations are summarised and based on the experimental and theoretical facts a mechanism for the formation of the different complexes is proposed.

3.4.1 General deprotonation reactions

The structure of the hydrido chloro complex **39'** offers three plausible positions for the abstraction of a proton (Scheme 45).

- First, the deprotonation of the metal bound *ipso*-carbon atom of the seven-membered ring yielding the anionic complex **68**. In chapter 3.2.3.4 the corresponding anionic benzo-cycloheptatriene complex **65** was already mentioned and the results from its quantum chemical investigation were discussed.
- Second, the proton is removed from methylene groups connecting the di-*tert*-butylphosphane moiety with the cycloheptatriene ring. This forms the anionic complex **70** with the negative charge localised at the bridging methyne carbon atom.
- Third, the abstraction of the metal bound hydrogen atom as a proton releasing the electron pair at the metal. Thereby forming the anionic structure **69** with the negative charge localised at the iridium centre.

In case of the comparable anionic hydrido chloro complex with benzo-cycloheptatriene backbone **65** the short *ipso*-carbon iridium bond and the unexpected elongation of the Ir-Cl bond were indicative for a significant localisation of the negative charge on the chlorine atom. Therefore a quite similar behaviour is expected for the cycloheptatriene backbone which might lead in the limiting case to the emission of a chloride ion and the formation of the uncharged Ir(I) carbene complex **71**.

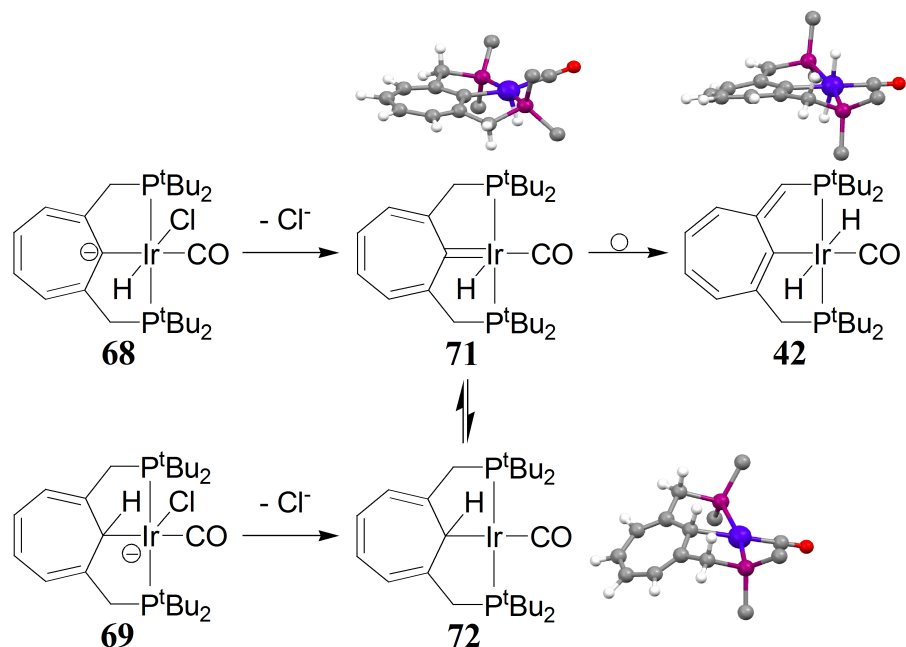


Scheme 45: The ball-stick structures show the result of the geometry optimisation (methyl groups are omitted for clarity).

The structural results obtained from the geometry optimisations (ball-stick structures) in Scheme 45 confirm the expected chloride formation for the deprotonation at the *ipso*-carbon atom **68** and the abstraction of the metal bound hydrogen **69**. These structures elucidate complexes with strongly displaced chlorine atoms as compared to **39'**. The remaining interactions between the chloride ion and the residual complex fragments **68** and **69** are not covalent. In the light of these structures the deprotonation of the metal bound methyne group does not form the anionic intermediate **68** but rather a β -elimination *via* the *ipso*-carbon iridium bond is induced (Scheme 46). The alternative base mediated abstraction of the iridium bound hydrogen forming the anionic complex **69** is also better described as a base induced reductive elimination of hydrochloric acid from the metal centre. In contrast to the structures of **68** and **69** the carbanionic hydrido chloro complex **70** turned out to be a stable intermediate of the deprotonation reaction. In this structure the negative charge is resonance stabilised by the poly-olefinic backbone resulting in a sp^2 -hybridisation of the methyne carbon atom connecting the phosphane moiety and the seven-membered ring.

In Scheme 46 the products of the β -elimination and the reductive elimination of hydrochloric acid from the uncharged hydrido chloro complex **39'** are depicted. In case of the β -elimination

the resulting carbene complex **71** is formed which might inter-convert *via* a 1,2 hydride shift with the isomeric square planar Ir(I) complex **72** obtained by the reductive elimination (compare Scheme 8 on page 8).



Scheme 46: The ball-stick structures show the result of the geometry optimisation (methyl groups are omitted for clarity).

The main structural difference is the location of the hydrogen atom either at the *ipso*-carbon atom yielding the square planar Ir(I) alkyl complex **72** or at the iridium forming the square pyramidal Ir(I) carbene **71** complex (compare **10** in Scheme 7 on page 8). The optimised geometry of the carbene **71** reveals an approximate C_2 symmetric structure with a planar cycloheptatriene ring. In this structure one of the four hydrogen atoms of the bridging methylene groups is in an adequate axial orientation and adjacent to the vacant coordination site of the iridium. Therefore the carbene **71** is expected to be able to allow 1,4 proton shifts (γ -eliminations) from the methylene bridges to the iridium yielding the *trans*-di-hydrido Ir(III) complex **42** with a redistributed π -system in the cycloheptatriene ring. Quite similarly is the 1,3 proton shift previously described in case of CO addition to the Ir(I) carbene complex **9** with an alkyl backbone (Scheme 7 on page 8).

In Figure 19 the relative energies of the presumably formed anions **68**, **69** and **70** are contrasted with the energies of the precursor complex **39'**. Additionally the products and their relative energies of most likely follow-up reactions of the anionic complex **68** (Scheme 46) are shown.

The relative energies (ΔE) are calculated as energies of formation according to the reaction from the reference compound to the respective product complex (equation 7).

$$\Delta E_{\text{product}} = \Delta E_{\text{reference}} + \Delta E_{\text{reactand}} - (\Delta E_{\text{product}} + \Delta E_{\text{reactand}}) \quad (7)$$

In case of the deprotonation reactions (Scheme 45) the hydroxide ion is assumed to be the base. Consequently the energy related to the uncharged compound **39'** is obtained from equation 8.

$$\Delta E_{\text{CHTPCPIrHCICO (68)}} = \Delta E_{\text{CHTPCPIrHCICO (39')}} + \Delta E_{\text{OH}^-} - (\Delta E_{\text{CHTPCPIrHCICO (68)}} + \Delta E_{\text{H}_2\text{O}}) \quad (8)$$

Due to the strong basicity of the hydroxide anion and the thermodynamic stability of the water molecule, all products are formed in a strong exergonic reaction (Figure 19). The formation of the anionic species obtained from the deprotonation of the bridging methylene groups **68** is 294.3 kJ/mol lower in energy than the neutral precursor **39'**. As discussed above the intermediates realised by the deprotonation at the alternative positions in **69** and **70** gain stabilisation energy in the gas-phase by an electro-statically bound chloride ion. In case of the abstraction of the metal bound hydrogen the gas-phase structure containing the chloride is by 67.7 kJ/mol more stable than the Ir(I) complex **72** which is ascribed to the *ipso*-CH chlorine interaction (Scheme 45). In comparison the stabilisation in the chlorine containing gas-phase structure **70** as compared to the carbene complex **71** is with 31.6 kJ/mol significantly smaller than the stabilisation in **69**. However these structures are labile in solution and therefore the square planar Ir(I) complex **72** and the Ir(I) carbene **71** are the expected solution structures which remain 87.4 kJ/mol and 6.5 kJ/mol higher in energy than the resonance stabilised anion **68**.

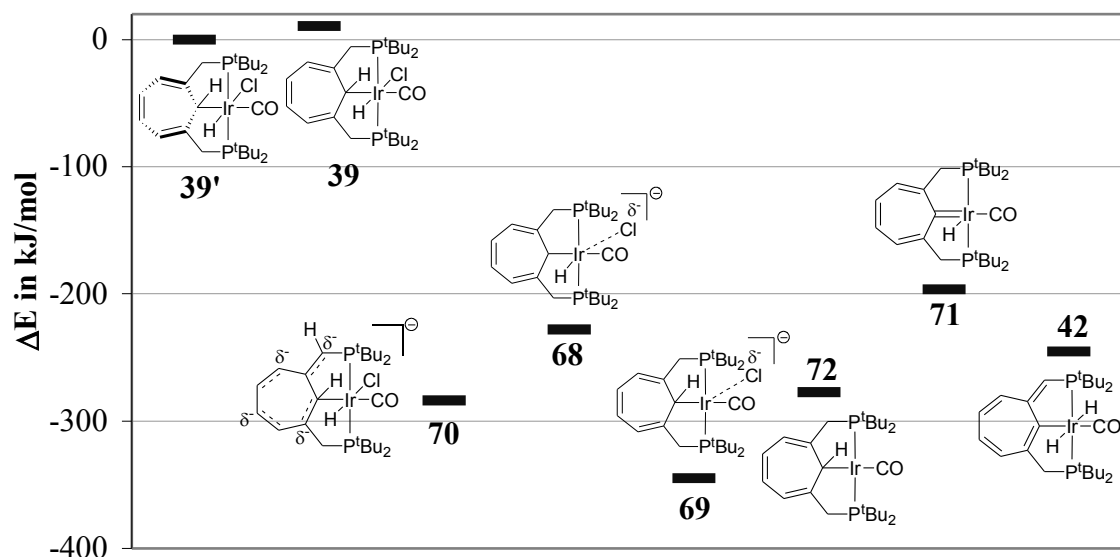
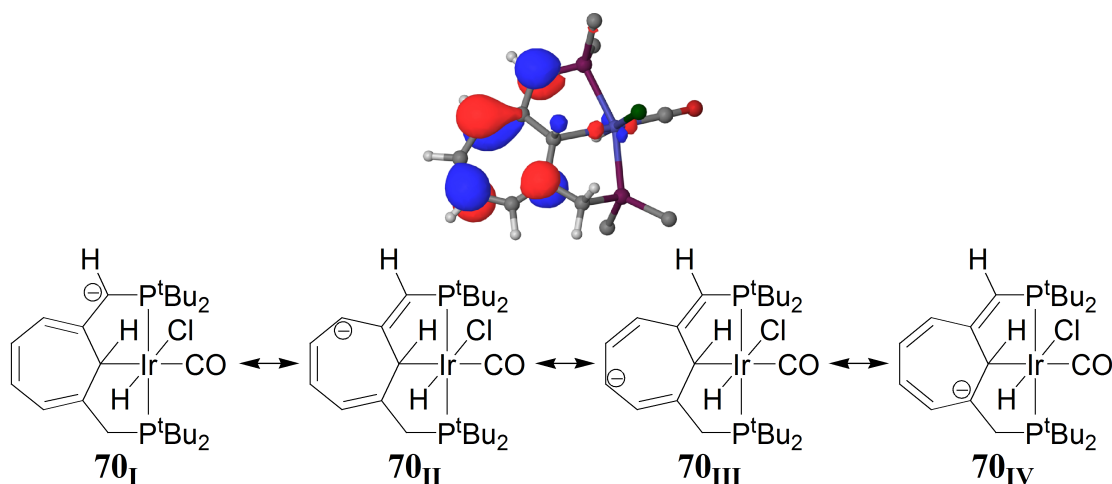


Figure 19: DFT energies relative to **39** for the different species given in Schemes 43 and 45.

Finally the di-hydrido complex **42** is formed in an exergonic reaction ($\Delta(\Delta E) = -49.0$ kJ/mol) from the carbene complex **71** which is in very good agreement with previous results.^{30,66} Furthermore the general trends discussed in chapter 2.3 concerning the stability of pincer complexes with an *ipso*-carbon metal double bond are perfectly supported (also compare Schemes 7, 8 and 9). In contrast to the spontaneous formation of **42** from the carbene, the di-hydride is obtained endergonically by 31.9 kJ/mol from the square planar Ir(I) complex **72**. Hence the formation of the di-hydrido complex **42** is most probably the result of the thermodynamic and kinetic instability of the Ir(I) carbene **71** with respect to a 1,4 proton shift from the methylene bridges to the iridium centre. The square planar Ir(I) complex **72** is ruled out as an intermediate in the formation of the observed complexes due to its thermodynamic stability as compared to the carbene **71** or di-hydride **42** and the lacking experimental hints for its formation. Furthermore the activation barrier for the deprotonation of the metal is expected to be higher than in the alternative positions which is associated with the bulky *tert*-butyl groups surrounding the metal centre.

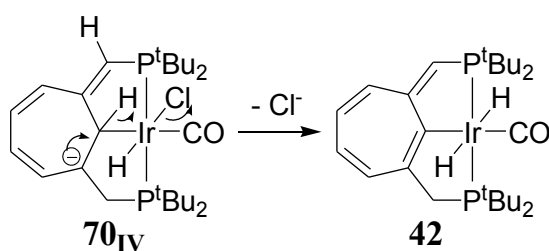
The thermodynamic instability of the anionic complex **68** as compared to the carbene **71** results in the irreversibility of the deprotonation reaction. Consequently the resonance stabilisation of the anion obtained by methylene bridge deprotonation **70** is responsible for the revers-

ibility of the proton abstraction and hence an equilibrium between the anionic complex **70** and the reprotonated uncharged complex is expected.



Scheme 47: The ball-stick structure show the HOMO of **70** (methyl groups are omitted for clarity).

A consequence of the resonance stabilisation in **70** besides the reversibility of the deprotonation is an equilibrium of differently reprotonated species derived from the respective resonance structure (Scheme 47). The localisation of the negative charge in the different resonance structures **70_I**, **70_{II}**, **70_{III}** and **70_{IV}** is also well reflected by the depicted HOMO of the anionic complex **70**. Reprotonating the resonance structure **70_I** the uncharged precursor complex **39** is regenerated while protonation of **70_{II}** and **70_{III}** are most probably the reason for the backbone rearrangements.

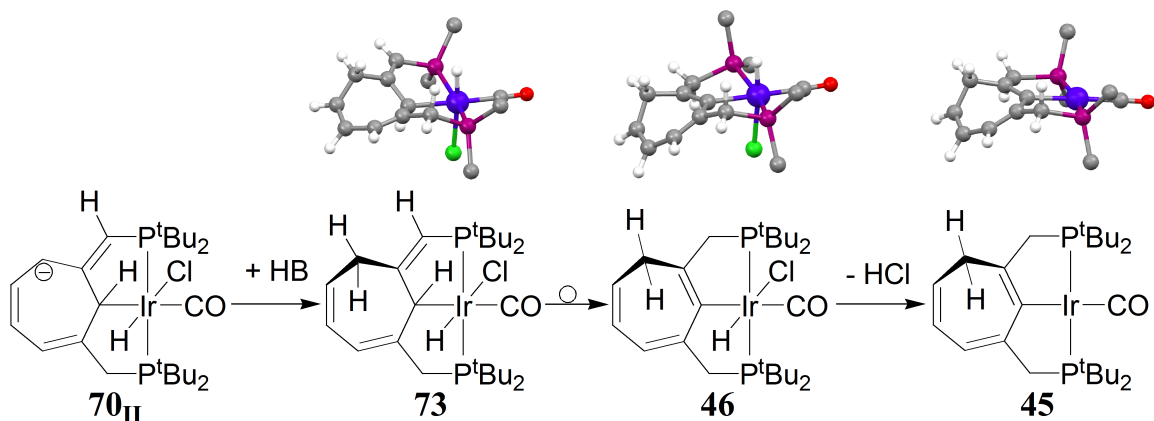


Scheme 48

There are no experimental hints for the protonation of the resonances structure **70_{IV}**, but from this structure the formation of the di-hydride **42** could also be archived (Scheme 48). This might be realised by an uni-molecular 1,2 hydride shift from the *ipso*-carbon atom to the metal with the simultaneous chloride elimination from the iridium centre. Thermodynamically

this reaction is calculated to be weakly endergonic with 38.4 kJ/mol but overall the di-hydrido complex **42** is stabilised by 245.5 kJ/mol as compared to the precursor **39'** (Figure 19).

In the Scheme 49 and 50 the complexes obtained from the reprotonation of the resonance structures **70_{II}** and **70_{III}** and the subsequently formed compounds are displayed.



Scheme 49: The ball-stick structures show the result of the geometry optimisation (methyl groups are omitted for clarity).

The protonation of **70_{II}** forms the uncharged compound **73** with a methylene group in the seven-membered ring and a methyne group connecting the ring with the phosphane moiety. Subsequently the 1,3 proton shift (allyl shift) from the *ipso*-carbon atom to the bridging methyne group is driven by expansion of the conjugated double bond system and the formation of the sp^2 -carbon metal bond in **46**. The reductive elimination generating the respective Ir(I) complex **45** might finally be realised with sterically less demanding but strong bases. Figure 20 shows the energetic differences following this reaction sequence. Surprisingly the isomerisation from the precursor complex **39'** to the backbone rearranged complex **73** is with 9.5 kJ/mol slightly endergonic. The subsequent 1,3 proton shift forms the 21.1 kJ/mol more stable complex **46** with the regenerated cycloheptatriene system. Finally the reductive elimination of hydrochloric acid yielding the corresponding Ir(I) compound **45** which is 13.4 kJ/mol higher in energy than its Ir(III) counterpart **46**. Overall the isomerised hydrido chloro Ir(III) compound **46** is 11.6 kJ/mol more stable than the starting complex **39'** and the respective Ir(I) complex **45** is 1.7 kJ/mol less stable than the starting complex **39'**.

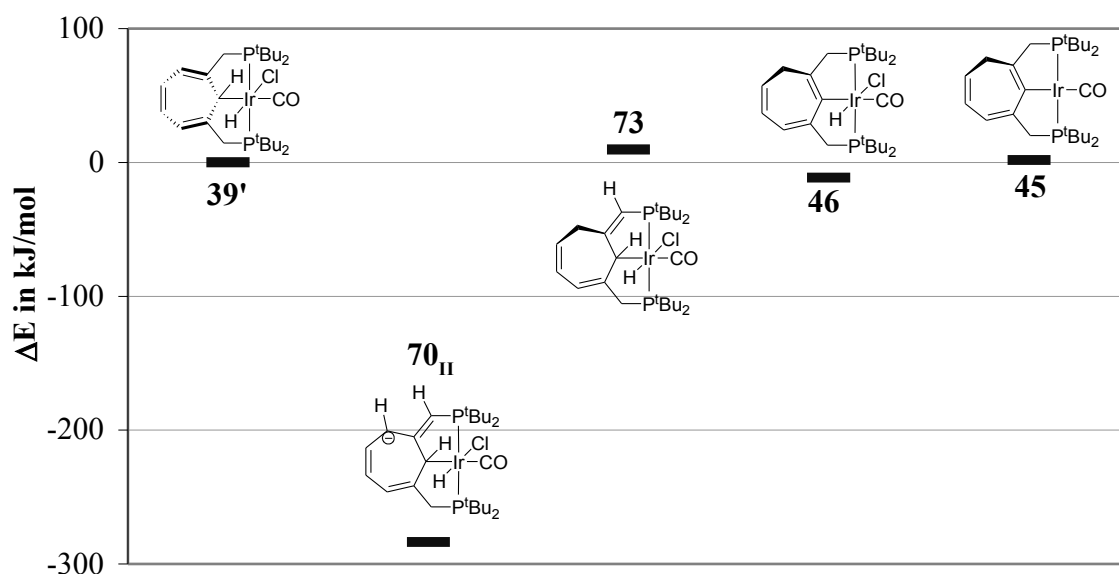
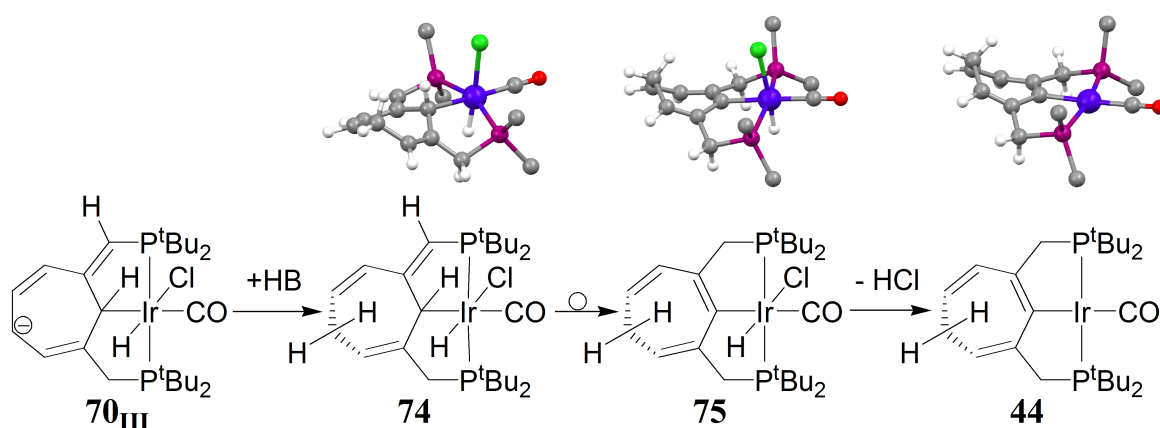


Figure 20: DFT energies relative to **39'** for the different species given in Scheme 49.

The second observed isomer with a methylene group in the seven-membered ring **44** (Scheme 50) is realised starting from the anionic complex **70** by the initial protonation of the resonance structure **70_{III}** forming the uncharged complex **74**. Again a 1,3 proton shift from the *ipso*-carbon atom to the bridging methyne group is responsible for the regeneration of the cycloheptatriene ring and the formation of the sp^2 -carbon iridium bond. Finally the reductive elimination of HCl from the metal centre yields the isomerised Ir(I) complex **44**.



Scheme 50: The ball-stick structures show the result of the geometry optimisation (methyl groups are omitted for clarity).

The energetic situation in Scheme 50 has slightly changed as compared to Scheme 49 because complex **74** is by 18.7 kJ/mol less stable than the isomeric precursor **39'** (Figure 21). Sub-

sequently the 1,3 proton shift to the bridging methylene group is a with 30.2 kJ/mol exergonic process and forms the isomerised Ir(III) complex **75** which is 11.5 kJ/mol more stable than **39'**. In contrast to Scheme 49 the reductive elimination of hydrochloric acid from **75** is a comparatively strong endergonic reaction ($\Delta(\Delta E) = +89.0$ kJ/mol) forming **44** which is 77.4 kJ/mol less stable than the precursor **39'**.

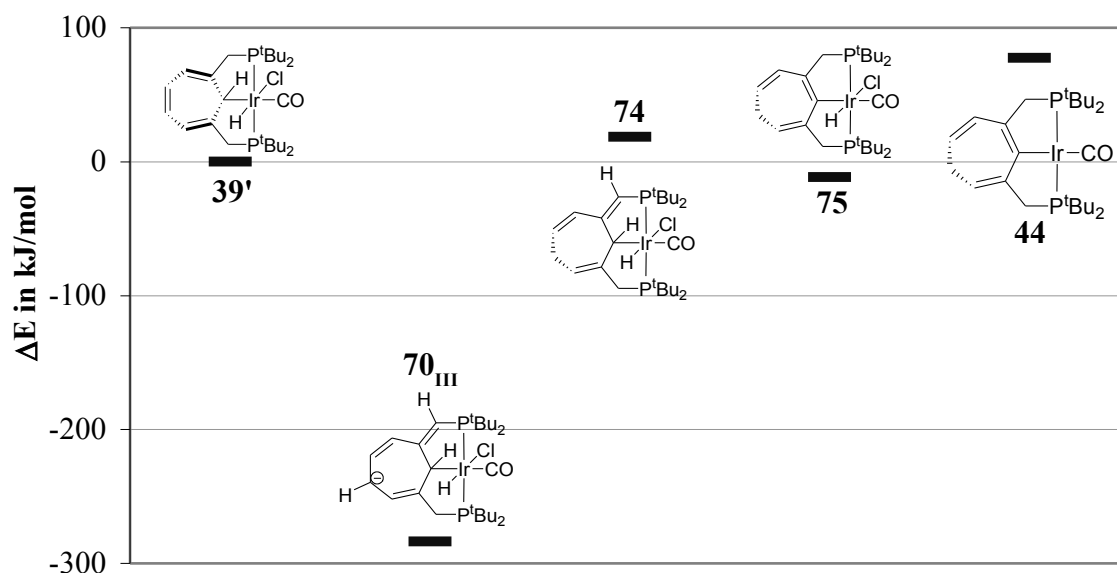


Figure 21: DFT energies relative to **39'** for the different species given in Scheme 50.

In Figure 22 the different uncharged complexes obtained by the deprotonation/reprotonation equilibrium are compared. It is noteworthy that the formation of the **73** is thermodynamically slightly favoured as compared to **74**, while experimentally the formation of **44** is observed. This is indicative for a kinetically favoured and therefore faster formation of **74** as compared to **73** and reflects the steric hindrance of the protonation step with a weakly acidic DBUH⁺. The subsequently formed Ir(III) complexes **46** and **75** with regenerated cycloheptatriene backbones are very similar in energy while their Ir(I) counterparts display different stabilities. This instability of **44** as compared to **45** is verified by the experimental data (Scheme 20) and most probably attributed to the different ring strains caused by the varying location of the methylene group in the seven-membered rings.

In conclusion the deprotonation of the bridging methylene groups is the thermodynamically and kinetically preferred reactions of **39'** with bases. The resonance structures of the resulting carbanion (Scheme 47) are the reason for the increased acidity of these methylene protons and

explain the ease of backbone rearrangements compared to alkyl pincer complexes. The isomeric Ir(I) complexes **73** and **74** (Scheme 20) can be obtained by reprotonating the resonance structures **70_{II}** and **70_{III}**, respectively by the conjugated acid (HB^+). Subsequently the Ir(III) complexes **46** and **75** are available by 1,3 proton shifts (allyl shifts) from the *ipso*-carbon atom to the bridging methyne group. Finally an endergonic reductive elimination of hydrochloric acid yields the respective Ir(I) complexes **44** and **45**. Furthermore it should be noted that also acid or base catalysed interconversions between **44** and **45** via 1,3 hydrogen shifts are conceivable (Scheme 20). At elevated temperatures the formation of **46** is experimentally realised without base addition from **39'** which is an indication for thermally induced 1,3 hydrogen shift in these complexes.^{30,66}

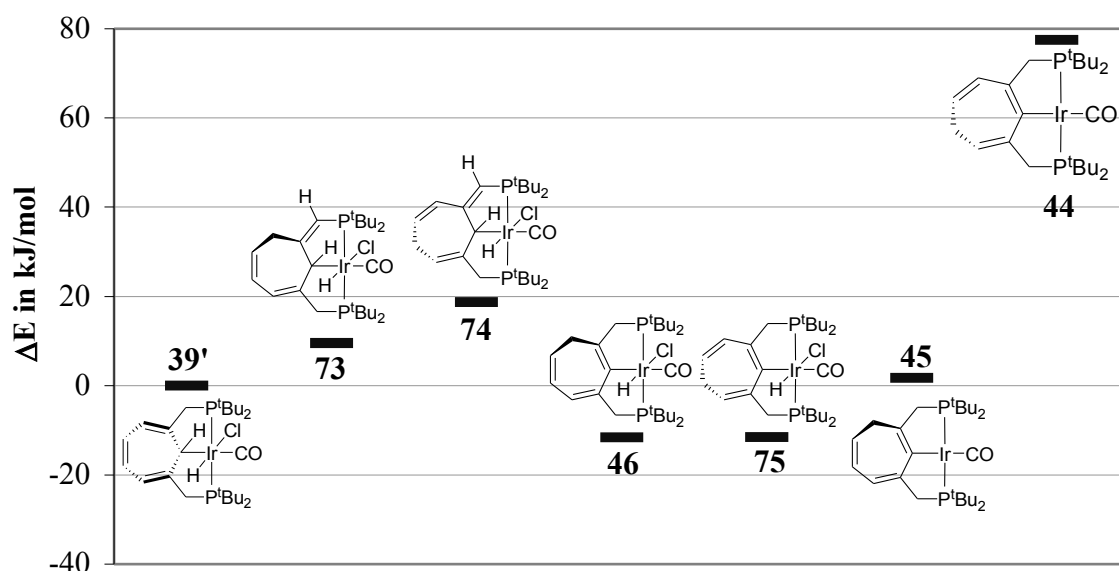


Figure 22: DFT energies relative to **39'** of selected isomerised complexes.

There are further possibilities of stabilisation pathways of the carbanion **70** which, finally leads to the di-hydride complex **42**. First a 1,3 proton shift (allyl shift) from the *ipso*-carbon to the bridging methyne carbanion followed by the elimination of a chloride ion from the iridium producing the carbene **71** and finally the di-hydride **42**. Second, an intra-molecular 1,2 hydride shift from the *ipso*-carbon to the metal accompanied by the elimination of a chloride from the metal forming the di-hydride **42** in a concerted reaction step (Scheme 48). The formation of **42** via the carbene **71** can be understood as a 1,4 proton shift (γ -elimination) from the methylene bridge to the metal. Mechanistically the formation of the Ir(I) complex **43** by elimination of H_2 from the di-hydrido complex **42** is due to the *trans*-orientation of hydrides either

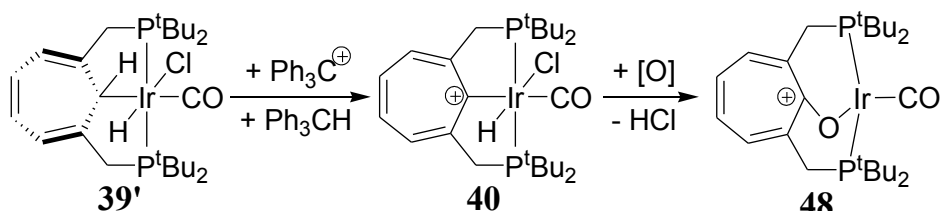
a bi-molecular process or a multi-step reaction *via* the carbene **71**. The metal bound hydride is thereby transferred to one of the methylene protons forming H₂ and the rearranged Ir(I) complex **43**.

The different behaviour of **39'** towards the different bases DBU, LiTMP, KH and NaOH (Schemes 19 and 20) can be explained by the steric hindrance and the basicity of KH and LiTMP. The strong bases do not allow reprotonation of **70** and therefore the carbanion is forced to eliminate a chloride ion yielding the carbene **71**. The bulkiness of the base (LiTMP) slows down the reaction rates of the deprotonation. The application of the significantly weaker base DBU at ambient temperature leads to the products **44** and **45**. While at higher temperatures the formation of the carbene is thermodynamically and presumably also kinetically achievable and consequently the products **42** and **43** are observed additionally.

The elimination of a hydride ion from **39'** yields the cationic hydrido chloro complex **40**. The deprotonation of the methylene bridges in **40** is expected to be easier than in the uncharged complex **39'** and is experimentally realised with stoichiometric amounts of hydroxide anions forming the rearranged Ir(III) complex **47** (Scheme 22). Subsequently the base assisted reductive elimination of HCl forms **44** during the addition of equimolar amounts of hydrochloric acid shifts the equilibrium back to complex **40** *via* **48**

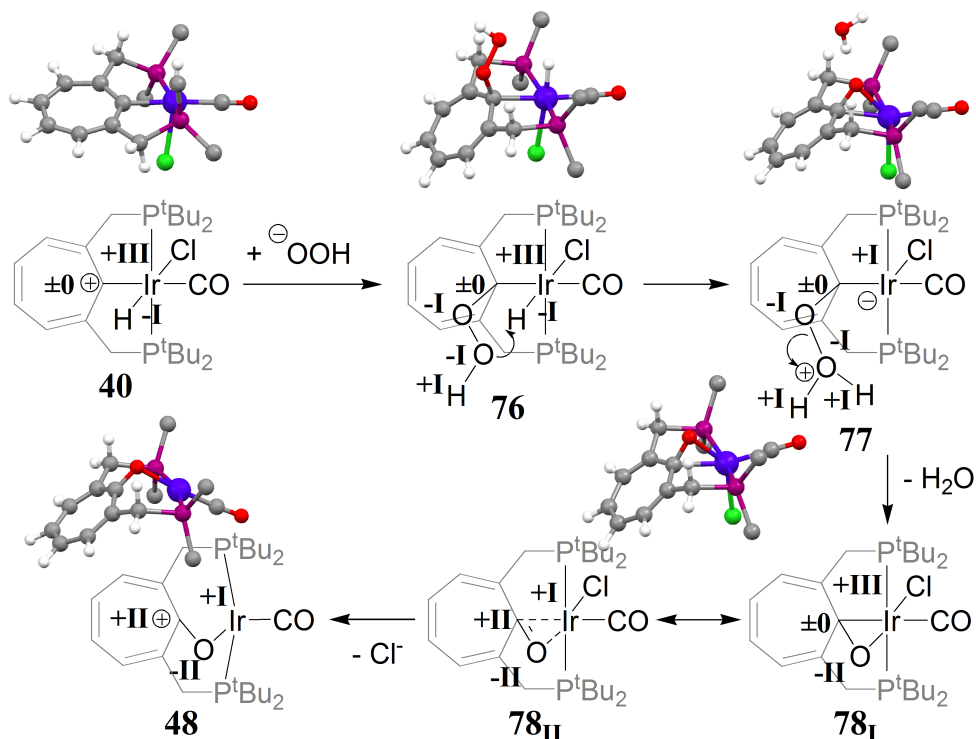
3.4.2 Formation of cycloheptatriene-oxo complex **48**

The formation of the cationic cycloheptatriene-oxo Ir(I) complex **48** from the cationic hydrido chloro complex **40** in the presences of an oxygen donor is a remarkable feature in pincer chemistry⁶⁶ (Scheme 23 on page 19).



Scheme 51

Surprisingly the treatment of the Ir(III) complex **40** with a great excess of 30% H₂O₂ yields the product complex **48** with an Ir(I) centre. In other words the reaction of **40** with a strong oxidising agent results in the oxidation of the *ipso*-carbon atom of the backbone and the reduction of the metal centre. Furthermore it is notable that no significant destruction of the pincer typical coordination is observed.



Scheme 52: The ball-stick structures show the result of the geometry optimisation (methyl groups are omitted for clarity).

Mechanistically it is assumed that the initial step of the formation of **48** is the interaction between the cationic backbone a deprotonated hydrogen peroxide (HOO^-) or the hydrogen peroxide (Scheme 52). The resulting compound might be uncharged complex **76** with a hydroperoxide moiety located at the *ipso*-carbon atom of the seven-membered ring. From the ball-stick structure the spatial proximity of the metal bound hydride and the terminal hydroxy group of the peroxide is obvious. The intra-molecular deprotonation of iridium centre by the hydroxy group preforms a water molecule and generates the metal located anion in complex **77**. Formally the metal deprotonation is accompanied by the reduction of the metal from Ir(III) to Ir(I) while the transferred proton was oxidised.

Table 9: Structural properties of single crystal XRD structure⁶⁶ and the calculated structure of the oxo-complex **48** and the geometry optimised structures in Scheme 52. Bond lengths d are given in pm.

	40 calcd.	76 calcd.	77' calcd.	78 calcd.	48	
					calcd.	exp.
$d(\text{Ir-Cl})$	253.3	255.5	249.4	251.3	-	-
$d(\text{Ir-}ipso\text{-C})$	209.9	222.6	221.6	222.2	269.2	264.0
$d(\text{Ir-O})$	-	321.4	211.3	212.1	213.8	210.2
$d(ipso\text{-C-O})$	-	148.9	136.2	135.5	129.6	127.6
$d(\text{Ir-C})$	192.2	190.1	189.6	189.3	182.3	180.0
$d(\text{C-O})$	115.0	115.8	116.2	116.3	116.3	116.1

The calculation of **77** yields a geometry which is best described as a tropone backbone side-on coordinated *via* the carbonyl group with the water molecule connected *via* a hydrogen-bridge to the carbonyl oxygen (**77'**). Subsequently the water molecule is expelled from the complex and the iridium oxygen bond is formed. There are no significant structural changes obvious between the complex stabilised by the water molecule **77'** and complex without water stabilisation **78**. Thereby **78** has to be described by the resonance structures **78_I** with an oxidatively added carbonyl group and **78_{II}** with and carbon oxygen double bond coordinated to an Ir(I) centre. The carbon oxygen bond length is 13.4 pm shorter than the in the hydro peroxide complex **76** while the Ir-C bond is only 0.6 pm shorter (Table 9). Finally the chloride is eliminated from the six-fold coordinated iridium centre forming the square planar Ir(I) oxo-complex **48**. In this complex the C-O bond length is again reduced by 5.9 pm speaking for an increased C-O double bond character while the Ir-O is lengthened by 1.7 pm. The strongest structural

influence is observed for the Ir-C bond length in **48** which is strongly elongated, by 47 pm as compared to the chlorine containing complex **78**. The comparison between the selected structural parameters of the geometry optimised structures and the single crystal structure in Table 9 are in rather good accordance. In conclusion the continuously decreasing *ipso*-carbon oxygen bond lengths with the shortest bond in **48** are indicative for the increasing double bond character of this bond. This and the strong elongation of the *ipso*-carbon iridium bond are indications for a cationic Ir(I) centre stabilised by a non-bonding electron pair located at oxygen atom of the carbonyl group. The relative energies given in Figure 23 are calculated according to the reaction equations in Schemes 51 and 52 and equation 7 on page 69. Energetically the different species in the Schemes 51 and 52 are formed strongly exergonic as compared to the precursor complex **39'**. The abstraction of a hydride from the *ipso*-carbon atom in **39'** with Ph_3C^+ forms the 129.8 kJ/mol more stable cationic complex **40**.

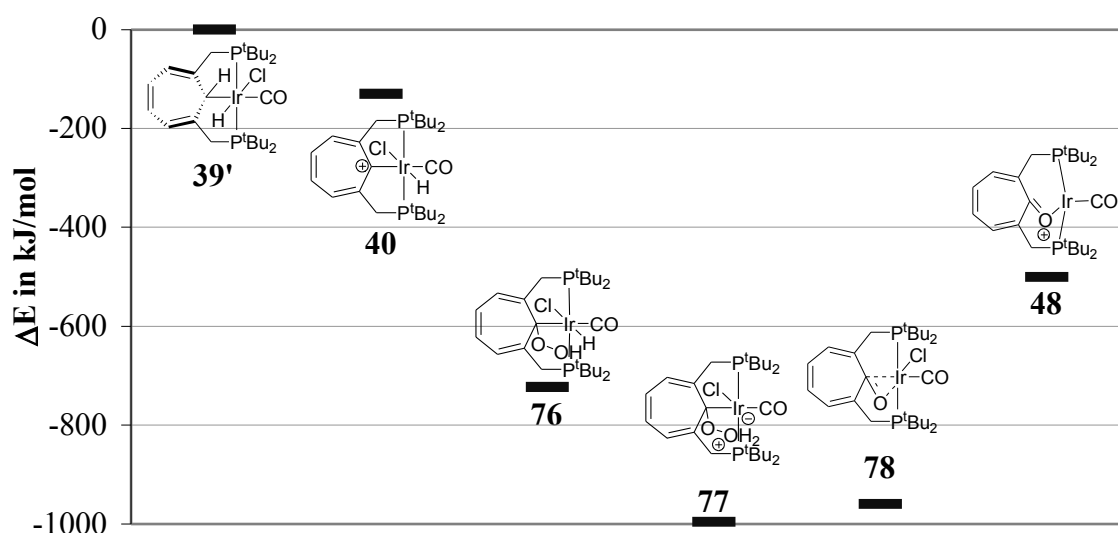


Figure 23: DFT energies relative to **39'** for the different species given in Schemes 51 and 52.

If now the hydro peroxide complex **76** is generated by adding a deprotonated hydrogen peroxide further 593.6 kJ/mol are liberated. The following complexes **77** and **78** are structurally very similar expect for the hydrogen bonded water molecule in **77**. Consequently the stabilisation of **77** by 36.2 kJ/mol as compared to **78** is mainly ascribed to the hydrogen bonding of the H_2O molecule. Nevertheless **78** is formed exergonically ($\Delta(\Delta E) = -236.8$ kJ/mol) from hydro peroxide **76** by elimination of the water molecule. Finally the Ir(I) oxo-complex **48** is

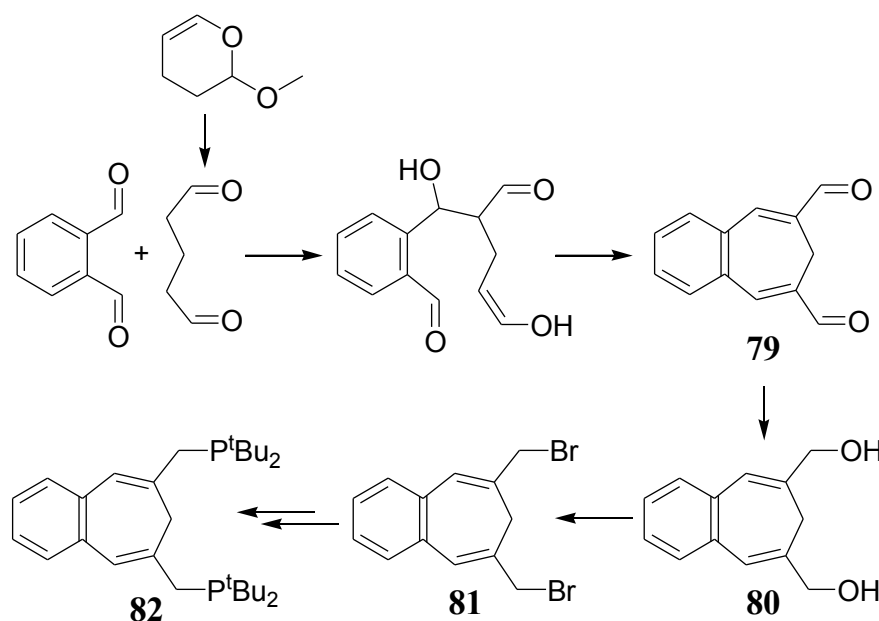
formed from **78** by emission of a chloride ion consuming 459.8 kJ/mol. Overall **48** is strongly stabilised by 500.4 kJ/mol and 370.6 kJ/mol as compared to the precursors **39'** and **40**.

3.5 Novel benzo-cycloheptatriene PCP pincer ligand

In the multi step synthetic procedure leading to the PCP pincer ligand with cycloheptatriene backbone **38** (Scheme 16 on page 15) the introduction of the acetyl groups is sophisticated. Consequently the reactions are achieved in yields below 50%. Therefore the overall yield of this multi step synthesis is rather small. This led to the development of the benzo fused cycloheptatriene PCP pincer backbone in the work-group of Johannes W. Wielandt (Scheme 53). In cooperation with Wielandt *et al.* this synthesis was reproduced and optimised in Tübingen by Sophie Wernitz.⁷⁷

3.5.1 Synthesis of the benzo-cycloheptatriene PCP Ligand

Starting from commercially available phthalic di-aldehyde and dihydro methoxy pyrane the benzo-cycloheptatriene di-aldehyde **79** is obtained in good yields *via* an acid catalysed double aldol reaction as previously described.⁷⁸ Subsequently the reduction with sodium boron-hydride results in the diol **80**, as a pale yellow solid in rather good yields. The bromination forming the di-bromide **81** was obtained in nearly 90% yield applying PBr₃ in diethyl ether.



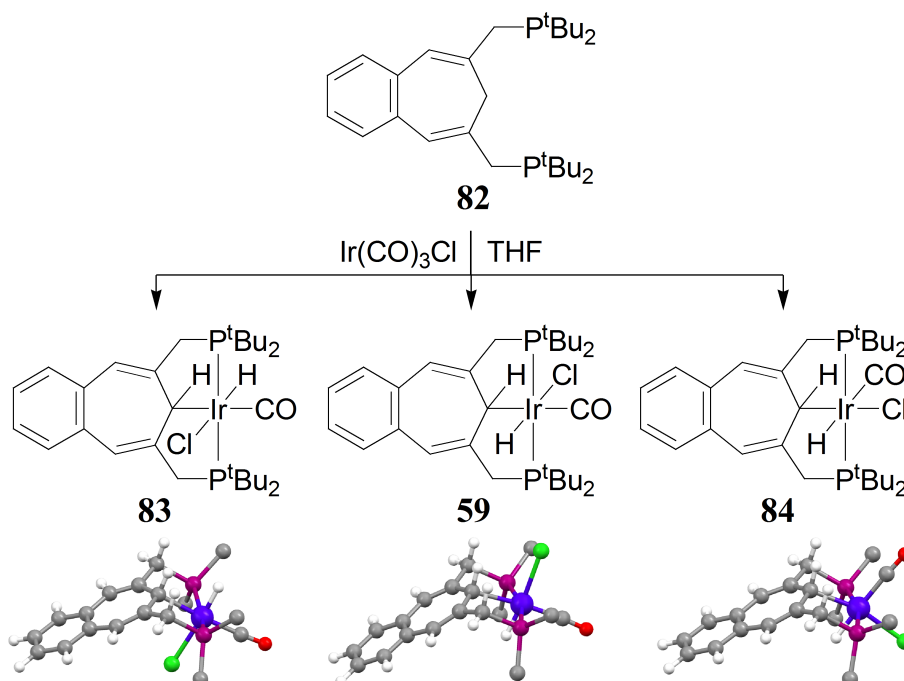
Scheme 53

Finally the introduction of the di-*tert*-butylphosphane moiety is achieved *via* the bis-phosphonium di-bromide and its subsequent deprotonation (compare Schemes 24 and 25). This

multi step synthesis displays higher overall yields and encompasses less steps than the synthesis of the corresponding cycloheptatriene backbone.

3.5.2 Coordination chemistry with iridium

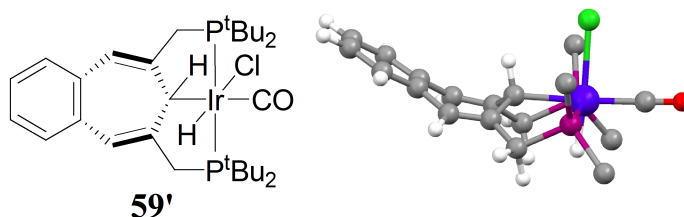
The formation of the benzo-cycloheptatriene iridium complex **59** is obtained quite similarly as compared to the cycloheptatriene counterpart **39**. Thereby the ligand **82** dissolved in THF is vigorously stirred with equimolar amounts of $\text{Ir}(\text{CO})_3\text{Cl}$ at temperatures between 40°C and 45°C . During the complete reaction time (between 9 h and 24 h) the reaction progress was monitored by $^{31}\text{P}\{^1\text{H}\}$ NMR without lock and if necessary further 0.25 equivalents of tricarbonyl iridium chloride were added. Additionally the elimination of carbon monoxide was supported by removing the atmosphere in the reaction vessel and hence the suspension was stirred under only the vapour pressure of the solvent. This procedure was repeated one or two times during the reaction time.



Scheme 54: The ball-stick structures show the result of the geometry optimisation (methyl groups are omitted for clarity).

Mostly this reaction yields a yellow to orange residue which contains up to three singlets in the $^{31}\text{P}\{^1\text{H}\}$ NMR spectrum at 61.5, 49.0 and 46.0 ppm in an intensity ratio of roughly 1:15:3. The proposal of the attributed Ir(III) complexes **84**, **59** and **83** (Scheme 54) are based on hetero-nuclear and homo-nuclear multidimensional NMR spectroscopy while the precise ligand

arrangement at the iridium centre could be derived from two dimensional nuclear Overhauser spectroscopy (H,H-NOESY).



Scheme 55: The ball-stick structures show the result of the geometry optimisation (methyl groups are omitted for clarity).

In case of the cycloheptatriene backbone in the uncharged hydrido chloro complex the isomer with non-planar backbone **39'** is more stable than the isomer containing a planar cycloheptatriene ring **39** (Scheme 44). Contrariwise the benzo-cycloheptatriene hydrido chloro complex favours the isomer with a planar seven-membered ring **59** (Scheme 54) while the isomer containing the non-planar backbone **59'** (Scheme 55) is 1.7 kJ/mol higher in energy. All the isomers shown in the Schemes 54 and 55 are C_s symmetric complexes and therefore each compound displays one singlet in the ³¹P{¹H} NMR spectrum.

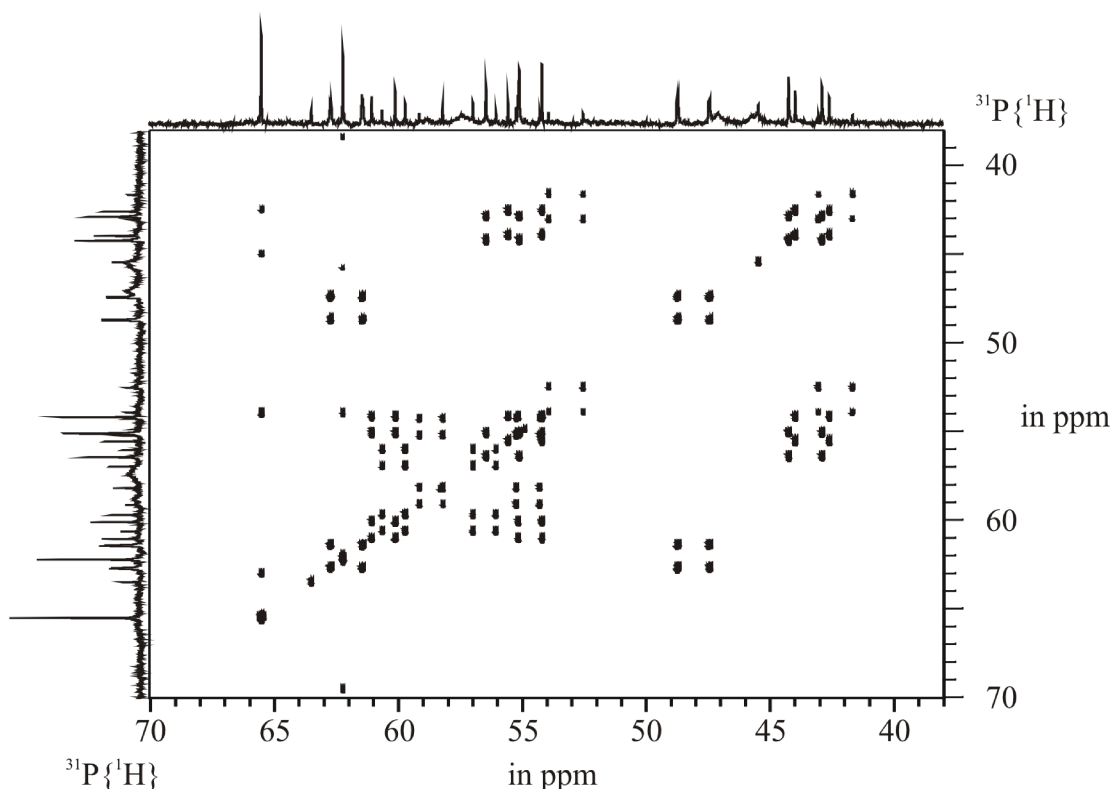
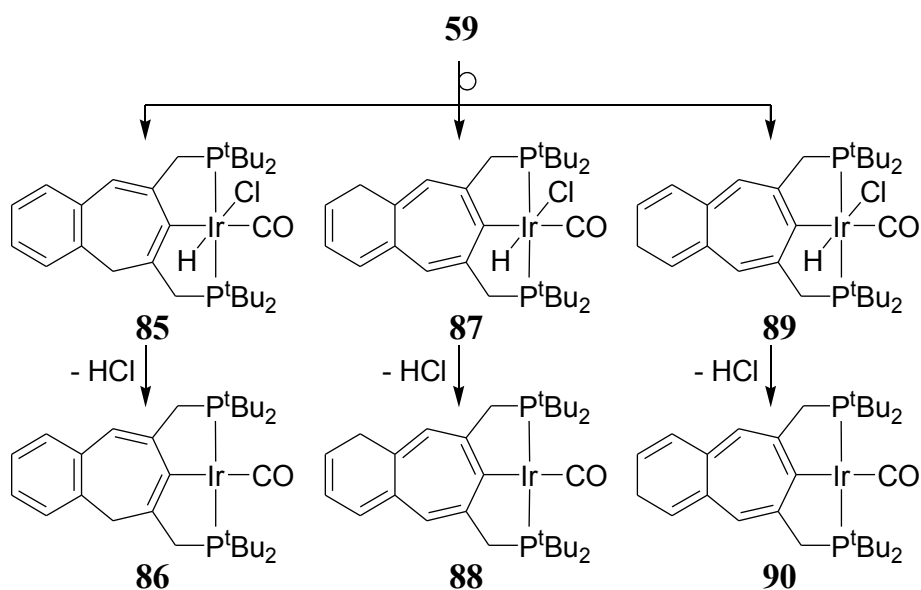


Figure 24: Proton decoupled ³¹P ³¹P COSY after decomposition of **59**

The proton decoupled $^{31}\text{P}\{^1\text{H}\}$ $^{31}\text{P}\{^1\text{H}\}$ COSY in Figure 22 displays several AB-patterns which are indicative for the formation of complexes in the point group C_1 . This sample was obtained by storing a NMR-sample of **59** dissolved in THF over 2 days at room temperature. Thereby the decomposition of **59** might be acid or base induced as described^{29,30,66} previously for the cycloheptatriene based complex **39** (Schemes 20, 49 and 50) or the reactions might also be initiated by light. The hydrido chloro Ir(III) complexes **85**, **87** and **89** are isomers of the precursor **59** with a methylene group shifted into the carbocyclic ring system of the backbone.

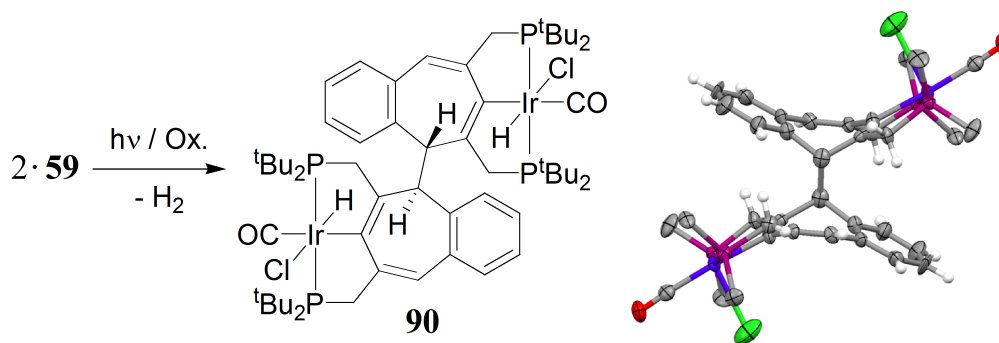


Scheme 56

Subsequently the reductive elimination of hydrochloric acid forming the respective Ir(I) complexes **86**, **88** and **90** is most probably a base induced reaction. Each of these complexes is expected to yield an AB-pattern in the $^{31}\text{P}\{^1\text{H}\}$ NMR spectrum with a P-P coupling constant between 250 Hz and 350 Hz characteristic for a mutual *trans*-arrangement of the phosphorus atoms. The ^{31}P chemical shift range of the different hydrido chloro Ir(III) complexes is expected to be rather similar as well as the ^{31}P chemical shift range of their Ir(I) counterparts. In the ^{31}P - ^{31}P correlated spectrum displayed in Figure 24 two different chemical shift domains can be discriminated each containing three AB-patterns. The doublets of the AB-patterns at higher fields are observed around 43 and 55 ppm while the doublets of the low field patterns are located at about 56 and 59 ppm. Considering the similarity of the ^{31}P chemical shifts of 50.3 and 49.0 ppm for the cycloheptatriene and the benzo-cycloheptatriene hydrido chloro complexes

39' and **59**, respectively the Ir(I) complexes **86**, **88** and **90** are expected at lower fields than their Ir(III) counterparts **85**, **87** and **89**. Unfortunately a more precise attribution of the resonances was not achieved due to the complexity of the mixture and the problems in separating single components.

However, from one attempt synthesising **59** crystals suitable for single crystal XRD could be obtained. They were separated from the NMR sample of the crude reaction mixture in THF which shows a similar composition as the decomposed sample of **59**, compare Figure 24. The structure derived from these crystals which is shown in Scheme 57, surprisingly displays a dimer which might be obtained by an oxidative coupling of the isomerised hydrido chloro complex **85**.



Scheme 57: The ball-stick structures show the result of the geometry optimisation (methyl groups are omitted for clarity).

Thereby a carbon carbon single bond connects the sp^3 -carbon atoms of the seven-membered rings. In the crystal structure the hydrogen atom at the sp^3 -carbon atoms in the organic backbone could not be refined as well as the hydride ligands located at the iridium centre. However, the pyramidal surrounding of these ring carbon atoms is indicative for the sp^3 -hybridisation and the presence of a methyne group. The hydride at the metal site is concluded by the Ir-Cl bond lengths which are both with 258.0 pm in the range of an iridium chlorine bond *trans* to a hydride ligand (compare Table 6). Structurally the DFT geometry optimisation of **90** is in very good agreement with the structure obtained from XRD. Furthermore its formation from **59** is predicted to be 53.4 kJ/mol endergonic. Due to the inhomogeneity and complexity of the mixture from which the crystals were obtained no NMR assignment could be achieved. Moreover conspicuous differences in the NMR data are only expected for the ^{13}C chemical shift and for the ^1H multiplet of the interconnecting methyne groups while the ^{31}P chemical shifts and multiplets are expected to be quite similar to **85**.

If **59** is treated with trifluoromethanesulfonic acid (triflic acid, HOTf) which contains small amounts of water a broad AB-spectrum is observed in the $^{31}\text{P}\{^1\text{H}\}$ NMR spectrum at room temperature (Figure 25). Measuring the $^{31}\text{P}\{^1\text{H}\}$ NMR spectra at -80°C reveals a second AB-pattern and therefore a second asymmetric complex while the exchange rate between both compounds is slower than the NMR time scale. At a temperature of around -40°C the coalescence of both AB-spectra is achieved while at temperatures above -40°C only one AB-pattern is observable.

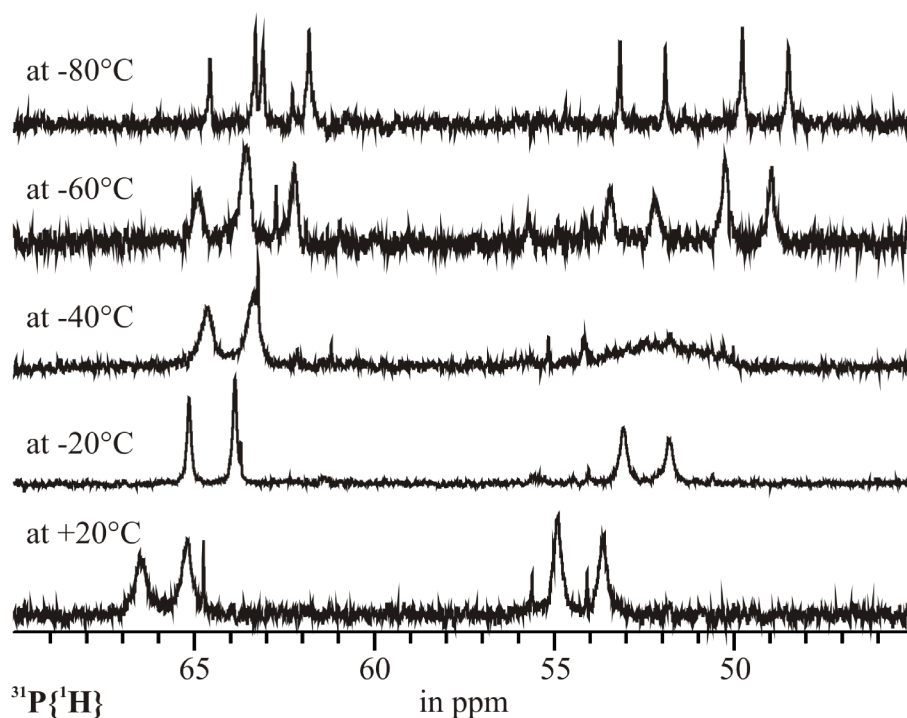


Figure 25: Temperature dependant $^{31}\text{P}\{^1\text{H}\}$ NMR spectra of **59** with $\text{H}_3\text{O}^+\text{Tf}$.

The proton spectra at the same temperatures display a quite similar dynamic behaviour which is very well observable for the hydride signals. Therefore both dynamically inter-converted complexes associated with the AB-patterns in the $^{31}\text{P}\{^1\text{H}\}$ NMR spectrum contain a metal bound hydrogen atom. From one of these NMR-samples crystals could be separated suitable for single crystal XRD. The refined structure (Figure 26) displays a square pyramidal coordinated iridium centre with an organic backbone containing a methylene group in the seven membered ring. Furthermore the triflate counter-ion in the elementary cell is an indication for a positively charged complex **94**. The absence of the hydride in the crystal structure is either attributed to the difficulty in locating a hydride next to a metal centre or ascribed to the loca-

tion of the positive charge on the metal. The very short Ir-Cl bond length of only 226.1 pm in **94**, which is more than 30 pm shorter than in the dimeric hydrido chloro complex **90**, indicates that a structural *trans*-effect ligand *trans* to the chlorine atom is missing.

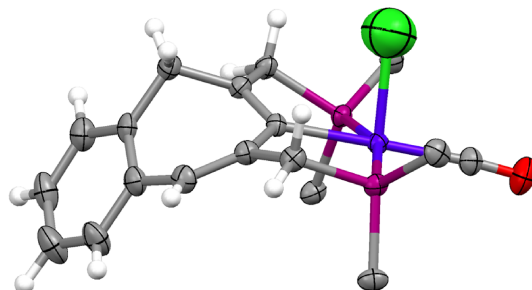
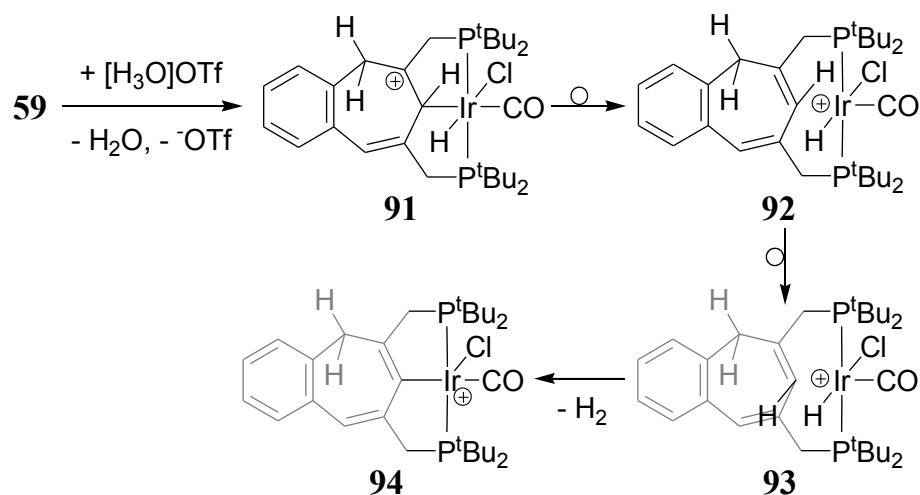


Figure 26: Single crystal XRD structure of **94**, (the triflate counterion and the methyl groups are omitted for clarity).

A plausible reaction sequence forming the cationic complex **94** is given in Scheme 58 assuming the initial protonation of a carbon-carbon double bond of the seven-membered ring **91**. The resulting carbenium ion might be stabilised by the cleavage of the *ipso*-carbon iridium bond thereby forming an iridium localised cation **92** which is η^2 -coordinated by a sp^2 -CH bond of the cycloheptatriene ring.

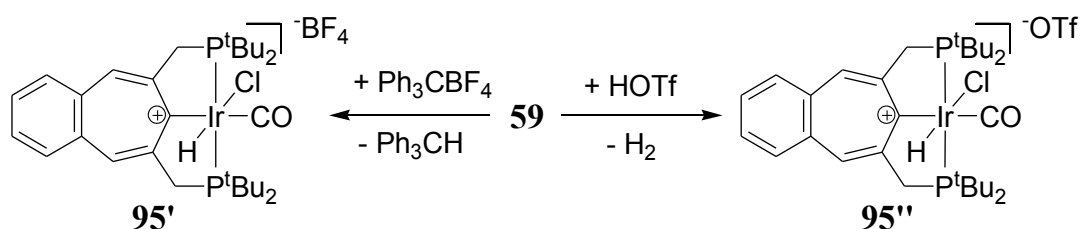


Scheme 58

Subsequently the conformational isomerisation forms **93** which presents an auspicious situation for the final dihydrogen elimination yielding the cationic Ir(III) complex **94**. Hence the dynamic NMR-spectra might be explained by the equilibrium between the conformers **92** and

93 which seems to be kinetically slow as compared to the NMR time scale at temperatures below -40°C .

The abstraction of the hydride from the *ipso*-carbon atom in the hydrido chloro complexes **59**, **83** and **84** is achieved with triphenylcarbenium tetrafluoroborate or with the trimethylsilyl triflate. Analogously the formation of the corresponding cationic cycloheptatriene complex **40** (Scheme 51) is realised. Interestingly the treatment of a solution of **59** in DCM with equimolar amounts of dry triflic acid leads to the formation of the **95''** and is accompanied by a vigorous development of dihydrogen. The resulting product **95** is extensively characterised by multi-nuclear 1D and 2D-NMR-spectroscopy, mass spectrometry (chapter 3.5.3.1.3 on page 94) and for **95'** also by single crystal X-ray diffraction (Figure 27).



Scheme 59

For the XRD structure the single crystals could be isolated from the crude reaction mixture in DCM. As depicted in Figure 27 the cationic complex **95** is nearly C_2 symmetric and contains a planar benzo-cycloheptatriene backbone. The iridium chlorine bond length (Table 10) is with 250.8 pm in the range of the previously described Ir-Cl bonds *trans* to the strong structural *trans*-effect ligand hydride.

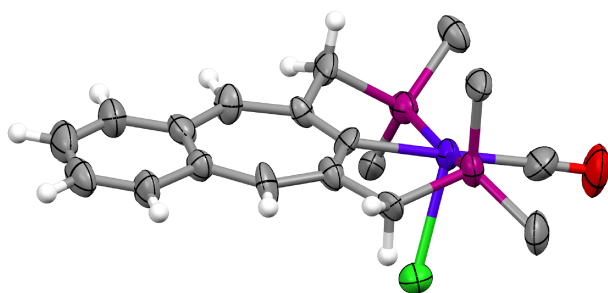


Figure 27: Single crystal XRD structure of **95'**, (solvent molecules, the tetrafluoroborate counterion and the methyl groups are omitted for clarity).

Table 10: Bond lengths d are given in pm.

	40' exp.	95' exp.
$d(\text{Ir-Cl})$	249.6	250.8
$d(\text{Ir-}ipso\text{-C})$	209.3	208.2
$d(\text{Ir-C})$	191.6	192.9
$d(\text{C-O})$	112.7	111.5

Comparing the details of the experimental XRD structures of the cationic cycloheptatriene hydrido chloro triflate complex **40'** with the positively charged benzo-cycloheptatriene hydrido chloro complex **95'** with tetrafluoroborate as counter-ion, there are no significant changes obvious. The slight elongation of the Ir-C bond accompanied by the slight shortening of the C-O bond are indicative for increased π -backbonding which reflects the reduced π -acidity of the benzo-cycloheptatriene as compared to the cycloheptatriene backbone (chapter 3.2.3.2 on page 47).

Mechanistically the formation of **95'** might be described by an electrophilic attack of the triphenylcarbenium ion at the hydrogen atom of the metal bound methyne group yielding triphenylmethane and the cationic product **95'**. However a $^{31}\text{P}\{^1\text{H}\}$ NMR spectrum of a solution of **59** and triphenylcarbenium tetrafluoroborate in DCM- d_2 at -60°C displays a singlet each for the uncharged complex **59** at 49.0 ppm, and the cationic product **95'** at 60.5 ppm as well as an AB-pattern at 45.2 and -63.4 ppm with an AB-coupling constant of 231.8 Hz. The large P-P-coupling constant is evident for a mutual *trans*-orientation of the phosphorus nuclei at the metal while the great chemical shift difference of 108.6 ppm speaks for a strong change in the electronic surrounding of one of the phosphorus nuclei. In the corresponding ^1H NMR spectrum three hydride signals are observed two triplets associated with complex **59** at -19.12 ppm and the product **95'** at -17.07 ppm and a broad multiplet at -14.68 ppm. A further characterisation of the asymmetric intermediate was not achieved due to its low concentration in the mixture. These observations are obviously in contradiction to a concerted formation of the triphenylmethane and the cation **95**. Therefore a multi-step mechanism is proposed involving the formation of a cationic intermediate whose structure remains still unclear.

The formation of the cationic oxo-complex **102** (Scheme 61) was first proposed analysing the different mass spectra of **59** (Table 11 and Scheme 64). The previously described synthetic approach with atmospheric air⁶⁶ was modified and applied to the cationic benzo-cycloheptatriene complex **95** to achieve the structural verification and characterisation. Therefore the uncharged hydrido chloro complex **59** dissolved in DCM- d_2 is treated with stoichiometric amounts of triphenylcarbenium tetrafluoroborate in an NMR-tube and the resulting crude mixture is saturated with pure oxygen. Surprisingly there is no singlet observed at around 87 ppm in the $^{31}\text{P}\{^1\text{H}\}$ NMR spectrum which might be attributed to the oxo-complex **102**. Due to the similarity of the ^{31}P chemical shifts of cycloheptatriene and benzo-cycloheptatriene

complexes the chemical shift of **102** is also expected to be very close to the chemical shift of the cycloheptatriene oxo-complex **48** ($\delta = 86.9$ ppm).⁶⁶

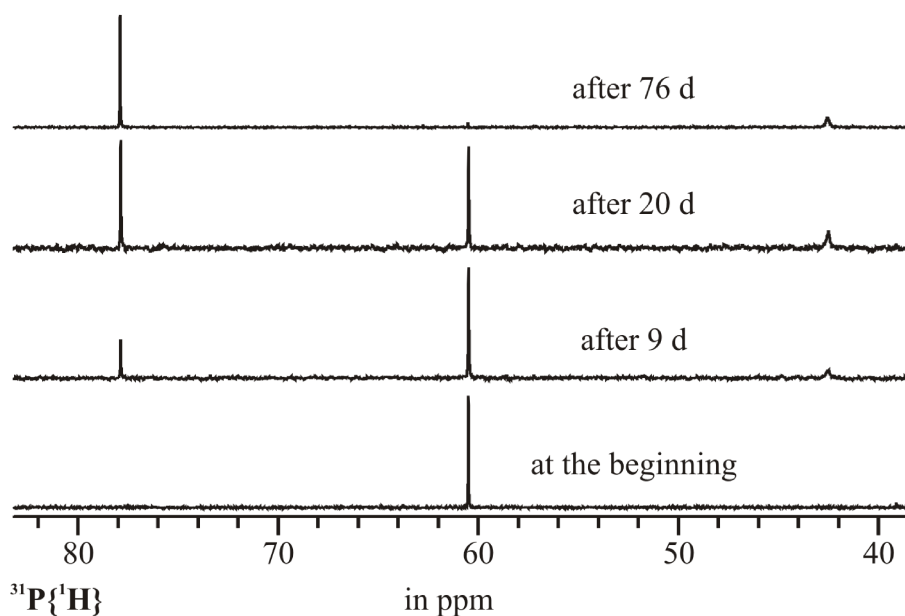
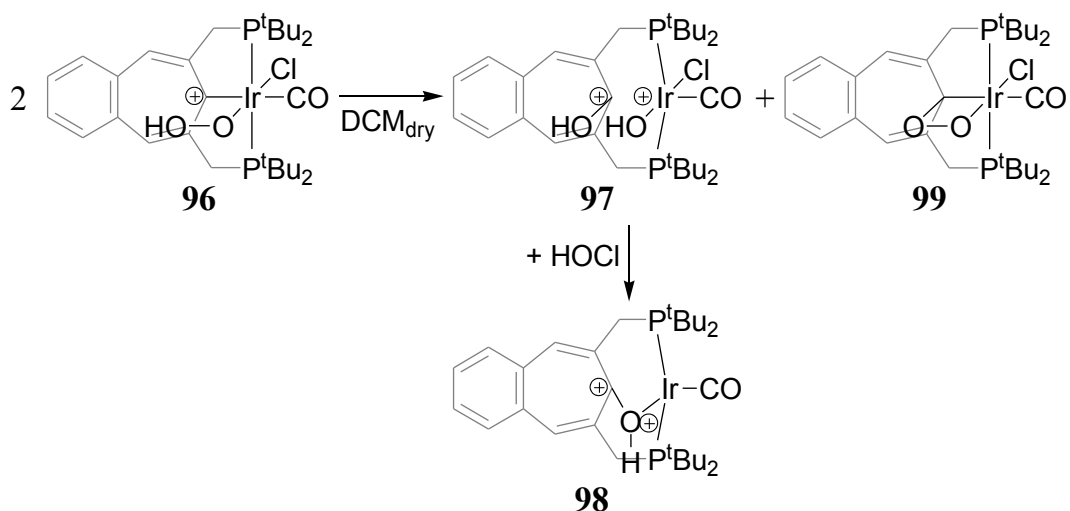


Figure 28: $^{31}\text{P}\{^1\text{H}\}$ NMR spectra of the reaction of **95'** with oxygen.

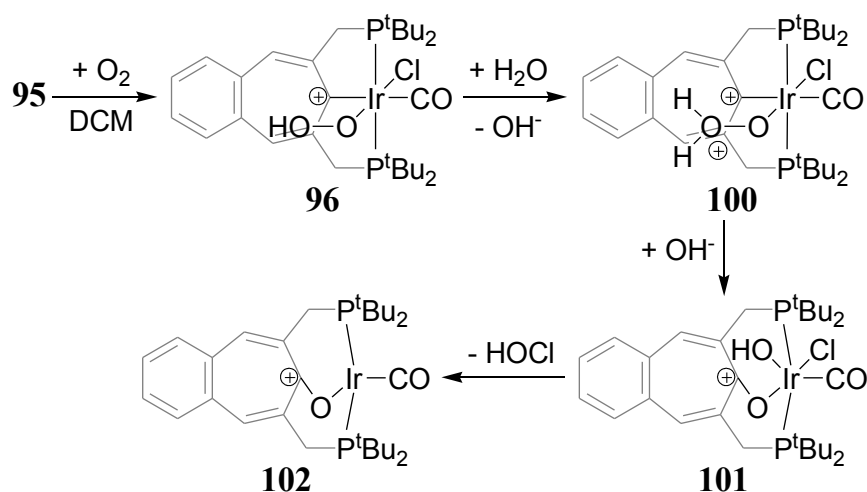
The monitoring of the reaction of the cation **95'** with pure oxygen over a period of 76 days is displayed in Figure 28. Thereby the cationic hydrido chloro complex **95** at 60.5 ppm is slowly transformed into two symmetric compounds with ^{31}P chemical shift of 77.9 and 42.5 ppm. Due to the different relaxation times of the compounds and the non-optimised $^{31}\text{P}\{^1\text{H}\}$ NMR spectra the integral values are not very reliable. However the ratio of 1:0.7 (77.9:42.5 ppm) is close to a 1:1 ratio which is expected for a disproportionation or a bimolecular proton exchange. The corresponding ^1H NMR spectra show the hydride signal of the cationic complex **95** but there are no further hydride signals observable. Furthermore the number of the signals of **95'** and the number of the proton signals of the intermediates are identical as well as the principal coupling patterns which are rather similar. The ^1H signals of the aromatic backbone and of the bridging methylene groups of the first intermediate ($\delta = 77.9$ ppm) are shifted to higher fields while the same signals of the other intermediate ($\delta = 42.5$ ppm) are shifted to lower fields as compared to the cationic species **95**. Due to these data the complexes **97** or **98** and **99** are proposed as intermediates in dry solvents however the attribution of the structures to the different NMR-signals is so far precarious. In contrast to **99** which is expected to be comparatively stable under the reaction conditions, the twofold positively charged complex

97 is capable to reductively eliminate hypochloric acid (HOCl) thereby forming the protonated oxo-complex **98**.



Scheme 60

As the reaction with atmospheric oxygen and the cationic cycloheptatriene-based complex **40** yields the respective oxo-complex **48**, it is assumed that the absence of water could be responsible for the different reaction products. This assumption is supported by mass spectrometric results in the following chapters while the synthetic verification of this assumption is still missing.



Scheme 61

The hydro-peroxide complex **96** is formed by the insertion of a molecule of singlet oxygen into the Ir-H bond (Scheme 61). If water is present in the reaction medium the terminal hy-

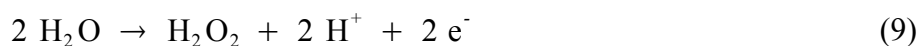
droxy group of the hydro-peroxide might become protonated. The resulting bis-cationic complex **100** eliminates the water molecule simultaneously forming the oxo-bridge and an iridium localised cation. This might be intercepted by a hydroxide ion or a water molecule yielding the mono-cation complex **101** which presents a hexa-coordinated metal centre with a *cis*-arrangement of the hydroxide and chloride ligand. Finally the reductive elimination of HOCl forms the Ir(I) oxo-complex **102**. Alternatively the elimination of hypochloric acid might also be realised by a direct nucleophilic attack of the hydroxide ion at the positively polarised chlorine ligand in **100** or **101**.

3.5.3 Mass spectrometry of benzo-cycloheptatriene complexes

3.5.3.1 Ionisation techniques and ionisation processes

3.5.3.1.1 Electro-spray ionisation

In the electro-spray ionisation (ESI) source the sample solution is passed through an injection cannula surrounded by a capillary tube applying a nitrogen pressure of approximately 200 kPa. This grounded nebuliser assembly is aligned perpendicular to the transfer capillary of the mass spectrometer inlet which is at about -3 kV potential. The spray of the sample solution passes the inlet of the mass spectrometer perpendicularly while the positive droplets are attracted by the negative potential and transferred to the ion optic of the mass spectrometer. Furthermore, the desolvation process of the droplets is supported by a heated flow of nitrogen in the opposite direction to the flow of positive charges. The ionisation mechanism in positive ion mode electro-spray sources for neutral analytes in dry organic solvents is most probably an electrochemical oxidation mechanism.⁷⁹ A single electron is removed from the analyte molecule (M) and transferred to the electro-spray needle (anode). If the applied solvent contains water, oxidation reactions of water according to equations (9) and (10) may occur concurrently.



Depending on the concentration of water these reactions might be the main reason for the charge formation in electro-spray ionisation of neutral molecules. Usually the $[\text{M}+\text{H}]^+$ peak is formed by protonating basic groups of the analyte like carbonyl or amino groups with protons generated *via* equation (9) or (10). When inorganic salts are present in the solution a further ionisation process is the oxidation of the anion, for example halide to halogen atom oxidation and formation of $[\text{M}+\text{cation}]^+$ clusters.

3.5.3.1.2 Fast atom bombardment ionisation

In fast atom bombardment (FAB) mass spectrometry the sample is dissolved in a non-volatile solvent (S) like 3-nitro-benzyl alcohol and the solution is sputtered by a beam of accelerated Xe^+ ions (a few keV) (historically by Ar, Kr or Xe atoms). Usually analyte molecules (M) containing proton accepting or donating moieties are observed as $[\text{M}+\text{H}]^+$ or $[\text{M}-\text{H}]^-$ ions

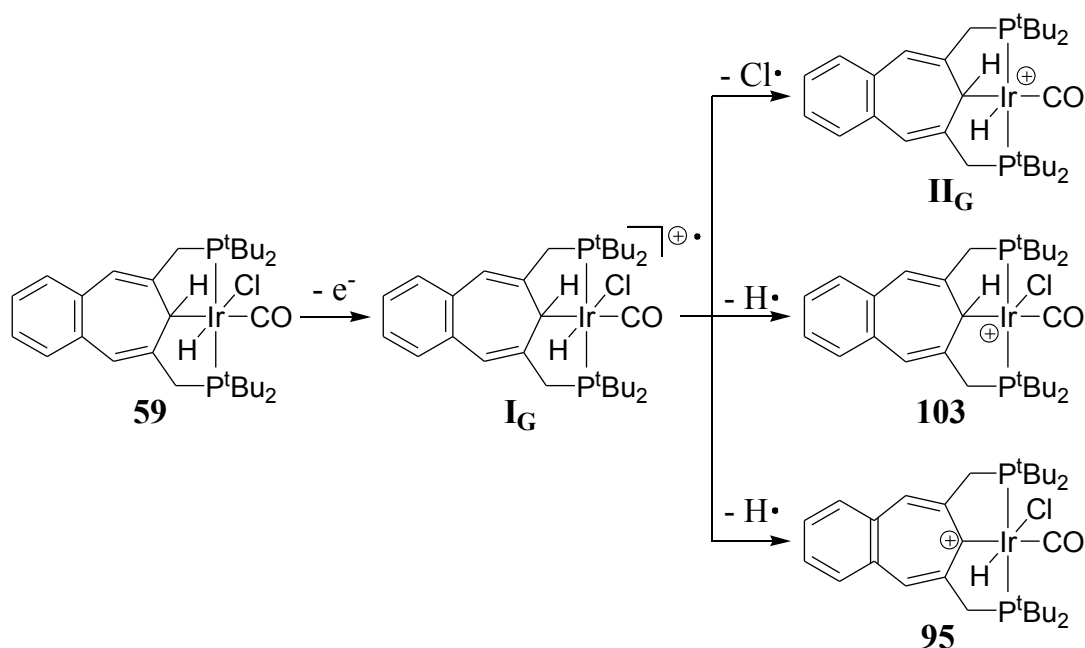
(11).⁸⁰ In case of $[M+H]^+$ ions the source of protons is believed to be the solvent. If the analyte molecule is able to emit a hydride ions $[M-H]^+$ are observable, too (12). Radical cation $[M]^{\bullet+}$ formation (13) is described for analyte molecules without proton accepting or hydride donating groups.



Mechanistically, the impact of the accelerated noble gas ion on the solution surface induces a cascade of collisions between the different molecules in the solution. Furthermore, the solution is sputtered or evaporated into the vacuum. The most important process of ionisation seems to be the high energy collisions between solvent (S^*) and analyte molecules (equations (11), (12), (13) and (14)) within an intermediate state between condensed and gas phase. This is also the reason for possible fragmentation reactions.⁸⁰

3.5.3.1.3 Ionisation process of **59**

A single electron oxidation process is assumed as the initial ionisation step for complex **59** in electro-spray as well as in fast atom bombardment ionisation (Scheme 62).



Scheme 62

The resulting radical cation \mathbf{I}_G $[\text{M}]^{+\bullet}$ is 561.2 kJ/mol higher in energy as compared to **59** (Figure 29) and is not observed in the mass spectra. If compound \mathbf{I}_G emits a chlorine atom, the metal centred cation \mathbf{II}_G is formed. The loss of a hydrogen atom from \mathbf{I}_G can proceed in two ways, either the removal of the hydrogen ligand from the metal (**103**) or the abstraction of the hydrogen from the metal bound carbon atom (**95**).

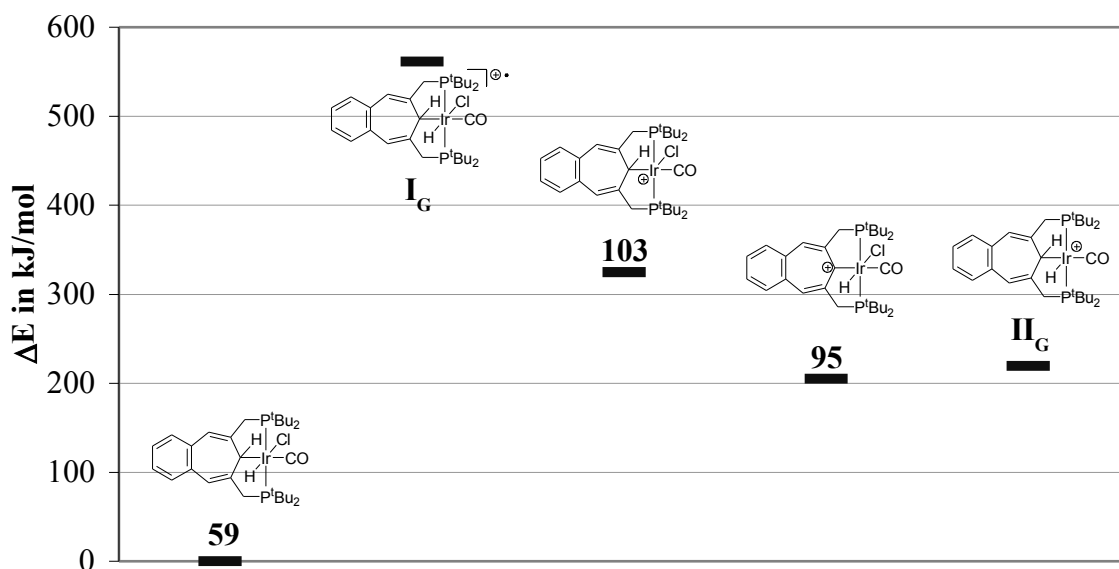


Figure 29: DFT results for initial ionisation processes (radical pathway).

Figure 29 shows the relative DFT energies of the different cationic structures. The formations of **103**, **95** and \mathbf{II}_G from the radical cation \mathbf{I}_G are thermodynamically favoured with 236.7, 356.1 and 341.8 kJ/mol, respectively. Hence, a hydrogen atom from \mathbf{I}_G is preferentially eliminated from the *ipso*-carbon atom generating the aromatic compound **95**. The emission of a chlorine atom from the radical cation \mathbf{I}_G is just 14.3 kJ/mol higher in energy than **95**.

In FAB mass spectrometry there are alternative heterolytic ionisation pathways according to (12) and (14). The energies of formation for the corresponding heterolytic bond cleavages forming the cationic complexes **103**, **95** and \mathbf{II}_G relative to **59** are additionally displayed in Figure 30. The elimination of hydride ions from the neutral complex **59** forming **103** (986.7 kJ/mol) and **95** (867.2 kJ/mol) is a highly endergonic process because of the poorly stabilised hydrogen anion. The abstraction of the better stabilised chloride ion from the metal centre building the cation \mathbf{II}_G (476.2 kJ/mol) is thermodynamically preferred compared to the formation of **103** and **95**.

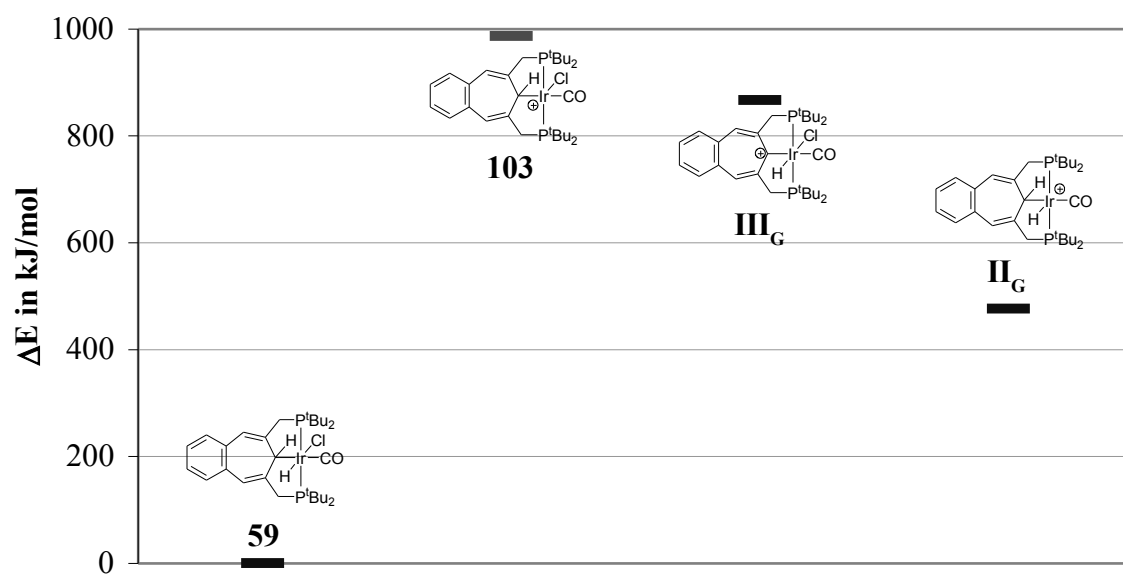


Figure 30: DFT results for initial ionisation processes (ionic pathway).

In sum the FAB processes containing collision ionisation allows the formation of higher energy intermediates or cations, while electro-spray ionisation avoids higher energy pathway because of the selectivity of the initial electrochemical oxidation.

3.5.3.2 Fast atom bombardment mass spectrometry of **59**

The FAB mass spectrum of **59** (Figure 31) in positive ion mode is measured in 3-nitro-benzyl alcohol as matrix.

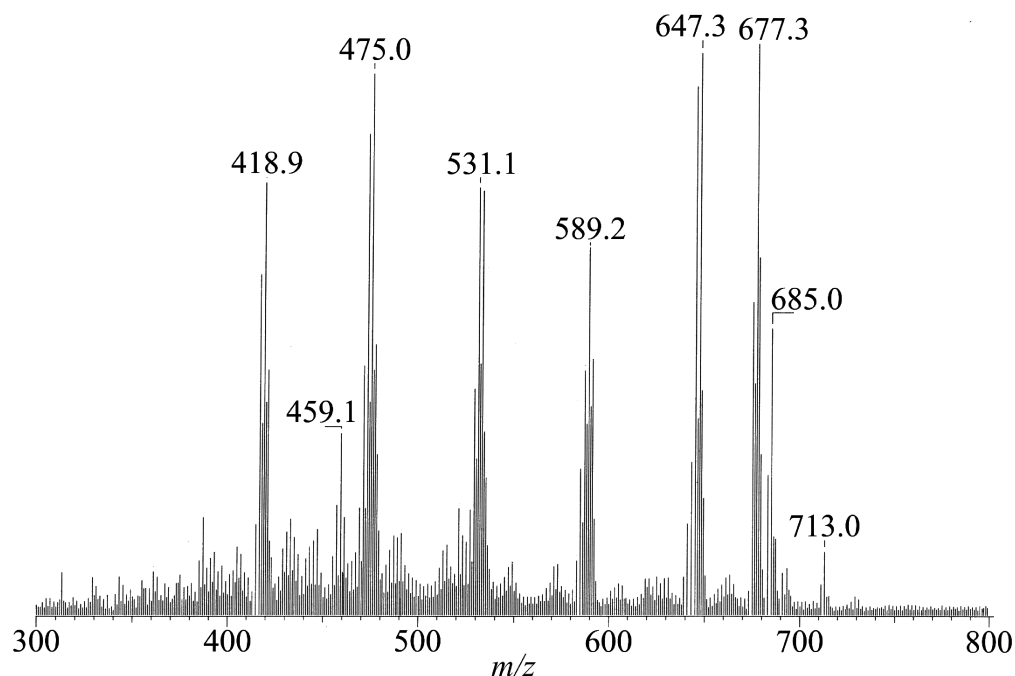
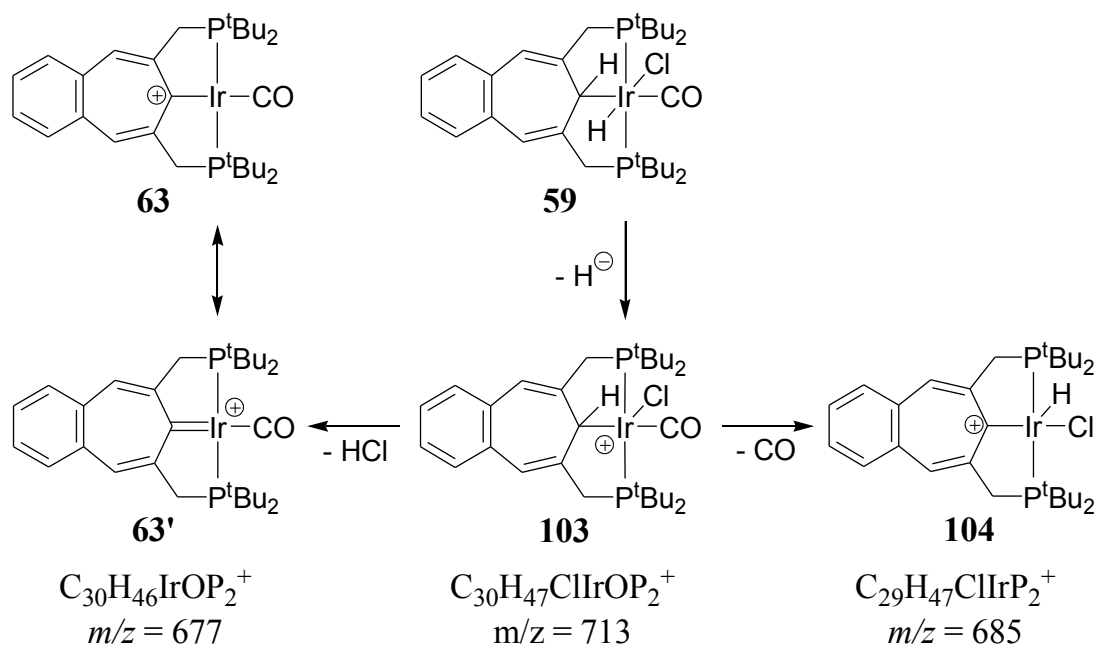


Figure 31: FAB mass spectrum of **59**

The obtained spectrum shows the molecular ion peak $[M-H]^+$ at $m/z = 713$ with weak intensity which indicates the low stability of this ion. From the two possible isomers of $[M-H]^+$, **103** and **95** (Scheme 62), isomer **103** is most likely the structure of the $[M-H]^+$ ion as it is by 119.4 kJ/mol less stable than **95** (Figure 30). The following signals $m/z = 685$ and 677 could be attributed to the structures **104** and **63**, respectively (Scheme 63). Complex **103** displays a metal located cation with a *syn*-periplanar orientation of hydrogen and chlorine. This auspicious situation in **103** is a good explanation for the lability towards an uni-molecular HCl elimination process, forming the carbene resonance structure **63'** ($m/z = 677$). Furthermore, the molecular ion **103** is able to emit carbon monoxide accompanied by the 1,2-hydride shift to the iridium centre leading to the $m/z = 685$ (**104**). Kinetically this process appears to be less favourable as the cleavage of the strong carbonyl metal bond is involved. Independent of the kinetic situation the generation of **63** and **104** are driven by the formation of an aromatic backbone.



Scheme 63

Energetically, the generation of the initial cations **103** from complex **59** is a highly endergonic process as mentioned in chapter 3.5.3.1.3. The elimination of HCl or CO from **103** forms the complexes **63** and **104** which are stabilised by 34.6 kJ/mol and 29.3 kJ/mol, respectively (Figure 32). While the corresponding reactions starting from **III_G** are endergonic processes.

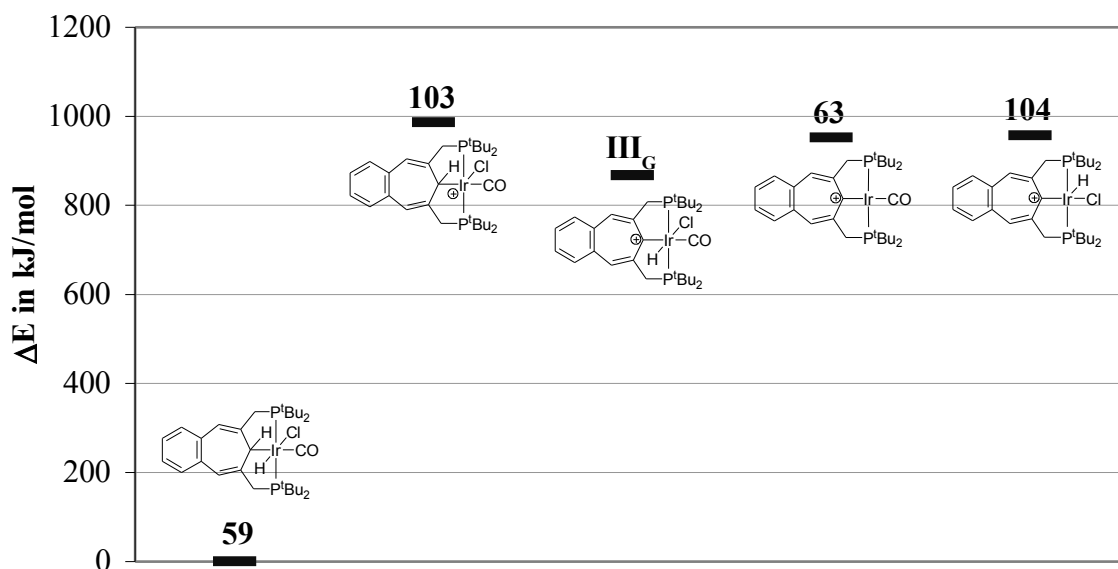
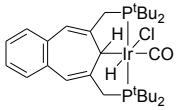
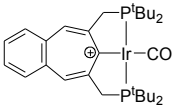
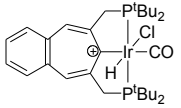
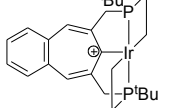
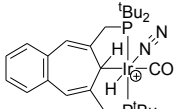
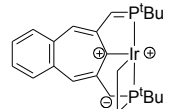
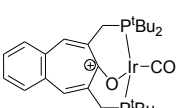
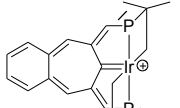
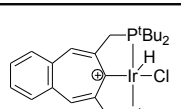
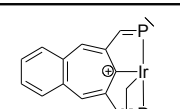
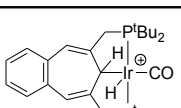
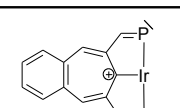


Figure 32: DFT results for initially formed ions and fragment ions in FAB-MS.

The discussion of the remaining fragments in the FAB mass spectra (Figure 31) follows in combination with the results of the MSⁿ measurements. Table 11 collects the mass to charge ratios, the proposed structures, the availability of high resolution mass spectra and the ionisation source of all experimentally verified fragments mentioned so far or in the following.

Table 11: Observed ions in the mass spectra of **59**

<i>m/z</i>	structure	source	HRMS	<i>m/z</i>	structure	source	HRMS
714	 59	-	-	677	 63	ESI, FAB	yes
713	 95	FAB	no	647	 106	ESI, FAB	yes
707	 105	ESI	yes	589	 107	ESI, FAB	yes
693	 102	ESI	yes	531	 108	ESI, FAB	no
685	 104	FAB	no	475	 109	FAB	no
679	 59	ESI	yes	419	 110	FAB	no

3.5.3.3 Electro-spray ionisation mass spectrometry of **59**

The assembly for routine mass spectra with the Bruker Daltonics esquire3000plus spectrometer is depicted in Figure 33.

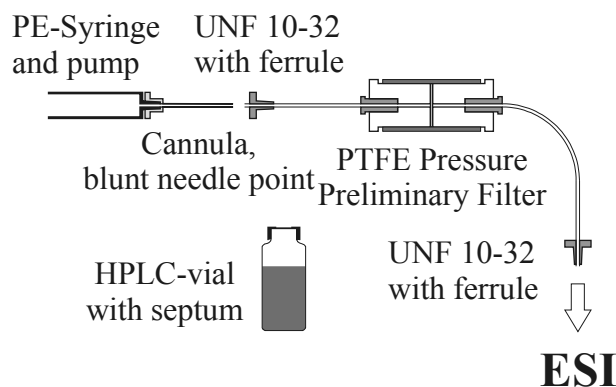


Figure 33: Routine infusion setup for ESI

A 10 μM sample solution was prepared under inert conditions in an HPCL vial with a septum. The inlet of the electro-spray chamber is connected to a transfer tube (PEEK) with or without an in-line filter and the syringe as well as the tubing are flushed with the dry solvent. Subsequently the sample is drawn up with the syringe, connected to the transfer tube and injected at a flow of 1 - 20 $\mu\text{L}/\text{min}$ with the syringe pump.

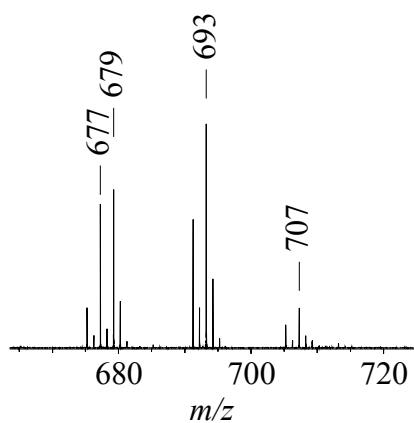
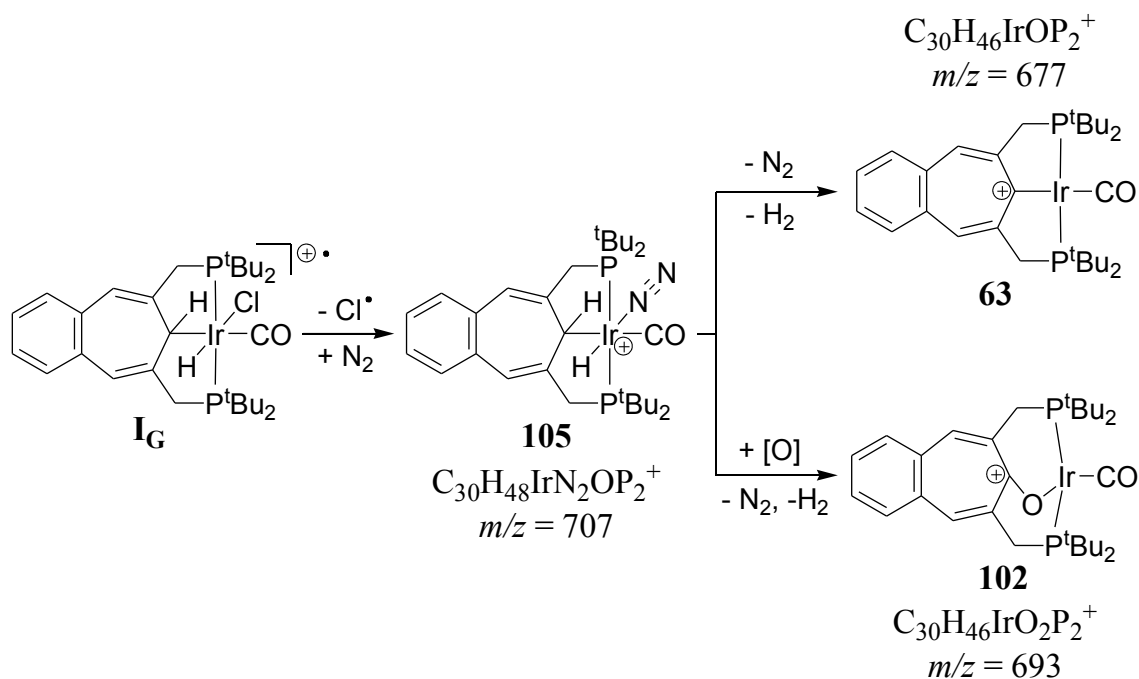


Figure 34: ESI HR mass spectrum of **59**

The mass analysis of **59** with the routine set-up displays a mixture of four m/z signals with the typical isotope pattern of iridium $^{191}\text{Ir} : ^{193}\text{Ir} \approx 37 : 63$ (Figure 34). The intensity of the m/z signals 677 is enhanced, while $m/z = 707$ decreases, with rising potentials of the transfer capil-

lary exit (analogue to cone voltage). This behaviour is an indication for the fragmentation of $m/z = 707$ in favour of $m/z = 677$ in the ESI source.



Scheme 64

An increasing capillary exit potential results in higher collision energies between the desolvated ions and the drying gas (N_2) and consequently ion fragmentation is observed in the spectra.

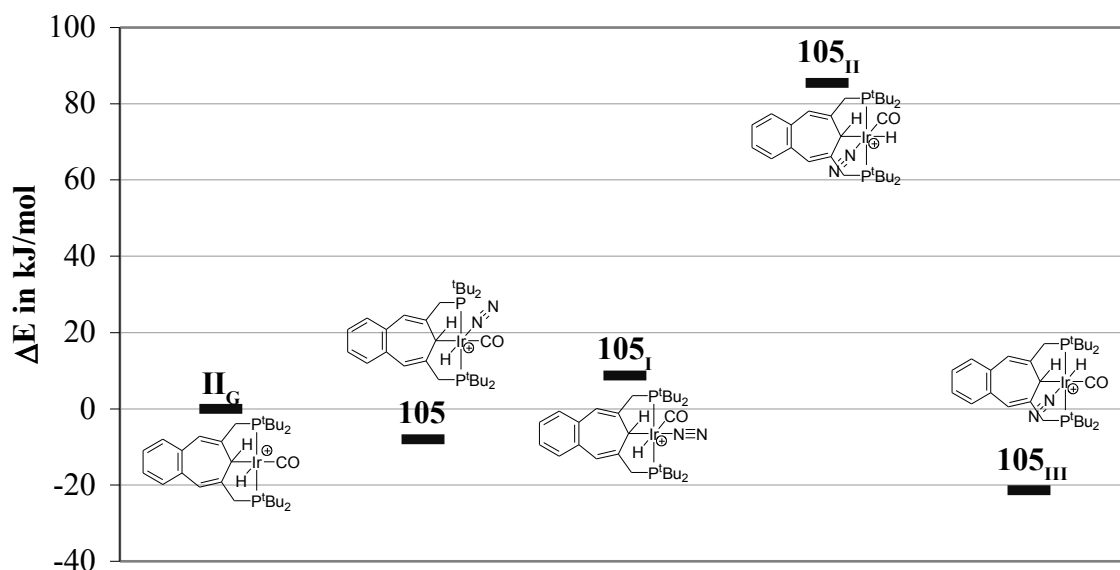


Figure 35: DFT results for nitrogen adduct complexes observed in ESI-MS.

This enforced fragmentation in electro-spray ionisation sources is called “in-source fragmentation”. High resolution mass spectrometry (HRMS) with a Fourier transform ion cyclotron resonance (FTICR) instrument and equipped with an ESI source and the routine infusion set-up (Figure 34) allowed the attribution of the $m/z = 677$, 679, 693 and 707 to their sum formulas (Scheme 64). Hence, **105** with $m/z = 707$ could formally be explained by the loss of a chloride ion from **59** and the subsequent coordination of dinitrogen. In Figure 35 the different geometry optimised isomers of the dinitrogen complex **105** are shown. The most stable structure ($\Delta(\Delta E) = -21.4$ kJ/mol relative to **II_G**) in Figure 35 is complex **105_{III}** with *syn*-periplanar orientation of the metal bound and the carbon bound hydrogen atoms. If the adduct is formed without any rearrangement at the metal centre, the resulting compound **105** is 8 kJ/mol lower in energy than **II_G**. The remaining structures **105_I** and **105_{II}** with *syn*-periplanar arrangement of the carbon bound hydrogen atom and the carbon monoxide ligand are 8.7 and 85.4 kJ/mol less stable than **II_G**.

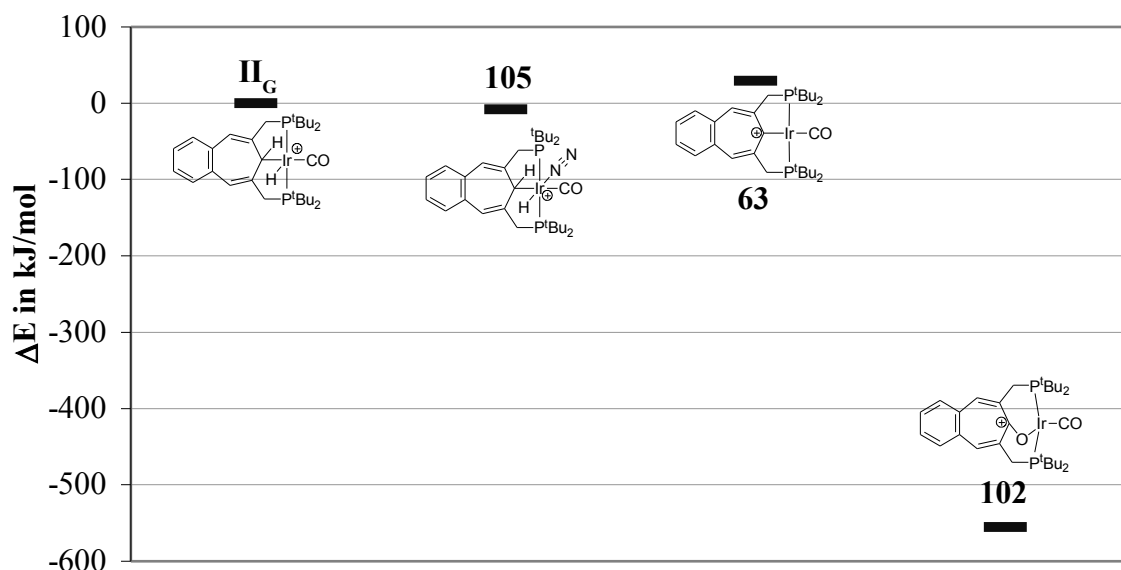


Figure 36: DFT results for nitrogen adduct complexes observed in ESI-MS.

Complex **63** with $m/z = 677$ is 37.3 kJ/mol endergonic compared to **105** and could be rationalised by the loss of a molecule of dihydrogen and dinitrogen from **105**. Whereas $m/z = 679$ (**II_G**) results just from chlorine atom abstraction from **I_G**. The sum formula of **102** reveals an additional oxygen atom as compared with **63**. Therefore the structure of **102** is proposed in analogy to the structure of the cycloheptatriene oxo-complex **48** which was characterised by single crystal XRD (Figure 1).⁶⁶ The formation of compound **102** is unexpected because an

oxygen donor (O_2 or H_2O) is required and the application of the routine set-up should avoid higher concentrations of oxygen or water in the sample solution. In order to locate the oxygen source an improved direct infusion set-up was developed which completely avoids the contact between the sample solution and the atmosphere.

Comparing Figures 33 and 37 it is apparent that the routine set-up is extended by an assembly of 3-way-valves. The central valve is the connection with the argon source and allows the flushing of the syringe and the tubing. An HPCL vial containing the sample solution is connected to the left-hand side 3-way-valve.

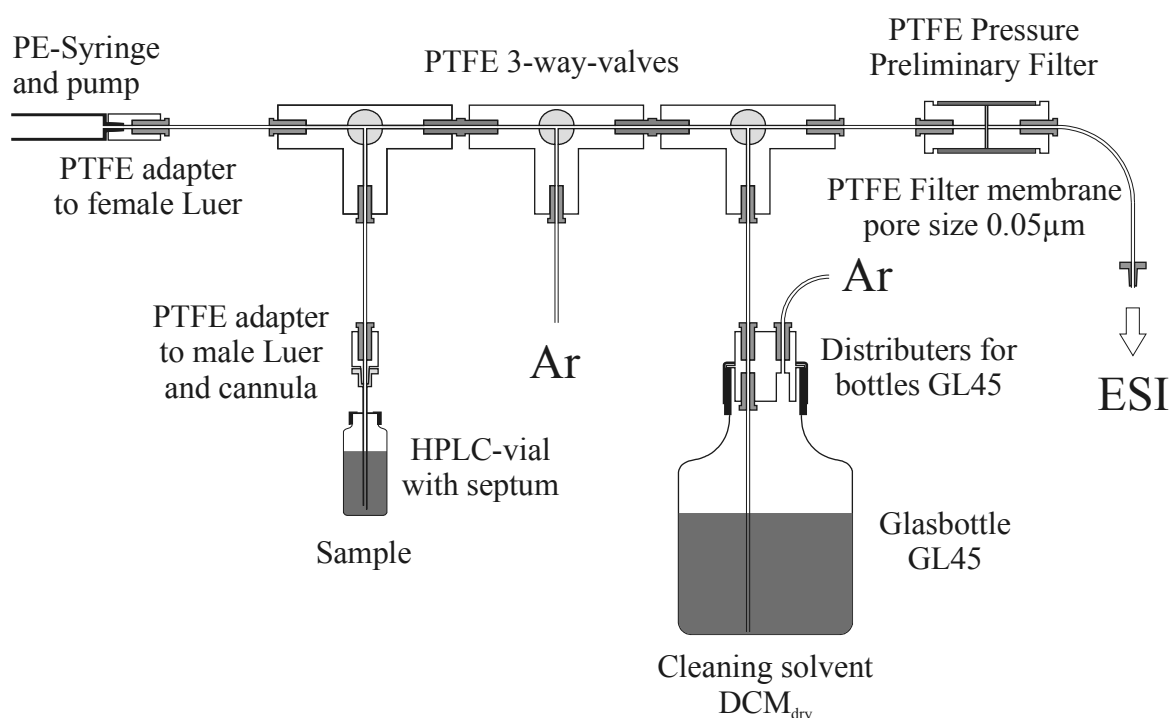


Figure 37: Improved infusion setup for ESI

The right-hand side valve is linked to a glass bottle, which is equipped with a distributor and for pressure equilibration with the argon source. Prior to injecting the sample, the dried cleaning solvent from the glass bottle is drawn up with the syringe and the complete assembly is flushed three times to remove water from the assembly surfaces. Subsequently, the sample solution is drawn up to the syringe and injected to the electro-spray chamber having all other lines closed. All components of the transfer assembly which are in contact with the sample solution are made of PTFE. Either a gas-tight 1 mL glass syringe or a single use 1 mL PE syringe is connected to the transfer assembly *via* a female luer adapter. A combination of a male luer adapter and a stainless steel cannula is used to attach the HPLC vial to the improved infu-

sion set-up. The not explicitly mentioned connections as the tube to valve transition is obtained with BOLA tube end fittings (UNF 1/4"-28) and flanges or BOLA double tube end fittings. The complete dead volume of the assembly doubles with approximately 70 μL as compared to the routine infusion set-up with about 20 μL (Figure 33).

The application of the improved infusion set-up (Figure 37) led to a mass spectrum of **59** which exclusively displays the $m/z = 707$ corresponding to complex **105** while $m/z = 677$ as well as $m/z = 693$ and therefore **63** and the oxygen containing complex **102**, respectively are missing (Figure 38).

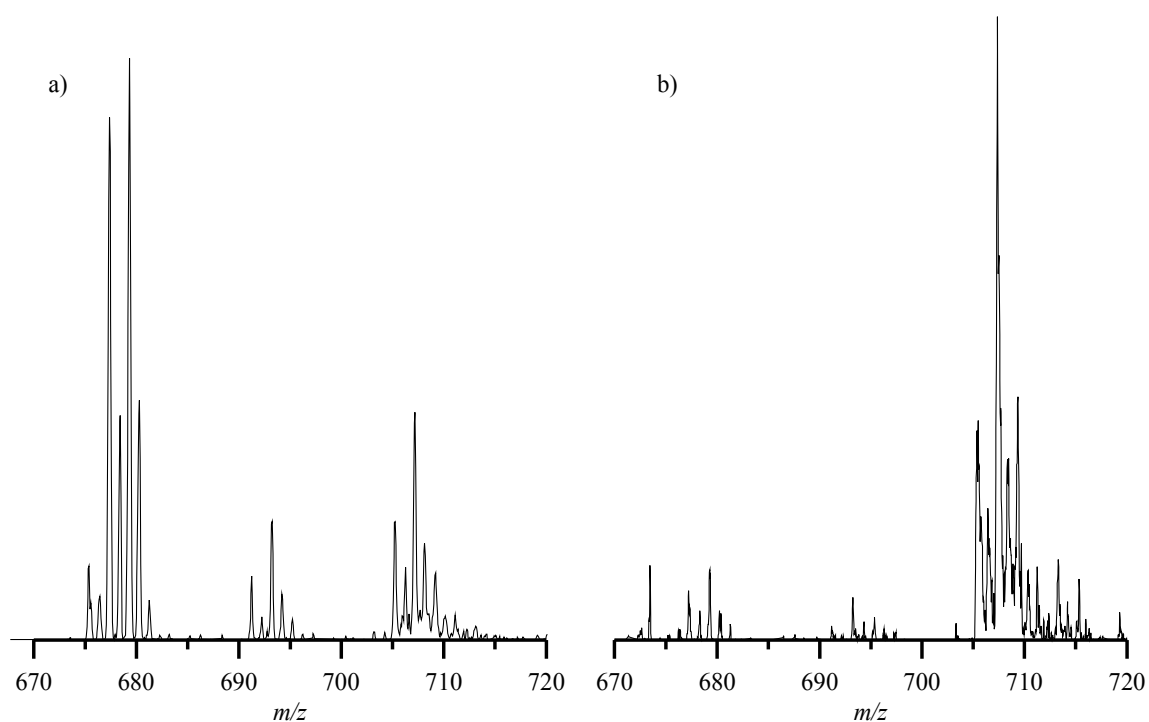


Figure 38: ESI mass spectra of **59**: a) with routine infusion setup and b) with the improved infusion setup

Complex **105** can be rationalised as the trapping product of II_G with nitrogen. The missing signals of the decomposition product **63** or of the reaction product **102** verifies II_G as the initially formed ion under inert conditions.

The differences in the mass spectra might be explained by:

- the concentration of residual water in the dried DCM which is in the worse case around 1 $\mu\text{g/L}$, corresponding with a molar concentration of water in DMC of roughly

60 nmol/L. This is about two orders of magnitude smaller than the initial molar concentration of **59** and should therefore not influence the spectra significantly.

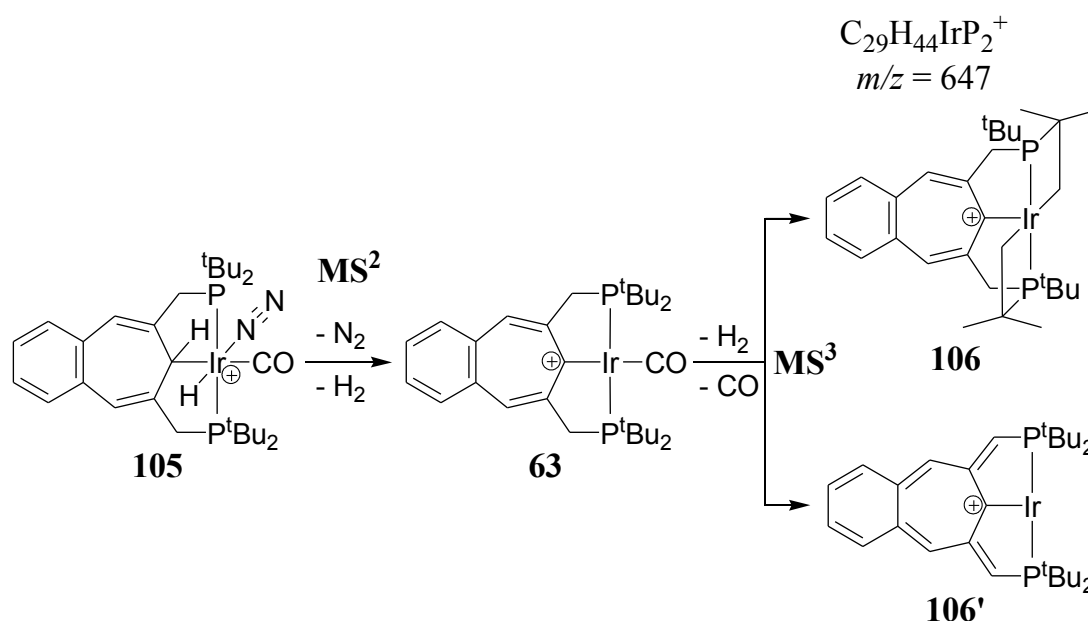
- the diffusion of atmospheric oxygen and/or water into the filled syringe in the routine infusion set-up. The final oxygen and/or water concentration depends on the initial concentrations of oxygen and/or water, the time for the diffusion processes between gas and liquid phase and the interface area between sample solution and atmosphere. As the diameter of the syringe cannula (0.8 mm) is comparatively small and the time between drawing up the solution and injection (10 s) is short, it seems unlikely to achieve concentrations equivalent to the concentration of the sample.

3.5.3.4 *MSⁿ experiments and FAB fragmentation*

The Bruker Daltonics esquire3000plus instrument uses an ion trap as m/z filter and is additionally able to perform experiments with collected ions. The ion trap consists of a three electrode set-up with a hyperbolic ring electrode and two hyperbolic end-cap electrodes. A substantially quadrupole electric field is established by a high voltage radio frequency potential applied to the ring electrode. Ions coming from the ion optic experience a potential trough originated in the 3D quadrupole field. In the ion trap the ions have to get rid of their internal energy by a collision gas (bath gas, He) to become stored at the bottom of the potential trough. The application of a second radio frequency potential to the end-cap electrode allows the successive ejection of ions with different m/z from the ion trap and therefore the scanning of the entire m/z range. Furthermore, ions with a selected m/z can be isolated in the ion trap and fragmented by excitation with a low voltage radio frequency potential applied on the end-cap electrode. The selected ions become accelerated in the trap (too less to become ejected) and the higher energy collisions with the bath gas (He) induces the fragmentation of the isolated ion. This process is called collision induced dissociation (CID). Afterwards, these new fragment ions can also be isolated and fragmented. These type of experiments are referred to as tandem mass spectrometry or MSⁿ experiments. The Bruker Daltonics esquire3000plus allows the subsequent isolation and fragmentation in up to ten steps.

The following schemes show the fragmentation pathway of **59** as derived from MSⁿ experiments and the FAB mass spectrum (Figure 33). The sum formulas in Scheme 65 and 66 are obtained from ESI in-source fragmentation experiments and HRMS. The tandem MS experiments were performed with the routine set-up for ESI infusion and the m/z isotope patterns at

677, 693 and 707 were isolated consecutively. There is no clean fragment ion signal observed for the collision induced dissociation of the ions with $m/z = 693$ (**102**). The first CID of the nitrogen adduct complex **105** ($m/z = 707$) forms the Ir(I) compound **63** ($m/z = 677$) by elimination of dinitrogen and dihydrogen (Scheme 65). This MS² result verifies the previous assumption of the fragmentation derived from the spectra with different capillary exit potentials (page 101). Starting from the dinitrogen complex **105**, the reaction to **63** is by 100 kJ/mol endergonic (Figure 36).



Scheme 65

A further CID step is accompanied by the formal removal of carbon monoxide and molecular hydrogen resulting in the isomeric complexes **106** or **106'** ($m/z = 647$). The Ir(III) complex **106** displays two cyclometallated *tert*-butyl groups and an aromatic backbone while **106'** contains an Ir(I) centre and a conjugated poly-olefinic backbone. The destruction of the aromatic backbone in **106'** destabilises this structure compared to the isomeric compound **106** by 70.0 kJ/mol (Figure 39). It is assumed that initially CO is released to create an active 14e⁻ Ir(I) species (**63_I**) which is 192.5 kJ/mol higher in energy than **63** and not observed in the mass spectra. Subsequently, there are two possible uni-molecular ways to transfer two hydrogen atoms from the ligand backbone to the metal centre in **63_I** to enable a reductive elimination of a hydrogen molecule. First *via* a consecutive cyclometallations of two *tert*-butyl groups consuming 190.2 kJ/mol and finally generating isomer **106**. Second the concerted shifts of two

γ -hydrogen atoms from the methylene bridges to the metal centre forming complex **106'**, which requires 260.2 kJ/mol. Furthermore, Figure 39 shows the alternative pathways with initial cyclometallation or γ -hydrogen shifts forming the carbonyl complexes **106_I** and **106'_I**.

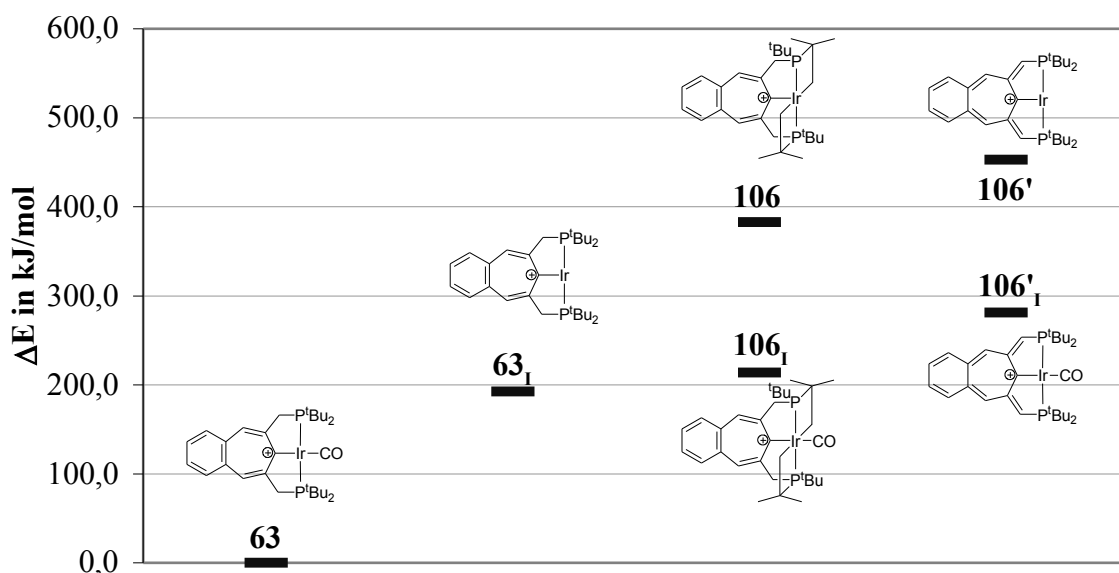
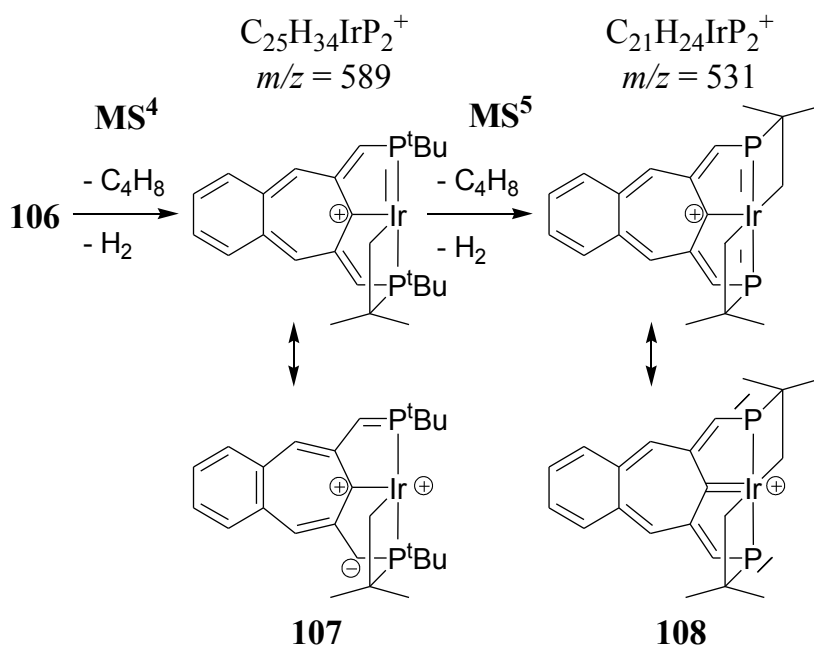


Figure 39: DFT energies for MS³ fragment ions in ESI-MS.

Although, the complexes **106** and **106'** are higher in energy (168.9 kJ/mol and 171.4 kJ/mol) than their carbonyl counterparts (**106_I** and **106'_I**), the formation of the 14e⁻ Ir(I) complex **63_I** is thermodynamically preferred by 21.3 kJ/mol and 88.8 kJ/mol as compared to **106_I** and **106'_I**. This justifies the assumption of the initial carbon monoxide emission and the subsequent removal of dihydrogen.

A further CID step applied on complex **102** (Scheme 66) generates a signal at $m/z = 589$ which is consistent with the result of *iso*-butene and dihydrogen elimination. In Scheme 66 the structures from formal 2+2 cycloeliminations as well as the corresponding resonance structure of the iridium complexes **107** and **108** are shown. The structure of compound **107** displays one metal coordinated *tert*-butyl phosphanylidene arm and one residual cyclometallated *tert*-butyl group while the cycloheptatriene ring has lost its planarity and hence its aromaticity. Due to decreasing intensities in MSⁿ spectra the last observable fragment ion in ESI-ion-trap-MS is $m/z = 531$ which is assigned to structure **107** (Scheme 66). The remaining *tert*-butyl groups in compound **108** were activated forming two four membered rings linked *via* the iridium atom and molecular hydrogen. Furthermore, the resonance structure of **108**

shows a carbene carbon atom coordinated to a positively charged Ir(III) centre and a non aromatic backbone.



Scheme 66

Energetically, the release of *iso*-butene from **106** is an endergonic reaction (75.8 kJ/mol) via a formal 2+2 cycloelimination and hence the formation of a formal iridium phosphorus double bond according to **107_I** in Figure 40.

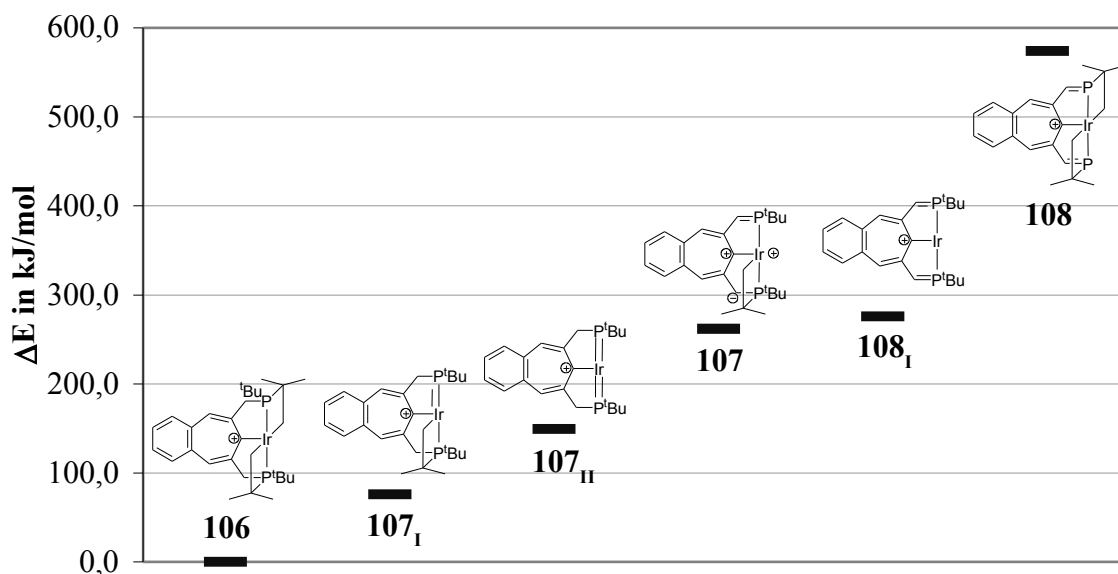
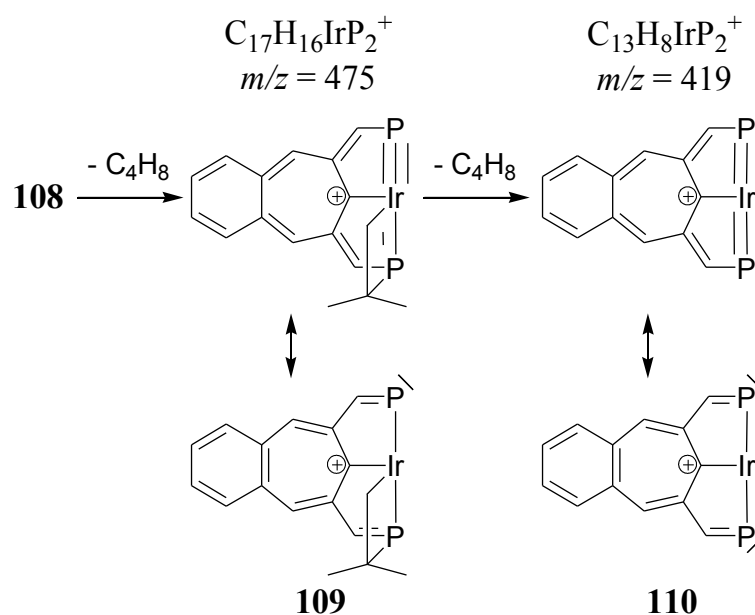


Figure 40: DFT energies for MS⁴ and MS⁵ fragment ions in ESI-MS.

Although, the subsequent emission of a further equivalent of *iso*-butene forming **107_{II}** is 112.5 kJ/mol less endergonic than the removal of dihydrogen leading to **107**, the mass experiment confirms the exclusive formation of **107** (186.0 kJ/mol relative to **107_I**). Therefore the activation barrier for *iso*-butene cycloelimination seems to be significantly higher than the barrier for γ -hydrogen shifts from the methylene bridges to the metal and subsequent reductive elimination of H₂. The cycloelimination of *iso*-butene from **107** affording the bis-*tert*-butylphosphanylidene complex **108_I** is only weakly endergonic (14.0 kJ/mol), while the consecutive cyclometallation of the *tert*-butyl groups and the elimination of dihydrogen forming **108** are in sum 297.9 kJ/mol higher in energy than **108_I**.

Additionally, to the *m/z* signals 647, 589 and 531 from the ESI MSⁿ experiments the FAB mass spectrum (Figure 31) displays two further fragment ions with *m/z* = 475 and 419. The consecutive elimination of two neutral *iso*-butene fragments with *m/z* = 56 explains the observed fragment masses and allows their attribution to the structures **109** and **110** (Scheme 67). Both structures were obtained from formal 2+2 cycloeliminations yielding the Ir(V) complexes with metal phosphorus multiple bonds.



Scheme 67

The shown resonance structure of compound **109** contains an Ir(III) centre with an almost planar carbo-cyclic backbone, one *tert*-butyl phosphanylidene arm with cyclometallated *tert*-butyl group and one coordinated phosphanylidenide moiety. In complex **110** the remain-

ing cyclometallated *tert*-butyl group was emitted as a *iso*-butene molecule forming a C_{2v} symmetric iridium complex with two coordinated phosphanylidenide arms and the central carbon metal bond. The iridium atom is located above the plane formed by the phosphorus atoms and the central carbon atom and seems to become stabilised by additional interactions with the phosphanylidenide methyne carbon atoms.

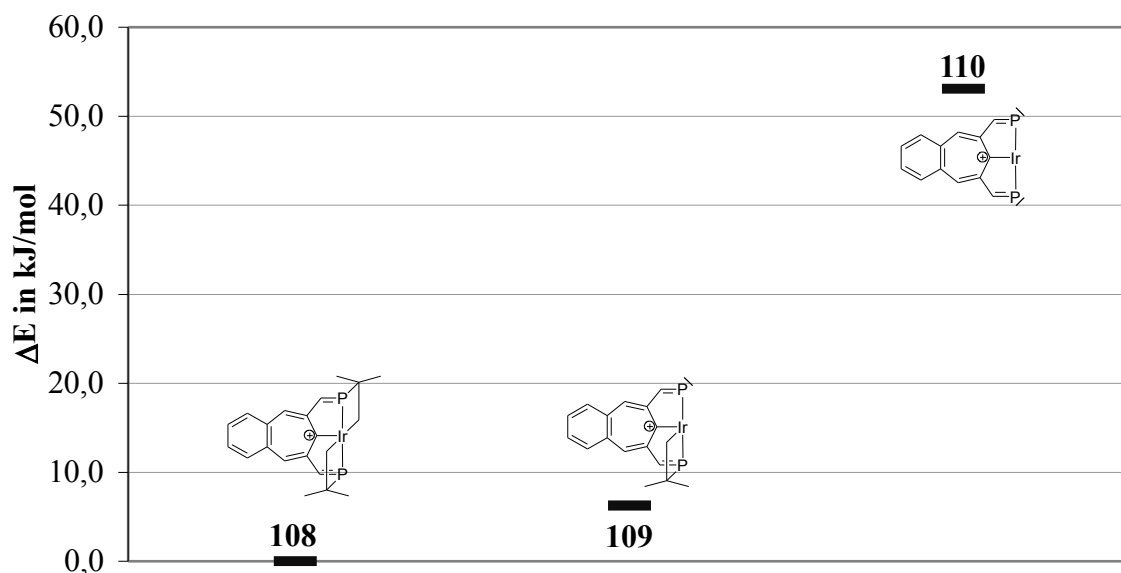


Figure 41: DFT energies for additional fragment ions in FAB-MS as compared to ESI-MS.

Thermodynamically, the cycloelimination of one *iso*-butene molecule from **108** is with 6.2 kJ/mol only slightly endergonic. On the other hand the elimination of the *iso*-butene molecule from **109** forming the bis-phosphanylidenide complex **110** is a comparatively energy consuming process (46.9 kJ/mol).

4 Computational details

4.1 General remarks on density functional theory

The electronic energy of a molecule is completely determined by the corresponding electron density. Furthermore the electronic energy can be obtained variationally from an initial guess for the electron density. These theorems⁸¹ are fundamental to DENSITY FUNCTIONAL THEORY (DFT). The development of the electron density on the basis of wave functions, the so-called KOHN-SHAM Orbitals and the application of the LOCAL SPIN DENSITY APPROXIMATION (LSDA)⁸² strongly improved the results of DFT calculations. LSDA locally treats the electron density as a uniform electron gas and therefore assumes the electron density to be a slowly varying function. Further improvements were achieved by adding derivatives of the electron density to the exchange correlation functional within the GENERAL GRADIENT APPROXIMATION (GGA). The DFT hybrid functional B3LYP is a combination of the BECKE three parameter exchange correlation functional⁸³ (B3) and the LEE, YANG and PARR⁸⁴ (LYP) correlation functional. B3 combines the LSDA exchange and the exact exchange with a B88 exchange correction term and adds a GGA correlation correction term to the LSDA correlation. The three parameters were obtained by fitting the functional form to experimental data. The correlation functional LYP is also a GGA functional containing four parameters which are determined by fitting to data for the helium atom.

Unless otherwise mentioned the B3LYP hybrid functional was used with the LOS ALAMOS LACVP* valence double zeta basis set⁸⁵ for all DFT calculations. LACVP is an EFFECTIVE CORE POTENTIAL (ECP) basis set treating the core electrons of heavier elements than Argon with a relativistic effective potential while the electrons of the valence shell (e.g. Iridium: 5s5p6s5d6p) are calculated explicitly. Elements lighter than Argon use the split valence 6-31G* basis set.⁸⁶⁻⁹⁰ Furthermore the LACVP* basis set is optimised for pseudospectral⁹¹ calculations. There are a few books and reviews released for further informations on calculation of transition metal complexes,⁹²⁻⁹⁴ Theoretical techniques and DFT.⁹⁵⁻⁹⁷

All calculations were performed with Jaguar, the *ab initio* quantum mechanic package from Schrödinger LLC.⁹⁸ Maestro⁹⁹ was used as graphical user interface to import or modify the input structures and generate the input files for Jaguar. Furthermore the Jaguar output structures, molecular orbitals and vibrational data were analysed with Maestro. Initially, an Intel Penti-

um4 3.2 GHz (32bit) and thereafter an Intel Core2Duo E8400 (64bit) personal computer was used as hardware platform which run under OpenSuSE Linux. The Core2Duo platform allowed the distributed calculation of one molecule on both processor cores.

Usually for all calculations the grid density for numerical integration and the accuracy level for integral cut-offs was set to “medium” and “quick” respectively. The default thresholds for the SCF steps amounted to an energy change below $5 \cdot 10^{-5}$ hartree and the RMS density matrix change was below $5 \cdot 10^{-6}$ bohr.

4.2 Geometry optimisations

Generally the input structures for geometry optimisations were obtained from modified or unmodified crystal structures or by modification of a previously calculated crystal structure. The default thresholds for geometry optimisation steps were: maximum element of gradient = $4.5 \cdot 10^{-4}$ hartree, RMS of gradient element = $3.0 \cdot 10^{-4}$ hartree, maximum element of nuclear displacement = $1.8 \cdot 10^{-3}$ bohr, RMS of nuclear displacement elements = $1.2 \cdot 10^{-3}$ bohr and energy difference between previous and current geometry iteration = $5.0 \cdot 10^{-5}$ hartree. There were no symmetry settings or structural constraints applied nor any *tert*-butyl group substitution prior to the calculations. If geometry convergence could not be achieved with the default settings, the grid density was increased to “maximum” and the pseudo-spectral calculation was turned off by setting the accuracy level to “fully analytic”. Regularly the vibrational frequencies were calculated from the hessian of the final geometry optimisation step to verify the minimum structure.

Optimisations of solvated minimum structures were started from gas phase optimised structures. The POISSON-BOLTZMANN solvation model (PBS) treats the solvent as a layer of charges which was fitted (POISSON-BOLTZMANN equation) to the charge distribution of the molecule. The calculated “charge layer” transfers to a surrounding point charge distribution in the quantum chemical calculation and the minimum structure is obtained self-consistently by continuously re-optimisation of the molecular structure and its “charge layer”.

4.3 Transition state optimisations

The quadratic synchronous transit (QST) method⁹⁷ was used to optimise transition state structures. Hence the input file for the calculation contains a proposal of the transition state structure and the previously optimised minimum structures of reactant and product. The frequency

calculation was performed with the hessian of the final optimisation step and was used to characterise the saddle point and the transition state. In the case of higher order saddle points (more than one negative vibrational frequencies) the negative normal vibrations were analysed to assure just one productive negative vibration beside mainly rotational vibrations of the *tert*-butyl groups.

5 Experimental section

5.1 Synthetic methods

5.1.1 Solvents and gases

All reactions and transformations were performed with Schlenk techniques under Argon atmosphere unless mentioned otherwise.

Argon with 99.998% (4.8) or 99.9990% (5.0) purity, oxygen 99.998% (4.8) and hydrogen 99.9990% (5.0) were obtained from Air Liquide and used without further purification. Gases in small containers like carbon monoxide 99.97% (3.7) or deuterium 99.5% (2.5) were purchased as minican from Linde and used with no further purification.

The solvents were obtained from the chemical store at the University of Tübingen except for THF in reagentplus quality which was purchased from Sigma-Aldrich and *n*-pentane 99+% extrapure from Acros Organics.

Solvents were dried according to literature methods and distilled under Argon. Diethyl ether and THF were dried over sodium/benzophenone, ethanol and 2-propanol over sodium, methanol over magnesium, dichloromethane over calcium hydride, *n*-pentane over sodium hydride and acetone over sicapent (P₂O₅). The dry solvents were stored under Argon in Schlenk flasks with activated molecular sieve (3Å or 4Å). Benzene, toluene and diglyme in puriss. quality with water contents below 0.005% and acetonitrile puriss. with less than 0.001% water were purchased from Sigma-Aldrich and used as delivered.

Deuterated solvents were obtained from Merck Chemicals or from Eurisotop (no less than 99.8% deuteration), transferred to Schlenk flasks with activated molecular sieves, degassed by three freeze-pump-thaw cycles and used without further purification.

5.1.2 Precursors and reagents

Lithium aluminium hydride pellets reagent grade (95%), sodium boron-hydride reagentplus (99%), dimethyl 5-amino-*iso*-phthalate (98%), 5-nitro-*iso*-phthalic acid (98%), tetra-bromo-methane reagentplus (99%) and thionyl bromide purum ($\geq 97\%$) were procured from Sigma-Aldrich. Sodium hydride (60%) dispersion in mineral oil, tri-phenylphosphane (99%), phosphorus tri-chloride (98%), 2-chloro-2-methylpropane (99%) and potassium-*tert*-butoxide

pure (98+%) were purchased from Acros Organics. $\text{IrCl}_3 \cdot n \text{H}_2\text{O}$, $(\text{CO})_3\text{IrCl}$, $[(\text{COD})\text{IrCl}]_2$ and $[(\text{COE})_2\text{IrCl}]_2$ were obtained from Strem. Di-*tert*-butylphosphane was prepared according to literature procedures^{100,101} or obtained in 98% purity from Strem. 3,5-Bis(di-*tert*-butyl-phosphano)methylenanisole⁶⁷ as well as 1,6-bis(di-*tert*-butyl-phosphano)methylenecyclohepta-1,3,5-triene²⁸ were synthesised as described in the literature. Reagents and precursors which are not mentioned otherwise were obtained from the chemical store at the University of Tübingen. The commercially available reagents were used without further purification unless otherwise specified.

5.2 Analytical methods and techniques

5.2.1 Nuclear magnetic resonances spectroscopy

All NMR spectra were recorded at a temperature of 299K on the following spectrometers:

- a Bruker DRX 250 MHz spectrometer equipped with a 5mm BBO probe with automatic tuning and matching for X and ^1H and controlled by a Xwin-NMR 3.5:

^1H : 250.13 MHz ^{11}B : 80.25 MHz ^{13}C : 62.90 MHz ^{31}P : 101.25 MHz.

- an Bruker Avance II 400 MHz spectrometer equipped with a 5mm QNP probe including Z-gradient; for ^1H , ^{13}C , ^{31}P and ^{19}F and controlled by TopSpin 2.0:

^1H : 400.13 MHz ^{13}C : 100.61 MHz ^{19}F : 376.50 MHz ^{31}P : 161.98 MHz.

- an Bruker Avance II+ 500 MHz spectrometer with a 5mm TBO probe including Z-gradient; for X, ^{11}B and ^1H and controlled by TopSpin 2.1:

^1H : 500.13 MHz ^{11}B : 160.46 MHz ^{13}C : 125.76 MHz ^{31}P : 202.46 MHz.

The different NMR spectra and different nuclei were recorded using the following Bruker pulse programs on the respective workstations:

1D NMR spectra and pulse programs		2D NMR spectra and pulse programs	
^1H	zg30	H-H-COSY	cosygpqf
$^{11}\text{B}\{^1\text{H}\}$	zgig30	H-H-DOFCOSY	cosygpmpqf
$^{13}\text{C}\{^1\text{H}\}$	zpgg30	P-P-COSY $\{^1\text{H}\}$	cosydcqf
$^{19}\text{F}\{^1\text{H}\}$	zgfhighqn	H-H-NOESY	noesygpqh
$^{31}\text{P}\{^1\text{H}\}$	zpgg30	H-C-HSQC	hsqcetgpsi2

1D NMR spectra and pulse programs		2D NMR spectra and pulse programs	
$^{31}\text{P}\{\text{sel. } ^1\text{H}\}$	zgcw30	H-C-HSQC w. DEPT	hsqcedetgp
$^{13}\text{C}\{^1\text{H}\}$ DEPT135	dept135	H-P-HSQC	hsqcetgp
		H-C-HMBC	hmbcgplpndqf

^1H NMR spectra were referenced to the residual signals of the deuterated solvent relative to 1 % TMS in CDCl_3 .¹⁰² ^{13}C NMR spectra were referenced to the signal of deuterated solvent relative to 1 % TMS in CDCl_3 .¹⁰² ^{11}B , ^{19}F and ^{31}P NMR spectra were referenced *via* deuterium lock externally to 15 % $\text{BF}_3\cdot\text{OEt}_2$ in CDCl_3 , CFCl_3 and 85 % H_3PO_4 .

Samples of organometallic compounds were prepared in Schlenk tubes under Argon atmosphere and exclusively measured in NMR tubes with screw cap or in J. Young tubes. For all other samples standard glass NMR tubes with plastic caps were used. The chemical shifts of ^{13}C were mainly obtained from H-C-correlated experiments because of the strongly increased sensitivity of the proton detected pulsesequences using pulsed field gradients.

The interpretation of the multiplet patterns in the analytic part of chapter 5.3 is especially, for the compounds containing phosphorus rather difficult due to the most often very complicated spin systems. The phosphorus nuclei in the C_s , C_2 or C_{2v} symmetric compounds like the phosphanes or phosphonium salts are chemically equivalent. However different coupling paths of each of the phosphorus into the organic backbone are the reason for their magnetically inequivalence leading to higher order spin systems (N-line spectra).

If higher order multiplets are observed in the spectra this is indicated in the analytic data as virtual multiplets (vd, vt, vdd, etc.). In case of assignable N-lines their distance is given in the analytic data. If the N-lines could not be assigned the coupling constants are determined as zero-order multiplet but without the declaration of the number of the bonds linking the coupled nuclei.

5.2.2 Infrared spectroscopy

A Bruker VERTEX 70 FT-IR spectrometer was used to record the spectra. KBr pellets were prepared with dried and degassed “KBr for infrared spectroscopy” from Merck Chemicals. A tip of a spatula of the sample and 2-3 spatulas of KBr were mixed in an adequate Schlenk tube and transferred to the pressing tool which was roughly evacuated and put under Argon. Then the pressing tool is rapidly completed, put into the press and subsequently compressed for two

minutes at around 1.25 GPa (10 tons). Spectra of solution were obtained using liquid sample cells with PTFE caps. The solution cell was stored in a drying cabinet and flushed some minutes with argon prior to filling in the separately prepared sample solution. For both liquid and solid state spectra a background spectrum with the pure solvent or KBr was recorded and the difference spectrum was calculated.

5.2.3 Mass spectrometry

FAB and EI mass spectra were measured routinely on a Finnigan MAT (Thermo Scientific) TSQ 70 triple quadrupole mass spectrometer and the samples were provided in snap-cap vials under argon but further handled in air. Alternatively, FAB, FD and EI mass spectra were obtained on a Finnigan MAT (Thermo Scientific) MAT 95 sector mass spectrometer with high resolution.

Finnigan MAT MAT 95					
EI		FAB		FD	
source temp.	200°C	source temp.	35°C	source temp.	35°C
vaporiser temp.	30-300°C	ionisation particles	Cs ⁺ - ions (20 kV)	emitter heating	0-50 mA
ionisation energy	70 eV	matrix	3-Nitrobenzyl-alcohol	counter electrode voltage	3-8 kV
accel. energy	4.7 keV	accel. energy	4.7 keV	accel. energy	4.7 keV

Finnigan MAT TSQ 70			
EI		FAB	
source temp.	200°C	source temp.	50°C
vaporiser temp.	30-300°C	ionisation particles	Xe atoms (8 kV)
ionisation energy	70 eV	matrix	3-nitro-benzyl-alcohol

ESI or APCI mass spectra were recorded with a Bruker Daltonics esquire3000plus mass spectrometer which is a quadrupole ion-trap instrument. Typically ESI mass spectra of organo-

metallic compounds were obtained by direct infusion of a 1-20 $\mu\text{mol/L}$ DCM solution with a syringe pump at a flow rate of 10-20 $\mu\text{L/min}$. The sample solutions were prepared with dry solvents in an HPLC vial equipped with an PTFE septum. Prior to the injection a gas-tight 0.5 mL or 1 mL Hamilton syringe with a blunt needle point was flushed five times with argon. The sample solution was drawn up, the filled syringe was placed in the syringe pump and connected to the PEEK transfer capillary of the spray chamber.

For HR-ESI mass spectra a Bruker Daltonics 4.7 T APEX II FT-ICR instrument was used with direct infusion of a $\leq 1 \mu\text{mol/L}$ sample solution containing methanol. As internal mass reference an adequate poly(ethylene glycol) was applied. In this case the sample preparation and the infusion process were done in air.

5.2.4 Elemental analysis (CHNS)

Elemental analysis was performed routinely on a Vario EL Analyser manufactured by Elemental Company. The samples were transferred in air to the tin containers which were closed and folded. In case of organometallic compounds the samples were prepared applying Schlenk technique.

5.2.5 Single crystal X-ray diffraction

Single crystal X-ray diffraction patterns were recorded on a Stoe IPDS 2T diffractometer using molybdenum K_{α} radiation and the Stoe X-AREA and WinGX software. The structures were refined using SHELXS while SHELXL was used to solve the structure.¹⁰³ The X-ray absorption was corrected numerically applying the Stoe software X-red and X-Shape.

5.3 Syntheses

5.3.1 Ligand syntheses

5.3.1.1 3,5-Di-(hydroxymethylene)aniline (51h)

The synthetic procedure and analytical data are previously described¹⁰⁴ therein as compound **2**.

5.3.1.2 N-3,5-di-(hydroxymethylene)phenyl tert-butoxycarbamate (51g)

A synthetic procedure¹⁰⁵ was adapted. 65 mg (424 μmol) of **51h** were dissolved in 6 mL THF and cooled to 0 °C. A solution of 92 mg (421 μmol ; 1 eq.) di-*tert*-butyl di-carbonate in 6 mL THF was added slowly and drop-wise. After complete addition the homogeneous reaction mixture was heated to reflux for 20 h. Following the mixtures was cooled and the solvent was removed by rotary evaporation. The resulting highly viscous residue was dissolved in 20 mL ethyl acetate and extracted 3 times with about 10 mL of water. Finally the organic phase was dried with MgSO_4 and the solvent is rotary evaporated. 95 mg white solid were obtained. The NMR analytic reveals a nearly 1:1 mixture of di-*tert*-butyl di-carbonate and the desired product **51g** (≈ 47 mg; $> 45\%$).

^1H NMR (25 °C, 400.13 MHz, acetone- d_6): 8.32 (1H, br s, $\text{NHCOOC}(\text{CH}_3)_3$); 7.43 (2H, m, 2Ar-*H*); 6.99 (1H, m, Ar-*H*); 4.58 (4H, s, 2 CH_2OH); 4.13 (2H, br s, 2 CH_2OH); 1.49 (9H, s, $\text{NHCOOC}(\text{CH}_3)_3$).

$^{13}\text{C}\{^1\text{H}\}$ NMR (25 °C, 100.61 MHz, acetone- d_6): 153.8 (Ar- $\text{CNHCOOC}(\text{CH}_3)_3$); 143.8 (Ar- CCH_2OH); 140.3 (Ar- $\text{CNHCOOC}(\text{CH}_3)_3$); 119.7 (2Ar-CH); 116.0 (Ar-CH); 79.8 (Ar- $\text{CNHCOOC}(\text{CH}_3)_3$); 64.8 (Ar- CCH_2OH); 28.5 (Ar- $\text{CNHCOOC}(\text{CH}_3)_3$).

5.3.1.3 N-3,5-di-(hydroxymethylene)phenyl acetamide (51e)

The synthetic procedure and analytical data are previously described¹⁰⁴ therein as compound **3**.

5.3.1.4 N-3,5-di-(hydroxymethylene)phenyl trifluoroacetamide (51f)

The synthetic procedure and analytical data are previously described¹⁰⁴ therein as compound **18**.

5.3.1.5 N-3,5-di-(bromomethylene)phenyl acetamide (52e)

The synthetic procedure and analytical data are previously described¹⁰⁴ therein as compound **4**.

5.3.1.6 N-3,5-di-(bromomethylene)phenyl trifluoroacetamide (52f)

The synthetic procedure and analytical data are previously described¹⁰⁴ therein as compound **19**.

5.3.1.7 N-3,5-bis-(di-tert-butyl-phosphanomethylene)phenyl acetamide (54e)

574 mg (1.79 mmol) of N-3,5-di-(bromomethylene)phenylacetamide (**52e**) were degassed and consecutively suspended in 5 mL dry acetone. Then 0.68 mL (523 mg; 3.58 mmol; 2 eq.) of di-tert-butylphosphane were added to the stirred suspension of **52e**. The reaction mixture was heated to reflux for about 3 h. After completing the reaction time the solvent was removed and the resulting pale yellow solid was transferred to an inert gas frit and washed with 10 mL acetone. 862 mg (1.41 mmol; 79%) of the white solid bis-phosphonium di-bromide (**53e**) could be isolated.

³¹P{¹H} NMR (25 °C, 161.98 MHz, D₂O): 47.3 (t, ¹J_{PD} = 68.03 Hz).

¹H NMR (25 °C, 400.13 MHz, D₂O): 7.11 (1H, s, Ar-H); 7.01 (2H, s, 2Ar-H); 3.94 (4H, d, A₂X, ²J_{PH} = 13.66 Hz, 2CH₂P); 3.87 (3H, s, H₃C CONH); 1.49 (36H, d, A₁₈X, ³J_{PH} = 16.84 Hz, 4P(CCH₃)₂).

862 mg (1.41 mmol) phosphonium salt (**53e**) were dissolved in 7 mL of degassed water and this solution was covered with a layer of 4 mL of dry benzene. Separately 320 mg (2.85 mmol, 2 eq.) KO^tBu were dissolved in 4 mL of water. 0.5 mL of this basic solution was added under vigorous stirring to the bi-phasic mixture of the phosphonium salt. For a few minutes the stirring was discontinued and the benzene layer containing the product was collected separately, while another 4 mL of dry benzene were added to the aqueous solution. This procedure was repeated until the complete KO^tBu solution was added to the solution of the phosphonium salt. From the combined benzene layers the solvent was removed applying oil-pump vacuum yielding a highly viscous and pale yellow residue. A few “pump and freeze” cycles were applied to obtain the pale yellow solid (500 mg; 1.11 mmol; 79% based on **53e**; 62% based on **52e**)

³¹P{¹H} NMR (25 °C, 161.98 MHz, C₆D₆): 32.8 (s).

^1H NMR (25 °C, 400.13 MHz, C_6D_6): 8.06 (1H, s, H_3CNHCO); 7.82 (2H, s, 2Ar-*H*); 7.40 (1H, s, Ar-*H*); 2.81 (4H, d, A_2X , $^2\text{J}_{\text{PH}} = 2.36$ Hz, $2\text{CH}_2\text{P}$); 1.82 (3H, s, H_3CCONH); 1.09 (36H, d, A_{18}X , $^3\text{J}_{\text{PH}} = 10.94$ Hz, $4\text{P}(\text{C}(\text{CH}_3)_3)_2$).

$^{13}\text{C}\{^1\text{H}\}$ NMR (25 °C, 100.61 MHz, C_6D_6): 169.1 (s, Ar-CN HCO); 142.4 (vd, AXX' , $\text{J}_{\text{PC}} = 12.71$ Hz, $2\text{Ar-CCH}_2\text{P}$); 139.5 (s, Ar-CN HCO); 126.9 (t, AX_2 , $^3\text{J}_{\text{PC}} = 8.63$ Hz, Ar-CH); 118.8 (vd, AXX' , $\text{J}_{\text{PC}} = 9.09$ Hz, 2Ar-CH); 31.8 (vd, AXX' , $\text{J}_{\text{PC}} = 24.30$ Hz, $2\text{Ar-CCH}_2\text{P}$); 30.1 (d, A_6X , $^2\text{J}_{\text{PC}} = 13.62$ Hz, $2\text{P}(\text{C}(\text{CH}_3)_3)_2$); 29.7 (d, A_2X , $^1\text{J}_{\text{PC}} = 25.66$ Hz, $2\text{P}(\text{C}(\text{CH}_3)_3)_2$); 24.8 (s, H_3CCONH).

5.3.1.8 *N*-3,5-bis-(di-*tert*-butyl-phosphanomethylene)phenyl trifluoroacetamide (**54f**)

The same procedure was applied as for the **54e** (chapter 5.3.1.7) with quite comparable yields for the bis-phosphonium di-bromide (**53f**) and the final product (**54f**).

N-3,5-bis-(di-*tert*-butyl-phosphoniummethylene)phenyl trifluoroacetamide di-bromide (**53f**):

$^{31}\text{P}\{^1\text{H}\}$ NMR (25 °C, 161.98 MHz, D_2O): 47.0 (t, $^1\text{J}_{\text{PD}} = 67.78$ Hz).

^1H NMR (25 °C, 400.13 MHz, D_2O): 7.67 (2H, s, 2Ar-*H*); 7.48 (1H, s, Ar-*H*); 4.01 (4H, d, A_2X , $^2\text{J}_{\text{PH}} = 13.92$ Hz, $4\text{CH}_2\text{P}$); 1.51 (36H, d, A_{18}X , $^3\text{J}_{\text{PH}} = 16.84$ Hz, $4\text{P}(\text{C}(\text{CH}_3)_3)_2$).

$^{19}\text{F}\{^1\text{H}\}$ NMR (25 °C, 376.50 MHz, D_2O): 75.5 (s, F_3CCO).

$^{13}\text{C}\{^1\text{H}\}$ NMR (25 °C, 100.61 MHz, D_2O): 157.7 (q, AY_3 , $^2\text{J}_{\text{CF}} = 38.34$ Hz, Ar-CN HCOCF_3); 137.7 (t, AX_2 , $^4\text{J}_{\text{PC}} = 2.06$ Hz, Ar-CN HCOCF_3); 134.7 (vdd, AXX' , $\text{J}_{\text{PC}} = 8.47$ Hz, $\text{J}_{\text{PC}} = 1.84$ Hz, $2\text{Ar-CCH}_2\text{P}$); 129.3 (t, AX_2 , $^3\text{J}_{\text{PC}} = 6.19$ Hz, Ar-CH); 123.3 (vdd, AXX' , $\text{J}_{\text{PC}} = 6.19$ Hz, $\text{J}_{\text{PC}} = 2.28$ Hz, 2Ar-CH); 116.3 (q, AY_3 , $^1\text{J}_{\text{CF}} = 286.54$ Hz, Ar-CN HCOCF_3); 33.7 (d, A_2X , $^1\text{J}_{\text{PC}} = 33.44$ Hz, $2\text{P}(\text{C}(\text{CH}_3)_3)_2$); 27.3 (s, $2\text{P}(\text{C}(\text{CH}_3)_3)_2$); 21.4 (vd, AXX' , $^2\text{J}_{\text{PC}} = 39.41$ Hz, $2\text{Ar-CCH}_2\text{P}$).

N-3,5-bis-(di-*tert*-butyl-phosphanomethylene)phenyl trifluoroacetamide (**54f**):

$^{31}\text{P}\{^1\text{H}\}$ NMR (25 °C, 161.98 MHz, C_6D_6): 34.9 (s).

^1H NMR (25 °C, 400.13 MHz, C_6D_6): 7.30 (1H, s, Ar-*H*); 7.05 (2H, s, 2Ar-*H*); 3.16 (4H, d, A_2X , $^2\text{J}_{\text{PH}} = 3.61$ Hz, $2\text{CH}_2\text{P}$); 1.16 (36H, d, A_{18}X , $^3\text{J}_{\text{PH}} = 10.88$ Hz, $4\text{P}(\text{C}(\text{CH}_3)_3)_2$).

$^{19}\text{F}\{^1\text{H}\}$ NMR (25 °C, 376.50 MHz, C_6D_6): 72.8 (s, F_3CCO).

$^{13}\text{C}\{^1\text{H}\}$ NMR (25 °C, 100.61 MHz, C_6D_6): 156.4 (q, AY_3 , $^2\text{J}_{\text{CF}} = 30.78$ Hz, Ar-CNHCOCF₃); 152.6 (br s, Ar-CNHCOCF₃); 143.8 (vd, AXX' , $\text{J}_{\text{PC}} = 12.83$ Hz, 2Ar-CCH₂P); 125.4 (s, Ar-CH); 120.83 (s, 2Ar-CH); 120.81 (q, AY_3 , $^1\text{J}_{\text{CF}} = 304.64$ Hz, Ar-CNHCOCF₃); 32.1 (d, A_2X , $\text{J}_{\text{PC}} = 22.46$ Hz, $2\text{P}(\text{C}(\text{CH}_3)_3)_2$); 30.1 (d, A_6X , $^2\text{J}_{\text{PC}} = 13.06$ Hz, $2\text{P}(\text{C}(\text{CH}_3)_3)_2$); 28.7 (vd, AXX' , $\text{J}_{\text{PC}} = 23.60$ Hz, 2Ar-CCH₂P).

5.3.1.9 5-Nitro-iso-phthalic acid dimethyl ester (50d)

The previously published synthetic procedure¹⁰⁶ was slightly modified. 106.0 g (502.3 mmol) of 5-nitro-iso-phthalic acid were suspended in a mixture of 120 mL methanol and 250 mL of toluene. The suspension was heated to reflux whereas a homogeneous solution is formed and 35 mL of concentrated sulphuric acid were added. Within a few minutes a bi-phasic mixture was obtained which was stirred for another 4.5 hours at the reflux temperature. The hot bi-phasic mixture was transferred into a separatory funnel and water phase was separated. The addition of 100 mL of hot water was accompanied by the formation of colourless precipitate. Therefore 100 mL of a hot NaHCO_3 solution (10%) were added and the resulting mixture was filtered. The separated colourless solid was washed with NaHCO_3 solution, water and toluene and dried at the oil-pump vacuum. Thereby 116.6 g (487.8 mmol, 97%) of pure 5-nitro-iso-phthalic acid dimethyl ester (**50d**) were obtained.

^1H NMR (25 °C, 400.13 MHz, CDCl_3): 9.00 (2H, m, 2Ar-H); 8.95 (1H, m, Ar-H); 4.01 (6H, s, CH_3).

$^{13}\text{C}\{^1\text{H}\}$ NMR (25 °C, 100.61 MHz, CDCl_3): 164.1 (Ar-CCO); 148.2 (Ar-CNO₂); 135.7 (Ar-CH); 132.4 (Ar-CCO); 128.1 (2Ar-CH); 53.0 (OCH_3).

5.3.1.10 5-Nitro-iso-phthalic acid di-chloride (55d)

50.0 g (237 mmol) of 5-nitro-iso-phthalic acid were suspended in 100 mL thionylchloride and heated to reflux for 24 h. The completeness of the reaction was verified by detecting the simultaneously formed hydrochloric acid with a universal indicator paper on top of the reflux condenser. The excessive thionylchloride was separated by distillation and could be recycled. After cooling down to room temperature a colourless solid is formed which could be recrystallised from petroleum ether yielding 58.3 g (236 mmol, 99 %) of 5-nitro-iso-phthalic di-chloride (**55c**).

^1H NMR (25 °C, 400.13 MHz, CDCl_3): 9.22 (2H, d, $^4J_{\text{HH}} = 1,65$ Hz, 2Ar-*H*); 9.12 (1H, t, $^4J_{\text{HH}} = 1.65$ Hz, Ar-*H*).

$^{13}\text{C}\{^1\text{H}\}$ NMR (25 °C, 100.61 MHz, CDCl_3): 165.5 (Ar-CCO); 148.9 (Ar-CNO₂); 137.2 (Ar-CH); 136.0 (Ar-CCO); 130.9 (2Ar-CH).

5.3.1.11 3,5-Di-(hydroxymethylen)nitrobenzene (51d)

920 mg (24.2 mmol; 3 eq.) sodium boron-hydride were degassed and dissolved in 20 mL of dry diglyme in a round bottom flask equipped with a massive magnetic stir bar and a dropping funnel. Then 2.007 g (8.13 mmol) of the di-chloride **55d** were degassed and dissolved in 10 mL diglyme and filled into the dropping funnel. Over a period of 1 h the NaBH_4 solution was added drop-wise into the vigorously stirred di-chloride solution while the temperature was kept below 10 °C. During the addition of the NaBH_4 solution the colour of the reaction mixture change to intensive red and a precipitate was formed. After the complete addition of the NaBH_4 solution the mixture was stirred for another 12 h at room temperature. The reaction was quenched by adding slowly about 40 mL of 1 M hydrochloric acid at temperatures below 10 °C. A homogeneous yellowish solution was obtained, which was transferred in a separatory funnel containing 100 mL of water. This mixture was extracted 6 times with 20 mL of ethyl acetate. Subsequently, the combined organic phases were washed with brine and water. The ethyl acetate was removed by rotary evaporation and the diglyme was removed at the oil-pump vacuum. 1.212 g (6.62 mmol, 81%) of the 3,5-di(hydroxymethylene)nitrobenzene **51d** were obtained as a yellow solid which was used without further purification.

^1H NMR (25 °C, 400.13 MHz, acetone- d_6): 8.11 (2H, m, 2Ar-*H*); 7.75 (1H, m, Ar-*H*); 4.77 (4H, s, CH_2OH); 4.63 (2H, br s, CH_2OH).

$^{13}\text{C}\{^1\text{H}\}$ NMR (25 °C, 100.61 MHz, CDCl_3): 149.4 (Ar-CNO₂); 145.7 (Ar-CCH₂OH); 131.1 (2Ar-CH); 120.1 (Ar-CH); 63.6 (Ar-CCH₂OH).

5.3.1.12 3,5-Di-(bromomethylen)nitrobenzene (52d)

700 mg (3.82 mmol) of the nitro diol **51d** and 2.662 g (8.124 mmol; 2.1 eq.) CBr_4 were degassed in single neck round bottom flask equipped with a septum and a magnetic stir bar and suspended in 12 mL dry DCM. In a separate flask 2.576 g (9.829 mmol; 2.57 eq.) Ph_3P were degassed and dissolved in 6 mL dry DCM. At temperatures below 5 °C the Ph_3P solution was

added portion-wise to the reaction suspension over a period of 20 min. After adding the Ph_3P solution the reaction mixture was stirred for about 6 h at room temperature. During the reaction time a white precipitate of Ph_3PO was formed. The completeness of the reaction could be monitored by thin layer chromatography on silica with ethyl acetate as eluent (r.f.(DiBr and Ph_3P) \approx 0.73, r.f.(DiOH) \approx 0.33 and r.f.(Ph_3PO) \approx 0.25) or with DCM as eluent (r.f.(DiBr) \approx 0.75, r.f.(Diol, Ph_3P and Ph_3PO) \approx 0.0). The reaction was quenched by the addition of silica and rotary evaporation at room temperature. The resulting yellow to orange, dry silica was put on a silica column of 4 cm high and a diameter of 4 cm and flushed with around 300 mL DCM. The organic solvent was removed from the filtrate by rotary evaporation and a pale yellow solid was obtained (831 mg, 2.708 mmol, 71%). The drying times with an applied vacuum should be kept short because of sublimation of the product. The di-bromide **52d** was used without further purification.

^1H NMR (25 °C, 400.13 MHz, CDCl_3): 8.17 (2H, m, 2Ar-H); 7.75 (1H, m, Ar-H); 4.52 (4H, s, CH_2Br).

$^{13}\text{C}\{^1\text{H}\}$ NMR (25 °C, 100.61 MHz, CDCl_3): 148.5 (Ar-CNO₂); 140.4 (Ar-CCH₂Br); 135.4 (2Ar-CH); 123.7 (Ar-CH); 30.8 (Ar-CCH₂Br).

5.3.1.13 3,5-Bis-(di-tert-butyl-phosphanomethylen)nitrobenzene (54d)

The same procedure was applied as for the **54e** (chapter 5.3.1.7) with quite comparable yields for the bis-phosphonium di-bromide (**53d**) and the final product (**54d**). However the yields for **53d** and **54d** in the literature³³ are with 93% and 97%, respectively, considerably better. The previously reported NMR data measured from CDCl_3 sample³³ are in rather good agreement with the data given in this work recorded in C_6D_6 .

$^{31}\text{P}\{^1\text{H}\}$ NMR (25 °C, 161.98 MHz, C_6D_6): 35.7 (s)

^1H NMR (25 °C, 400.13 MHz, C_6D_6): 8.13 (2H, s, 2Ar-H); 7.78 (2H, s, 2Ar-H); 2.60 (4H, d, A_2X , $^2\text{J}_{\text{PH}} = 2.55$ Hz, CH_2P); 0.99 (36H, d, A_{18}X , $^3\text{J}_{\text{PH}} = 10.76$ Hz, $\text{P}(\text{C}(\text{CH}_3)_3)_2$).

$^{13}\text{C}\{^1\text{H}\}$ NMR (25 °C, 100.61 MHz, C_6D_6): 148.8 (s, Ar-CNO₂); 144.3 (vd, AXX' , $\text{J}_{\text{PC}} = 13.85$ Hz, 2Ar-CCH₂P); 137.2 (t, AX_2 , $^3\text{J}_{\text{PC}} = 9.65$ Hz, Ar-CH); 121.9 (vdd, AXX' , $\text{J}_{\text{PC}} = 9.08$ Hz, $\text{J}_{\text{PC}} = 1.59$ Hz, 2Ar-CH); 31.9 (d, A_2X , $^1\text{J}_{\text{PC}} = 23.84$ Hz, $\text{P}(\text{C}(\text{CH}_3)_3)_2$); 29.8 (d, A_6X , $^2\text{J}_{\text{PC}} = 13.62$ Hz, $2\text{P}(\text{C}(\text{CH}_3)_3)_2$); 28.7 (vd, AXX' , $\text{J}_{\text{PC}} = 26.57$ Hz, 2Ar-CCH₂P).

5.3.1.14 2,7-Bis-(di-tert-butyl-phosphanomethylen)benzo[1,2-d]-1H-[7]annulene (82)

The synthetic procedure was previously described⁷⁷ therein as compound **6**.

$^{31}\text{P}\{^1\text{H}\}$ NMR (25 °C, 202.46 MHz, DCM- d_2): 16.1 (s)

^1H NMR (25 °C, 500.13 MHz, DCM- d_2): 7.15 (2H, m, 2[6]CHCHC[7]CH); 7.01 (2H, m, 2[6]CHCHC[7]CH); 6.45 (2H, br s, 2[6]CHCHC[7]CH); 2.81 (4H, d, A_2X , $^2J_{\text{PH}} = 4.30$ Hz, 2[7]CCH $_2$ P); 2.76 (2H, t, A_2X_2 , $^4J_{\text{PH}} = 1.30$ Hz, [7]CCH $_2$ C); 1.19 (36H, d, $A_{18}X$, $^3J_{\text{PH}} = 10.65$ Hz, 4P(C(CH $_3$) $_3$) $_2$).

$^{13}\text{C}\{^1\text{H}\}$ NMR (25 °C, 125.76 MHz, DCM- d_2): 143.5 (vdd, $A_{XX'}$, $J_{\text{PC}} = 11.54$ Hz, $J_{\text{PC}} = 0.88$ Hz, 2[7]CCH $_2$ P); 137.7 (vt, $A_{XX'}$, $N = |^4J_{\text{PC}} + ^5J_{\text{PC}}| = 2.39$ Hz, 2[6]CHCHC[7]CH); 130.1 (vd, $A_{XX'}$, $J_{\text{PC}} = 1.26$ Hz, 2[6]CHCHC[7]CH); 127.1 (vd, $A_{XX'}$, $J_{\text{PC}} = 7.95$ Hz, 2[6]CHCHC[7]CH); 125.7 (s, 2[6]CHCHC[7]CH); 36.2 (t, A_2X_2 , $^3J_{\text{PC}} = 9.43$ Hz, [7]CCH $_2$ C); 34.5 (vdd, $A_{XX'}$, $J_{\text{PC}} = 24.57$ Hz, $J_{\text{PC}} = 4.18$ Hz, 2[7]CCH $_2$ P); 32.6 (d, A_2X , $^1J_{\text{PC}} = 23.94$ Hz, 2P(C(CH $_3$) $_3$) $_2$); 30.5 (d, A_6X , $^2J_{\text{PC}} = 13.46$ Hz, 2P(C(CH $_3$) $_3$) $_2$).

5.3.2 Phenyl PCP complex syntheses

5.3.2.1 Reaction of AcNHPCP with $\text{IrCl}_3 \cdot \text{H}_2\text{O}$

139 mg (308 μmol) of ligand **54e** and 103 mg (308 μmol , 1eq.) of degassed $\text{IrCl}_3 \cdot \text{H}_2\text{O}$ were suspended in 2.4 mL of a mixture of 2-propanol water 7:1. The greenish suspension was stirred at different temperatures for different times and $^{31}\text{P}\{^1\text{H}\}$ NMR spectra (without deuterium lock) were recorded to monitor the reaction progress (see Figure 2 on page 27). No uniform product formation was observed.

5.3.2.2 Reaction of AcNHPCP with $[\text{Ir}(\text{COD})\text{Cl}]_2$

Approach with 0.5eq. $[\text{Ir}(\text{COD})\text{Cl}]_2$:

62 mg (132 μmol) of ligand **54e** and 46 mg (69 μmol , 0.5eq.) of degassed $[\text{Ir}(\text{COD})\text{Cl}]_2$ were suspended in 4 mL benzene. The resulting brownish suspension was stirred at different temperatures for different times and $^{31}\text{P}\{^1\text{H}\}$ NMR spectra (without deuterium lock) were recorded to monitor the reaction progress (see Figure 3 on page 28). No uniform product formation was observed.

Approach with eq. $[\text{Ir}(\text{COD})\text{Cl}]_2$:

68 mg (151 μmol) of ligand **54e** and 101 mg (151 μmol , 1eq.) of degassed $[\text{Ir}(\text{COD})\text{Cl}]_2$ were suspended in 4 mL toluene. The resulting red-brown suspension was stirred at different temperatures for different times and $^{31}\text{P}\{^1\text{H}\}$ NMR spectra (without deuterium lock) were recorded to monitor the reaction progress (see Figures 4 on page 29). No uniform product formation was observed.

5.3.2.3 Reaction of *AcNHPCP* with $[\text{Ir}(\text{COE})_2\text{Cl}]_2$

50 mg (111 μmol) of ligand **54e** and 49.6 mg (55.3 μmol , 1eq.) of degassed $[\text{Ir}(\text{COE})_2\text{Cl}]_2$ were suspended in 1 mL of toluene. This suspension was stirred for 17 h at room temperature and was subsequently heated to reflux for 3 d. The reaction progress was monitored using $^{31}\text{P}\{^1\text{H}\}$ NMR spectra (see Figure 5 on page 30). During the heating time a red precipitate was formed which was separated by filtration, dissolved in DCM-d_2 and characterised.

$^{31}\text{P}\{^1\text{H}\}$ NMR (25 $^\circ\text{C}$, 161.98 MHz, acetone- d_6): 55.9 (d, $J_{\text{PP}} = 20.00$ Hz); 57.6 (d, $J_{\text{PP}} = 20.00$ Hz).

^1H NMR (25 $^\circ\text{C}$, 400.13 MHz, DCM-d_2): -25.72 (d, $2J_{\text{PH}} = 22.05$ Hz, IrH); -27.07 (d, $2J_{\text{PH}} = 23.65$ Hz, IrH).

5.3.2.4 Reaction of *^FAcNHPCP* with $[\text{Ir}(\text{COD})\text{Cl}]_2$

50 mg (99.9 μmol) of ligand **54e** and 34 mg (50.6 μmol , 0.5eq.) of degassed $[\text{Ir}(\text{COD})\text{Cl}]_2$ were suspended in 0.4 mL of benzene- d_6 in a J Young NMR tube. The resulting suspension was kept at different temperatures for different times and the NMR tube was shaken vigorously from time to time. The reaction progress was monitored using $^{31}\text{P}\{^1\text{H}\}$ NMR and ^1H NMR (see Figures 4 on page 29). No uniform product formation was observed.

5.3.3 Benzo-cycloheptatriene PCP complex syntheses

5.3.3.1 *BCHTPCPIrHCICO* (**59**, **83**, **84**)

General Procedure:

101 mg (220 μmol) of the ligand **82** were mixed in solid state with 70.4 mg (226 μmol , 1 eq.) with degassed $\text{Ir}(\text{CO})_3\text{Cl}$. The reaction was started by the addition of 2 mL of THF. The resulting yellow to brown suspension was vigorously stirred at temperatures between 40 $^\circ\text{C}$ and 45 $^\circ\text{C}$ without pressure equilibration. At temperatures higher than 50 $^\circ\text{C}$ the products of iso-

merisation process were also formed as side products. The overall reaction times vary significantly between 14 h and 30 h which is the reason for the monitoring of the reaction *via* $^{31}\text{P}\{^1\text{H}\}$ NMR. If there was no further reaction progress observable, another up to 0.25 eq of degassed $\text{Ir}(\text{CO})_3\text{Cl}$ were added. After there are more than 90% (based on the integration of the $^{31}\text{P}\{^1\text{H}\}$ data) of **59** formed the solid components of the suspension were separated by centrifugation. The dark solid was washed three times with 2 mL of THF and from the combined yellow solution containing the product the solvent was removed at oil-pump vacuum. A pure yellow solid was obtained in nearly quantitative yields containing mainly **59** and occasionally **83** and **84**. If the colour of the reaction solution turned to orange most probably also isomerisation took place. The purification of these product mixtures is rather difficult and is therefore accompanied by heavy losses of **59**.

IR: $\tilde{\nu}(\text{C}=\text{O}) = 2000 \text{ cm}^{-1}$ and $\tilde{\nu}(\text{Ir}-\text{H}) = 2280 \text{ cm}^{-1}$ in KBr; $\tilde{\nu}(\text{C}=\text{O}) = 2009 \text{ cm}^{-1}$ and $\tilde{\nu}(\text{Ir}-\text{H}) = 2258 \text{ cm}^{-1}$ in tetrachloromethane.

HR-MS: exp. 707.28862 $[\text{M}-\text{Cl}+\text{N}_2]^+$; calc. 707.28656 for $^{12}\text{C}_{30} \text{ } ^1\text{H}_{48} \text{ } ^{193}\text{Ir} \text{ } ^{14}\text{N}_2 \text{ } ^{16}\text{O} \text{ } ^{31}\text{P}_2$ (see chapter 3.5.3.1.3 on page 94).

Elemental analysis: exp. C 50.43%, H 7.05%; calc. C 50.44%, H 6.77% for $\text{C}_{30}\text{H}_{48}\text{IrOP}_2\text{Cl}$.

Isomer **59**:

$^{31}\text{P}\{^1\text{H}\}$ NMR (25 °C, 161.98 MHz, DCM- d_2): 49.0 (s)

^1H NMR (25 °C, 400.13 MHz, DCM- d_2): 7.12 (2H, m, 2[6]CHCHC[7]CH); 7.12 (2H, m, 2[6]CHCHC[7]CH); 6.68 (2H, m, 2[6]CHCHC[7]CH); 3.68 (1H, m, [7]CH($\cdot\cdot$ IrCl)Ir); 3.52 (2H, m, 2[7]CCH($\cdot\cdot$ IrCl)HP); 3.06 (2H, m, 2[7]CCHH($\cdot\cdot$ IrH)P); 1.47 (18H, vt, $[\text{A}_9\text{X}]_2$, $N = |^3J_{\text{PH}} + ^5J_{\text{PH}}| = 14.08 \text{ Hz}$, 2PC(CH $_3$) $_3$ $\cdot\cdot$ IrCl); 1.36 (18H, vt, $[\text{A}_9\text{X}]_2$, $N = |^3J_{\text{PH}} + ^5J_{\text{PH}}| = 13.16 \text{ Hz}$, 2PC(CH $_3$) $_3$ $\cdot\cdot$ IrH); -18.85 (1H, t, AX $_2$, $^2J_{\text{PH}} = 14.29 \text{ Hz}$, IrH).

$^{13}\text{C}\{^1\text{H}\}$ NMR (25 °C, 100.61 MHz, DCM- d_2): 177.7 (t, AX $_2$, $^2J_{\text{PC}} = 7.10 \text{ Hz}$, IrCO); 154.5 (AXX', $N = |^2J_{\text{PC}} + ^4J_{\text{PC}}| = 13.62 \text{ Hz}$, 2[7]CCH $_2$ P); 137.6 (s, 2[6]CHCHC[7]CH); 129.9 (s, 2[6]CHCHC[7]CH); 125.7 (s, 2[6]CHCHC[7]CH); 122.7 (AXX', $N = |^3J_{\text{PC}} + ^5J_{\text{PC}}| = 14.99 \text{ Hz}$, 2[6]CHCHC[7]CH); 45.7 (AXX', $N = |^1J_{\text{PC}} + ^3J_{\text{PC}}| = 32.92 \text{ Hz}$, 2[7]CCH $_2$ P); 42.8 (t, AX $_2$, $^2J_{\text{PC}} = 2.72 \text{ Hz}$, [7]CHIr); 39.1 (AXX', $N = |^1J_{\text{PC}} + ^3J_{\text{PC}}| = 16.57 \text{ Hz}$, 2PC(CH $_3$) $_3$ $\cdot\cdot$ IrCl); 36.0 (AXX', $N = |^1J_{\text{PC}} + ^3J_{\text{PC}}| = 26.56 \text{ Hz}$, 2PC(CH $_3$) $_3$ $\cdot\cdot$ IrH); 31.2 (AXX', $N = |^2J_{\text{PC}} + ^4J_{\text{PC}}| = 3.79 \text{ Hz}$, 2PC(CH $_3$) $_3$ $\cdot\cdot$ IrH); 29.5 (AXX', $N = |^2J_{\text{PC}} + ^4J_{\text{PC}}| = 4.20 \text{ Hz}$, 2PC(CH $_3$) $_3$ $\cdot\cdot$ IrCl).

Isomer 83:

$^{31}\text{P}\{^1\text{H}\}$ NMR (25 °C, 161.98 MHz, DCM- d_2): 46.0 (s)

^1H NMR (25 °C, 400.13 MHz, DCM- d_2): 6.85 (3H, m, 2[6]CHCHC[7]CH); 6.63 (2H, m, 2[6]CHCHC[7]CH); 5.49 (2H, m, 2[6]CHCHC[7]CH); 3.81 (1H, m, [7]CH($\cdot\cdot$ IrCl)Ir); 2.79 (2H, m, 2[7]CCH($\cdot\cdot$ IrCl)HP); 2.79 (2H, [ABX] $_2$, $^2J_{\text{HH}} = 14.52$ Hz, $N = |^2J_{\text{PH}} + ^4J_{\text{PH}}| = 6.56$ Hz, 2[7]CCHH($\cdot\cdot$ IrCl)P); 2.15 (2H, [ABX] $_2$, m, 2[7]CCHH($\cdot\cdot$ IrH)P); 1.54 (18H, vt, [A $_9$ X] $_2$, $N = |^3J_{\text{PH}} + ^5J_{\text{PH}}| = 14.16$ Hz, 2PC(CH $_3$) $_3$ $\cdot\cdot$ IrCl); 1.32 (18H, vt, [A $_9$ X] $_2$, $N = |^3J_{\text{PH}} + ^5J_{\text{PH}}| = 13.24$ Hz, 2PC(CH $_3$) $_3$ $\cdot\cdot$ IrH); -17.77 (1H, t, AX $_2$, $^2J_{\text{PH}} = 12.76$ Hz, IrH).

$^{13}\text{C}\{^1\text{H}\}$ NMR (25 °C, 100.61 MHz, DCM- d_2): 146.3 (AXX', $N = |^2J_{\text{PC}} + ^4J_{\text{PC}}| = 7.15$ Hz, 2[7]CCH $_2$ P); 136.2 (s, 2[6]CHCHC[7]CH); 131.2 (s, 2[6]CHCHC[7]CH); 126.9 (s, 2[6]CHCHC[7]CH); 126.3 (AXX', $N = |^3J_{\text{PC}} + ^5J_{\text{PC}}| = 14.65$ Hz, 2[6]CHCHC[7]CH); 39.7 (AXX', $N = |^1J_{\text{PC}} + ^3J_{\text{PC}}| = 17.26$ Hz, 2PC(CH $_3$) $_3$ $\cdot\cdot$ IrCl); 37.8 (s, [7]CHIr); 37.1 (AXX', $N = |^1J_{\text{PC}} + ^3J_{\text{PC}}| = 24.29$ Hz, 2[7]CCH $_2$ P); 36.4 (AXX', $N = |^1J_{\text{PC}} + ^3J_{\text{PC}}| = 24.52$ Hz, 2PC(CH $_3$) $_3$ $\cdot\cdot$ IrH); 31.3 (AXX', $N = |^2J_{\text{PC}} + ^4J_{\text{PC}}| = 3.97$ Hz, 2PC(CH $_3$) $_3$ $\cdot\cdot$ IrCl); 30.1 (AXX', $N = |^2J_{\text{PC}} + ^4J_{\text{PC}}| = 5.22$ Hz, 2PC(CH $_3$) $_3$ $\cdot\cdot$ IrH); carbonyl unobserved.

Isomer 84:

$^{31}\text{P}\{^1\text{H}\}$ NMR (25 °C, 161.98 MHz, acetone- d_6): 61.5 (s)

^1H NMR (25 °C, 400.13 MHz, DCM- d_2): -10.09 (1H, t, AX $_2$, $^2J_{\text{PH}} = 14.54$ Hz, IrH).

Since **84** is characterised from a complex mixture the ^1H -NMR and $^{13}\text{C}\{^1\text{H}\}$ NMR spectra display overlaid signals and are not reported in detail.

5.3.3.2 BHTPCPIrHCICO BF $_4$ (95')

General Procedure:

8.58 mg (12.0 μmol) of **59** in a J. Young NMR-Tube were dissolved in 0.2 mL of DCM- d_2 . A solution of 4.23 mg (12.8 μmol , 1eq.) of degassed Ph $_3$ CBF $_4$ in 0.2 mL of DCM- d_2 was prepared separately. The Ph $_3$ CBF $_4$ solution was added speedily to the solution in the J. Young tube, thereby the colour of the reaction mixture turns instantly from yellow to red-orange. The $^{31}\text{P}\{^1\text{H}\}$ spectrum reveals the nearly quantitative formation of the cationic complex **95'**. The red crystalline product could be obtained by adding *n*-pentane to the red DCM solution.

$^{31}\text{P}\{^1\text{H}\}$ NMR (25 °C, 161.98 MHz, DCM- d_2): 59.6 (s)

$^{19}\text{F}\{^1\text{H}\}$ NMR (25 °C, 376.50 MHz, DCM- d_2): -150.6 (s, BF_4^-).

$^{11}\text{B}\{^1\text{H}\}$ NMR (25 °C, 80.25 MHz, DCM- d_2): 0.8 (s, BF_4^-).

^1H NMR (25 °C, 400.13 MHz, DCM- d_2): 9.25 (2H, s, 2[6]CHCHC[7]CH); 8.44 (2H, m, 2[6]CHCHC[7]CH); 8.18 (2H, m, 2[6]CHCHC[7]CH); 4.89 (2H, [ABX] $_2$, $^2J_{\text{HH}} = 16.73$ Hz, $N = |^2J_{\text{PH}} + ^4J_{\text{PH}}| = 7.68$ Hz, 2[7]CCHH($\cdot\cdot\text{IrCl}$)P); 4.32 (2H, [ABX] $_2$, $^2J_{\text{HH}} = 16.73$ Hz, $N = |^2J_{\text{PH}} + ^4J_{\text{PH}}| = 8.03$ Hz, 2[7]CCHH($\cdot\cdot\text{IrH}$)P); 1.51 (18H, vt, [A $_9$ X] $_2$, $N = |^3J_{\text{PH}} + ^5J_{\text{PH}}| = 14.78$ Hz, 2PC(CH $_3$) $_3\cdot\cdot\text{IrCl}$); 1.32 (18H, vt, [A $_9$ X] $_2$, $N = |^3J_{\text{PH}} + ^5J_{\text{PH}}| = 14.15$ Hz, 2PC(CH $_3$) $_3\cdot\cdot\text{IrH}$); -16.91 (1H, t, AX $_2$, $^2J_{\text{PH}} = 12.53$ Hz, IrH).

$^{13}\text{C}\{^1\text{H}\}$ NMR (25 °C, 100.61 MHz, DCM- d_2): 228.2 (t, AX $_2$, $^2J_{\text{PC}} = 2.56$ Hz, [7]C ^+Ir); 176.3 (t, AX $_2$, $^2J_{\text{PC}} = 7.21$ Hz, IrCO); 165.6 (AXX', $N = |^2J_{\text{PC}} + ^4J_{\text{PC}}| = 13.62$ Hz, 2[7]CCH $_2$ P); 146.2 (AXX', $N = |^2J_{\text{PC}} + ^4J_{\text{PC}}| = 13.74$ Hz, 2[6]CHCHC[7]CH); 141.1 (s, 2[6]CHCHC[7]CH); 136.7 (s, 2[6]CHCHC[7]CH); 136.2 (s, 2[6]CHCHC[7]CH); 46.1 (AXX', $N = |^1J_{\text{PC}} + ^3J_{\text{PC}}| = 27.48$ Hz, 2[7]CCH $_2$ P); 39.6 (AXX', $N = |^1J_{\text{PC}} + ^3J_{\text{PC}}| = 21.23$ Hz, 2C(CH $_3$) $_3\cdot\cdot\text{IrCl}$); 37.6 (AXX', $N = |^1J_{\text{PC}} + ^3J_{\text{PC}}| = 26.79$ Hz, 2PC(CH $_3$) $_3\cdot\cdot\text{IrH}$); 30.2 (s, 4PC(CH $_3$) $_3$).

5.3.3.3 Reaction of BHTPCPIrHClCO with Me $_3$ SiTf / HTf

53 mg (74 μmol) **59**, dissolved in 3 mL THF was quickly mixed with 15 μl (82 μmol , 1 eq.) Me $_3$ SiTf. Thereby the colour turned instantly from yellow to dark orange.

5.3.3.4 Reaction of BHTPCPIrHClCO BF $_4$ (95') with O $_2$

In a J. Young NMR tube a solution of **95'** in DCM- d_2 was prepared as described in chapter 5.3.3.2 and used without separating the simultaneously formed triphenylmethane. This solution was degassed by three pump-freeze-thaw cycles and consecutively the solution is saturated with oxygen. Over a period of 2.5 months this sample was stored at room temperature, in the presence of daylight and was vigorously shaken from time to time.

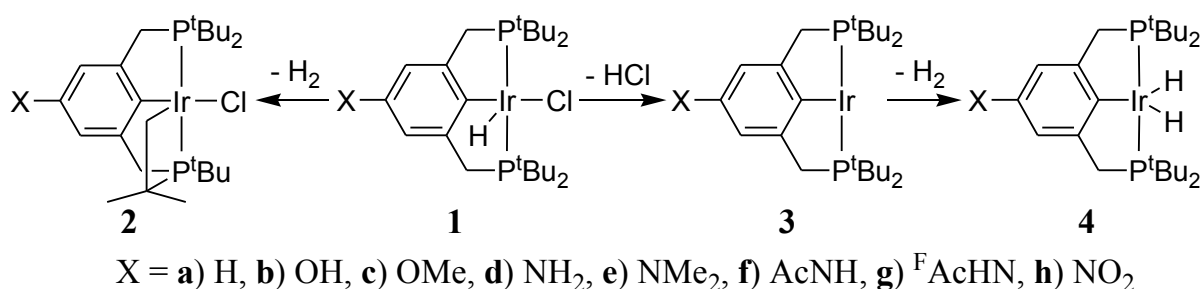
$^{31}\text{P}\{^1\text{H}\}$ NMR (25 °C, 202.46 MHz, DCM- d): 76.9 (s)

^1H NMR (25 °C, 500.13 MHz, DCM- d_2): 8.59 (2H, m, 2[6]CHCHC[7]CH); 8.16 (2H, m, 2[6]CHCHC[7]CH); 7.98 (2H, s, 2[6]CHCHC[7]CH); 3.68 (2H, [ABX] $_2$, $^2J_{\text{HH}} = 14.23$ Hz, $N = |^2J_{\text{PH}} + ^4J_{\text{PH}}| = 9.50$ Hz, 2[7]CCHHP); 3.55 (2H, [ABX] $_2$, $^2J_{\text{HH}} = 14.23$ Hz, $N = |$

${}^2J_{\text{PH}}+{}^4J_{\text{PH}} = 6.58 \text{ Hz}$, 2[7]CCHHP); 1.57 (18H, vt, $[\text{A}_9\text{X}]_2$, $N = |{}^3J_{\text{PH}}+{}^5J_{\text{PH}}| = 14.44 \text{ Hz}$,
2PC(CH_3)₃); 1.32 (18H, vt, $[\text{A}_9\text{X}]_2$, $N = |{}^3J_{\text{PH}}+{}^5J_{\text{PH}}| = 14.44 \text{ Hz}$, 2PC(CH_3)₃).

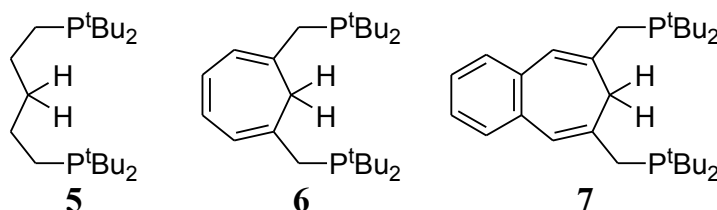
6 Summary

Since the first introduction of phenyl PCP pincer complexes in 1976 the diversity of pincer-type compounds has increased drastically. In these complexes the metal centre is *mer*-coordinated by the tridentated ligand with the mutual *trans*-orientation of the donor atoms **1**. Especially, in the phenyl PCP pincer complexes the structure is significantly enforced by the formation of the sp^2 -carbon metal bond resulting in extraordinary high thermal stabilities. The accessibility of the metal centre is dominated by the steric demand of the substituents at the donor atoms while also the electronic properties of the donor atoms are influenced by these groups. Considering the resonance structures of the pincer complexes **1** with +M or -M substituents in *para*-position to the metal, it is expected that the substituent X affects the electronic properties of coordinating (*ipso*) carbon atom.



Scheme 1

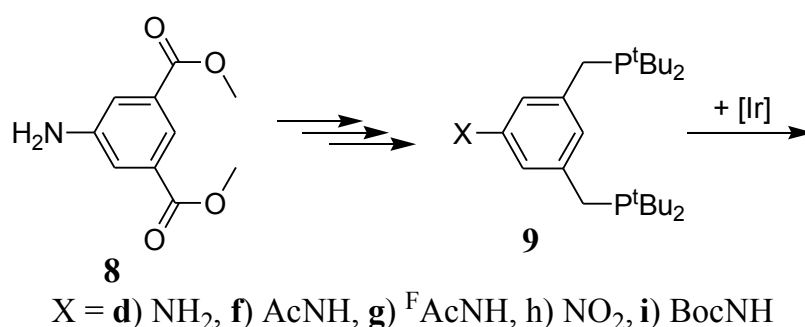
The iridium PCP pincer complexes **1** or **4** are suitable precursors for the catalytic dehydrogenation of alkanes. Experimental as well as theoretical mechanistic investigations of this reaction propose the formation of the 14e⁻ Ir(I) species **3** as catalytically active intermediate. The iridium pincer complexes **2c** is one rare example of an intra-molecular activation of a sp^3 -C-H bond of one of the *tert*-butyl groups of the phosphane.



Scheme 2

One aim of the present work is therefore the elucidation of the influence of the backbone substituent X onto the reaction depicted in Scheme 1. For this purpose the energies of formation for the respective reaction, the optimised geometries of the complexes and the molecular orbitals of the ligands obtained from DFT calculations were correlated with the electronic properties of the backbone substituent X. The different data show clearly a significant dependence of the π -acceptor capabilities of the metal coordinated *ipso*-carbon atom from the -M character of the backbone substituent X. Additionally, the principal impact of the backbone is discussed using the theoretically predicted complexes with the aliphatic ligand backbone **5**, the cycloheptatriene backbone **6** and benzo-cycloheptatriene backbone **7** (Scheme 2). Furthermore, the cationic complexes derived from **5**, **6** and **7** obtained by abstraction of a hydride from the *ipso*-C-H group and the respective anionic complexes achieved by the deprotonation of the *ipso*-C-H group are investigated. Thereby, the uncharged ligands **5**, **6** and **7** leave a high electron density at the metal centre due to lacking π -acceptor orbitals at the *ipso*-carbon. Contrariwise the cationic backbones present strong π -acceptor and reduced σ -donating capabilities while the anionic backbones are strong σ - and π -donating ligands.

Synthetically, the successful introduction of the protected amino functionalised PCP pincer ligands **9f** and **9g** (Scheme 3) is described in this work. Starting from the 3-amino-*iso*-phthalic acid **8** the acetamide functionalised ligand **9f** and the trifluoroacetamide ligand **9g** are obtained in multi step reaction sequences in quite good overall yields. The final de-protection of **9** yielding the amino functionalised ligand **9d** failed, due to the decomposition of the phosphane moieties in basic media. For this reason, the *tert*-butoxycarbonyl (Boc) protecting group was introduced which is cleavable in acidic media.

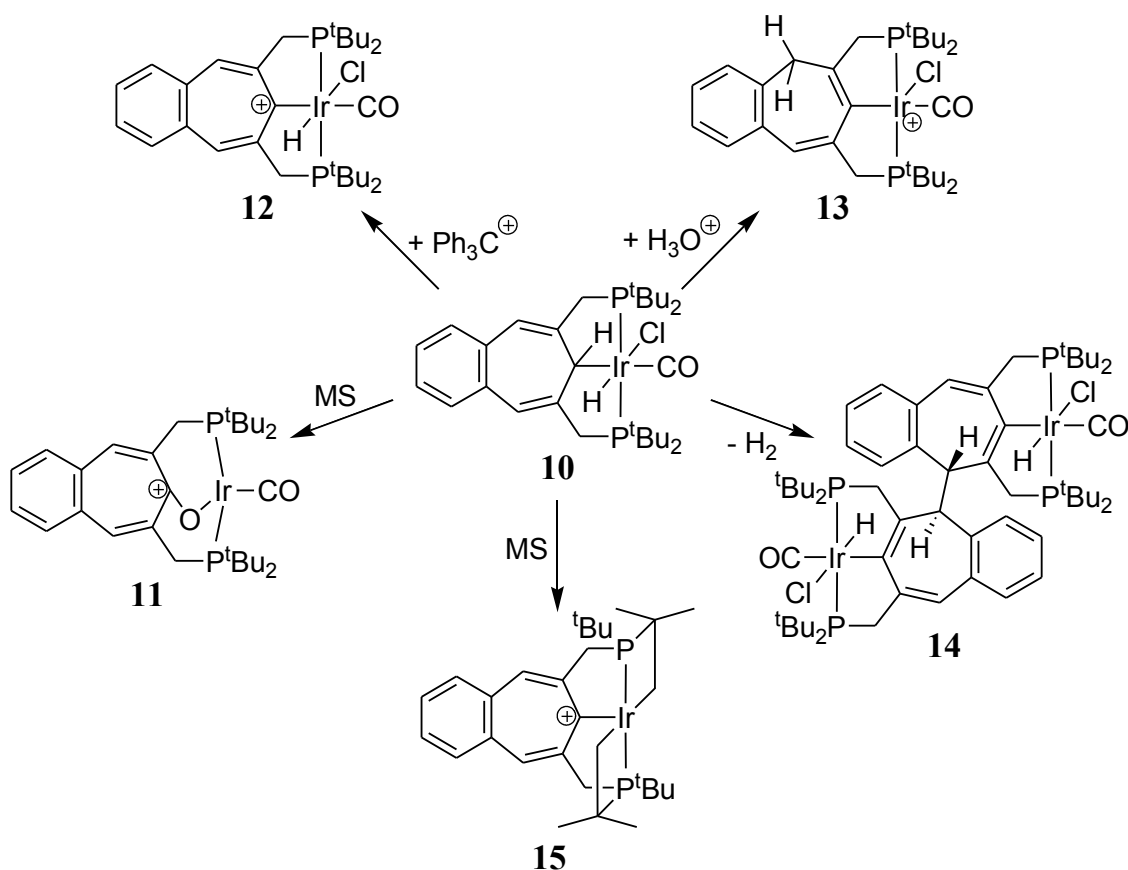


Scheme 3

In order to synthesise the hydrido chloro iridium PCP pincer complexes **1f** and **1g**, the isolated ligands **9f** and **9g** were treated with several iridium precursor compounds. However the result-

ing product mixtures which were obtained are indicative for a significantly different coordination behaviour of these ligands as compared to the unmodified and the methoxy functionalised PCP ligands **9a** and **9c**, respectively.

Finally the chemistry of the novel benzo-cycloheptatriene PCP pincer ligand **7** and its iridium complexes is elucidated and discussed in the present work. Thereby, the synthesis of the hydrido chloro carbonyl iridium complex **10** is achieved quite comparable to the corresponding complexes with cycloheptatriene backbone. The more detailed exploration of the chemical properties displays the feasibility of rearrangement reactions in **10** and also the abstraction of the hydride from the *ipso*-C-H group forming **12** is realised for the benzo-cycloheptatriene complex **10**. This behaviour is well known from the cycloheptatriene counterparts. However, some remarkable and unexpected novel complex structures like the Ir(III) complexes **13** and **14** could be characterised by single crystal X-ray diffraction.



Scheme 4

Moreover the mass spectrometric characterisation of complex **10** displays the formation of the oxo complex **11** besides an abundance of fragmentation products like **15**. The more extensive

elucidation of the observed products required the development of a setup appropriate to handle and apply the sample solutions in oxygen and water-free conditions. These improvements, the application of different ion sources and MSⁿ techniques as well as the optimisation of the proposed structures using modern DFT calculations allowed a consistent explanation of all signals observed in the mass spectra. In order to obtain the cationic oxo complex **11** synthetically, the cationic hydrido chloro complex **12** is treated in dry DCM in an atmosphere of pure oxygen. Actually, the observed product is not the oxo complex **11** but rather a hydro-peroxide intermediate which might form **11** if water is present in the solvent.

7 References

- (1) Shaw, B. L. *J. Am. Chem. Soc.* **1975**, *97*, 3856-3857.
- (2) Shaw, B. L. *J. Organomet. Chem.* **1980**, *200*, 307-318.
- (3) Albrecht, M.; van Koten, G. *Angew. Chem., Int. Ed.* **2001**, *40*, 3750-3781.
- (4) *The Chemistry of Pincer Compounds*; Morales-Morales, D.; Jensen, C. M., Hrsg.; Elsevier, 2007.
- (5) van der Boom, M. E.; Milstein, D. *Chem. Rev.* **2003**, *103*, 1759-1792.
- (6) Ohff, M.; Ohff, A.; van der Boom, M. E.; Milstein, D. *J. Am. Chem. Soc.* **1997**, *119*, 11687-11688.
- (7) Haenel, M. W.; Oevers, S.; Angermund, K.; Kaska, W. C.; Fan, H.; Hall, M. B. *Angew. Chem., Int. Ed.* **2001**, *40*, 3596-3600.
- (8) Krogh-Jespersen, K.; Czerw, M.; Kanzelberger, M.; Goldman, A. *J. Chem. Inf. Model.* **2001**, *41*, 56-63.
- (9) Moulton, C. J.; Shaw, B. L. *J. Chem. Soc., Dalton Trans.* **1976**, 1020-4.
- (10) Eller, P. G.; Bradley, D. C.; Hursthouse, M. B.; Meek, D. W. *Coord. Chem. Rev.* **1977**, *24*, 1-95.
- (11) Jensen, C. M. *Chem. Commun.* **1999**, 2443-2449.
- (12) Creaser, C. S.; Kaska, W. C. *Inorg. Chim. Acta* **1978**, *30*, L325-L326.
- (13) van Koten, G. *Pure Appl. Chem.* **1989**, *61*, 1681-1694.
- (14) Gozin, M.; Weisman, A.; Ben-David, Y.; Milstein, D. *Nature* **1993**, *364*, 699-701.
- (15) Knapen, J. W. J.; van der Made, A. W.; de Wilde, J. C.; van Leeuwen, P. W. N. M.; Wijkens, P.; Grove, D. M.; van Koten, G. *Nature* **1994**, *372*, 659-663.
- (16) Miyazaki, F.; Yamaguchi, K.; Shibasaki, M. *Tetrahedron Lett.* **1999**, *40*, 7379-7383.
- (17) Bedford, R. B.; Draper, S. M.; Noelle Scully, P.; Welch, S. L. *New J. Chem.* **2000**, *24*, 745-747.

- (18) Olsson, D.; Nilsson, P.; El Masnaouy, M.; Wendt, O. F. *Dalton Trans.* **2005**, 1924-1929.
- (19) Motoyama, Y.; Koga, Y.; Nishiyama, H. *Tetrahedron* **2001**, *57*, 853-860.
- (20) Motoyama, Y.; Koga, Y.; Kobayashi, K.; Aoki, K.; Nishiyama, H. *Chem.--Eur. J.* **2002**, *8*, 2968-2975.
- (21) Takenaka, K.; Uozumi, Y. *Org. Lett.* **2004**, *6*, 1833-1835.
- (22) Nishiyama, H.; Shiomi, T.; Tsuchiya, Y.; Matsuda, I. *J. Am. Chem. Soc.* **2005**, *127*, 6972-6973.
- (23) Gupta, M.; Hagen, C.; Flesher, R. J.; Kaska, W. C.; Jensen, C. M. *Chem. Commun.* **1996**, 2083-2084.
- (24) Zhao, J.; Goldman, A. S.; Hartwig, J. F. *Science* **2005**, *307*, 1080-1082.
- (25) Vigalok, A.; Milstein, D. *Acc. Chem. Res.* **2001**, *34*, 798-807.
- (26) Liang, L. *Coord. Chem. Rev.* **2006**, *250*, 1152-1177.
- (27) Gunnoe, T. B. *Eur. J. Inorg. Chem.* **2007**, *2007*, 1185-1203.
- (28) Nemeh, S.; Flesher, R. J.; Gierling, K.; Maichle-Moessmer, C.; Mayer, H. A.; Kaska, W. C. *Organometallics* **1998**, *17*, 2003-2008.
- (29) Winter, A. M.; Eichele, K.; Mack, H.; Kaska, W. C.; Mayer, H. A. *Organometallics* **2005**, *24*, 1837-1844.
- (30) Winter, A. M.; Eichele, K.; Mack, H.; Kaska, W. C.; Mayer, H. A. *Dalton Trans.* **2008**, 527-532.
- (31) Ashkenazi, N.; Vigalok, A.; Parthiban, S.; Ben-David, Y.; Shimon, L. J. W.; Martin, J. M. L.; Milstein, D. *J. Am. Chem. Soc.* **2000**, *122*, 8797-8798.
- (32) Mohammad, H. A. Y.; Grimm, J. C.; Eichele, K.; Mack, H.; Speiser, B.; Novak, F.; Quintanilla, M. G.; Kaska, W. C.; Mayer, H. A. *Organometallics* **2002**, *21*, 5775-5784.
- (33) Grimm, J. C. Funktionalisierte Iridium-PCP-Pincerkomplexe für den Einbau in Interphasen, Eberhard-Karls-Universität Tübingen, 2001.
- (34) Riehl, J. F.; Jean, Y.; Eisenstein, O.; Pelissier, M. *Organometallics* **1992**, *11*, 729-737.

-
- (35) Krogh-Jespersen, K.; Czerw, M.; Zhu, K.; Singh, B.; Kanzelberger, M.; Darji, N.; Achord, P. D.; Renkema, K. B.; Goldman, A. S. *J. Am. Chem. Soc.* **2002**, *124*, 10797-10809.
- (36) Novak, F.; Speiser, B.; Mohammad, H. A. Y.; Mayer, H. A. *Electrochim. Acta* **2004**, *49*, 3841-3853.
- (37) Diversi, P.; Iaconi, S.; Ingrosso, G.; Laschi, F.; Lucherini, A.; Zanello, P. *J. Chem. Soc., Dalton Trans.* **1993**, 351-352.
- (38) Diversi, P.; Iaconi, S.; Ingrosso, G.; Laschi, F.; Lucherini, A.; Pinzino, C.; Uccello-Barretta, G.; Zanello, P. *Organometallics* **1995**, *14*, 3275-3287.
- (39) Ceccanti, A.; Diversi, P.; Ingrosso, G.; Laschi, F.; Lucherini, A.; Magagna, S.; Zanello, P. *J. Organomet. Chem.* **1996**, *526*, 251-262.
- (40) Nemeh, S.; Jensen, C.; Binamira-Soriaga, E.; Kaska, W. C. *Organometallics* **1983**, *2*, 1442-7.
- (41) Conner, D.; Jayaprakash, K. N.; Cundari, T. R.; Gunnoe, T. B. *Organometallics* **2004**, *23*, 2724-2733.
- (42) Tsvetkov, N. P.; Laird, M. F.; Fan, H.; Pink, M.; Caulton, K. G. *Chem. Commun.* **2009**, 4578-4580.
- (43) Crocker, C.; Empsall, H. D.; Errington, R. J.; Hyde, E. M.; McDonald, W. S.; Markham, R.; Norton, M. C.; Shaw, B. L.; Weeks, B. *J. Chem. Soc., Dalton Trans.* **1982**, 1217-24.
- (44) Flesher, R. J. The synthesis of organometallic carbenes and their reactions, University of California, Santa Barbara, 1999.
- (45) Vigalok, A.; Ben-David, Y.; Milstein, D. *Organometallics* **1996**, *15*, 1839-44.
- (46) Vigalok, A.; Milstein, D. *Organometallics* **2000**, *19*, 2061-2064.
- (47) Gusev, D. G.; Lough, A. J. *Organometallics* **2002**, *21*, 2601-2603.
- (48) Gusev, D. G.; Lough, A. J. *Organometallics* **2002**, *21*, 5091-5099.
- (49) Kuznetsov, V. F.; Abdur-Rashid, K.; Lough, A. J.; Gusev, D. G. *J. Am. Chem. Soc.* **2006**, *128*, 14388-14396.
-

- (50) Weng, W.; Parkin, S.; Ozerov, O. *Organometallics* **2006**, *25*, 5345-5354.
- (51) Kanzelberger, M.; Zhang, X.; Emge, T. J.; Goldman, A. S.; Zhao, J.; Incarvito, C.; Hartwig, J. F. *J. Am. Chem. Soc.* **2003**, *125*, 13644-13645.
- (52) McLoughlin, M. A.; Keder, N. L.; Harrison, W. T. A.; Flesher, R. J.; Mayer, H. A.; Kaska, W. C. *Inorg. Chem.* **1999**, *38*, 3223-3227.
- (53) McLoughlin, M. A.; Flesher, R. J.; Kaska, W. C.; Mayer, H. A. *Organometallics* **1994**, *13*, 3816-22.
- (54) Kaska, W. C.; Nemeh, S.; Shirazi, A.; Potuznik, S. *Organometallics* **1988**, *7*, 13-15.
- (55) Huang, K.; Han, J. H.; Musgrave, C. B.; Fujita, E. *Organometallics* **2007**, *26*, 508-513.
- (56) Green, M. L. H.; Ng, D. K. P. *Chem. Rev.* **1995**, *95*, 439-473.
- (57) Johnson, R. P. *Chem. Rev.* **1989**, *89*, 1111-1124.
- (58) Matzinger, S.; Bally, T.; Patterson, E. V.; McMahon, R. J. *J. Am. Chem. Soc.* **1996**, *118*, 1535-1542.
- (59) Tamm, M.; Hartl, H. *Chem. Commun.* **1997**, 2227-2228.
- (60) Tamm, M.; Grzegorzewski, A.; Brudgam, I.; Hartl, H. *J. Chem. Soc., Dalton Trans.* **1998**, 3523-3528.
- (61) Gridnev, I. D.; del Rosario, M. K. C. *Organometallics* **2005**, *24*, 4519-4527.
- (62) Allison, N. T.; Kawada, Y.; Jones, W. M. *J. Am. Chem. Soc.* **1978**, *100*, 5224-5226.
- (63) Lu, Z.; Jones, W. M.; Winchester, W. R. *Organometallics* **1993**, *12*, 1344-1350.
- (64) Winter, A. M. Iridium-Cycloheptatrien-Pincer - Ihr ungewöhnliches Verhalten gegenüber Basen, Eberhard-Karls-Universität Tübingen, 2001.
- (65) DuBois, D. L.; Blake, D. M.; Miedaner, A.; Curtis, C. J.; DuBois, M. R.; Franz, J. A.; Linehan, J. C. *Organometallics* **2006**, *25*, 4414-4419.
- (66) Winter, A. M. Cycloheptatrienyl pincer iridium complexes - an experimental and theoretical approach., Eberhard-Karls-Universität Tübingen, 2004.
- (67) Mohammad, H. A. Y. Iridium-PCP-Pincer-Komplexe - Oxidative C-H-Additionsreaktionen und Funktionalisierung, Eberhard-Karls-Universität Tübingen, 2002.

-
- (68) Jean, Y.; Eisenstein, O. *Polyhedron* **1988**, *7*, 405-407.
- (69) *Molecular orbitals of transition metal complexes*; Jean, Y., Hrsg.; Oxford University Press, New York, 2005.
- (70) Li, S.; Hall, M. B. *Organometallics* **2001**, *20*, 2153-2160.
- (71) Coe, B. J.; Glenwright, S. J. *Coord. Chem. Rev.* **2000**, *203*, 5-80.
- (72) Appleton, T. G.; Clark, H. C.; Manzer, L. E. *Coord. Chem. Rev.* **1973**, *10*, 335-422.
- (73) Hinderling, C.; Plattner, D. A.; Chen, P. *Angew. Chem., Int. Ed.* **1997**, *36*, 243-244.
- (74) Scott, N. M.; Dorta, R.; Stevens, E. D.; Correa, A.; Cavallo, L.; Nolan, S. P. *J. Am. Chem. Soc.* **2005**, *127*, 3516-3526.
- (75) van der Boom, M. E.; Iron, M. A.; Atasoylu, O.; Shimon, L. J. W.; Rozenberg, H.; Ben-David, Y.; Konstantinovski, L.; Martin, J. M. L.; Milstein, D. *Inorg. Chim. Acta* **2004**, *357*, 1854-1864.
- (76) Goettker-Schnetmann, I.; White, P.; Brookhart, M. *J. Am. Chem. Soc.* **2004**, *126*, 1804-1811.
- (77) Wernitz, M. S. Benzoannelierte Cycloheptatrien-PCP-Pincer-Platinkomplexe, Eberhard-Karls-Universität Tübingen, 2009.
- (78) Lepage, L. L. *Bull. Soc. Chim. Fr.* **1988**, 591-4.
- (79) Van Berkel, G. J.; Kertesz, V. *Anal. Chem.* **2007**, *79*, 5510-5520.
- (80) Takayama, M. *J. Mass Spectrom. Soc. Jpn.* **1996**, *44*, 501-530.
- (81) Hohenberg, P.; Kohn, W. *Phys. Rev.* **1964**, *136*, B864-B871.
- (82) Kohn, W.; Sham, L. J. *Phys. Rev.* **1965**, *140*, A1133-A1138.
- (83) Becke, A. D. *J. Chem. Phys.* **1993**, *98*, 5648-5652.
- (84) Lee, C.; Yang, W.; Parr, R. G. *Phys. Rev. B* **1988**, *37*, 785-789.
- (85) Hay, P. J.; Wadt, W. R. *J. Chem. Phys.* **1985**, *82*, 299-310.
- (86) Ditchfield, R.; Hehre, W. J.; Pople, J. A. *J. Chem. Phys.* **1971**, *54*, 724-728.
- (87) Hehre, W. J.; Pople, J. A. *J. Chem. Phys.* **1972**, *56*, 4233-4234.
-

- (88) Hariharan, P. C.; Pople, J. A. *Theor. Chim. Acta* **1973**, *28*, 213-222.
- (89) Binkley, J. S.; Pople, J. A. *J. Chem. Phys.* **1977**, *66*, 879-880.
- (90) Francl, M. M.; Pietro, W. J.; Hehre, W. J.; Binkley, J. S.; Gordon, M. S.; DeFrees, D. J.; Pople, J. A. *J. Chem. Phys.* **1982**, *77*, 3654-3665.
- (91) Friesner, R. A.; Murphy, R. B.; Ringnalda, M. N. In *Encyclopedia of computational chemistry*; von Schleyer, P. R., Hrsg.; Wiley, 1998; Bd. 3: M - P, S. 2290--2300.
- (92) Frenking, G.; Frohlich, N. *Chem. Rev.* **2000**, *100*, 717-774.
- (93) Niu, S.; Hall, M. B. *Chem. Rev.* **2000**, *100*, 353-406.
- (94) *Computational organometallic chemistry*; Cundari, T. R., Hrsg.; Dekker, 2001.
- (95) *Density-functional theory of atoms and molecules*; Parr, R. G. ; Y., Hrsg.; Oxford University Press, 1994.
- (96) *Encyclopedia of computational chemistry*; von Schleyer, P. R., Hrsg.; Wiley, 1998; Bd. 1-5.
- (97) *Introduction to computational chemistry*; Jensen, F., Hrsg.; Wiley, 1999.
- (98) *Jaguar, version 6.5-7.6*; Schrödinger, LLC, New York, NY, 2009.
- (99) *Maestro, version 7.5-9.0*; Schrödinger, LLC, New York, NY, 2009.
- (100) Hoffmann, H.; Schellenbeck, P. *Chem. Ber.* **1966**, *99*, 1134-1142.
- (101) Fild, M.; Stelzer, O.; Schmutzler, R.; Doak, G. O. In *Inorg. Synth.*; Wold, A.; Ruff, J. K., Hrsg.; McGraw-Hill Book Company, 1975; Bd. 14.
- (102) Gottlieb, H. E.; Kotlyar, V.; Nudelman, A. *J. Org. Chem.* **1997**, *62*, 7512-7515.
- (103) Sheldrick, G. M. *Acta Crystallographica Section A* **2008**, *64*, 112-122.
- (104) Toledo Rodriguez, F. Pd(II) and Rh(III)-XCX pincer complexes and their immobilisation into silica-gel, nanoparticles and silsesquioxanes, Eberhard-Karls-Universität Tübingen, 2008.
- (105) Vigroux, A.; Bergon, M.; Zedde, C. *J. Med. Chem.* **1995**, *38*, 3983-3994.
- (106) Rauchschalbe, G.; Beitzke, B.; Fiege, H. Process for the preparation of the 5-nitro-isophthalic-di- C1-C4-alkyl esters **1998**.

Meine akademischen Lehrer:

K. Albert, H. Clement, T. Chassé, D. Christen, H. Eckstein, H.-J. Egelhaaf, G. Gauglitz, A. Grossmann, G. Häfelinger, V. Hoffmann, W. Jäger, G. Jung, R. Kleiner, H. Kneifel, W. Koch, D. Kölle, D. Krug, N. Kuhn, E. Lindner, M. E. Maier, H. A. Mayer, H.-J. Meyer, U. Nagel, H. Oberhammer, C. Ochsenfeld, D. Oelkrug, E. Plies, H. Pommer, G. Reinhardt, V. Schurig, M. Schwarz, E. Schweda, J. Strähle, G. J. Wagner, U. Weimar, L. Wesemann, K.-P. Zeller, T. Ziegler, C. Zimmermann

Lebenslauf:

Geburt: 8. März 1978 in Stuttgart.

Ausbildung:

- 1984-1988 Grundschole Hemmingen.
- 1988-1993 Hauptschole Hemmingen.
- **1993** **Hauptschulabschluss.**
- 1993-1995 2-jährige-Berufsfachschule Leonberg.
- **Juli 1995** **Fachschulreife.**
- 1995-1998 Naturwissenschaftliches technisches Gymnasium und Ausbildung zum Chemisch technischen Assistenten an der Kerschsteinerschule in Stuttgart Feuerbach.
- **Juli 1998** **fachgebundene Hochschulreife.**
- Sept. 1998 **Zivildienst** am Landesgesundheitsamt Baden Württemberg.
- Okt. 1999 Beginn des Diplom-Chemie Studiums an der Eberhard Karls Universität Tübingen.
- 16. August 2001 Diplomvorprüfung in Chemie (Eberhard Karls Universität Tübingen).
- **1. Juni 2005** **Diplomprüfung in Chemie** (Eberhard Karls Universität Tübingen).
- seit Juni 2005 Promotion in Anorganischer Chemie im Arbeitskreis von Prof. Dr. Hermann A. Mayer an der Eberhard Karls Universität Tübingen mit dem Titel: „Ligand Backbone Effects in Iridium Pincer Complexes - An Experimental and Theoretical Approach“.